Investigation of the impact of atmospheric ionisation on middle atmosphere chemistry and dynamics - model studies with ExoTIC and EMAC

Zur Erlangung des akademischen Grades eines
DOKTORS DER NATURWISSENSCHAFTEN (Dr. rer. nat.)
von der KIT-Fakultät für Physik des
Karlsruher Instituts für Technologie (KIT)

genehmigte

DISSERTATION

von

M.Sc Monali Borthakur
aus Sivasagar, Indien

Tag der mündlichen Prüfung:	29.11.2024
Referent:	Prof. Dr. Peter Braesicke
Korreferent:	PD Dr. Michael Höpfner

Abstract

Solar coronal mass ejections can accelerate charged particles, mostly protons, to high energies, causing Solar Proton Events (SPEs). Such energetic particles can precipitate upon the Earth's atmosphere, mostly in polar regions because of the geomagnetic shielding. Here, SPE induced chlorine activation due to ion-chemistry can occur and the activated chlorine depletes ozone in the polar middle atmosphere. These events can also influence the dynamics of the middle atmosphere across scales from variations in the EUV radiation to extreme solar particle events. We use the state of the art 1D stacked-box Exoplanetary Terrestrial Ion Chemistry model (ExoTIC), of atmospheric ion and neutral composition to investigate such events in the Northern Hemisphere (NH). The Halloween SPE that occurred in late October 2003 is used as a test case for our study. This event has been extensively studied before using different 3D models and satellite observations. Our main purpose is to use such a large event that has been well observed by MIPAS on ENVISAT to evaluate the performance of the ion-chemistry model. Sensitivity tests were carried out for different model settings with a focus on the chlorine species of HOCl and $ClONO_2$ as well as O_3 and reactive nitrogen, NO_y. The model simulations were performed in the Northern Hemisphere at a high latitude of 67.5°N, inside the polar cap. Comparison of the simulated effects against MIPAS observations for the Halloween SPE revealed a rather good temporal agreement, also in terms of altitude range for HOCl, O_3 and NO_y. For $ClONO_2$, a good agreement was found in terms of altitude range. The model showed $ClONO_2$ enhancements after the peak of the event. The best model setting was the one with full ion-chemistry where $O(^1D)$ was set to photo-chemical equilibrium. HOCl and ozone changes are very well reproduced by the model, specially for night-time. HOCl was found to be the main active chlorine species under night-time conditions resulting in an increase of more than 0.2 ppbv. Further, $ClONO_2$ enhancements of 0.2-0.3 ppbv have been observed both during daytime and nighttime. Model settings that compared best with MIPAS observations were applied to an extreme solar event that occurred in 775 A.D., presumably a once in a 1000 year event and also to a high energetic electron precipitation (HEEP) event that occurred over the Moscow region. With the model applied to the extreme scenario, an assessment can be made what is to be expected at worst for effects of a SPE on the middle atmosphere concentrating on effects of ion-chemistry compared to crude parameterisations. Here, a systematic analysis comparing the impact of the Halloween SPE and the extreme event on the Earth's middle atmosphere is presented. As seen from the model simulations, both events were able to perturb the polar stratosphere and mesosphere, with a high production of NO_y and HO_x. Longer lasting and stronger stratospheric ozone loss was seen for the extreme event. Qualitative difference between the two events and a long lasting impact on HOCl and HCl for the extreme event was found. Chlorine ion-chemistry

contributed to a stratospheric ozone loss of 2.4% for daytime and 10% for nighttime during the Halloween SPE as seen with time dependent ionisation rates applied to the model. Furthermore, while comparing the Halloween SPE and the extreme scenario, with ionisation rate profiles applied just for the event day, the inclusion of chlorine ion-chemistry added an ozone loss of 10% and 20% respectively. Studies were performed with the 3D chemistry climate model EMAC to assess the impact of particle forcings and EUV (extreme ultra violet solar flux) forcings during sudden stratospheric warmings (SSWs) to look at the response of coupling from the upper atmosphere. The EUV and thereby the photo-ionisation was varied, that dominates the changes during high solar activity. With EUV forcings, for the simulations with NO_x based parameterisation, ozone levels decrease by 15% in the stratosphere with changing EUV, which went down to the troposphere. The loss was more for higher EUV and higher particle forcing. With the five ion-chemistry reactions in the upper atmosphere included, there is no ozone loss in the stratosphere and below. Instead there is a small ozone formation of 5-10%. In case of the temperatures, the results also showed significant increase of 10-20 K after the event with changing EUV in the altitude range of 50-100 km, which was more consistent in time with higher particle forcing. With five ion-chemistry, there is a decrease in temperature just after the event between 50-100 km and an increase around 100 km, which continues in time. The zonal mean zonal wind shows an increase after the event, which is strong with higher particle forcing and is also continuous in time around 50 km. At 100 km, the zonal mean zonal wind shows a decrease which is stronger for EUV/2. With the five ion-chemistry, there is an acceleration at 100 km and deceleration above, at 150 km. And deceleration at 50 km. The strengthening of the zonal mean zonal wind in the stratosphere with changing EUV is due to dynamical feedback from ozone. The changes in the middle atmosphere overall were found to be quite significant.

Zusammenfassung

Sonnenkoronale Massenauswürfe können geladene Teilchen, meist Protonen, auf hohe Energien beschleunigen und so solare Protonenereignisse (SPEs) verursachen. Solche energiereichen Teilchen können sich in der Erdatmosphäre niederschlagen, vor allem in den Polarregionen aufgrund der geomagnetischen Abschirmung. Hier kann es zu einer durch SPE induzierten Chloraktivierung aufgrund der Ionenchemie kommen, und das aktivierte Chlor baut Ozon in der polaren mittleren Atmosphäre ab. Diese Ereignisse können auch die Dynamik der mittleren Atmosphäre über Skalen hinweg beeinflussen, von Variationen der EUV-Strahlung bis hin zu extremen solaren Teilchenereignissen. Wir verwenden ein hochmodernes 1D-Stacked-Box-Modell für die Exoplaneten-Terrestrische Ionenchemie (ExoTIC) der atmosphärischen Ionen- und Neutralzusammensetzung, um solche Ereignisse in der nördlichen Hemisphäre (NH) zu untersuchen. Das Halloween-SPE, das Ende Oktober 2003 stattfand, dient als Testfeld für unsere Studie. Dieses Ereignis wurde zuvor mithilfe verschiedener 3D-Modelle und Satellitenbeobachtungen umfassend untersucht. Unser Hauptziel ist es, ein so großes Ereignis, das von MIPAS auf ENVISAT aufgezeichnet wurde, zu nutzen, um die Leistung des Ionenchemiemodells zu bewerten. Es wurden Sensitivitätstests für verschiedene Modelleinstellungen durchgeführt, wobei der Schwerpunkt auf den Chlorspezies HOCl und $ClONO_2$ sowie O_3 und reaktivem Stickstoff, NO_y, lag. Die Modellsimulationen wurden auf der Nordhalbkugel in einer hohen Breite von 67,5°N innerhalb der Polkappe durchgeführt. Ein Vergleich der simulierten Effekte mit MIPAS-Beobachtungen für das Halloween-SPE ergab eine recht gute zeitliche Übereinstimmung, auch in Bezug auf den Höhenbereich für HOCl, O_3 und NO_y. Für $ClONO_2$ wurde eine gute Übereinstimmung in Bezug auf den Höhenbereich festgestellt. Das Modell zeigte $ClONO_2$-Verstärkungen nach dem Höhepunkt des Ereignisses. Die beste Modelleinstellung war die mit vollständiger Ionenchemie, bei der $O(^1D)$ auf photochemisches Gleichgewicht eingestellt wurde. HOCl- und Ozonänderungen werden vom Modell sehr gut reproduziert, insbesondere nachts. HOCl erwies sich unter nächtlichen Bedingungen als die wichtigste aktive Chlorspezies, was zu einer Erhöhung um mehr als 0,2 ppbv führte. Darüber hinaus wurden sowohl tagsüber als auch nachts $ClONO_2$-Erhöhungen von 0,2-0,3 ppbv beobachtet. Modelleinstellungen, die am besten mit MIPAS-Beobachtungen übereinstimmten, wurden auf ein extremes Sonnenereignis angewendet, das im Jahr 775 n. Chr. auftrat, vermutlich ein Jahrtausendereignis, und auch auf ein Ereignis mit hochenergetischer Elektronenniederschlagung (HEEP), das über der Region Moskau auftrat. Mit dem auf das extreme Szenario angewendeten Modell kann beurteilt werden, was im schlimmsten Fall an Auswirkungen eines SPE auf die mittlere Atmosphäre zu erwarten ist, wobei man sich auf die Auswirkungen der Ionenchemie im Vergleich zu groben Parametrisierungen konzentriert. Hier wird eine systematische Analyse präsentiert,

die die Auswirkungen des Halloween-SPE und des Extremereignisses auf die mittlere Erdatmosphäre vergleicht. Wie aus den Modellsimulationen hervorgeht, konnten beide Ereignisse die polare Stratosphäre und Mesosphäre stören, mit einer hohen Produktion von NO_y und HO_x. Beim Extremereignis wurde ein länger anhaltender und stärkerer stratosphärischer Ozonverlust beobachtet. Es wurden qualitative Unterschiede zwischen den beiden Ereignissen und eine lang anhaltende Auswirkung des Extremereignisses auf HOCl und HCl festgestellt. Die Chlorionenchemie trug während des Halloween-SPE zu einem stratosphärischen Ozonverlust von 2.4% tagsüber und 10% nachts bei, wie anhand der auf das Modell angewendeten zeitabhängigen Ionisationsraten zu sehen ist. Beim Vergleich des Halloween-SPE und des Extremszenarios mit Ionisationsratenprofilen, die nur für den Ereignistag angewendet wurden, führte die Einbeziehung der Chlorionenchemie außerdem zu einem Ozonverlust von 10% bzw. 20%. Mit dem 3D-Klimachemiemodell EMAC wurden Studien durchgeführt, um die Auswirkungen von Partikel- und EUV-Antrieben (extrem ultravioletter Sonnenfluss) während plötzlicher Stratosphärenerwärmungen (SSWs) zu bewerten und die Reaktion der Kopplung aus der oberen Atmosphäre zu untersuchen. Der EUV und damit die Photoionisation wurden variiert, was die Veränderungen während hoher Sonnenaktivität dominiert. Bei EUV-Antrieben sanken bei den Simulationen mit auf NOx basierender Parametrisierung die Ozonwerte in der Stratosphäre mit sich ändernden EUV-Antrieben um 15%, was bis in die Troposphäre vordrang. Der Verlust war bei höheren EUV- und Partikelantrieben stärker. Unter Berücksichtigung der fünf Ionenchemie-Reaktionen in der oberen Atmosphäre gibt es in der Stratosphäre und darunter keinen Ozonverlust. Stattdessen gibt es eine geringe Ozonbildung von 5-10%. Bei den Temperaturen zeigten die Ergebnisse auch einen signifikanten Anstieg von 10-20 K nach dem Ereignis mit sich ändernden EUV im Höhenbereich von 50-100 km, der zeitlich konsistenter mit höheren Partikelantrieben war. Bei fünf Ionenchemie-Reaktionen gab es direkt nach dem Ereignis zwischen 50-100 km einen Temperaturabfall und bei etwa 100 km einen Anstieg, der sich zeitlich fortsetzt. Der zonale Mittelwert des zonalen Windes zeigt nach dem Ereignis einen Anstieg, der bei höheren Partikelantrieben stark ist und sich auch zeitlich um 50 km fortsetzt. Bei 100 km zeigt der zonale mittlere Wind eine Abnahme, die bei EUV/2 stärker ist. Bei der Fünf-Ionen-Chemie gibt es eine Beschleunigung bei 100 km und eine Verzögerung darüber, bei 150 km. Und eine Verzögerung bei 50 km. Die Verstärkung des zonalen mittleren Windes in der Stratosphäre bei sich änderndem EUV ist auf dynamische Rückkopplung von Ozon zurückzuführen. Die Veränderungen in der mittleren Atmosphäre erwiesen sich insgesamt als recht signifikant.

Publications

Parts of this thesis was published as a peer-reviewed article in the Journal of Atmospheric Chemistry and Physics. The work discussed in Chapter 4 and Chapter 5 are taken literally from this article:
Borthakur, M., M. Sinnhuber, A. Laeng, T. Reddmann, P. Braesicke, G. Stiller, T. von Clarmann, B. Funke, I. Usoskin, J. Wissing, and O. Yakovchuk, 2023: Impact of chlorine ion chemistry on ozone loss in the middle atmosphere during very large solar proton events, Atmospheric Chemistry and Physics, https://doi.org/10.5194/acp-23-12985-2023

Contents

1 Introduction

High energetic particles (e.g. electrons and protons) of solar and cosmic origin precipitate at high latitudes and can alter the chemical composition of the atmosphere by different photo-chemical reactions. This happens via primary collision processes and subsequent ion and neutral chemistry reactions. Such reactions ordered by increasing energy are, e.g., excitation, photo-dissociation, photo-ionisation and dissociative ionisation. These particles come from various particle sources in the outer and near Earth space, accelerated by different processes to different energies. The Earth's atmosphere is vulnerable to such high energetic particles. The vulnerability of the atmospheric ozone layer is clearer through the discovery of the pronounced ozone losses. Extraterrestrial factors can have influences on ozone. This study involves solar proton events which can also induce geomagnetic disturbances in the Earth's magnetosphere, leading to energetic electron precipitation (EEP) events. The solar ultraviolet flux reaches the planet's atmosphere and varies with solar activity, e.g. the Schwabe (11 year) cycle and the distance between the Earth and the Sun. The changing ultra-violet fluxes give rise to varying ozone production and loss rates. During the energetic solar proton events, the fluxes of the energetic protons increase. The protons collide with the atmospheric molecules to yield odd oxides of nitrogen (NO_x=N,NO,NO_2) and hydrogen (HO_x=H,OH,HO_2) which can destroy ozone through their catalytic cycles. The energetic particles precipitate mainly in the polar cap regions, in the mid to high latitudes and can destroy ozone, although the impact is small compared to ozone destruction by anthropogenic forcings, for example.
In this work, an analysis of the impact of atmospheric ionisation from solar proton events (SPEs), energetic electron precipitation (EEP), and hard EUV radiation on the chemical composition and its influence on the dynamics of the atmosphere is presented. Chapter 2 introduces the theoretical background. Chapter 3 is about the description of the methods, i.e., the models and auxilliary data used for the studies. Firstly, a one dimensional ion-chemistry model, ExoTIC, based on Sinnhuber et al. (2012) is used to investigate the impact of Solar Proton Events (SPEs) on the atmospheric composition for short time scales. Secondly, a description of the AISstorm model which is used to calculate the ionisation rates from particle fluxes is given. These ionisation rates are used as an input in the ExoTIC model. Thirdly, a description of balloon observations, as an energetic electron precipitation (EEP) observation methods is provided. Fourthly, the overview of the MIPAS satellite instrument used for validation of the ExoTIC model is discussed. And lastly, a global 3D coupled chemistry climate model (CCM), EMAC (ECHAM/MESSy Atmospheric chemistry) that is used for investigations of dynamical coupling to the chemistry of the atmosphere is discussed. Chapter 4 shows results of model validation with MIPAS satellite observations with a focus on HOCl, $ClONO_2$, total NO_y and ozone loss. Chapter 5 is based on ExoTIC studies of

chlorine activation and ozone loss during extremely large atmospheric ionisation events. A worst case scenario of a solar event that occurred in 775 A.D. and an exceptional case of energetic electron precipitation event over Moscow was considered. The results obtained in this work have contributed to the publication Borthakur et al. (2023). Chapter 5 shows the results of the investigations carried out to study the dynamical coupling to the chemistry of the atmosphere with a focus on Sudden Stratospheric Warmings (SSWs). Simulations of SSW 2009 for free-running EMAC are shown. Then, effects on the chemistry of the middle atmosphere due to different forcings from the upper atmosphere are studied. After that the dynamical feedback from the chemistry is investigated.

2 Theoretical Background

This chapter provides a theoretical basis including a general introduction to the atmosphere and its motion in Sect. 2.1. This is followed by an introduction to the research field: particle precipitation from outer space and near Earth space into the Earth's atmosphere in Sect. 2.2 which includes descriptions of Energetic Electron Precipitation, Solar Proton Events and Galactic Cosmic Rays. The effects of these energetic particles on the chemistry of the Earth's atmosphere are discussed in Sect. 2.4, particularly with a focus on NO_x and HO_x, ozone and chlorine chemistry. Finally, dynamical properties of the middle atmosphere are also discussed in Sect. 2.6 with a focus on the stratospheric polar vortex and its development during sudden stratospheric warmings (SSWs).

2.1 The Earth's Atmosphere

The atmosphere of the Earth is divided into layers based on the vertical structure of the temperature field. These layers are the troposphere, stratosphere, mesosphere and thermosphere and are separated by the tropopause, stratopause and the mesopause. Below the mesopause, the eddy processes keep the constituents well mixed and ionisation plays a minor role. The upper atmosphere is the region above the homopause ($\sim$ 80 km), where molecular diffusion begins to dominate over eddy mixing so that constituents become separated vertically according to their molecular masses and increased ionisation. The main focus of this thesis is on the processes in the stratosphere, mesosphere and lower thermosphere as they affect the middle atmosphere.

2.1.1 The Middle Atmosphere

This is the altitude region of the atmosphere that covers 10-90 km including the stratosphere and the mesosphere. The mean vertical distribution of T in the middle atmosphere is shown in figure 2.1 and can be approximately explained in terms of absorption and emission of radiation. The troposphere is characterised by strong turbulence and vertical mixing. The highest abundance of water vapour and atmospheric phenomena such as clouds and precipitation can be seen in this layer. The temperature minimum is seen at the tropopause which is referred to as the cold point. Cold point tropopause is an important boundary in the tropics with predominant upwelling. However, this definition of the tropopause is irrelevant for water vapor transport into the stratosphere at higher latitudes (Tegtmeier et al., 2020). There is also the lapse rate tropopause, which, offers a globally applicable definition of the tropopause, marking a vertical discontinuity in the static stability (Tegtmeier et al., 2020). The tropopause is the limitation of the

troposphere and is about 15 km in the tropics and at 7 km in polar regions. The temperature gradient above the tropopause is reversed in the layer named the stratosphere. The stratosphere contains about 90% of atmospheric ozone absorbing the ultra-violet (UV) radiation which explains the positive lapse rate. Compared to the troposphere, the stratosphere is very dry and vertical mixing is hindered. The temperature peak at the stratopause at 47-51 km is due to the absorption of solar ultraviolet radiation by ozone, and the minimum at the mesopause around 85-95 km is primarily due to the large decrease in ozone concentration at that level due to absorption by O_2 in the far UV/EUV, which greatly reduces the absorption of solar radiation. The depth of this minimum is driven by atmospheric dynamics, not radiation. The mesosphere is not close to radiative equilibrium (different to the stratosphere). This negative lapse rate in the mesosphere increases again in the thermosphere. The heights of the boundary layers depends on the season and latitude. A minimum temperature of less than 185 K is found in the summer hemisphere at the mesopause which is placed at approximately 80 km. The temperature above the mesopause increases to reach maximum values due to the photolysis of O_2 and N_2 as well as ionisation. This last layer is called the thermosphere.

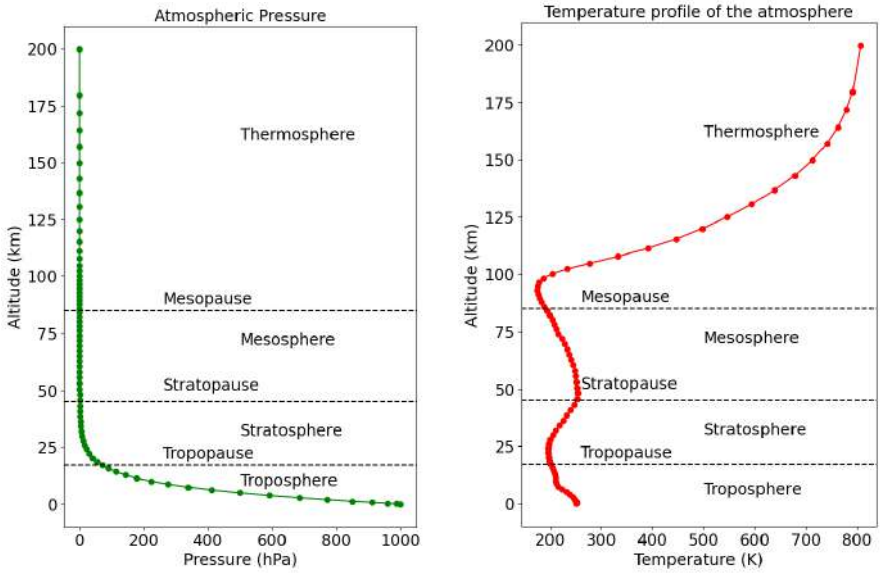

Figure 2.1: Vertical layers of the middle atmosphere. Pressure (left panel) and temperature (right panel) calculated from EMAC.

Given the vertical profile of temperature, the vertical profiles of pressure and density can be determined by use of the ideal gas law and the hydrostatic equation:

$$p = \rho RT, \tag{2.1}$$

$$\frac{\partial p}{\partial z} = -\rho g, \tag{2.2}$$

where R and g are the gas constants for dry air (=287 J K^{-1} kg^{-1}) and the magnitude of the acceleration due to gravity, respectively, and z is the geometric height. All symbols used in this thesis are also summarised in the list of symbols and abbreviations.

The Hypsometric Equation and Scale Height

The geopotential is defined as the work required to raise a unit mass to height z from mean sea level:

$$\Phi = \int_0^z g dz. \tag{2.3}$$

Using Eqs. 2.1-2.3, the hydrostatic equation can be expressed as:

$$\frac{\partial \Phi}{\partial \ln p} = -RT, \tag{2.4}$$

yielding the hypsometric equation upon integration in p:

$$Z_2 - Z_1 = \frac{R}{g_0} \int_{p_2}^{p_1} T d \ln p. \tag{2.5}$$

Z is the geopotential height defined by:

$$Z = \frac{\Phi}{g_0} \tag{2.6}$$

where g_0 = 9.80665 m s^{-2} is the global average of gravity at mean sea level. The difference between geopotential height Z and geometric height z is negligible in the troposphere, but increasingly significant in the upper mesosphere due to the decrease of g with height. The geopotential height difference $\Delta Z = Z_2 - Z_1$ between the pressure levels p_2 and p_1 is known as the thickness of the layer. If a layer mean temperature is defined as

$$< T(p_1, p_2) > \equiv \frac{(\int_{p_2}^{p_1} T d \ln p)}{(\int_{p_2}^{p_1} d \ln p)}. \tag{2.7}$$

then from Eq. 2.5,

$$Z = -\frac{[R < T(p, p_0) >]}{g_0} \ln \frac{p}{p_0} \tag{2.8}$$

where p_0 is the pressure at Z = 0. In an isothermal atmosphere of temperature <T>, pressure decreases exponentially with height by a factor of 1/e. This increase in altitude is called the scale height ($H \equiv R<T>/g_0$).

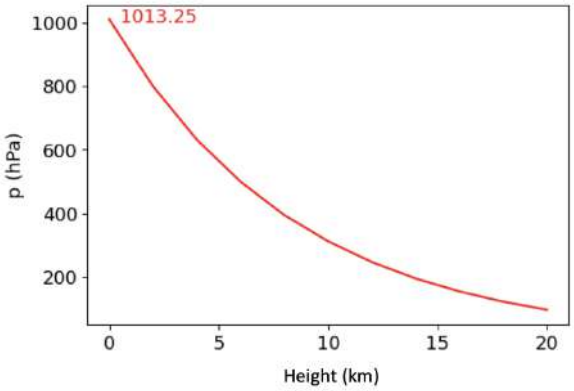

Figure 2.2: The earth atmosphere's scale height is about 8.5 km, as can be confirmed from this diagram of air pressure p by altitude h: At an altitude of 8.5, the pressure is about 370 hPa.

Potential Temperature

The potential temperature of a parcel of dry air at pressure P is the temperature that the parcel would attain if it is adiabatically brought to a standard reference pressure P_0, usually 1,000 hPa (1,000 mb). The potential temperature is denoted by θ and, for an ideal gas is given by

$$\theta = T\left(\frac{P_0}{P}\right)^{\kappa}, \tag{2.9}$$

where $\kappa \equiv \frac{R}{c_p} \approx \frac{2}{7}$ and c_p is the specific heat capacity of dry air at constant pressure. Following Eq. 2.2, if the potential temperature θ decreases with height, the atmosphere is unstably stratified and vertical acceleration of an air parcel is enhanced. And if it increases with height, the atmosphere is stably stratified and the vertical acceleration of an air parcel is negative. If the potential temperature is constant with height, vertical acceleration of an air parcel is zero.

2.2 Particle precipitation

Particle precipitation occurs in the planet's upper atmosphere that causes heating, ionization, and emission (aurora). Nowadays, due to the availability of in-situ data from both the Earth and other planets in the Solar System, the complex coupling of the processes that leads to excitation or ionisation of particles and their effects on planets' upper atmosphere can be properly investigated. The origins of these particles are crucial for unveiling the underlying physics of the planet's atmosphere. High-energy particles (e.g. electrons and protons) precipitate at high latitudes and can alter the chemical composition of the atmosphere, mainly the upper stratosphere to the lower thermosphere by different photo-chemical reactions. This mainly happens due to primary collision processes and subsequent ion and neutral chemistry reactions. Such reactions ordered by increasing energy are e.g. excitation, photo-dissociation, photo-ionization, and dissociative ionization. These particles can come from various sources in outer space, accelerated by different processes to different energies and affect different altitude ranges of the

atmosphere. Such sources are e.g. galactic cosmic rays (GCRs), with protons and heavier nuclei of energies ranging from hundreds of mega-electron volt to giga-electron volt; coronal mass ejections and solar proton events (SPEs) with protons of energies (MeV to GeV); auroral electrons during sub-storms accelerated to energies from 10 keV to hundreds of kilo-electron volt; and medium- and high-energy electrons in the radiation belts to energies from tens of kilo-electron volt to the mega-electron-volt range. Fig. 2.3 shows a schematic of various types of energetic particles as well as solar EUV and X-rays that are involved in atmospheric ionization. The particles that precipitate into the atmosphere, on average, depends on their kinetic energy; the higher the energy, the further down into the atmosphere they will precipitate. Consequently, GCRs will mostly affect the lower stratosphere and troposphere, solar protons the mid stratosphere to the mesosphere, auroral electrons the upper mesosphere and lower thermosphere, and relativistic electrons the mid-stratosphere to the upper mesosphere.

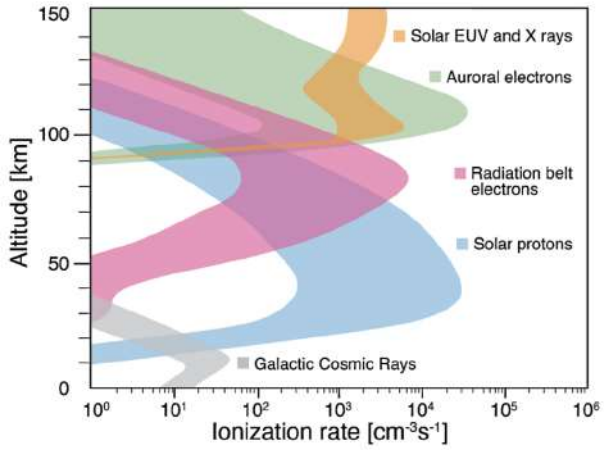

Figure 2.3: Schematic of the various types of energetic particle precipitation into Earth's atmosphere, as well as the altitude profile of the ionization they create. Particle sources: galactic cosmic rays (gray), solar protons (blue), radiation belt electrons (red), and auroral electrons (green). And Photo-ionization due to solar extreme ultraviolet (EUV) rays and X-rays (orange). Figure taken from : Mironova et al. (2015) based on original figure by Baker et al. (2012)

The impact of energetic particle precipitation on the chemical composition of the atmosphere has been studied since the 1960s, and there are a number of observations and model studies concerning especially the auroral impact and large solar particle events. Both SPEs and energetic electron precipitation can have a long-lasting impact on the stratospheric composition, particularly, the stratospheric ozone during polar winter. As ozone is one of the key species in radiative heating and cooling of the stratosphere, changes in its concentration can cause dynamical changes in the middle atmosphere, which can couple down into the troposphere and possibly the surface and affect regional climate patterns. This is due to a coupling of chemical composition changes affecting atmospheric heating and cooling rates, the mean circulation, and wave propagation and breaking. The impact of relativistic electrons from the radiation belts on the mesosphere above 70 km is now also well established from observations; however, a direct impact of

relativistic electrons on stratospheric composition is still a matter of debate. Thus, energetic particle precipitation impacts have been implemented in chemistry-climate models reaching from the surface up to the mesosphere or lower thermosphere. However, there are still a number of open questions in the theoretical description of the energetic particle precipitation impact; the most important are uncertainties in the formation rate of different NO_x species due to energetic particle precipitation, and the complex coupling between chemical changes, atmospheric heating and cooling rates, and atmospheric dynamics.

2.2.1 Earth's Magnetosphere

Earth's magnetic field is generated from the movement of molten iron in the Earth's outer core, creating powerful electric currents. These electric currents are around the lines of the magnetic field between the poles that extend beyond Earth's atmosphere. The Earth's magnetic axis is tilted about 11° from Earth's rotational axis. The magnetic field above the poles extends far into space and shields the Earth from many of the energetically charged particles coming from the Sun and more distant sources in the galaxy deflecting them and trapping them on these field lines. Earth's magnetic field lines are not symmetric with respect to its magnetic axis, unlike those of a bar magnet. The impact of a continuous stream of solar particles (the solar wind) causes the lines facing the Sun to be compressed. The field lines facing away from the Sun get stretched and elongated, forming the Earth's magnetotail. The bullet shaped magnetic bubble formed by the terrestrial magnetic field lines on a whole is called the Earth's magnetosphere. The magnetosphere extends into the vacuum of space, on average, from approximately 60,000 kilometres sun-ward, and trails out more than 300,000 kilometres away from the Sun in the magnetotail. Without the magnetosphere, Earth's layered atmosphere would deteriorate due to the constant bombardment of solar wind. And without our uniquely layered atmosphere, we will be left open to harmful ultraviolet (UV) radiation.

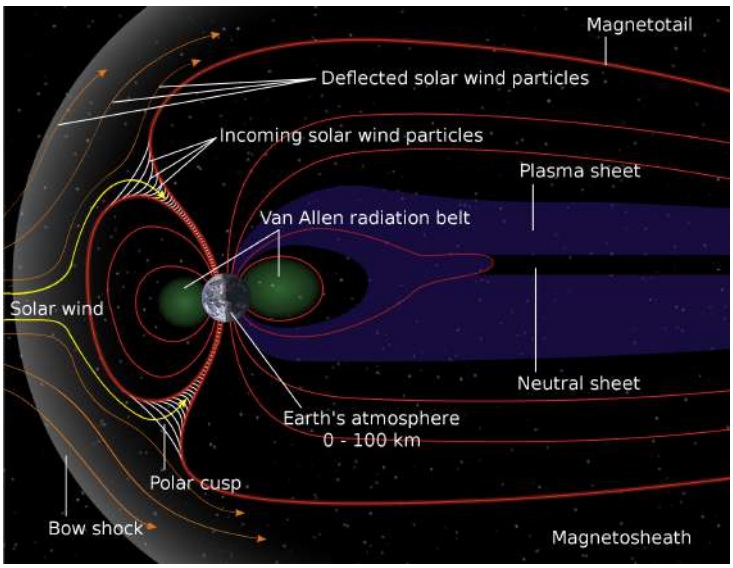

Figure 2.4: Diagram of Earth's magnetosphere. Original Source: NASA (copyrighted)

2.2.2 Energetic Electron Precipitation

Energetic charged particles can become trapped in the Earth's magnetic field much like they can be trapped in the magnetic bottle of a plasma confinement chamber. These trapped particles comprise the Van Allen radiation belts and are a threat to space vehicles, potentially causing single event upsets and deep dielectric charging. Very Low Frequency (VLF) electromagnetic waves propagating in the magnetosphere are capable of interacting with trapped energetic electrons to remove them from the radiation belts. VLF waves can be generated by either natural phenomena, such as lightning, or man-made transmitters and these waves play a major role in controlling the radiation belt populations. A particle's motion can be modified so that instead of remaining trapped in the magnetic bottle of the magnetosphere, it precipitates upon the upper atmosphere where it will harmlessly collide with the neutral particle population and lose its energy. Energetic electron precipitation (EEP) can create communications interferences and other disturbances. Electrons trapped by Earth's magnetic field spiral around field lines to form the Van Allen radiation belt. The electrons are from the solar wind and may remain trapped above Earth for an indefinite period of time (in some cases years). Relativistic electron precipitation changes the chemistry of the upper atmosphere and contributes to depletion of ozone. Energetic electron precipitation (EEP) leads to the enhancement of odd nitrogen NO_x and odd hydrogen HO_x, which play a key role in the ozone balance of the middle atmosphere (e.g., Sinnhuber et al. (2012)). The effect of high latitude EEP on atmospheric composition and ozone is confirmed by various observations (e.g., Sinnhuber et al. (2016)) and 3D chemistry–climate models (e.g. Verronen et al. (2016a)) that account for EEP-induced ionization.

2.2.3 Solar Proton Events

Huge plasma clouds are ejected into space through coronal mass ejections, for example, which may lead to greatly enhanced particle fluxes around Earth. In these plasma clouds, protons may be accelerated to energies of tens to hundreds of MeV, sufficient to precipitate down into the mesosphere and upper stratosphere. These events are therefore also called Solar Proton Events or SPEs. These particles interact with the Earth's magnetosphere and are guided by the Earth's magnetic field towards the north and south poles where they can penetrate into the upper atmosphere. They precipitate into the atmosphere mainly in the polar cap regions pole-ward of 60° geomagnetic latitude, where the geomagnetic field couples to the interplanetary magnetic field. During large SPEs, the polar caps can expand considerably and then reach further into mid-latitudes. The energy loss $\frac{-dE}{dx}$ of a charged particle can be approximately calculated using the Bethe-Bloch formula (Leo, 1994).

$$-\frac{\mathrm{dE}}{\mathrm{dx}} = 2\pi \mathrm{N_a} {\mathrm{r_e}}^2 \mathrm{m_e c^2} \rho \frac{\mathrm{Z}}{\mathrm{A}} \frac{\mathrm{z}^2}{\beta^2} [\ln \frac{2\mathrm{m_e} \gamma^2 \mathrm{v}^2 \mathrm{W_{max}}}{\mathrm{I}^2} - 2\beta^2] \tag{2.10}$$

where the factor, $2\pi \mathrm{N_a} {\mathrm{r_e}}^2 \mathrm{m_e c^2}$ = 0.1535 MeV cm^2/g, r_e is the classical electron radius, which is given by:

$$r_e = \sqrt{\frac{1}{4\pi\varepsilon_0}\frac{e^2}{F_c}}, \tag{2.11}$$

where F_c is the Coulomb force of attraction between two electrons, e is the electron charge, e = 1.6 $\times$ 10^{-19} Coulomb; m_e = 0.511 MeV is the relativistic electron mass, N_a is the Avogadro's constant, I is the average excitation potential, Z is the atomic number of the absorber, A is the atomic weight of the absorber, ρ is the absorber density, z is the charge of the incident particle, $\beta = \frac{v}{c}$ of the incident particle, $\gamma = \frac{1}{\sqrt{1-\beta^2}}$. The classical electron radius, r_e = 2.817 $\times$ 10^{-13} cm. The maximum energy transfer is that produced by a head-on or knock-on collision. For an incident particle of mass M, kinematics gives (Leo, 1994):

$$W_{max} = \frac{2m_e c^2 \eta^2}{1 + 2s\sqrt{1+\eta^2} + s^2}, \tag{2.12}$$

where, $s = \frac{m_e}{M}$. If $M \sim m_e$, then the relationship for maximum energy transfer becomes, $W_{max} = 2m_e c^2 \eta^2$, which is mostly in case of protons. For η, the following applies: $\eta = \beta.\gamma$. The linear energy loss is lower in higher atmospheric layers than in the lower, because the density of the atmosphere is lower there. On their way down the protons lose energy and hence their speed. With decreasing speed the energy loss per distance increases. So both effects ensure that the linear energy loss in the atmosphere increases with penetration depth or decreasing height. This leads to what is called the knee, a sharp increase in linear energy loss just before the proton reaches its full potential.

Polar cap absorption events

Polar cap absorption (PCA) events are due to energetic particles (mainly protons) from the Sun during major solar storms. These protons are guided into the polar regions because of the magnetic field and collide with atmospheric constituents and release energy through ionization at D-region heights or below. During these events in the polar ionosphere, high frequency and very high frequency radio waves are absorbed and low frequency and very low frequency radio waves are reflected at lower altitudes than normal. These events commence and last as long as the energy of incoming protons at approximately greater than 10 MeV exceeds roughly 10 pfu (particle flux units or particles sr^{-1} cm^{-2} s^{-1}) at geosynchronous satellite altitudes.

Ground level enhancements

A Ground Level Enhancement or Ground Level Event (GLE), is a special subset of extremely intense SPEs where charged protons from the Sun having sufficient energy in excess of 200 MeV generate effects which can be measured at the Earth's surface. These particles (mostly protons) are accelerated to high energies either within the solar atmosphere or in interplanetary space, with some debate as to the predominant acceleration method. While solar particle events typically involve solar energetic particles

at 10–100 MeV, GLEs involve particles with energies higher than about 400 MeV. These rare events are known as ground level enhancements (or GLEs). Presently, 73 GLE events are known. The strongest known GLE event was detected on 23-Feb-1956. Some events produce large amounts of HZE ions with heavier nuclei, although their contribution to the total radiation is small compared to the level of protons.

2.2.4 Galactic Cosmic Rays

Galactic Cosmic Rays (GCRs) are the slowly varying, highly energetic background source of energetic particles, consisting mostly of protons and α particles that constantly bombard the Earth. GCRs originate outside the solar system and are likely formed by explosive events such as supernova. These highly energetic particles consist of essentially every element ranging from hydrogen, accounting for approximately 89% of the GCR spectrum, to uranium, which is found in trace amounts only. These nuclei are fully ionized, thereby interacting with and are influenced by magnetic fields. The strong magnetic fields of the Sun modulate the GCR flux and spectrum at Earth. Over the course of a solar cycle the solar wind modulates the fraction of the lower-energy GCR particles such that a majority cannot penetrate to Earth near solar maximum. Near solar minimum, in the absence of many coronal mass ejections and their corresponding magnetic fields, GCR particles have easier access to Earth. Just as the solar cycle follows a roughly 11-year cycle, so does the GCR, with its maximum, however, coming near solar minimum. But unlike the solar cycle, where bursts of activity can change the environment quickly, the GCR spectrum remains relatively constant in energy and composition, varying only slowly with time. These charged particles are traveling at large fractions of the speed of light and have tremendous energy ranging from several 100 MeV far into the EeV range though the particle fluxes decrease strongly with energy, from about 10^4 m^{-2} s^{-1} at 1,000 MeV to $\sim$ 1 km^{-2} year^{-1} at 1 EeV (e.g., Anchordoqui et al. (2003); Abraham (2010)). When these particles hit the atmosphere, large showers of secondary particles are created with some even reaching the ground. Due to the high energies these particles are hardly affected by the Earth's magnetic field and precipitate into the atmosphere everywhere upto the surface. The mesosphere and lower thermosphere region (MLT) is unaffected by GCRs because their flux is too low; secondary particle showers, which provide large fluxes, form at lower altitudes.

2.3 Halloween Solar Proton Event of 2003: Case study I for model validation

The Halloween SPE of 2003 was a series of solar storms involving solar flares and coronal mass ejections that occurred from mid October to early November lasting about two weeks. This event is used as a test scenario for model evaluation and model studies in Chapters 4 and 5. This series of storms generated one of the most intense solar flare ever in the history of space age recorded by the GOES system. The activity produced by the Sun during this period originated from large and complex sunspot groups. The arrival of transient solar wind from Earth directed CMEs produces extreme geomagnetic storming. The severe Halloween solar storm of 2003, for example, disrupted aviation radio communications for

over two weeks and prompted the re-routing of some polar flights. Major solar flare activity was often accompanied by around 43 Coronal Mass Ejections (CMEs) (Gopalswamy et al., 2005), eight X-class flares, and strong energetic particle events of the solar cycle. They also consist of interplanetary shocks, intense geomagnetic storms, and SEPs. The 2003 October-November CMEs were fast and were very energetic. Nearly 20% of the very fast and wide CMEs (speed $\geq$ 2000 km/s) of cycle 23 occurred in October-November. The Halloween SPE peaked on 28^{th} October 2003, which was the fourth largest proton event at > 10 MeV on record and the fastest CME of the study period ($\sim$ 2700 km s^{-1}) occurred on the 4^{th} November 2003. The solar eruptions originated in three active regions (ARs) with NOAA numbers 484, 486 and 488 (Gopalswamy et al., 2005). Each region was large, with Region 486 being the most significant.

2.3.1 28 October, 2003

CME eruption from the Sun was observed on 26 October at 18:19 UTC. The shock driven by the CME arrived at 01:30 UTC on 28 October. Solar wind speed enhanced upto 570 km/s from 450 km/s and the total magnetic field increased from 10 to 20 nT. B_z kept a generally northward orientation, with the exception of a very brief interval of southward orientation shortly after the arrival of the shock. Hence, the geomagnetic disturbance on Earth was limited to isolated periods of minor storming (LCDR M.Weaver, 2004).

2.3.2 29-30 October, 2003

During the Halloween storms, the sixth largest geomagnetic storm on record occurred on 29^{th} of October. The Sun to earth transit took place in less than 19 hours. Solar wind speeds were upto 1900 km/s and strong interplanetary magnetic field variations in the magneto-sheath region was observed. IMF B_z went northward and was that way for 10 hours. Interplanetary magnetic field B_z rotated southward around 18:00 UTC on the 29^{th} of October. This storm gradually weakened on 30 October.

2.3.3 30-31 October, 2003

Another Earth directed halo CME occurred which was 400 km/s slower than the 29^{th} October event. The deceleration of the CME through the interplanetary medium was minimal which impacted Earth's magnetic field at around 16:20 UTC on 30 October, after the 19 hour transit. Initial IMF B_z turning was strong southward and geomagnetic response was intense. On November 1, by 00:00 UTC, the IMF B_z rotated northward. This was the second strongest geomagnetic storm of Solar Cycle 23.

2.4 Chemistry of the middle atmosphere

The structure and composition of the middle atmosphere is determined by radiative and dynamical processes as well as chemical photo-reactions, and the interplay between. Composition is largely dominated

by the chemistry with important cycles such as the O_x, OH_x and NO_x. In this section, the impact of particle precipitation on the composition of the MLT region is discussed, both from the particle-air interaction, and from ion-chemistry. Then, the most important changes to the neutral atmosphere, i.e., the formation of NO_x, O_x and HO_x and the catalytic cycles of ozone loss in the middle atmosphere are discussed.

2.4.1 Aspects of ion-chemistry

EPP affects the chemical composition in the atmosphere through primary excitation as well as the formation of excited states of N_2 and O_2 in the middle and lower atmosphere (Porter et al., 1976; Rusch et al., 1981), atomic oxygen, O in the upper mesosphere and lower thermosphere (MLT) region and He and H in the upper thermosphere (Jones and Rees, 1973). Atmospheric constituents are generally electrically neutral, but charged molecules and atoms together with free electrons play a substantial role in the middle and upper atmosphere. They can be ionised either by short wavelength solar radiation (UV and x-rays), or by precipitating energetic particles:

$$X + h\nu \longrightarrow X^+ + e^- \tag{R1}$$

$$X + e^* \longrightarrow X^+ + 2e^- \tag{R2}$$

with e^* representing an energetic electron. These processes are the starting points for a series of reactions which determine the structure of the ionosphere with significant concentrations of ions of thermal energy. It can be divided into a number of characteristic layers according to the mean vertical profile of electron density as shown in Figure 2.5. The ionosphere is a weakly ionized fluid of net neutral charge. The D-region is located between 60 and 85 km. In this layer, ionization results mostly from photo-ionization of NO by Lyman α radiation at 121.6 nm. High energy cosmic rays also contribute to the ionization of O_2 and N_2 below 70 km.

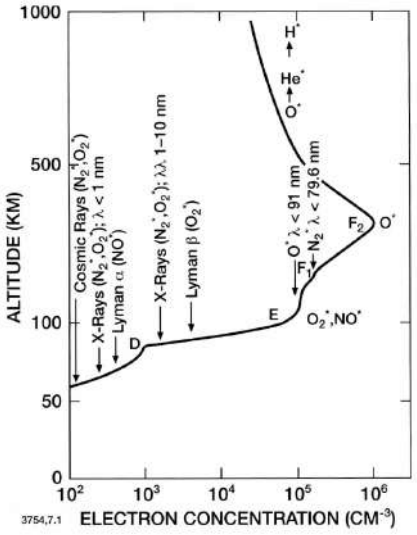

Figure 2.5: Electron density profile with main ionisation sources. Figure taken from Brasseur (2005). Originally by Banks and Kockarts (1973).

The E-region extends from about 85 to 130 km. It is produced by ionization of molecular and atomic oxygen, and molecular nitrogen, by x-rays and Lyman β radiation. Although the predominant ions in this layer are O_2^+ and NO^+, relatively large concentrations of Fe^+, Ca^+, Si^+ and Mg^+ are also observed. The F-region begins above 130 km and is subdivided into two layers F_1 and F_2. It is primarily produced by ionisation of atomic oxygen and molecular nitrogen by extreme ultraviolet radiation (9-91 nm). The atomic oxygen ion, O^+ dominates. In D, E and F_1 layers, the electron concentration is greatest at maximum solar elevation. The electrons disappear almost entirely in the D region, and their density is reduced by a factor of 100 in the E and F_1 regions. In these layers, the lifetime of the ions is short compared to the transport time scale, and the charged particle concentrations are therefore determined by a photo-chemical equilibrium between production (by ionisation processes) and loss (by recombination of positive ions with electrons or with negative ions). In the F_2 region, the electron density is no longer due to a simple equilibrium between ionisation and recombination and the effects of transport by molecular diffusion must be considered, particularly above 300 km. The diatomic nitrogen ions undergo rapid charge exchange reactions:

$$N_2^+ + O_2 \longrightarrow N_2 + O_2^+ \tag{R2}$$

$$N_2^+ + O \longrightarrow N_2 + O^+ \tag{R3}$$

and are therefore effectively removed. The main ionic constituents in the E-region are O_2^+, NO^+ and electrons. The D-region ion-chemistry is much more complex because in the presence of water vapour O_2^+ and NO^+ are transferred to proton hydrates $H^+(H_2O)_n$, and other cluster ions such as $H^+(H_2O)(OH)$, $NO^+(H_2O)$, NO^+N_2, $NO^+(CO_2)$, etc. Electron attachment to molecules of high electron affinity, e.g. oxygen compounds, produce molecular anions. In the D-region, their concentrations exceed electron

concentrations. The ions of N_2 and O_2 are also affected due to the dissociation and ionisation processes. The primary interactions leading to composition changes in the MLT region are dissociation and dissociative ionisation of O_2 and N_2 as well as ionisation of O_2, N_2 and O:

$$O_2 + x \longrightarrow O + O + p \tag{R4}$$

$$N_2 + x \longrightarrow N + N + p \tag{R5}$$

$$N_2 + x \longrightarrow N_2^+ + p + e^- \tag{R6}$$

$$O_2 + x \longrightarrow O_2^+ + p + e^- \tag{R7}$$

$$N_2 + x \longrightarrow N^+ + N + p + e^- \tag{R8}$$

$$O + x \longrightarrow O^+ + p + e^- \tag{R9}$$

x is the incident particle (primary proton, electron or ion, or secondary electron). All processes can form the excited states of the reactants as well, that is, excited states of N, O, N_2^+, O_2^+, N^+, or O^+ (e.g., Jones and Rees (1973); Porter et al. (1976)). The excited species and ions are much more reactive compared to the neutral atoms and molecules. Their formation leads to a chain of very fast reactions, which considerably change the chemical composition of the atmosphere. This includes the formation of odd nitrogen species, NO_x (N and NO) in the auroral regions of the lower thermosphere to the stratosphere, the formation of odd hydrogen species, HO_x (H and OH) in the mesosphere, and formation of nitrous oxide (N_2O) in the MLT region, as well as catalytic ozone loss in the stratosphere and mesosphere. In the lower mesosphere and stratosphere, negative ion-chemistry reactions also lead to the formation of HNO_3 (Verronen et al., 2011) and affect chlorine compounds (Winkler et al., 2009) below 70 km, where energetic electron precipitation does not contribute significantly to ionization.

Formation of NO_x

NO_x is typically defined as the sum of N+NO. During particle precipitation, NO formation occurs by three mechanisms in different altitudes. In the thermosphere, NO is formed via ground state atomic nitrogen, $N(^4S)$, with molecular oxygen:

$$N(^4S) + O_2 \longrightarrow NO + O(^3P, ^1D) \tag{R10}$$

This reaction takes place at high temperatures. In the stratosphere, mesosphere and lower thermosphere (Rusch et al., 1981; Barth, 1992), excited state of atomic nitrogen, $N(^2D)$ can also react with O_2 to form NO:

$$N(^2D) + O_2 \longrightarrow NO + O(^3P, ^1D) \tag{R11}$$

NO can be also destroyed by the scavenging reaction, R12, which is weakly temperature dependent.

$$N(^4S) + NO \longrightarrow N_2 + O \tag{R12}$$

The temperature dependency of the two opposing reactions leads to an efficient NO formation for temperatures higher than several hundreds of K, in the thermosphere above $\sim$ 150 km. Enhanced electron precipitation leads to enhanced Joule heating, maximizing in the auroral regions of the lower thermosphere above $\sim$ 120 km (Barth, 1992). Reaction R10 is temperature dependent and is a major source of NO in this region. NO production is also initiated by ion chemistry reaction chains in the MLT region forming NO^+, for example Sinnhuber and Funke (2020):

$$N_2^+ + O \longrightarrow NO^+ + N \tag{R13}$$

$$N^+ + O_2 \longrightarrow NO^+ + O \tag{R14}$$

$$O^+ + N_2 \longrightarrow NO^+ + N \tag{R15}$$

$$O_2^+ + N_2 \longrightarrow NO^+ + NO \tag{R16}$$

Recombination of NO^+ with electrons leads to the formation of atomic nitrogen:

$$NO^+ + e^- \longrightarrow N + O \tag{R17}$$

The excited states of N can form NO (Reaction R11) while ground state can destroy NO (Reaction R12). Reactions R13, R15 and R17 dominantly form the excited state N(^{2}D). This chain of NO formation by ion-chemistry and via the excited state of N dominates in the mesosphere and lower thermosphere. Ion-chemistry contributes to about 13%-19% of the total NO formation (Rusch et al., 1981; Porter et al., 1976) below $\sim$ 65 km, but the efficiency of this reaction chain increases into the lower thermosphere because of the higher availability of the atomic oxygen needed for Reactions R13 and R15. The effectiveness of NO formation depends on the ratio of the formation of the excited to the ground state of N, as the ground state would lead to the scavenging loss of NO at temperatures below 500 K. Based on Porter et al. (1976), the ratio of excited state (N^{2}D) to ground state N(^{4}S) during the dissociation is nearly equal, i.e., 45%-55%. NO_x formation is set to be 1.25 molecules per ion pair. Based on observations, a much lower ratio of the N(^{4}S) production of 20% (Rusch et al., 1981) and 14%-27% (Baumgaertner et al., 2010a) is predicted.

Formation of HO_x

HO_x is the sum of H and OH that are formed by the uptake of water vapour into large positive cluster ions and the subsequent release of hydrogen during recombination reactions of these cluster ions. HO_x formation during EPP events along with the ion-chemistry processes were first considered by Solomon et al. (1981). They take place after the initial formation of ion pairs. OH is released through ion-pairs:

$$O_4^+ + H_2O \longrightarrow O_2^+(H_2O) + O_2 \tag{R18}$$

$$O_2^+(H_2O) + H_2O \longrightarrow H^+(H_2O) + OH + O_2 \tag{R19}$$

Protonised water cluster ions $H^+(H_2O)_n$ can grow by uptake of more water vapour, and recombination reactions with electrons release H:

$$H^+(H_2O)_n + e^- \longrightarrow H + nH_2O \tag{R20}$$

Another possibility is the formation of H_3O^+ containing ions via:

$$O_2^+(H_2O) + H_2O \longrightarrow H_3O^+(OH) + O_2 \tag{R21}$$

which release both H and OH during recombination with electrons. In this chain, H and OH are formed in equal amounts, balancing the uptake of H_2O. Water cluster ions can also be formed by reaction of NO^+ with H_2O, forming $NO^+(H_2O)$, and subsequent reaction with water vapour form the protonised water cluster:

$$NO^+(H_2O)_n + H_2O \longrightarrow H^+(H_2O) + HNO_2 \tag{R22}$$

HO_x formation depends on the availability of water vapour, which decreases significantly in the upper mesosphere above $\sim$ 80 km; HO_x formation is therefore restricted to the mid to lower mesosphere and stratosphere. Studies such as Verronen and Lehmann (2015) show that HO_x can be produced solely by neutral gas-phase chemistry following enhanced particle precipitation as a consequence of the increase in NO, which changes the partitioning between OH and HO_2, impacting the lifetime of HO_x.

2.4.2 Ozone formation

Ozone is a very important species in the stratosphere that absorb the ultra violet (UV) radiation which is harmful to life. Figure 2.6 shows an ozone profile in number density and volume mixing ratio for the mid-latitudes between 10 to 120 km. The ozone layer lies between 20 to 40 km, while its peak in volume mixing ratio (8-11 ppmv) is located around 35 km. The number density peak of ozone is however situated at a lower altitude of about 15-25 km, since pressure decreases exponentially with increasing height. S.Chapman (1930) suggested a theory for ozone formation and destruction in the stratosphere, called the Chapman mechanism:

$$O_2 + h\nu(\lambda < 242\text{nm}) \longrightarrow 2O \tag{R23}$$

$$O + O_2 + M \longrightarrow O_3 + M \tag{R24}$$

$$O_3 + h\nu(\lambda = 242 - 336\text{nm}) \longrightarrow O(^1D) + O_2 \tag{R25}$$

$$O(^1D) + M \longrightarrow O + M \tag{R26}$$

$$O + O_3 + M \longrightarrow 2O_2 + M \tag{R27}$$

Here, $h\nu$ is the energy of a photon, λ denotes the wavelength of electromagnetic radiation and M is any molecule in the atmosphere. The atomic oxygen from Reaction R23 is in the ground level triplet

state O(^{3}P) and highly reactive due to its two unpaired electrons. The O(^{3}P) immediately reacts with an oxygen molecule and produces ozone in Reaction R24 which is significant in the area where the concentration of O is high such as the upper stratosphere or low latitudes. Ozone is also photolysed by the UV radiation at wavelengths below 336 nm.

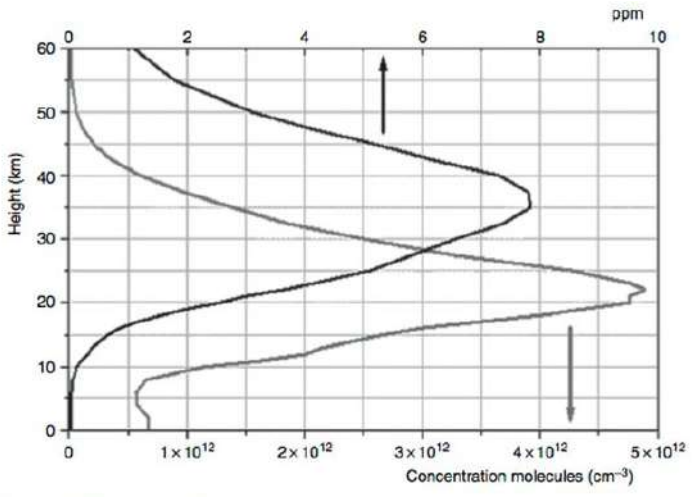

Figure 2.6: Vertical profile of ozone in the troposphere and stratosphere (U.S. Standard Atmosphere), in mixing ratio (ppm), peaking at about 36 km and concentration peaking at about 22 km.

2.4.3 Catalytic cycles of ozone destruction

NO_x and HO_x:

NO_x and HO_x contribute to ozone loss in catalytic cycles of the form:

$$X + O_3 \longrightarrow XO + O_2 \tag{R28}$$

$$XO + O \longrightarrow X + O_2 \tag{R29}$$

$$\text{Net} : O_3 + O \longrightarrow 2O_2 \tag{R30}$$

where reactant X is reformed in the second step, usually either by reaction with atomic oxygen or by photolysis. In the middle and upper mesosphere above $\sim$ 60 km, catalytic cycles with X = H dominate whereas in the lower stratosphere (10-30 km), X = HO_2. In every chain of Reactions R28 and R29, one molecule of O_3, O(^{3}P), or O(^{1}D) is lost while reforming H and OH. In the upper stratosphere in the altitude range between 30 and 45 km, catalytic cycles with NO_x i.e., X = NO are most important (Lary, 1997). Energetic electron precipitation therefore leads to ozone loss in both the stratosphere and the mesosphere, by different mechanisms. In the upper mesosphere and lower thermosphere, ozone loss is negligible because NO is not efficient for ozone loss there and HO_x production is low.

Chlorine catalytic cycles:

A significant part of the total anions in the mesosphere is negative chlorine species (Chakrabarty and Ganguly, 1989). The chloride ion (Cl^-) is an abundant ion in the lower D-region during both daytime and night-time. Other D-region negative ions like O_2^-, O^-, CO_3^-, OH^-, NO_2^- and NO_3^- can react with HCl to produce Cl^- which forms $Cl^-(X)$, where X = (HCl, H_2O, CO_2 and HO_2) (Kopp and Fritzenwallner, 1997). Cl^- and $Cl^-(H_2O)$ are the most abundant chlorine ions in the mesosphere, as indicated by previous studies like Kopp and Fritzenwallner (1997), Chakrabarty and Ganguly (1989) and Turco (1977a). Both species can react with H, re-releasing HCl and some of the recombination reactions of negative chlorine species with positive ions like H^+ release Cl, ClO, $ClNO_2$ and Cl_2. Since the ion reactions are faster, the SPE impacts due to chlorine ion-chemistry are expected to occur without any notable delay.

Apart from the NO_x and HO_x catalytic cycles, solar proton events can also affect stratospheric chlorine chemistry, but whether solar protons effectively activate or deactivate chlorine depends on illumination conditions. The ion production rates increase during a SPE and influence the chemistry of both charged and uncharged chlorine species. The neutral compounds of chlorine can then contribute to ozone loss. The chlorine catalytic cycles of ozone destruction are very efficient around 40 km (Lary, 1997). SPE induced changes of chlorine species can contribute to the short-term ozone depletion occurring after the SPE (von Clarmann et al., 2005). This influence is indirect and is mainly caused by NO_x and HO_x enhancements. The ClO_x ozone loss catalytic cycle, where ClO photolyses:

$$ClO + O \longrightarrow Cl + O_2 \tag{R31}$$

$$Cl + O_3 \longrightarrow ClO + O_2 \tag{R32}$$

$$\text{Net} : O_3 + O \longrightarrow O_2 + O_2 \tag{R33}$$

is the main cycle responsible for ozone loss in the middle and upper stratosphere between 40 and 50 km (Daniel et al., 1999). This cycle stops when Cl and ClO are converted to the reservoir species, HCl and $ClONO_2$ by reactions with CH_4 and NO_2.

$$Cl + CH_4 \longrightarrow HCl + CH_3 \tag{R34}$$

$$ClO + NO_2 + M \longrightarrow ClONO_2 + M \tag{R35}$$

O is formed by the photolysis of O_2 and O_3 and is available during daytime. The catalytic cycle involving hypochlorous acid (HOCl) and ClO acts as a link between chlorine and HO_x enhancements as a result of the SPEs (Reactions R37, R38, R39, R40 and R41) (Lary, 1997). HOCl can photolyse during daytime and the OH formed can react with O_3 reforming HO_2 and Cl reforming ClO thereby recycling HOCl again through Reaction R37. This cycle mainly plays a role in the sunlit polar lower stratosphere (Lary, 1997). Reactive Cl can also be formed via reaction of OH with HCl.

$$OH + HCl \longrightarrow H_2O + Cl \tag{R36}$$

$$ClO + HO_2 \longrightarrow HOCl + O_2 \tag{R37}$$

$$HOCl + h\nu \longrightarrow Cl + OH \tag{R38}$$

$$Cl + O_3 \longrightarrow ClO + O_2 \tag{R39}$$

$$OH + O_3 \longrightarrow HO_2 + O_2 \tag{R40}$$

$$\text{Net} : 2O_3 \longrightarrow 3O_2 \tag{R41}$$

von Clarmann et al. (2005) showed an enhancement of chlorine monoxide, ClO and HOCl immediately after the SPE. They concluded that this was due to the Reactions R39 and R37. During an SPE, HOCl and reactive Cl present in the stratosphere can react with OH and HO_2 respectively, to form ClO. Other reactions of Cl with HO_2 and H_2O_2 can yield in the production of HCl, which is the most important stratospheric reservoir species of Cl.

$$HOCl + OH \longrightarrow ClO + H_2O \tag{R42}$$

$$Cl + HO_2 \longrightarrow ClO + OH \tag{R43}$$

$$Cl + HO_2 \longrightarrow HCl + O_2 \tag{R44}$$

$$Cl + H_2O_2 \longrightarrow HCl + HO_2 \tag{R45}$$

This is another effective ozone loss cycle involving SPE induced NO_x enhancements between 15 and 40 km (Lary, 1997). ClO can react with nitric oxide (Reactions R46, R47, R48 and R49), that is most important in the 15 to 50 km altitude range as suggested by J. C. Farman and Shanklin (1985). NO_x enhancements are also essential regarding the production of $ClONO_2$. López-Puertas et al. (2005) and von Clarmann et al. (2005) reported the first experimental confirmation of Reaction R50 under SPE conditions. ClO reacts with nitrogen dioxide, NO_2 which is most efficient in the lower stratosphere, forming $ClONO_2$ (Reactions R50, R51, R52, R53 and R54).

$$ClO + NO \longrightarrow Cl + NO_2 \tag{R46}$$

$$NO_2 + O(^3P) \longrightarrow NO + O_2 \tag{R47}$$

$$Cl + O_3 \longrightarrow ClO + O_2 \tag{R48}$$

$$\text{Net} : O(^3P) + O_3 \longrightarrow 2O_2 \tag{R49}$$

$$ClO + NO_2 \longrightarrow ClONO_2 \quad \text{(R50)}$$

$$ClONO_2 + h\nu \longrightarrow Cl + NO_3 \quad \text{(R51)}$$

$$NO_3 + h\nu \longrightarrow NO + O_2 \quad \text{(R52)}$$

$$Cl + O_3 \longrightarrow ClO + O_2 \quad \text{(R53)}$$

$$\text{Net} : O(^3P) + O_3 \longrightarrow 2O_2 \quad \text{(R54)}$$

Polar Ozone Depletion

Exceptionally high ClO in the winter plays a role in the ozone destruction in the polar vortex (see subsection 2.6.3).

$$ClO + ClO + M \longrightarrow ClOOCl + M \quad \text{(R55)}$$

$$ClOOCl + h\nu \longrightarrow ClOO + Cl \quad \text{(R56)}$$

$$ClOO + M \longrightarrow Cl + O_2 + M \quad \text{(R57)}$$

$$2 \times (Cl + O_3) \longrightarrow 2 \times (ClO + O_2) \quad \text{(R58)}$$

$$\text{Net} : 2O_3 \longrightarrow 3O_2 \quad \text{(R59)}$$

Another catalytic cycle involving Br radicals important for ozone depletion:

$$ClO + BrO + M \longrightarrow Cl + Br + O_2 \quad \text{(R60)}$$

$$(ClO + BrO \longrightarrow BrCl + O_2 \quad \text{(R61)}$$

$$BrCl + h\nu \longrightarrow Cl + Br) \quad \text{(R62)}$$

$$Cl + O_3 \longrightarrow ClO + O_2 \quad \text{(R63)}$$

$$Br + O_3) \longrightarrow BrO + O_2 \quad \text{(R64)}$$

$$\text{Net} : 2O_3 \longrightarrow 3O_2 \quad \text{(R65)}$$

Since sunlight is required for these cycles, ozone cannot be destroyed by these reactions during polar night. High values of ClO is sustained by extremely cold temperatures inside the polar vortex. Heterogeneous reactions on polar stratospheric clouds (PSCs) produce ClO_x. On PSCs particles, the Cl_x reservoirs HCl and $ClONO_2$ are converted to active chlorine through reactions R66 and R67.

$$HCl + ClNO_3 \xrightarrow{\text{PSC}} Cl_2 + HNO_3 \quad \text{(R66)}$$

$$Cl_2 + h\nu \longrightarrow 2Cl \quad \text{(R67)}$$

2.5 Radiation

The rate of chemical reactions in the atmosphere between two constituents usually depends on the local temperature which is affected by scattering, absorption and emission of solar and terrestrial radiation.

The solar radiation of particular energies dissociates and ionizes important atmospheric molecules like N_2 and O_2 producing their reactive ions, that participates in important processes. The energy of a photon is given by:

$$E = \frac{hc}{\lambda} = h\nu = hc\bar{\nu} \tag{2.13}$$

where h = 6.626 $\times$ 10^{-34} Js is the Planck's constant. Table 2.1 gives the regions of electromagnetic spectrum and the magnitude of solar variability in each spectral region. The photons absorbed can induce transitions between ground and excited states. There are rotational and vibrational energy states and the difference between rotational energy levels are much smaller than those of the vibrational states. Due to relatively high energies required to dissociate or ionize atmospheric gases, photo-chemistry is initiated by less than 1% of the solar photons, those whose characteristic wavelengths are in the X-ray, UV or visible region.

Subregion	Range	Solar Variability	Comments
X-rays	$\lambda < 10$ nm	10-100 %	Photoionizes all thermospheric species.
Extreme UV	$10 < \lambda < 100$ nm	50 %	Photoionizes O_2 and N_2 and photodissociates O_2
Far UV	$100 < \lambda < 200$ nm	7-80 %	Dissociates O_2.
Middle UV, or UV-C	$200 < \lambda < 280$ nm	1-2 %	Dissociates O_3 in intense Hartley bands.

Table 2.1: Important regions of electromagnetic spectrum. Adapted from Thomas and Stamnes (2002)

Radiation can be quantified from a black body that obeys the Planck's law:

$$B_\nu = \frac{2h\nu^3}{c^2(e^{\frac{h\nu}{k_B T}} - 1)}, \tag{2.14}$$

where k_B is the Boltzmann's constant and h is the Planck's constant. It can also be expressed in wavelength,

$$B_\lambda = \frac{2hc^2}{\lambda^5(e^{\frac{hc}{\lambda k_B T}} - 1)} \tag{2.15}$$

The total energy flux F emitted by a black body can be estimated by integration of equation 2.15 over all wavelengths and a half sphere, giving F = σ T^4. σ_s is the Stefan Boltzmann's constant. At ultraviolet wavelengths below 400 nm, ozone is the primary absorber of radiation. Molecules in the atmosphere scatter incoming solar radiation into random directions. This is known as Rayleigh scattering and is responsible for the reduction in irradiance throughout the visible part of the spectrum. Molecular oxygen, O_2 is responsible for some absorption of light in the red and near infrared region (600 nm – 800 nm), as is water vapour, H_2O, which also has strong absorption bands for light in the mid-infrared region up to 3000 nm. Carbon dioxide, CO_2 begins to contribute to absorption of light above approximately 2500 nm. Local effects, such as weather and pollution levels can further change the terrestrial spectrum. In space,

the solar spectrum is more like the radiation of a black body and covers different wavelengths. However, the Earth's surface absorbs the selected sunlight, regulated by the atmosphere at a certain wavelength. Sunlight comprises photons, minuscule particles that carry the electromagnetic waves originating from the sun and traveling through space. According to figure 2.7, the solar spectral irradiance curve covers a broad range of wavelengths and forms the distribution of extraterrestrial radiation. However, the atmosphere attenuates several parts of the spectrum and regulates the solar radiation delivered to the Earth's surface by the elimination of x-rays, for instance.

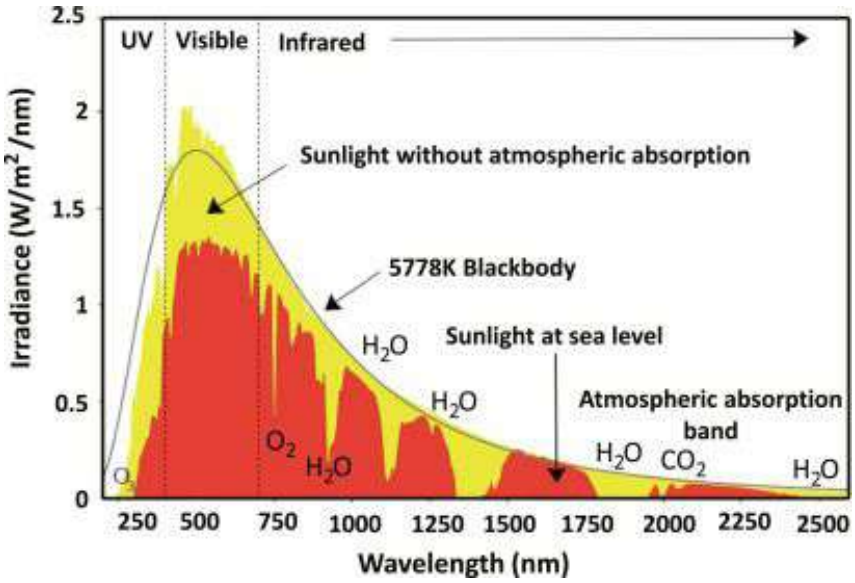

Figure 2.7: Solar spectra as a function of wavelength. Figure taken from Cleveland and Morris (2013)

2.5.1 Radiative Transfer Equation

Incoming radiation that passes through the atmosphere is attenuated due to scattering, emission and absorption by gases. The attenuation of the radiation depends on the intensity of radiation, the local concentration of the medium and the effectiveness of the absorbers and scatterers. Solar photons are scattered and absorbed as they undergo collisions with atmospheric molecules. The absorption probability depends on the type of the molecule and wavelength of the incoming photon. The radiative transfer equations describes the intensity of the monochromatic radiation along a path s in the medium. Figure 2.8 shows an atmospheric layer of thickness 'δs' where I_λ is the incident intensity of wavelength, λ at a height 's' above ground (unit: wavelength $\times$ area $\times$ solid angle). k_λ is the air's absorption cross-section (with units of area/mass) and ρ is air's density. Scattering is ignored in this case.

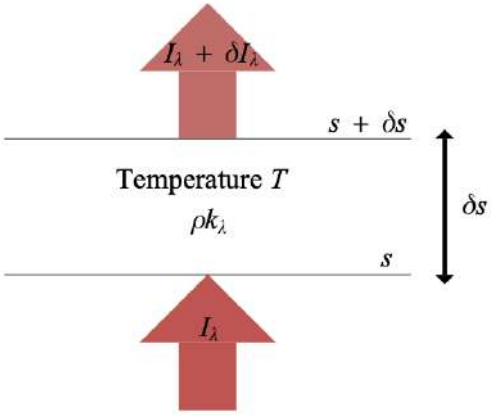

Figure 2.8: Radiation traversing an atmospheric layer of thickness δs

The emission of radiance from the layer involves the Planck function, $B_\lambda(T)$, which is a function of the layer's temperature, T. $B_\lambda(T)$ has the same units as I_λ. In a unit area of radiation into which the radiation passes, the mass of the layer is $\rho\delta$s. So the area of the emitter is then $k_\lambda\rho\delta$s. The contribution from emission is thus,

$$\delta I_{emission} = k_\lambda \rho \delta s B_\lambda(T), \tag{2.16}$$

The absorption of radiance from the layer, also known as the Beer-Lambert law is described as:

$$\delta I_{absorption} = -k_\lambda \rho \delta s \times I_\lambda \tag{2.17}$$

with,

$$k_\lambda \rho = k_a = \sigma n \tag{2.18}$$

where k_a is the absorption coefficient (cm^{-1}) and is related to the effective cross section σ_a and concentration n (cm^{-3}) of the absorbing medium. Therefore, the total change in radiation which gives the combined effect, also known as the radiative transfer is:

$$\frac{dI_\lambda}{ds} = \rho k_\lambda (B_\lambda(T) - I_\lambda) \tag{2.19}$$

If equation 2.19 is multiplied by an integrating factor, $e^{\int_0^s \rho k_\lambda ds'}$, it becomes,

$$\frac{dI_\lambda}{ds} e^{\int_0^s \rho k_\lambda ds'} = \rho k_\lambda (B_\lambda(T) e^{\int_0^s \rho k_\lambda ds'} - I_\lambda e^{\int_0^s \rho k_\lambda ds'}) \tag{2.20}$$

The optical thickness $\tau_\nu(s_1, s_2)$ between two points s_1 and s_2 on the line of sight is defined as:

$$\tau_\nu(s_1, s_2) = \int_{s_1}^{s_2} \rho k_\lambda ds \tag{2.21}$$

and the corresponding attenuation $\eta_\nu(s_1, s_2)$ is given by,

$$\eta_\nu(s_1, s_2) = e^{-\tau_\nu(s_1, s_2)}. \tag{2.22}$$

The transmittance $\tau(s)$ in the atmosphere is defined as the attenuation factor that a radiation suffers if it were to traverse from height s to the top of the atmosphere:

$$\tau(s) = e^{-\int_s^\infty \rho k_\lambda \, ds}, \tag{2.23}$$

or,

$$\tau(s) = e^{-\tau_\nu(s,\infty)}. \tag{2.24}$$

2.5.2 Solar zenith Angle

The solar zenith angle is the zenith angle between the sun's rays (line of sight from the ground to the sun) and the vertical direction from that point to the sun. The higher the sun is in the sky, the lower is the solar zenith angle. The angle between the local zenith line and the line of sight to the satellite is called the viewing zenith angle. The value of the solar zenith angle, θ_z, depends on local date and time on the Earth, season, latitude and its position.

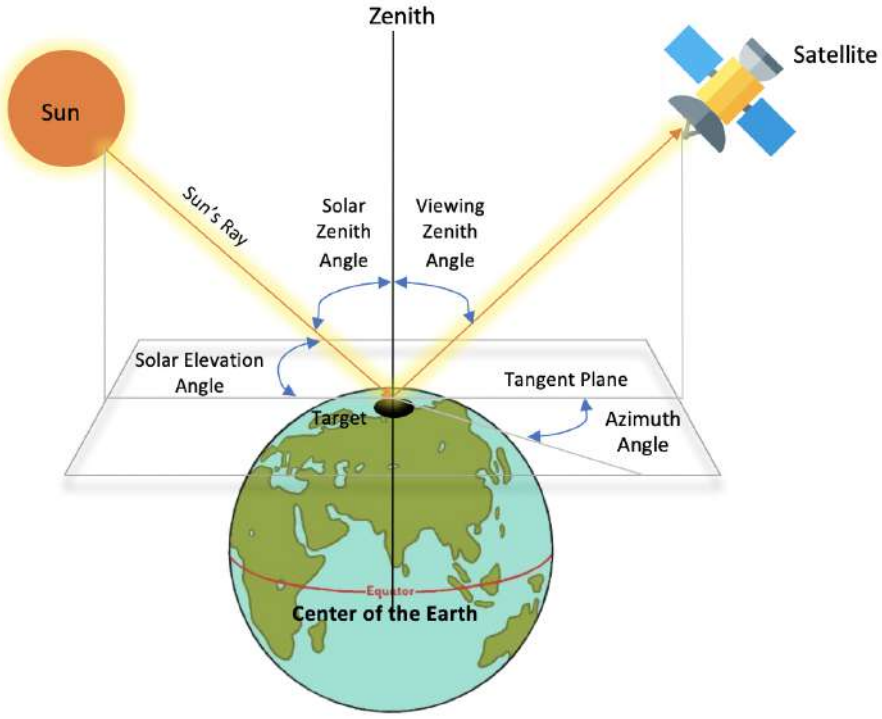

Figure 2.9: Schematic illustration of the Solar Zenith Angle (SZA), Viewing Zenith Angle (VZA), solar elevation angle and azimuth angle for observations from satellite-based instrument.

$$\cos\theta_z = \sin\alpha_s = \sin\delta\sin\phi + \cos\delta\cos\phi\cos\omega, \tag{2.25}$$

α_s is the solar elevation angle or solar altitude angle. δ is the declination of the sun, depending on the season, ϕ is the latitude in the Northern Hemisphere (defined as positive) and ω is the hour angle, which is 0° for the local noon and increments by 15° each hour from noon. The latter is a measure of the local time, i.e., it is defined as the angle through which the earth must turn to bring the meridian of the location of observation directly under the Sun. It is basically the dihedral angle between the meridian (containing the axis of the Earth and passing through the zenith). The solar declination is independent of the location and is a function of the day of the year. Figure 2.10 shows the solar zenith angle (SZA) from the ExoTIC model from 26th October-4th November 2003 and the MIPAS overpass from 26th-29th October 2003.

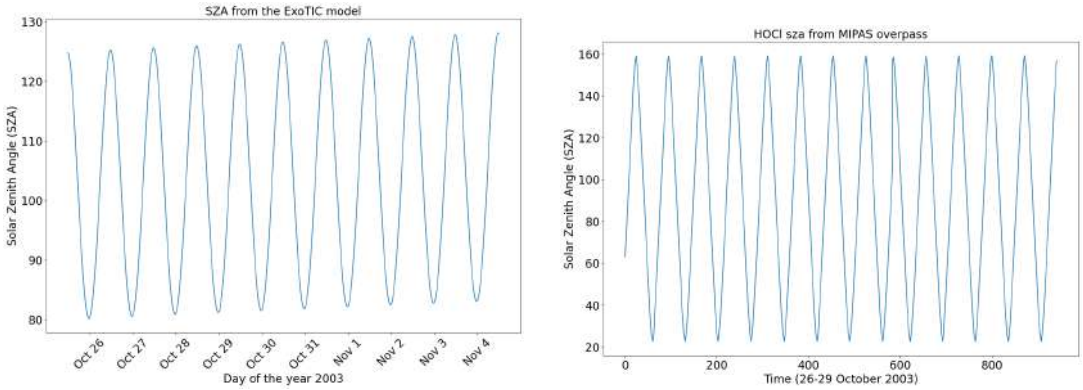

Figure 2.10: Solar zenith angle (SZA) output from the ExoTIC model from 26th October-4th November 2003 (left) and solar zenith angle (SZA) from MIPAS footprints: 26th-29th October 2003 (right).

2.6 Dynamics of the middle atmosphere

The dynamics is rather complex covering from the global scale circulations (the Brewer-Dobson and the meridional circulation) to many scales spatial and temporal propagating waves (atmospheric tides, gravity waves, planetary waves, etc.) leading to the Sudden Stratospheric Warmings (SSWs), which are the most dramatic meteorological phenomenon in the stratosphere and affect the distribution of trace constituents in the stratospheric and tropospheric weather. Radiative processes takes place through the absorption of the solar radiation (mainly in the UV, visible and near-IR), and its partial conversion into atmospheric heat; and the atmospheric cooling, occurring mainly at IR wavelengths. Afterwards, the interaction of particles with atmospheric dynamics and long term impacts of EPP are discussed.

2.6.1 Fundamental description of atmospheric dynamics

The processes in the atmosphere are governed by Newton's laws of motion, and mass and energy conservation. The response of the atmosphere to external forces from outer space and the surface of the Earth is governed by the Newton's second law. In the Earth's frame of reference, which describes the motion of the fluid with the rotating Earth, the first fundamental equation called the momentum equation is given by:

$$\frac{d\tilde{v}}{dt} + \frac{1}{\rho}\vec{\nabla}p + 2\tilde{\Omega} \times \tilde{v} = \tilde{g} + \tilde{F} \tag{2.26}$$

where $\vec{v}$ represents the velocity vector of an air parcel, p is the air pressure, $\vec{\Omega}$ is the angular rotation of the Earth, ρ is the air density, $\vec{g}$ is the acceleration due to gravity (including centrifugal force of the Earth), and $\vec{F}$ is the frictional force. The second term in equation 2.26 is the pressure gradient force and the third term is the Coriolis force, which arises because the frame of reference used to describe the motion is rotating. The second fundamental equation is the conservation of energy:

$$c_p \frac{dT}{dt} - \frac{1}{\rho}\frac{dp}{dt} = Q \tag{2.27}$$

where T is the temperature, c_p represents the specific heat of air at constant pressure and Q is the net heating rate per unit mass (due to physical processes such as radiative effects or release of latent heat). This expression basically describes expansion cooling or compression heating associated with adiabatic processes taking place in a compressible fluid. The remaining term on the right hand side represents diabatic processes involving heating and cooling of the parcel. In the stratosphere and mesosphere, this rate is due to the difference between heating by absorption of solar UV radiation by ozone and in the upper mesosphere and lower thermosphere by molecular oxygen. And cooling by infrared emission by CO_2, O_3, H_2O and other radiatively active molecules. The third is the continuity equation, or conservation of mass,

$$\frac{d\rho}{dt} + \rho\vec{\nabla}.\vec{v} = 0 \tag{2.28}$$

The net radiative heating Q, is the only source of external forcing in the energy conservation. For Q = 0 and for a moving frame of reference, equation 2.27 becomes:

$$c_p \frac{dT}{dt} = \frac{1}{\rho}\frac{dp}{dt}, \tag{2.29}$$

which upon integrating yields,

$$T = Ap^{\kappa} \tag{2.30}$$

where A is a constant and $\kappa = \frac{2}{7} = 0.286$ for dry air. Equation 2.26 can generally be written as three scalar equations often expressed in spherical coordinates, from which the last momentum equation can be simplified to what is called the hydrostatic approximation (for a detailed description, see Chapter 3 of Solomon et al. (1981)):

$$\frac{1}{\rho}\frac{\partial p}{\partial z_g} + g = 0 \tag{2.31}$$

with z_g being the geometric altitude. In the vertical direction, the most important forces acting on an air parcel are the vertical pressure gradient and gravity. Vertical distribution of pressure and air density can be represented by:

$$p(z_g) = p_0 \exp[-\int_{z_{g,o}}^{z_g} \frac{dh}{H_g(h)}] \tag{2.32}$$

$$n(z_g) = \frac{n_o T_o}{T(z)} \exp[-\int_{z_{g,o}}^{z_g} \frac{dh}{H_g(h)}] \tag{2.33}$$

where H_g is the atmospheric scale height and o denotes that value is defined at some reference altitude $z_{g,0}$. If scale height and temperature vary little with altitude,

$$p(z_g) \approx p_o \exp[-\frac{z_g - z_{g,o}}{H_g}] \tag{2.34}$$

$$n(z_g) \approx n_o \exp[-\frac{z_g - z_{g,o}}{H_g}] \tag{2.35}$$

2.6.2 Zonal mean temperature and wind distributions

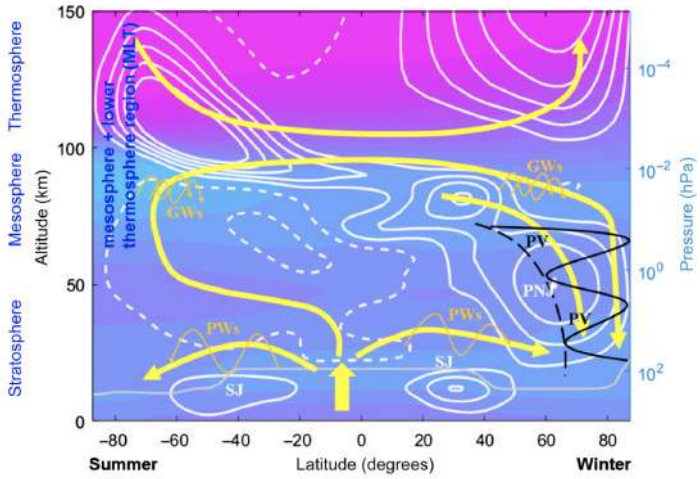

Figure 2.11: Schematic view of the atmosphere from the surface to the lower thermosphere. Figure taken from Sinnhuber and Funke (2020).

In the absence of eddy motions (i.e., departures from zonal symmetry) the middle atmosphere would be close to radiative equilibrium at all latitudes with a solstice temperature distribution similar to Figure 2.11. Although the globally averaged temperature field at each altitude in the stratosphere and mesosphere is in approximate radiative equilibrium, eddy motions induce substantial local departures from equilibrium, especially in the winter stratosphere and near the mesopause in both winter and summer. The overall latitudinally dependent temperature distribution in the middle atmosphere arises from a balance between the net radiative drive (i.e., the sum of the solar heating and infrared heating or cooling) and the heat transport plus local temperature change (often called the dynamical heating or cooling) produced by these motions. Fig. 2.11 shows the atmospheric layers from surface to the lower thermosphere and their connections by wave-driven large-scale circulation. The colored contours in the background are monthly mean zonal temperatures for the Northern hemisphere winter, with temperatures as low as

$\sim$ 120K at the high-latitude summer mesopause (80-100 km shown in light blue) and the highest temperatures of more than 600K in the thermosphere above 130 km (shown in violet). The thin gray line in the lower part of the figure is the tropopause, the transition between the troposphere and the stratosphere. White lines mark the mean zonal winds, easterlies in dashed and westerlies in solid. Westerlies and easterlies are planetary winds that blow from west to east and east to west respectively. They blow in the same direction all year round. Westerlies have a greater speed and force during the winter season. The global wind pattern is also known as the general circulation and the surface winds of each hemisphere are divided into three wind belts: Polar easterlies (60-90°N/S), prevailing westerlies (From 30-60° latitude) and tropical easterlies (From 0-30° latitude). The subtropical jet (SJ) is indicated in the subtropical upper troposphere and the subpolar jet (PJ) at the edge of the polar vortex (PV, marked by black lines) in the stratosphere and lower mesosphere, and the change in wind direction around the mesopause. Yellow lines indicate the mean meridional (residual) circulation, an inter-hemispheric circulation system of the stratosphere and mesosphere characterized by upwelling in the tropics, downward and poleward transport in the lower stratosphere in both hemispheres, upward motion throughout the summer hemisphere in the upper stratosphere and mesosphere, transport from the summer pole to the winter pole, and large-scale downwelling over the winter pole. The stratospheric branch of the circulation, called the Brewer-Dobson circulation is driven by dissipating planetary waves (PWs), which are more active in the Northern hemisphere in boreal winters. The mesospheric branch of the circulation, the meridional overturning circulation is driven by dissipating gravity waves (GWs), that are generated in the troposphere either by topography (orographic GWs) or fronts and convection (non-orographic GWs). The mesosphere-lower thermosphere (MLT region), typically used to encompass the upper mesosphere and lower thermosphere (70-150 km) is a transitional region where signals from the space environment are transferred into the atmosphere and vice versa.

2.6.3 Stratospheric Polar Vortex

The stratospheric polar vortex is a large region of cold, rotating air of low pressure. Polar vortices encircle both polar regions of Earth. The term polar vortex is used to describe both the tropospheric and stratospheric polar vortex. They are both distinct phenomena with different structures, seasonal cycles and impacts on weather. The stratospheric polar vortex is an area of high-speed, cyclonically rotating winds around 15 km to 50 km high, poleward of 50°, and it exists in winter and is the strongest in mid-winter and weakens during an SSW. It forms in Autumn when Arctic or Antarctic temperatures cool rapidly as the polar night begins. A polar vortex strengthens in the winter and weakens in the summer because of its dependence on the temperature difference between the equator and the poles. The increased temperature difference between the pole and the tropics causes strong winds, and the Coriolis effect causes the vortex to spin up. In the Arctic, the distribution of land masses at high latitudes in the Northern Hemisphere gives rise to Rossby waves which contribute to the breakdown of the polar vortex, whereas in the Southern Hemisphere the vortex is less disturbed. The stratospheric polar vortex

breaks down in Spring as the polar night ends. Weather forecasters examine the polar vortex by looking at conditions tens of thousands of feet up in the atmosphere. When we feel extremely cold air from the Arctic regions at Earth's surface, it is sometimes associated with the polar vortex. This is not confined to the United States. Portions of Europe and Asia also experience cold surges connected to the polar vortex. By itself, the only danger to humans is the magnitude of how cold temperatures will get when the polar vortex expands, sending Arctic air southward into areas that are not typically that cold.

2.6.4 Sudden stratospheric warmings and role of dynamics

Sudden stratospheric warmings (SSWs) are events that disturb the circulation in the winter hemisphere. They affect the stratosphere, the mesosphere and the thermosphere. They are mainly characterised by the breakdown of the polar vortex and increase of North Pole temperatures by more than 50K over a few days. This warming of stratospheric air can reverse the circulation in the Arctic Polar Vortex from counter-clockwise to clockwise. A signature of an SSW is the reversal of the zonal mean zonal wind which is a downward propagating feature that begins near the stratopause ($\sim$50 km altitude) and descends to the lowest levels of the stratosphere ($\sim$15 km altitude). The changes in the stratosphere are due to changes in the troposphere below. The stratospheric wind structure filters the smaller scale waves, only allowing the tropospheric planetary waves to propagate up into the stratosphere, break, and deposit energy and momentum during the Northern Hemisphere winter. These waves are forced by mountain systems of the northern hemisphere and the land sea contrasts between continents and oceans. The waves are also characterised by their very large scales, referred to as the planetary scale waves. When planetary waves (with wave numbers of 1 or 2) deposit their momentum, the polar night jet slows down and even reverses. An example of an effect on the troposphere is the change in speed of the Atlantic Ocean circulation pattern. As the waves move upward into the stratosphere they have two effects: first they will often push the polar vortex away from the North Pole, thereby bringing warmer mid-latitude air pole-ward, and second, they produce a downward motion field that also warms the polar region. SSWs are either displacement events in which the stratospheric polar vortex is displaced from the pole or split events in which the vortex splits into two or more vortices. The vortex split is known as wave-2 pattern since there are two high and two low centres. Vortex displacement events are known as wave-1 pattern. Figure 2.12 shows a vortex displacement and a vortex split event of an SSW.

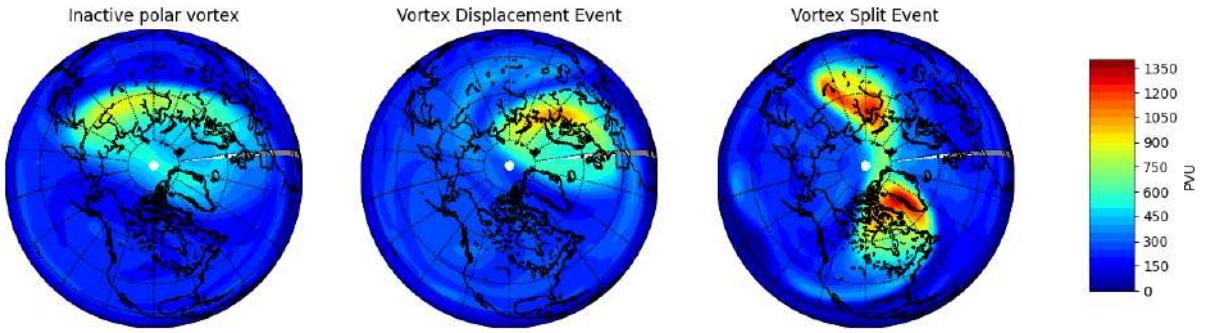

Figure 2.12: Inactive polar vortex, displaced polar vortex (on 20 February 2008) and split polar vortex (on 23 January 2009) to illustrate a vortex displacement and a vortex split SSW using Ertel's potential vorticity (PV) at 10 hPa pressure surface.

The most dramatic sudden stratospheric warmings are known as major warmings. During a major warming, at about 30 km (or 10 hPa) in the winter hemisphere, the normal cold poleward from 60°N and warm mid-latitude gradient is reversed and the west-to-east polar night jet reverses to an east-to-west flow. Sudden warmings are always characterized by large-scale, large-amplitude wave events. While major warmings only occur every other winter or so in the Northern Hemisphere, they have not been observed in the Southern Hemisphere. Wave events of weaker amplitude occur frequently during the winter season. All of these wave events act to warm and increase ozone levels in the polar region generally in proportion to their amplitude. The waves cumulatively act to keep the polar region much warmer and ozone much higher during the winter than would occur in their absence. Major warmings occurred between mid 1950s to 1991 about every other year, but between 1992 and 1998, there were no major warmings. The frequency of major warmings in the Arctic is increasing as seen by the dynamical activity in the recent winters (Charlton-Perez et al., 2008). There is an increase in the occurrence of major warmings recently and has not translated into early final warmings in most cases. In case of minor warmings, the temperature gradient in the stratospheric polar caps reverses. SSWs are minor if the temperature increase observed is at least 25° in a period of week or less at any stratospheric level anywhere in the winter hemisphere. A decrease in the circumpolar westerly wind speeds occur but the reversal of the westerlies to easterlies do not (Limpasuvan et al., 2004; Baldwin et al., 2021). They occur in the upper stratosphere more frequently and also in both the hemispheres. After the final warming, the stratospheric polar vortex doesn't recover after the break up and it dissipates. It happens in spring. Therefore, the winds change the direction and do not change back until the following winter and that is called the summer easterly phase.

SSW 2009

Figure 2.13 shows the polar stereographic plots for two days, i.e. on 13th and 23rd January 2009 as simulated from the EMAC model. The figures are shown at 30 km and 10 hPa. Low levels of ozone and lower temperatures associated with an inactive polar vortex can be seen from the ozone plot. The

inactive polar vortex is symmetric and is centered near the North Pole as seen from the PV plot on 13th January 2009. Ozone levels at the edge of the polar vortex are higher compared to the centre. During the Northern Hemisphere winter, the cold temperatures that can drop to below 195 K can rise by about 50-100K, which is characterised as a sudden stratospheric warming (SSW). In this case, as seen from the bottom row, the temperatures rise upto 286 K ($\sim$ 100 K). Usually in the polar winter, the temperatures drop below 195 K. This event was also characterised by polar vortex split, as seen from the potential vorticity plot. The downward penetration of the SSW 2009 was tremendous. It is one of the few SSWs associated with reversing of the zonal mean zonal wind upto 100 hPa.

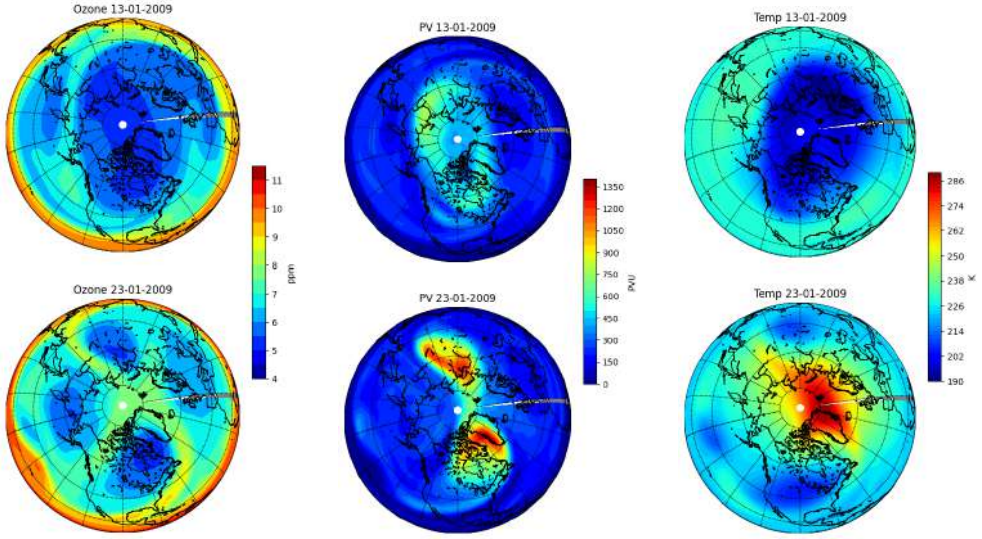

Figure 2.13: Northern hemisphere total ozone, potential vorticity and temperature on the 10 hPa pressure surface for 13 and 23 January 2009. The figure is based on EMAC simulations

3 Methods: Models and Data

In this chapter, description of the models and data sets that are used throughout the thesis are provided. Firstly, a description of the ExoTIC, 1D ion-chemistry model, is provided. Secondly, a description of the AISstorm model that calculates ionisation rates based on particle fluxes is provided. The ExoTIC and AISstorm models are used in Chapter 3 and 4. Thirdly, the working principle of the MIPAS satellite instrument is described that is used for the ExoTIC model evaluation studies to assess the impact of chlorine ion-chemistry is provided. The MIPAS data is used in Chapter 5. And lastly, a description of the 3D chemistry climate model, EMAC (ECHAM5/MESSY) is provided which is used for the study of dynamical coupling. The analysis with EMAC is provided in Chapter 6.

3.1 The ExoTIC model overview

ExoTIC is a one dimensional stacked box model of the atmospheric neutral and ion composition (Herbst et al., 2022). ExoTIC stands for Exoplanetary terrestrial ion-chemistry. The neutral chemistry model is based on the chemistry module of the SLIMCAT model which stands for Single Layer Isentropic Model of Chemistry and Transport by Chipperfield (1999). And ion-chemistry is based on the UBIC (University of Bremen Ion-Chemistry) model developed by Winkler et al. (2009) for the terrestrial middle atmosphere. Ion chemistry models aim to simulate the composition and properties of the ionosphere in interaction with the neutral chemistry. They can be used to study the perturbations and the subsequent effects on neutral species during single SPEs in detail. Recent studies such as Verronen et al. (2005), which studied energetic particle precipitation (EPP) events, found significant co-variability in mesospheric ozone with proton and electron fluxes. HNO_3 increases measured during SPEs cannot be reproduced using the standard parameterization of HO_x and NO_x production, while models considering D-region ion-chemistry in detail agree with the observations (Verronen et al., 2016b). This finding highlighted the need to improve ion-chemistry modelling in the D-region for altitudes below 90 km in the ionosphere (Funke et al., 2011) to capture the EPP ozone interaction. The HO_x and NO_x parameterization cannot reproduce the longer-term effects of ion-chemistry on e.g. the reactive nitrogen partitioning, ozone and dynamics of the middle atmosphere (Kvissel et al., 2012).

3.1.1 Neutral chemistry model

The neutral chemistry model uses a family approach where it is appropriate, basically in the stratosphere and lower mesosphere, whereas the non-family concept is applied for the upper region. SLIMCAT

considers 53 chemical species. According to their different reactivities, they are assigned to four groups and treated in different ways. The concentrations (molecules/volume) of the species are assumed to vary with air density, photo-dissociation and ion-chemistry thus they are determined by the meteorology. The other chemical species considered change their local concentrations through photo-chemical reactions but they do it on different timescales. In order to save computing time, SLIMCAT does not integrate closely coupled species independently but treats them in "families". For instance, O_3, $O(^3P)$, and $O(^1D)$ are combined to form the pseudo-species O_x (odd oxygen). The ratios of the species within a family are determined by assuming steady state conditions. This is justified by the fact that the family members are inter-converted on timescales shorter than that over which other concentrations vary, and it is therefore a commonly used approach in atmospheric chemical modelling. It enables a moderate integration time-step of 15 minutes, and it reduces the dimension of M, compared to a fully independently resolved chemistry. A description of SLIMCAT, the included reactions, and the model's treatment of heterogenous reactions is given in Chipperfield (1999). Important species relevant for the stratosphere and mesosphere, include long-lived tracers and tropospheric source gases as well as photochemically reactive species of the O_x, NO_x, HO_x, ClO_x and BrO_x families as shown in Table 3.1. SLIMCAT uses a radiation transfer scheme which accounts for multiple scattering, and reflection from Earth's surface in a two dimensional spherical geometry upto a solar zenith angle of 98°. The mean solar spectrum, surface albedo and absorption cross sections of the chemical species are the basic input data. The radiative scheme calculates wavelength dependent radiation enhancement factors from which in turn the local photolysis rates of the different species are derived. Absorption cross sections and quantum yield coefficients are also based on JPL-2006.

Short-lived species	$O_x(= O_3 + O(^3P) + O(^1D))$, $NO_x(= N + NO + NO_2)$, $ClO_x(= Cl + ClO + 2 \times Cl_2O_2)$, $BrO_x(= Br + BrO)$, HCl, HOCl, OClO, $ClONO_2$, HBr, HOBr, BrCl, CH_2O, NO_3, N_2O_5, HNO_3, HNO_4, H_2O_2, $BrONO_2$
Long-lived species	CH_4, N_2O, CO, H_2O, $CFCl_3$, CF_2Cl_2, CHF_2Cl, $C_2F_3CL_3$, CH_3Cl, CH_3CCl_3, CCl_4, CH_3Br, $CBrClF_2$, $CBrF_3$, COF_2, COFCl, HF
Steady State	H, OH, HO_2, CH_3, CH_3O_2, CH_3O, HCO, CH_3OOH
Fixed	N_2, O_2, H_2

Table 3.1: The chemical species in the SLIMCAT model

3.1.2 Ion-chemistry model

The ion-chemistry model covers the D-region and lower E-region of the ionosphere. In this thesis, the impacts of SPEs are of main interest. The investigation is carried out mainly to study the interaction between the precipitating particles and the ion-chemistry. The ionisation in this case is driven by prescribed ionisation rates and by photo-ionisation of NO, with the primary positive charges being distributed onto N_2, N, O_2 and O balanced with electrons (Sinnhuber et al., 2012). These rates of the primary ions are calculated by ionisation cross sections based on Rusch et al. (1981) and Jones and Rees (1973). All of

the processes like dissociation and dissociative ionisation of O_2 and N_2 as well as ionisation of O_2, N_2 and O can form the excited states of N, O_2^+, N_2^+ and N^+, which are also included in the model. The ion-chemistry model accounts for photo-ionisation of NO by Lyman-α radiation, photo-dissociation of charged species, and photo-detachment of electrons but doesn't contain any diffusion or horizontal and vertical transport. The ion-chemistry scheme is used in combination with the neutral chemistry model. Table 3.2 shows the species currently included in the model. Positive nitrogen, hydrogen and oxygen compounds are included in the model.

Negative ions	Cl^-, Cl_2^-, Cl_3^-, $Cl^-(CO_2)$, $Cl^-(H_2O)$, $Cl^-(HCl)$, $Cl^-(HO_2)$, NO_3^-, $NO_3^-(HCl)$, NO_2^-, ClO^-, O_3^-, OH^-, O^-, O_2^-, O_4^-, CO_3^-, CO_4^-, HCO_3^-, HSO_4^-, $O_2^-(H_2O)$, $O^-(H_2O)$, $OH^-(H_2O)$, $CO_3^-(H_2O)$, $O_2^-(H_4O_2)$, $O_3^-(H_2O)$, $O_3^-(H_4O_2)$, $NO_3^-(H_2O)$, $NO_2^-(H_2O)$, $NO_3^-(H_4O_2)$, $CO_3^-(H_4O_2)$,
Positive ions	$O(^4S)^+$, $O(^2D)^+$, $O(^2P)^+$, $H^+(H_2O)CO_2$, $H^+(H_2O)N_2$, $H^+(H_2O)$, $H^+(H_4O_2)$, $H^+(H_6O_3)$, $H^+(H_8O_4)$, $H^+(H_{10}O_5)$, $H^+(H_{12}O_6)$, $H^+(H_{14}O_7)$, $H^+(H_2O)N_2$, $H^+(H_4O_2)N_2$, $H^+(H_4O_2)CO_2$, NO^+, N_2^+, N^+, H^+, $H^+(CH_3CN)(H_2O)$, $H^+(CH_3CN)(H_2O)_2$, $H^+(CH_3CN)(H_2O)_3$, $H^+(CH_3CN)(H_2O)_4$, $H^+(CH_3CN)(H_2O)_5$, $NO^+(N_2)$, $NO^+(CO_2)$, $NO^+(H_2O)$, $NO^+(H_4O_2)$, $NO^+(H_6O_3)$, $NO^+(H_2O)N_2$, $NO^+(H_2O)CO_2$, $NO^+(H_4O_2)N_2$, $NO^+(H_4O_2)CO_2$, $NO_2^+(H_2O)$, $NO_2^+(H_4O_2)$, $NO_2^+(H_6O_3)$ O_2^+, $O_2^+(H_2O)$, $O_2^+(H_2CO_3)$, $O_2^+H_4O_2$, $O_2^+N_2$, $O_2^+(CO_2)$, CO^+, CO_2^+, O_4^+, O_5^+, $O_2^+a_4$
Neutrals	$N(^4S)$, $N(^2D)$, NO, NO_2, H, OH, H_2, H_2O, N_2O_5, HNO_3, HNO_2, $O(^3P)$, $O(^1D)$, O_3, CH_3CN, N_2, O_2, CO_2

Table 3.2: ExoTIC positive and negative ions and ion clusters.

ExoTIC first simulates a neutral atmosphere and contains the time evolution of 106 charged and 58 neutral species that interact due to neutral, neutral-ion and ion-ion gas-phase reactions as well as photolysis and photo-electron attachment and detachment reactions (Sinnhuber et al., 2012). The evolution of the neutral and ionizated atmosphere are calculated consecutively, but not independently of each other. The neutral chemistry and the ion-chemistry model are calculated iteratively as follows:

1. The neutral model is time-dependent and calculates the volume mixing ratios of the neutral species with a variable time step. These are then used as an input for the ion chemistry model.

2. The ion-chemistry in the equilibrium state is calculated, calling it hourly from the neutral model. The highest level and the lowest levels for which the ion-chemistry is calculated depends on the initialisation.

3. The equilibrium state of the ion-chemistry is computed using an iterative chemical equilibrium approach. Then the net effective production and loss rates are calculated for the equilibrium ion-chemistry using the initial values of the neutral composition as provided to the ion chemistry.

4. The production rates resulting from the ion-chemistry computation are then fed back to the 1D neutral chemistry. These net production rates are then used by the neutral chemistry module as additional chemical tendencies until the ion chemistry model is called again or the ionization rate is set to zero.

5. Lastly, this state is again returned to the ion-chemistry model for the following computation. This is repeated as long as the rate of atmospheric ionization is non-zero.

The ion-chemistry model calculates the formation and loss rates of neutral species due to atmospheric ionization. Table 3.3 provides the species for which the production and loss rates are calculated.

Neutrals	$N(^4S)$, NO, NO_2, NO_3, N_2, N_2O, N_2O_5, H, OH, H_2, H_2O, HNO_3, HNO_2, $O(^3P)$, $O(^1D)$, O_3, CH_3, CH_4, CH_3CN, O_2, CO, CO_2, HCO_3, HOCl, $ClONO_2$, H_2SO_4

Table 3.3: ExoTIC neutrals for which the production and loss rates are calculated.

The results of ExoTIC simulations regarding some neutral species are sensitive to the changes in the $O(^1D)$ branching ratio, $\beta = \Delta O(^1D)/(\Delta O(^1D) + \Delta O(^3P))$, which is discussed in Winkler et al. (2009). Winkler et al. (2011) reported the $O(^1D)$ corrections in the UBIC model in more detail. $O(^1D)$ is formed from the dissociation of O_2 and CO_2 by particle impact ionisation but also in the ion chemistry reactions themselves. $O(^1D)$ generally goes into photo-chemical equilibrium, which is not considered in the ion-chemistry model, so the rate of $O(^1D)$ formation passed to the neutral chemistry is too large. There are a few other short-lived neutral species in the ion chemistry model, like the excited states of N, e.g. $N(^2D)$, which are treated like ions. The main source of $O(^1D)$ is through Reaction R11. Since $O(^1D)$ is mostly short-lived but is not considered to go into equilibrium in the ion-chemistry stage, a large rate of formation of $O(^1D)$ is produced and is added to the neutral chemistry. The time constants for the quenching $O(^1D) + M \longrightarrow O(^3P) + M$ in the stratosphere are significantly smaller than the chosen integration time step in the ion chemistry model, which was also reported in Winkler et al. (2011). This causes too high $O(^1D)$ concentrations and an unrealistically strong effect through Reaction R68. $O(^1D)$ can react with species like H_2O, H_2 and CH_4 in the lower stratosphere and also with HCl in the stratosphere and mesosphere to produce OH. Higher OH results in higher enhancements of HOCl, $ClONO_2$ and even higher ozone loss in the middle atmosphere. Therefore, either setting the formation rates of $O(^1D)$ to zero or calculating them in photo-chemical equilibrium, for which the rates of the forward and backward reactions are equal, can make a difference to the full ion-chemistry through Reactions R68–R71.

$$O(^1D) + H_2O \longrightarrow 2OH \tag{R68}$$

$$O(^1D) + H_2 \longrightarrow OH + H \tag{R69}$$

$$O(^1D) + CH_4 \longrightarrow CH_3 + OH \tag{R70}$$

$$O(^1D) + HCl \longrightarrow OH + Cl \tag{R71}$$

The ExoTIC model extends the applicability of UBIC to atmospheres of (rocky) planets other than Earth with a wide range of orbital parameters, stellar systems and base compositions as discussed by Herbst, Konstantin et al. (2019). Reaction rate constants and photo-chemical data in general follow the JPL-2006 recommendations from Sander et al. (2006).

3.2 The AISstorm model

The Atmospheric Ionisation during Substorm (AISstorm) model, is an enhanced version of the Atmospheric Ionisation Module Osnabrück (AIMOS) model (Wissing and Kallenrode, 2009) that calculates the atmospheric ionisation rates from the particle fluxes. The model includes magnetospheric and solar particles while GCRs are omitted. The energy and height range over which the ionisation occurs is limited to the particle instrument and thus only a small portion of the solar protons during the event. Mewaldt et al. (2005) studied the Halloween solar storms by combining instruments with different energy ranges to yield a more comprehensive spectrum. Electrons precipitating into the atmosphere have also been analysed, that are assumed to be from the magnetosphere. At the lower energies, they are just auroral electrons. The fluxes derived from the observations with a polar orbiting satellite are assumed to be uniform over the auroral oval (Callis et al., 1996a,b, 1998). The AIMOS model computes ionisation rates by precipitating electrons, protons and alpha particles for the whole atmosphere based on particle flux measurements from different satellites. Since a wide range of particles is considered in AIMOS, the model atmosphere should extend to heights of several hundred kilometres. It goes from ground to 1.7×10^{-5} Pa, between 250-600 km depending on latitude, season and solar activity. This allows ionisation modelling in the stratosphere, mesosphere and thermosphere. The spatial grid is $3.6° \times 3.6°$ in the horizontal with 67 logarithmically equidistant height layers. In the AISstorm model, both the time resolution (0.5 h) and the spatial resolution have been improved compared to AIMOS (2 h). The AIMOS model consists of two parts: a GEANT-4 based Monte Carlo simulation and a sorting algorithm to assign observations from two polar-orbiting satellites to horizontal precipitation cells, depending on geomagnetic activity. The AIMOS model provides a tool to simulate the 3-D ionization effects of almost the total particle inventory on the entire atmosphere depending on geomagnetic activity. A better inter-comparison of observations and simulations is achieved and a comparison of the relative contributions of the different particle populations to atmospheric chemistry is also obtained. This is important for long-term studies of atmospheric ionization that rely on proxies such as kp index for magnetospheric particles. In addition, the horizontal resolution also provides the necessary quality for local measurements such as the comparison of radar echoes at different locations in the polar cap and polar oval. AIMOS consistently models ion-pair production due to precipitating particles for the entire particle inventory of energetic solar and magnetospheric particles. The model is designed to convert observations of energetic particles from satellites into a 3-D ionization pattern in the atmosphere. The AIMOS scheme consists of two parts:

1. The retrieval of energetic particle spectra and the horizontal precipitation pattern from observations.

2. Monte-Carlo simulation of particle interaction with the atmosphere that is performed using mono-energetic particle beams of different energies, angles of incidence and particle species for every single grid point. The observed particle spectrum is convoluted with the large number of mono-energetic beams to give the 3-D atmospheric ionization (or ion pair production) rates.

The energy range of precipitating particles in AISstorm are shown in Table 3.4.

Species	Energy	Pressure	Altitude
Protons	150 eV-500 MeV	10^{-5}-10^{4} Pa	18-240/440 km
Electrons	150 eV-5 Mev	10^{-5}-10^{2} Pa	48-240/440 km
Alpha Particles	4 MeV-500 MeV	10^{-1}-10^{3} Pa	33-92

Table 3.4: AISstorm species, their energy ranges, pressure and altitude levels. The first number indicates the solar minimum and second number the solar maximum conditions (Wissing, 2011).

For each order of magnitude of energy, equidistant mono-energetic beams are calculated, giving a total of 264 mono-energetic beams, depending on particle species. For the angular distributions, 9 different equally spaced directions of incidence w.r.t the vertical are considered. Each beam consists of 10000 electrons, 100 protons and α particles. Electrons are higher because bremsstrahlung is included. A complex retrieval mechanism is required because energetic particle measurements are in situ measurements. Thus, it is not possible to obtain some snapshot of particle distributions at the top of the atmosphere. Instead, a combination of data from at least two polar-orbiting spacecraft is required to determine such a precipitation map. Wissing et al. (2008) combined data from two POES spacecrafts to analyse that and found contribution from protons and electrons in the polar cap and auroral oval where magnetospheric electrons precipitate. This combination of two polar orbiting satellites allows for an approximation of the fluxes inside the polar cap and auroral oval. This map depends on particle energy or rigidity, because the geomagnetic cutoff depends on rigidity. They also depend on local magnetic time and geomagnetic activity: with increasing geomagnetic activity the polar cap and the auroral oval expand equator-ward. The particle precipitation maps in AISstorm have in total 56 regions based on the local times, which is due to the disturbance of the magnetosphere from the Sun. For the whole globe, there are 14 different regions, seven in the North and seven in the south pole, subdivided into four local time sectors which depends on scaling of the particle fluxes with real time measurements, for each 0.5 h time interval. Particles tend to precipitate mainly in the auroral oval and the equatorial region is shielded. The fluxes in the equatorial region originates from trapped particles in the magnetosphere and are neglected in AISstorm. TED captures particles precipitating higher in latitude compared to MEPED. The model simulation of the particle interaction with the atmosphere assumes the density and temperature profiles of the atmosphere, with the latter depending on season, latitude and solar activity. Different runs can be performed for different states of the atmosphere. So, a given input of precipitating particles yields different ionization profiles

for different seasons and/or different levels of solar activity. The atmosphere most adequate for a given day is chosen by date/season and F10.7 index as a measure for solar activity. The model's limitations are determined by the spatial resolution of the model atmosphere and by the energy spectrum covered by the particle instruments as mentioned above.

3.2.1 Particle fluxes

Satellites observe electron fluxes for a short period of time (minutes/seconds) in each orbit and provides an instant picture of EEP energies and fluxes from space. Table 3.5 shows particles measured and their energy ranges in the different energy channels of the TED and MEPED detectors for the POES (NOAA 15 and 16) satellites and GOES 10 and 11 satellites. The Space Environment monitor, SEM-2 instruments are on board POES, Meteorological Operational satellites (Metop), and EPS instruments on GOES 10 and 11. The POES instruments measure electrons upto 2.5 MeV and protons upto 6.7 MeV and no alpha particles. Protons with higher energies $\sim$ 500 MeV are measured by GOES satellite. The GOES system also carry on board the SEM subsystem which contains a magnetometer, energetic particle sensor and x-ray sensor and is providing data since 1974. The energetic particle sensor of GOES has two channels, E1 and I1 that responds primarily to trapped outer-zone particles. The I2 channel responds to trapped particles during magnetically disturbed conditions. More information about the description of POES and GOES satellites can be found in Wissing and Kallenrode (2009). There is a problem in the AISstorm model, which is due to the limited spatial coverage by the satellites. These data gaps occur mainly at the geomagnetic poles during every satellite orbit. Due to the orbital inclination, data from one pole might be missing and hence are taken from the other pole thereby fixing the problem with the data gaps. The POES satellite has different energy channels as described above and the lower energy channels measure higher flux and higher energies measure lower flux. The correlation between the particle fluxes at both the poles can be found in Wissing (2011). Figure 3.1 shows proton and electron fluxes for the polar cap region (latitude 69-70°N) for October-November 2003 event for different TED channels with top row being the lowest in energy, with high flux and bottom row being the highest, with low flux. Figure 3.2 shows daily averages of proton and electron fluxes for January-February 2009 for lower energy TED channels of band 4 and 8 respectively. There is a periodicity that is observed for these time series, which might be due to the difference in the tilt of the rotational axes of the Earth w.r.t the Sun which can cause a particle precipitation shift.

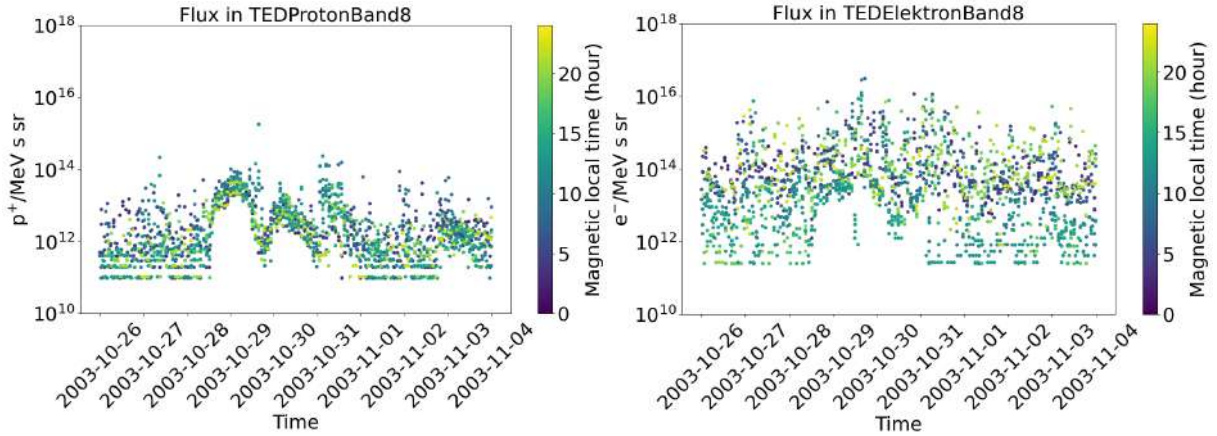

(a) Channel TED proton band 8

(b) Channel TED electron band 8

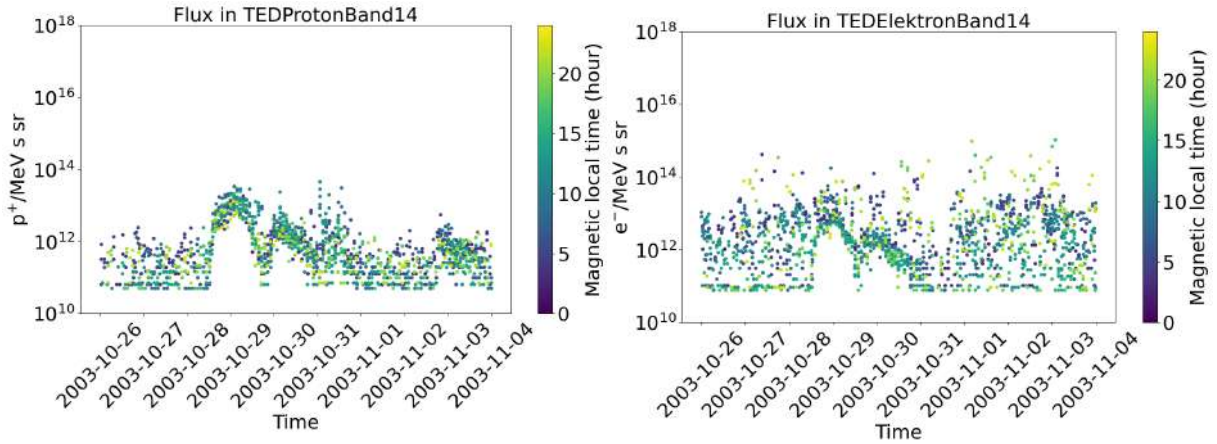

(c) Channel TED proton band 14

(d) Channel TED electron band 14

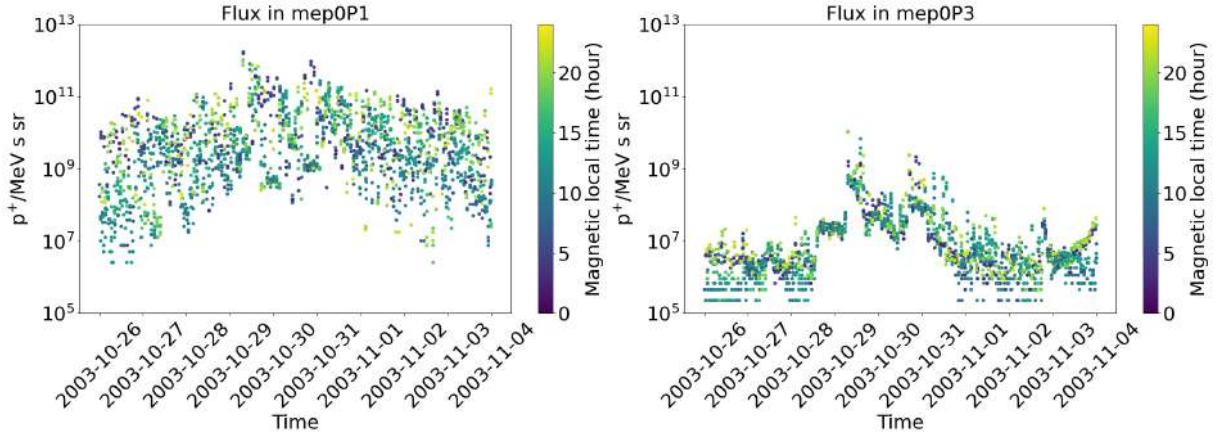

(e) MEPED mep0P1

(f) MEPED mep0P1

Figure 3.1: Fluxes of protons and electrons precipitating in the polar cap region during October-November 2003 event for different energy channels of the POES 15/16 satellite. Colorbar denotes the magnetic local time (MLT). Data source: NOAA National Centers for Environmental Information (https://ngdc.noaa.gov/stp/satellite/poes/dataaccess.html) for the POES 15 and 16 and Metop particle data (Level 1b).

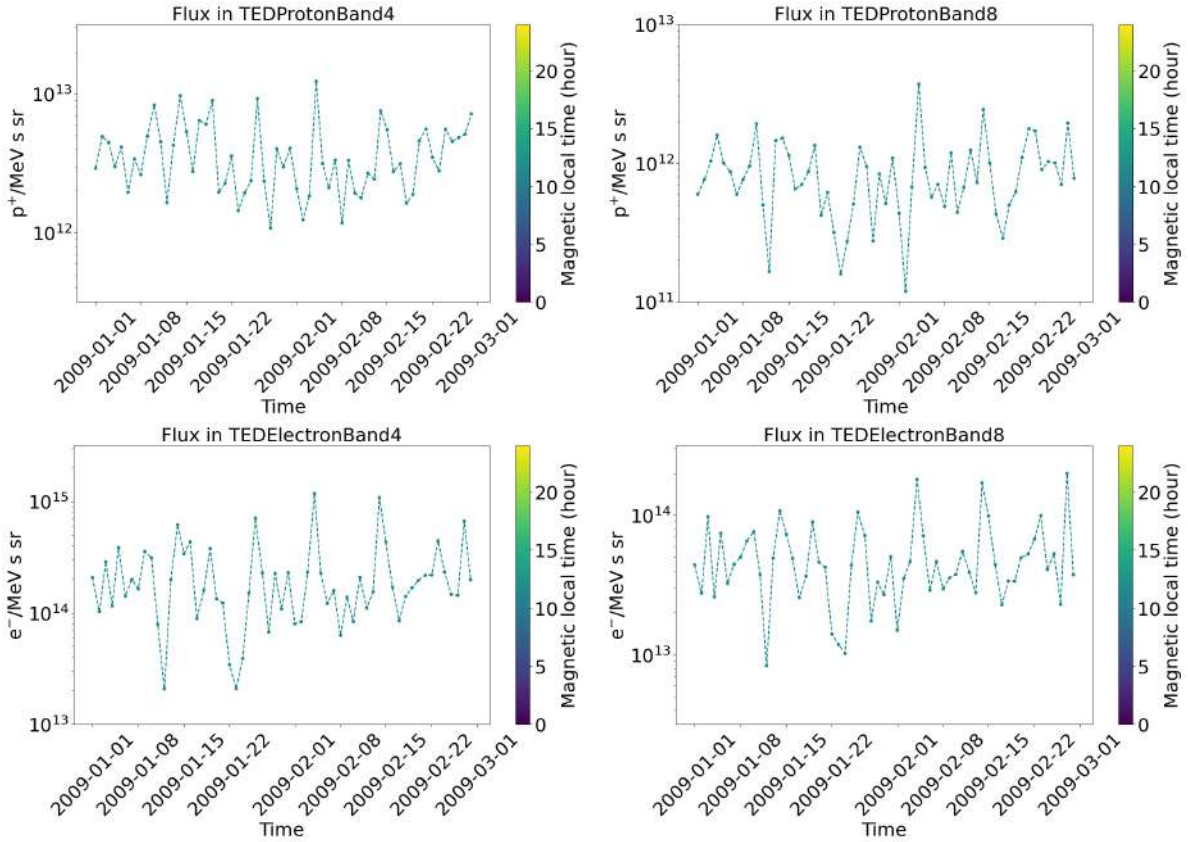

Figure 3.2: Daily mean of fluxes of protons and electrons in the lower energy channel TED Band 8 for January-February 2009 in the polar cap region. Data source: NOAA National Centers for Environmental Information (https://ngdc. noaa.gov/stp/satellite/poes/dataaccess.html) for the POES 15 and 16 and Metop particle data (Level 1b).

Particle species	Instrument	Energy Channels	Energy range
Electrons	POES 15 and 16	TED Electron Band 4	0.000154-0.000224 MeV
		TED Electron Band 8	0.000688-0.0001000 MeV
		TED Electron Band 11	0.002115-0.003075 MeV
		TED Electron Band 14	0.006503-0.009457 MeV
		MEPED mep0e1-e2	0.03-0.1 MeV
		MEPED mep0e2-e3	0.1-0.3 MeV
		MEPED mep0e3	0.3-2.5 MeV
Protons	POES 15 and 16	TED Proton Band 4	0.000154-0.000224 MeV
		TED Proton Band 8	0.000688-0.0001000 MeV
		TED Proton Band 11	0.002115-0.003075 MeV
		TED Proton Band 14	0.006503-0.009457 MeV
		MEPED mep0P1	0.03-0.08 MeV
		MEPED mep0P2	0.08-0.24 MeV
		MEPED mep0P3	0.24-0.8 MeV
		MEPED mep0P4	0.8-2.5 MeV
		MEPED mep0P5	2.5-6.9 MeV
	GOES 10 and 11	telescope z_p2	4-9 MeV
		telescope z_p3	9-15 MeV
		dome z_p4	15-40 MeV
		dome z_p5	40-80 MeV
		dome z_p6	80-165 MeV
		dome z_p7	165-500 MeV
Alpha Particles	GOES 10 and 11	telescope a_a1	4-10 MeV/particle
		telescope a_a2	10-21 MeV/particle
		telescope a_a3	21-60 MeV/particle
		dome a_a4	60-150 MeV/particle
		dome a_a5	150-250 MeV/particle
		dome a_a6	300-500 MeV/particle

Table 3.5: Satellite instruments used to measure the fluxes of different particles used in AISstorm (Wissing, 2011).

Ionisation rates

The calculation of ionisation rates is based on the GEANT4 algorithm (Wissing and Kallenrode, 2009) in the AISstorm model. The total ionisation rate at a pressure level is defined as the integration of the mean ionisation rate of an isotropic particle (with energy E) and the particle flux at this energy. Wissing and Kallenrode (2009) stated that the particle flux differ in each of the 56 regions and is given by a power law:

$$\phi = \phi_0 . (\frac{E}{E_0})^{-\gamma} \tag{3.1}$$

At every pressure level l, the total ionisation is given by,

$$\mathrm{I_l} = \int_{\mathrm{E_1}}^{\mathrm{E_2}} \mathrm{G_l(E)} \phi(\mathrm{E}) \mathrm{dE}, \tag{3.2}$$

where G(E) is the aberration (green's function) based on the intermediate ionisation rates calculated by GEANT4. E_1 and E_2 represent the thresholds of the corresponding power law fits.

3.3 Balloon observations

One of the EEP observation methods is the measurements of bremsstrahlung on balloons generated by precipitating electrons in the altitudes of stratosphere. The balloon measurements are performed by a radiosonde lifted up to the heights of 30-35 km and returning information on the ionizing particle fluxes at different levels of the atmosphere. The radiosonde sensor consists of two Geiger Müller tubes arranged as a telescope, with a 2 mm A1 interlayer between the tubes. The device returns the count rates of the upper single tube and the telescope. The single tube is sensitive to X-rays and charged particles (electrons, protons and muons), while a telescope measures only energetic charged particles but does not respond to the X-ray flux by the atmosphere. During quiet conditions, the radiosonde records the fluxes of secondary cosmic rays. Precipitating electrons are absorbed at altitudes above 50 km, but they generate X-rays via bremsstrahlung, which penetrates into the atmosphere down to altitudes of $\sim$ 20 km and can be recorded only by the single tube. Intrusion into the atmosphere of solar particles causes a count rate enhancement for both the single tube and the telescope, which enables us to distinguish between solar proton and magnetospheric electron precipitation. In case of smooth growth of the Geiger-Müller tube count rates with altitude, we assume that it is caused by X-ray absorption in air rather than by temporal variation in X-ray flux. Observations were used from the balloon experiment that have been performed by the Lebedev Physical Institute (LPI) every few days since 1957, which has so far recorded 589 EEP events at polar latitudes, L $\simeq$ 5.5, over 1961-2019 (Makhmutov et al. (2016); Mironova et al. (2022);Bazilevskaya et al. (2020)), and is complemented by regular balloon launches at mid-latitudes. Observations of EEP events in mid-latitudes are very rare. However, several candidates have been found since the beginning of the 2000s. The event presented in Chapter 4 is the most outstanding EEP event recorded in the Moscow region so far. The LPI balloon observation at 13:26-13:45 UT on 14 December 2009, demonstrate a substantial enhancement in the count rate of the single Geiger-Müller tube above $\sim$ 20 km (residual pressure $\sim$ 55 hPa).

3.4 MIPAS instrument overview

MIPAS, the Michelson Interferometer for Passive Atmospheric Sounding, was a mid-infrared emission spectrometer selected for the core payload of ENVISAT by ESA due to several favourable properties (Fischer et al., 2000). Within this part of the atmospheric spectrum, there is a wide variety of important molecules which have vibration-rotation bands with absorption lines well suited for detection (Figure 3.3). Atmospheric signals of thermal emission are generally higher than in other parts of the spectrum because the Planck function maximizes at about 10 μm for atmospheric temperatures. The instruments working in the mid-infrared can be significantly smaller than those operating at longer wavelengths. This

is dictated by diffraction limits and the high spectral resolution needed to observe the trace species of interest. An advantage of the MIPAS instrument being in mid-infrared in comparison to spectral regions with shorter wavelengths covering 4.1-14.6 μm, is that the instrument can allow measurements during both day and night parts of ENVISAT orbit, with an azimuth scan geometry in the anti-flight direction which ensures complete coverage of the globe. The MIPAS instrument used the principle, that trace gases have characteristic emission and absorption lines, represented by their absorption coefficients, which are unambiguous "fingerprints" of the particular trace gases. The atmospheric spectra were inverted into vertical profiles of atmospheric pressure, temperature and volume mixing ratios (vmrs) of at least 30 trace constituents. One can study the stratospheric chemistry and dynamics, stratosphere-troposphere exchange, chemistry and physics of the upper atmosphere, as well as climatologies and improvement of weather forecasting. Within the MIPAS spectrum, important trace gases like the NO_y family, for example, the source gas N_2O are accessible to the instrument. An advantage of instruments operating in the mid-infrared is that they can be calibrated by observing cold space and black bodies. In contrast, the reference calibration is not accessible for the instruments operating in ultraviolet/visible region. The MIPAS fourier transform spectrometer was selected after a trial of different fourier transform spectrometers. MIPAS-B (balloon) was the precursor to the MIPAS instrument. The interferometer has achieved feasibility to measure the mid-infrared emission spectra with the aid of optical system with a cooling of 200 K or liquid He temperatures (Friedl-Vallon et al., 1993; Fischer and Oelhaf, 1996). MIPAS-B has successfully experimented since 1989 in Southern France and Northern Sweden. Another similar instrument is MIPAS-FT in the Transall aircraft (Gulde et al., 1994). These interferometers measure thermal emission and its basic knowledge is taken for the MIPAS on ENVISAT. MIPAS-B data gave vertical trace gas profiles of species like: O_3, HDO, H_2O, CH_4, N_2O, $CFCl_3$, CF_2Cl_2, CHF_2Cl, CCl_4, CF_4, NO_2, HNO_3, HNO_4, N_2O_5 and $ClONO_2$. The balloon instrument didn't cover the whole region of mid-infrared spectra (Fischer, 1992; Von Clarmann et al., 1995; von Clarmann et al., 1996; Oelhaf et al., 1995; Wetzel et al., 1995). MIPAS FT findings of horizontal trace-gases distributions were relevant for stratospheric ozone research.

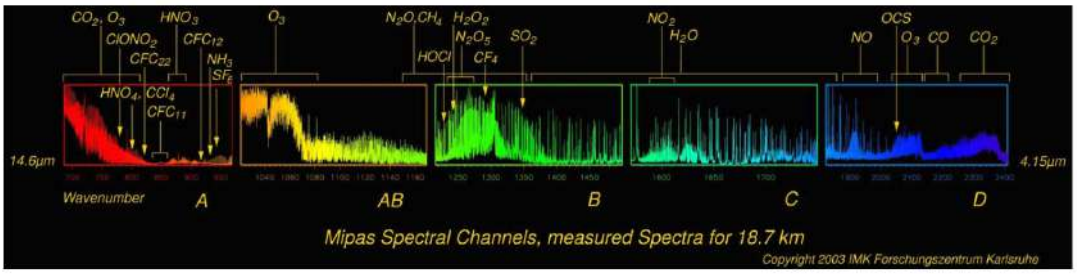

Figure 3.3: The total spectral region of MIPAS (4.15-14.6 μm) as measured at 18.7 km tangent altitude, is divided into five spectral intervals (A, AB, B, C, D); the large number of spectral emission lines demonstrates the enormous amount of information in the measurements; a considerable number of trace constituents can be detected as indicated. From Fischer et al. (2008).

3.4.1 Michelson Interferometer principle

The Michelson interferometer consists a beam splitter/a half silvered mirror which is used along with a fixed and a movable mirror. Figure 3.4 shows a schematic of the Michelson interferometer. The light from the source travels through the beam splitters and gets reflected and traverses back and falls on the detector. The Michelson interferometer configuration is used in a different number of applications like the Fourier transform spectrometer. An interferogram is generated by the movable mirror that converts discrete points of light into an interferogram. It converts an interferogram into an actual spectrum through fast fourier transform (FFT). The detector monitors all wavelengths from the signal. In case of a noisy detector, a good signal to noise ratio is obtained in the infrared region. The Michelson interferometer has applications in the upper atmosphere, measuring temperature, winds using different remote sensing methods measuring the Doppler widths and shifts in spectra of the aurora and airglow.

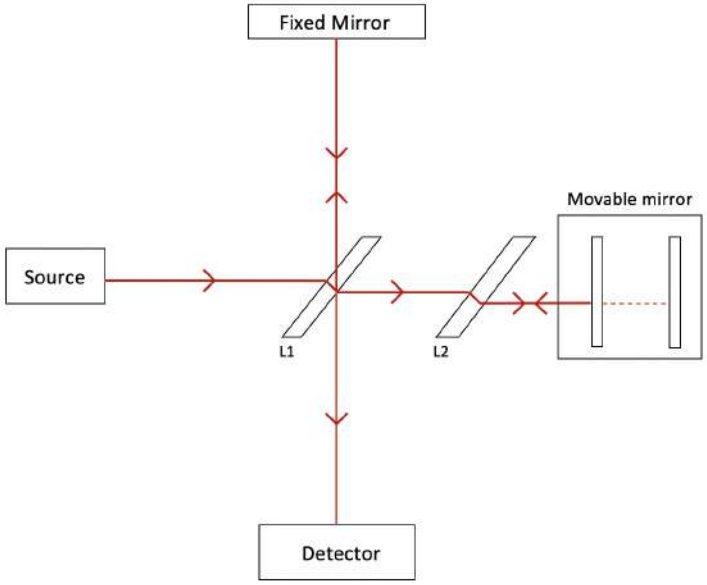

Figure 3.4: Schematic of the Michelson Interferometer.

3.4.2 Observing capability

The MIPAS instrument observes the emitted radiance from the atmosphere at the limb, which is the line of sight that penetrates the atmosphere down to a minimum altitude, called the tangent altitude and then, emerges towards space because of the Earth's curvature. The observation is selective to the signal emitted from the tangent altitude layer. The limb sequence is acquired with a different set of tangent altitudes that determines the vertical profiles of atmospheric parameters, which MIPAS can observe in the altitude range from 5-160 km, with minimum and maximum steps of 1 and 8 km. To access an air volume in the atmosphere, MIPAS uses two mirrors. To determine the location of the observed air volume, the azimuth mirror is used and to select the limb altitude, the elevation mirror is used which corrects for platform

altitude, orbital altitude and Earth's geoid geometry. The azimuth mirror provides access to limb targets rearwards within a 35° wide range around the anti flight direction and sideways within a 30° wide range of the anti-Sun of the satellite.

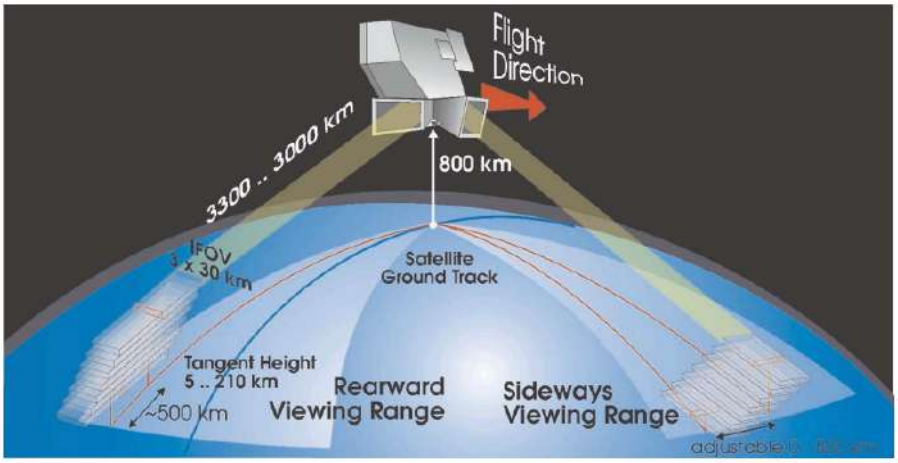

Figure 3.5: MIPAS Observation Geometry. Source: ESA

The viewing of MIPAS is in the rearward direction. The sampling strategy is to keep the azimuth mirror fixed during each limb scanning sequence, which is performed by changing the orientation of the elevation mirror and discrete steps in tangent altitude. At each nominal position of the elevation mirror, an interferometer sweep is acquired while the elevation mirror is actively controlled in order to maintain a constant tangent altitude. With decreasing tangent altitude, the location moves away from the platform. Limb sequence is performed scanning down from high to low altitudes, so that the geometrical effect partially compensates for the movement of the platform and an almost vertical sequence of tangent altitude points is obtained. Changing the azimuth angle w.r.t. the rearward direction, it is possible to move the tangent location away from the satellite ground track. The satellite ground track is limited to the latitude region between about 80°S and 80°N, which is due to the inclination of the orbit. The azimuth angle is occasionally changed during the orbit in order to perform observations from pole to pole. Simultaneous changes of azimuth and elevation angle between subsequent sweeps can be considered in order to compensate for the platform movement. To record a full resolution spectrum, the time required is 4.5 seconds. A nominal limb scanning sequence consists of 17 spectra measured at tangent altitudes from 6 to 68 km with a spacing of 3 km at low altitudes and larger spacing above, and is acquired in a total time of 76 seconds. During each orbit, about 72 limb sequences are acquired as well as calibration measurements. About 14 orbits are obtained every day for a total of about 1000 limb sequences or profiles per day. The MIPAS observation strategy includes emission measurements by MIPAS with continuous observations independently of the presence of external radiation sources and of the day/night conditions. Limb sounding techniques are with good resolution of the vertical distribution of the at-

mospheric parameters. The polar orbit is carried out with azimuth correction for global (pole to pole) mapping. Broadband FTS measurements were carried out with simultaneous observation of an almost complete survey of the atmospheric constituents. The combination of these features makes it possible to obtain a comprehensive picture of the atmospheric chemistry with daily 3D global maps of the concentration of a considerable number of constituents for the full duration of the instrument mission. This was the first satellite instrument to combine all these features for the investigation of the middle atmosphere phenomena.

3.4.3 MIPAS Averaging Kernels

Figure 3.6 shows an example of averaging kernel matrices for $ClONO_2$ on the 25th of October at 6:15 and 6:30 pm. The diagonal elements at a lower altitude are higher than 0.4. And the values at a higher altitude of 40 km decreases and are less compared to lower altitudes.

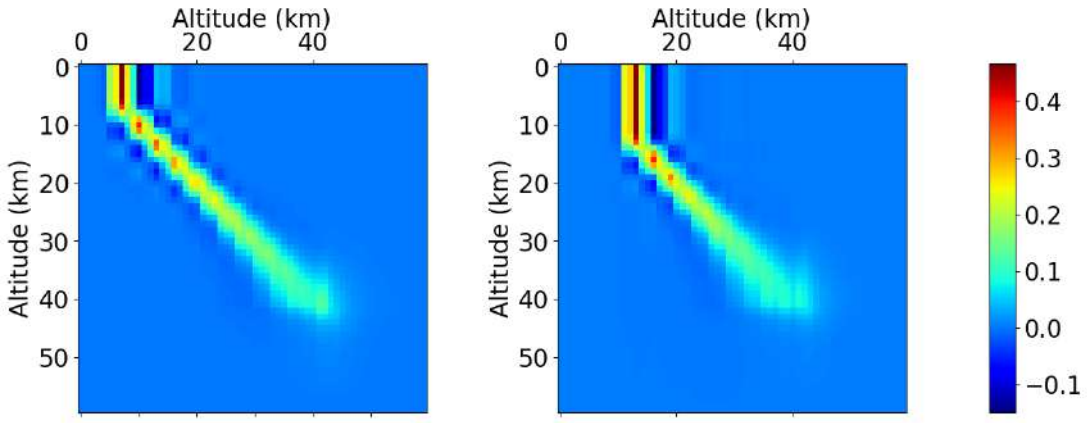

Figure 3.6: Example of averaging kernel matrices for $ClONO_2$ on the 25th of October at 6:15 and 6:30 pm.

3.4.4 Inverse method and Optimal Estimation

The following subsection is based on Chapter 3 of the book "Inverse methods for atmospheric sounding theory and practice" by C.D. Rodgers. An inverse problem can have an infinite number of possible solutions, out of which there is an optimal one. It is necessary to determine what can be optimised sensibly and how the solution is to be related to the true state. The retrieved state could be most likely consistent with all of the available information. Error analysis can be applied to any inverse method, which will show how a retrieval is related to the true state of the atmosphere, and how various sources of error propagate into the final product. The analysis can help identify characteristics of retrievals that can be optimised, and is in any case an essential part of the documentation of any retrieved dataset. The forward model **F**, modelling radiative transfer, required to relate the state to the measured signal, as well as a full description of the measuring instrument and sensor characteristics, describes the measurement y as a function of the true state parameters of the atmosphere **x** and true model parameters **b**:

$$\mathbf{y} = \mathbf{F}(\mathbf{x}, \mathbf{b}) + \varepsilon \tag{3.3}$$

with a measurement error ε. The retrieved state vector $\hat{x}$ is given by the inverse model, **I**:

$$\hat{x} = \mathbf{I}(\mathbf{y}, \hat{b}, x_a, \mathbf{c}) \tag{3.4}$$

The parameter '$\hat{\text{b}}$', is the estimate of the forward function parameters, as distinct from the true value '**b**' and it comprises those quantities which influence the measurement, are known to some accuracy, but are not intended as quantities to be retrieved. An example is spectral line strengths. The error term ε includes errors from sources such as detector noise, which are not related to the forward function parameters, but clearer if left as an explicit term. '**c**' and x_a stands for an additional parameter which constrain the retrieved state and together comprise parameters that do not appear in the forward function, but affects the retrieval. $\mathbf{x}_a$ is any a priori estimate of x that may be used, and **c** contains any other parameters of this nature.

The transfer function

Substituting equation 3.3 to 3.4, we can relate the retrieval to the true state by:

$$\hat{\text{x}} = \mathbf{I}(\mathbf{f}(\text{x}, \text{b}) + \varepsilon, \hat{\text{b}}, \text{x}_\text{a}, \text{c}) \tag{3.5}$$

This is regarded as a Transfer Function describing the operation of the whole observing system, including both the measuring instrument and the retrieval method which is done for the characterisation of the atmosphere. It means the sensitivity of the retrieval to the true state, expressed as $\partial\hat{x}/\partial\text{x}$, and error analysis means the sensitivity of the retrieval to all of the sources of error in the transfer function, including noise in the measurement, error in the non-retrieved parameters and in the retrieval method parameters, and the effect of modelling the true physics of the measurement by some forward model. The transfer function can be linearised w.r.t the various parameters involved, by replacing the forward function by a forward model, **F**, with associated errors:

$$\mathbf{F}(\text{x}, \text{b}) \simeq \mathbf{f}(\text{x}, \text{b}, \text{b}') \tag{3.6}$$

where **b** has been separated into **b** and **b'**, with **b'** representing the forward function parameters, ignored in the construction of the forward model. The linearised form with an included error term:

$$\hat{\text{x}} = \mathbf{I}(\mathbf{F}(\text{x}, \text{b}) + \Delta\text{f}(\text{x}, \text{b}, \text{b}') + \varepsilon, \hat{\text{b}}, \text{x}_\text{a}, \text{c}) \tag{3.7}$$

where Δf is the error in the forward model relative to the real physics:

$$\Delta\text{f} = \text{f}(\text{x}, \text{b}, \text{b}') - \mathbf{F}(\text{x}, \text{b}) \tag{3.8}$$

where Δf is the error in the forward model. Linearising the forward model with x = x_a and b = $\hat{\text{b}}$:

$$\hat{x} = \mathbf{I}(\mathbf{F}(x_a, \hat{b}) + \mathbf{K}_x(x - x_a) + K_b(b - \hat{b}) + \Delta f(x, b, b') + \varepsilon, \hat{b}, x_a, c) \tag{3.9}$$

where the matrix $\mathbf{K}_x$ is the sensitivity of the forward model to the state, $\partial\mathbf{F}/\partial x$, the weighting function or Jacobian matrix, and $\mathbf{K}_b$ is the sensitivity of the forward model to the forward model parameters, $\partial\mathbf{F}/\partial b$. Linearising the inverse method w.r.t. its first argument y:

$$\hat{x} = \mathbf{I}[\mathbf{F}(x_a, \hat{b}), \hat{b}, x_a, c] + \mathbf{G}_y[\mathbf{K}_x(x - x_a) + \mathbf{K}_b(b - \hat{b}) + \Delta f(x, b, b') + \varepsilon] \tag{3.10}$$

where $\mathbf{G}_y = \partial\mathbf{I}/\partial y$ is the sensitivity of the retrieval to the measurement, which is the same as its sensitivity to the measurement error. Rearranging to give:

$$\hat{x} - x_a = \mathbf{I}[\mathbf{F}(x_a, \hat{b}), \hat{b}, x_a, c] + \mathbf{A}(x - x_a) + \mathbf{G}_y\varepsilon_y \tag{3.11}$$

where,

$$\mathbf{A} = \mathbf{G}_y\mathbf{K}_x = \frac{\partial\hat{x}}{\partial x} \tag{3.12}$$

is known as the averaging kernel that gives the sensitivity of the retrieval to the true state and the total measurement error is given by:

$$\varepsilon_y = \mathbf{K}_b(b - \hat{b}) + \Delta f(x, b, b') + \varepsilon \tag{3.13}$$

is the total measurement error in the relative to the forward model. The first term in equation 3.11, is called the bias, the error that would result from a simulated retrieval using a simulated error-free measurement of the apriori state computed with the forward model. Apriori represents the knowledge of the state before the measurement is made. If the measurements are consistent with the state being equal to the apriori, then an inverse method should return the apriori. The second term, averaging kernel, **A**, represents the way in which the observing system smoothens the profile. The difference between the retrieval and the linearisation point is obtained by operating on the difference between the true state and the linearisation point with the matrix **A**:

$$\hat{x} = x_a + \mathbf{A}(x - x_a) + \mathbf{G}_y\varepsilon_y = (\mathbf{I}_n - \mathbf{A})x_a + \mathbf{A}x + \mathbf{G}_y\varepsilon_y \tag{3.14}$$

Here, $\hat{x}$ is the new adjusted profile, x is the original/true profile and x_a is the a priori profile. The rows of the averaging kernel **A** can be regarded as smoothing functions, generally peaked functions and their half-width is a measure of the spatial resolution of the observing system, providing simple characterisation of the relationship between the retrieval and the true state. The columns of **A** give the response of the retrieval to a δ-function perturbation in the state vector. The third term of equation 3.11 is the error in the retrieval due to the total measurement, which we will call retrieval error, ε_y. In spectroscopy, the resolution of a spectrometer is a measure of its ability to distinguish two point sources in one or two

dimensions. Following Rodgers (2000), together with the maximum a posteriori solution for Gaussian pdf,

$$\hat{\mathrm{x}} = \mathrm{x_a} + (\mathbf{K}^T\mathbf{S}_\varepsilon^{-1}\mathbf{K} + \mathbf{S}_\mathrm{a}^{-1})^{-1}\mathbf{K}^T\mathbf{S}_\varepsilon^{-1}(\mathrm{y} - \mathbf{K}\mathrm{x_a}) \tag{3.15}$$

From equation 3.15, the retrieval gain matrix is:

$$\mathbf{G}_y = (\mathbf{K}^T\mathbf{S}_\varepsilon^{-1}\mathbf{K} + \mathbf{S}_a^{-1})^{-1}\mathbf{K}^T\mathbf{S}_\varepsilon^{-1} \tag{3.16}$$

and substituting the equation from above in equation 3.12, we have the averaging kernel:

$$\mathbf{A} = \mathbf{G}_y\mathbf{K} = (\mathbf{K}^T\mathbf{S}_\varepsilon^{-1}\mathbf{K} + \mathbf{S}_a^{-1})^{-1}\mathbf{K}^T\mathbf{S}_\varepsilon^{-1}\mathbf{K} \tag{3.17}$$

3.5 ECHAM5/MESSy Atmospheric Chemistry

EMAC (ECHAM5/MESSy Atmospheric Chemistry) is a 3 dimensional coupled chemistry climate model that is a combination of the general circulation model ECHAM5 as the dynamical core (Roeckner et al., 2006) and 60 different sub-models (Jöckel et al., 2010). The second version MESSy2 (Modular Earth Submodel System 2) is used in EMAC for linking multi-institutional computer codes. In this study, ECHAM version 5.3.02 and MESSy version 2.55.2 is used. EMAC here is used in the upper atmosphere mode which is extended upto the lower thermosphere ($\sim$ 220 km). It is based on T42 horizontal truncation corresponding to a resolution of 2.8° $\times$ 2.8° in latitude and longitude and L74 resolution with 74 levels of pressure (upto $3e^{-7}$ hPa, EMAC submodule EDITH). Several important processes have been implemented, for example, Joule heating and ion-drag (Hong and Lindzen, 1976), molecular and turbulent diffusion (Schmidt et al., 2006), radiative cooling due to NO etc.

3.5.1 Chemistry Setup

For gas-phase reactions in the stratosphere and mesosphere, the MECCA submodule is used. MECCA is an atmospheric chemistry module that is contained in the atmospheric chemistry box model CAABA (Chemistry of the Atmosphere As a Box model Application) described in Sander et al. (2011). A five ion-chemistry scheme with the important ions of O_2^+, N_2^+, N^+, NO^+ and O^+ in the upper atmosphere was implemented to calculate the particle impact ionisation in the thermosphere. These ions are included in the submodule CAABA and the SPE module is used to derive the tendencies of these ions. The parameterisation of NO_x production by energetic particles in the middle atmosphere, based on (Nieder et al., 2014) is also included in the chemical module. The initial branching ratios of $N(^4S)$ and $N(^2D)$ according to this parameterisation are:

$$N(^4S) = 0.5694$$

$$N(^2D) = 0.5355$$

MECCA contains a comprehensive chemical mechanism with tropospheric and stratospheric chemistry of both the gas and the aqueous phase. In this setup, only the gas-phase chemistry are considered for troposphere and stratosphere. The gas phase has 93 species and 202 gas-phase reactions, 46 photolysis reactions and 20 heterogeneous reactions. The stratospheric chemistry is based on the model of Steil et al. (1998) and Mainz Chemical Box Model (Meilinger, 2000). In addition to the basic HO_x=(OH+HO_2), NO_x=(NO+NO_2), and methane chemistry, it also includes non-methane hydrocarbons (NMHCs) and halogen (Cl and Br) chemistry. The rates of the photolysis reactions are calculated by an external module, the submodule JVAL (Landgraf and Crutzen, 1998) and then supplied to the MECCA chemistry. JVAL is a part of EMAC so the chemical and photo-chemical schemes are identical to the 3-D simulations. Tropospheric halogen chemistry is based on Sander et al. (2006) and von Glasow et al. (2002). The concentration of chemical species evolve in time according to differential law of mass action kinetics. A numerical simulation requires an implementation of the differential laws and a numerical integration in time. For numerical integration of the concentration of chemical species, MECCA uses the KPP (Kinetic Pre-Processor) software. KPP selects the species and reactions, the numerical solver can be chosen visa a namelist, where the default is Rosenbrock 4.

3.5.2 Ionisation rates

Ionisation rates from particle impact for auroral electrons, auroral and solar protons and heavier ions are provided by AIMOSv2.0-AISstorm model (see Section 3.2). Photo-ionisation is parameterised by Solomon and Qian (2005) as an additional source of NO. The SPE submodule (Baumgaertner et al., 2010b) in EMAC parameterizes the effects of energetic protons, electrons and EUV radiation by calculating ionisation rates and the NO_x and HO_x production rates. The production rates of the five ions for the ion-chemistry scheme is also calculated by the SPE submodule, i.e., the tendencies (net production rates) of some ions and some neutrals are calculated and added to the respective number densities. The SPE submodule is not coupled to any other MESSy submodules.

3.6 The ERA-5 Reanalysis Dataset

The ERA-5 is the fifth generation ECMWF atmospheric reanalysis of the global climate covering the period from January 1950 to present (Hersbach et al., 2020). It provides global hourly estimates of atmospheric, ocean-wave and land-surface variables, for example, like air pressure, temperature, winds at different altitudes, at a horizontal resolution of 31 km and 137 levels in the vertical from the surface to 0.01 hPa ($\sim$ 80 km). Climate reanalyses provide a description of the climate that has evolved over several decades. ECMWF uses forecast models periodically to reanalyse archived observations creating global datasets describing the recent history of the atmosphere. Reanalyses have been continuously developed to include coupled processes involving land, sea ice, ocean and atmosphere together. We use ERA-5 to nudge the model upto 10 Pa for simulations with specified dynamics.

4 Studies on the chemical composition of the atmosphere using the ExoTIC model and evaluation with MIPAS observations

This chapter describes studies on the composition changes of the middle atmosphere during Solar Proton Events (SPEs) performed using a one dimensional ion-chemistry model. An evaluation of the overall ability of the model to reproduce observed atmospheric perturbations generated by the SPEs using a wide range of trace gases, i.e., NO_y, chlorine species and ozone changes in comparison to satellite observations is provided. A well-studied solar proton event, i.e., the Halloween SPE 2003 (described in Section 2.3) is used for the model evaluation. The Halloween solar storms were used due to the following reasons:

1. They are well studied by satellites and provides details of how the atmospheric chemical composition changes in the middle atmosphere.
2. This event was one of the strongest events in the satellite era and was observed by multiple spacecrafts throughout the heliosphere. So, it represents a good way for model validation and intercomparison.

4.1 Ionisation rates

The Halloween SPE based ionisation rates (IRs) were obtained from the AISstorm model described in Section 3.2. Figure 4.1 shows daily averaged ionisation rate profiles for a high latitude of 69.76°N (top) and a latitude at the edge of the polar vortex and inside the auroral oval, 58.6°N (bottom) during quiet conditions without any influence of solar particles. The protons are shown in solid and electrons in dashed lines. It can be seen that in the stratosphere and lower mesosphere (below 75 km), the protons show higher ionisation rates compared to electrons whereas higher up in the mesosphere and lower thermosphere (MLT) region (above 75 km), the electrons have a higher ionisation rate that exceeds the protons by an order of magnitude. The protons penetrate deeper into the atmosphere and electrons are higher up (e.g. auroral electrons). In case of protons, in the polar cap (at the latitude of 69.76°N), the ionisation rate profiles don't differ much in magnitude in the stratosphere and lower mesosphere for the different days. Higher up in the MLT region there is some difference. However in case of electrons, the difference is quite pronounced. At 58.6°N at the edge of the polar vortex, the ionisation rate profiles for both protons and electrons show a decrease in magnitude over the entire altitude range w.r.t. time, except

for the 7th of October, which shows the maximum ionisation rate. The profiles for protons are spread out more at the edge of the polar vortex as compared to high up in the polar cap (69.76°N). In both cases, the maximum ionisation by the precipitating particles occur at the lower thermosphere; the ionisation rates are by one order of magnitude larger than the mesopause.

Figure 4.2 shows the temporal evolution and daily averages for protons, electrons and alpha particles from 25th October to 4th November 2003 at a latitude of 67.5°N, for the town of Apatity. This town was chosen because it was at a high latitude. These are in the polar cap and also inside the polar vortex that was used for ExoTIC model simulations. With increasing time and decreasing ionisation rates, stronger dynamics of the IRs is observed. The ionisation rates predicted by AISstorm might differ from the real ones observed. The SPE ionization happened in the denser atmosphere, therefore the conversion from particle fluxes into ionization should be more or less precise in terms of total ionization and altitude. The main uncertainty of SPE ionization in AISstorm is the size of the area that is affected by high energetic particle precipitation. This cannot be derived from the channels but is taken from a lower energy channel on another satellite and that might be an underestimate of the polar cap size.

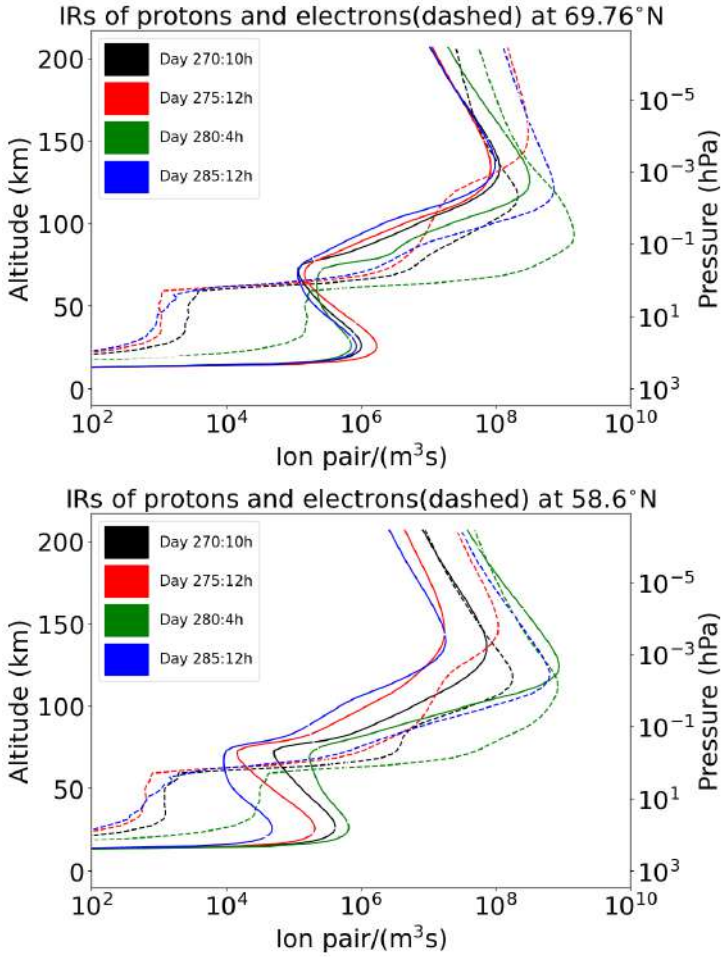

Figure 4.1: Daily mean ionisation rate (IR) profiles of protons (solid lines) and electrons (dashed lines) at a latitude:[69.76°N (polar cap) (top) and 58.6°N (at the edge of the polar vortex and inside the auroral oval) (bottom)] during geo-magnetically quiet conditions for 27th September, 2nd, 7th and 12th October.

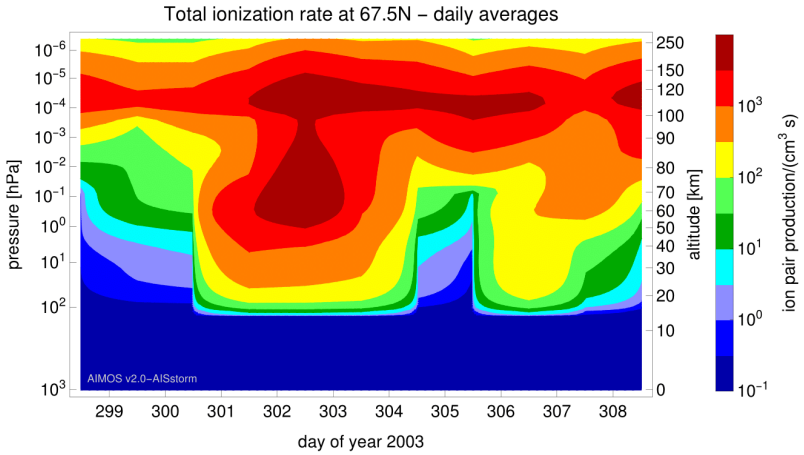

Figure 4.2: Time dependent and daily averaged ionisation rates (IRs) from 25th October to 4th November 2003 obtained from AISstorm model for a latitude of 67.5°N.

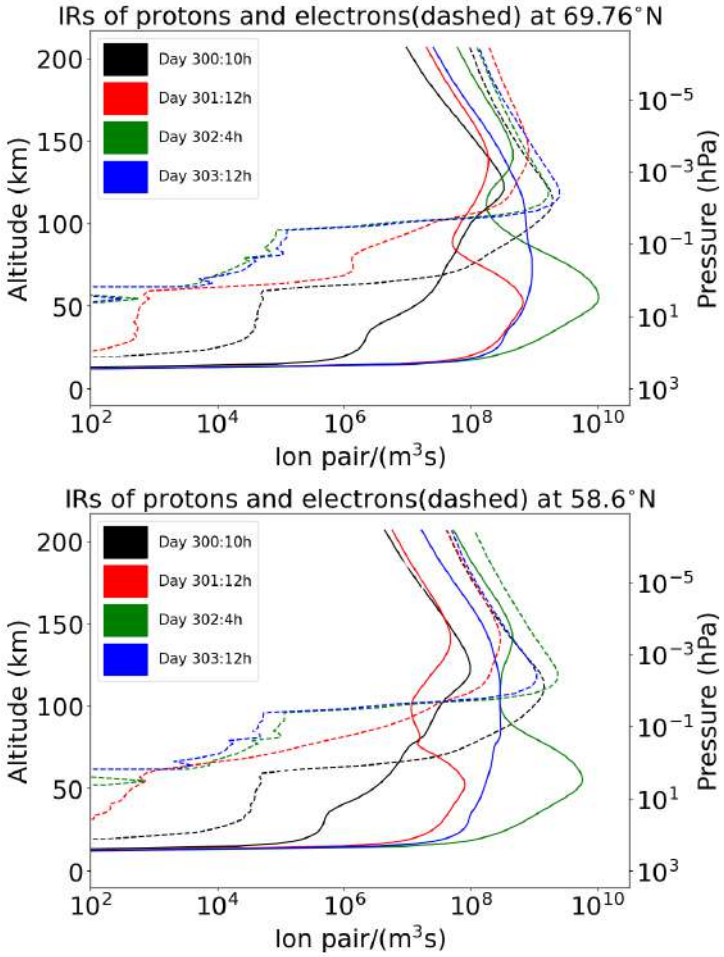

Figure 4.3: Daily mean ionisation rate (IR) profiles of protons (solid lines) and electrons (dashed lines) at a latitude:69.76°N (polar cap) (top) and 58.6°N (at the edge of the polar vortex and inside the auroral oval) (bottom) for four days: 300, 301, 302 and 303 at times 10h, 12h, 4h and 12h respectively.

Figure 4.3 shows daily mean ionisation rate profiles for days 26th, 27th, 28th and 29th of October 2003 for different times. Comparing to figure 4.1, the ionisation rates for protons in the stratosphere and lower mesosphere increased by 4 orders of magnitude on the 28th of October (event peak) and by 2 orders for the 27th in the polar cap (69.76°N) and also at the edge of the polar vortex (58.6°N). The electrons showed an increase in the mesosphere and lower thermosphere (above 75 km). On the 29th of October (day 303), the ionisation rates showed a decrease for both protons and electrons. And figure 4.4 shows ionisation rates for 27th and 28th October 2003 for four different time intervals, i.e., early event time, event phase, event maximum and late phase. In case of protons, on the 27th, in two hours, i.e., early event time and event phase, there is a drastic increase in the stratosphere but quite similar values in the mesosphere and decreasing in the thermosphere . It showed a small decrease in case of electrons. However, the IRs for electrons are higher for the early event time compared to the event phase but for protons, it is the opposite. During the event maximum, the IRs were the highest in the stratosphere and for the late phase, that is the case for the mesosphere. For the late phase, the ionisation rates increased

for the altitude range until the mesopause thereby decreasing in the thermosphere above. The temporal development of the profiles for both electrons and protons follow a similar pattern.

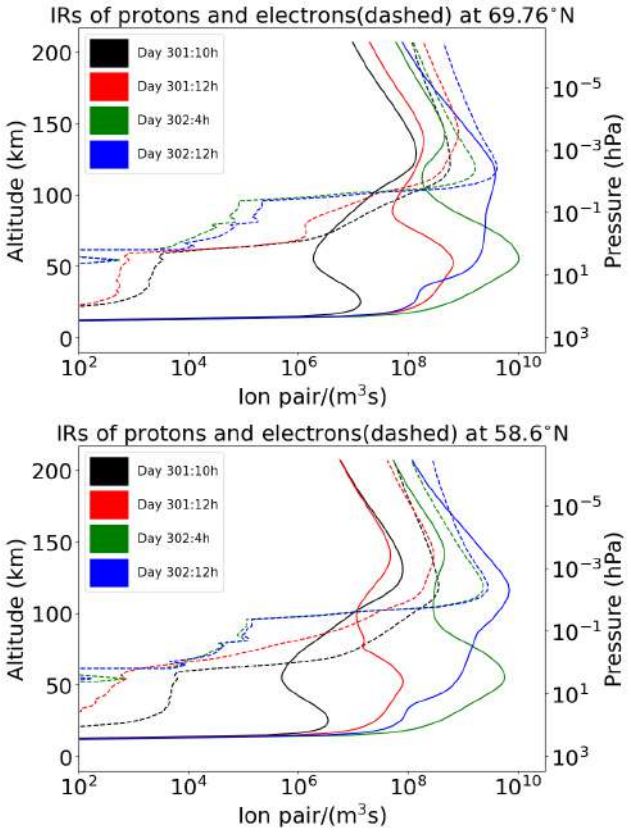

Figure 4.4: Daily mean ionisation rate (IR) profiles of protons (solid lines) and electrons (dashed lines) at a latitude:[69.76°N (polar cap) (top) and 58.6°N (at the edge of the polar vortex and inside the auroral oval) (bottom). Time shown are event peak days 301 and 302 and four different time intervals: early event time (Day 301:10h), event phase (Day 301:12h), event maximum (Day 302:4h) and late phase (Day 302:12h).

4.2 Description of Model Simulations: Sensitivity Studies

For the ExoTIC model evaluation, different sensitivity studies have been carried out. The comparison is done for the model simulations with different settings. Firstly, the simulations were carried out with full ion-chemistry. Since it produced quite high enhancements of neutral species because of its sensitivity to O(^{1}D) branching ratio, a sensitivity study with O(^{1}D) set to photo-chemical equilibrium, as discussed in Chapter 3 is also conducted. Thirdly, with the same setting, the reactions containing the uptake of Cl^- ions from gas-phase is set to zero. And lastly, a NO_x and HO_x parameterised model was used for the validation. Since ExoTIC does not have diffusion or horizontal and vertical transport, the time period of interest for the comparison was rather short. The model results are compared with MIPAS observations for a total of 9 days from 26th October to 3rd November 2003. The results and discussions are based on Borthakur et al. (2023). The model experiment details are shown concisely in Table 4.1.

Sensitivity Studies	Solar zenith angle (SZA)	Simulation time period
Full ion-chemistry	Day-time (sza <= 90°) and Night-time (sza > 98°)	Day 298-Day 307, 2003
IC O(^{1}D) P.E.	Day-time (sza <= 90°) and Night-time (sza > 98°)	Day 298-Day 307, 2003
IC w/o Cl ions	Day-time (sza <= 90°) and Night-time (sza > 98°)	Day 298-Day 307, 2003
NO_x and HO_x para	Day-time (sza <= 90°) and Night-time (sza > 98°)	Day 298-Day 307, 2003

Table 4.1: ExoTIC model sensitivity studies description

4.3 Model evaluation

In this section, different model sensitivity studies described in the previous section, have been carried out to compare the ExoTIC model results to MIPAS observations with a focus on the chlorine species of HOCl, $ClONO_2$, ozone and odd oxides of nitrogen species (NO_y) using the Halloween SPE 2003 as a test scenario. The model simulations are performed for a high latitude of 67.5°N. The model data are sampled in the MIPAS altitude grid as well. The day and night for the MIPAS data are sorted according to the solar zenith angle (sza) (day $\leq 90°$; night > 98°). The solar zenith angle for the 1D model were chosen such that, for each day, this is the mean solar zenith angle for the MIPAS data plus or minus the standard error of the mean (SEM), with N being the number of data points for each day.

$$\text{SEM} = \frac{\text{standard deviation}}{\sqrt{N}} \tag{4.1}$$

4.3.1 Estimation of the polar vortex edge using MIPAS data

The MIPAS data are taken for the polar cap region, zonally averaged over geographic latitudes of 70-90°N such that the MIPAS data are inside the polar vortex, vortex core or vortex edge depending on the tracer properties. This sampling is done in order to have a better comparison of ExoTIC simulations with the MIPAS observations. As discussed in Chapter 2, the stratospheric polar vortex is a large circumpolar cyclone that is formed due to decreased solar insolation in the polar winter stratosphere as a manifestation of a strong meridional temperature gradient caused by a lack of high-latitude solar heating during polar night and dominates the dynamics ((Harvey et al., 2015)). The assumption is that the air inside the polar vortex is horizontally well-mixed and separated from the air masses outside the vortex. This allows to simulate it better in a 1D vertical model. The ionisation during particle precipitation in the polar cap is also assumed to be inside the polar vortex, where NO_x is conserved, which makes it better comparable to the 1D model. There are different methods of estimating the polar vortex edge, and one of the widely used methods is to use CO as a tracer of vortex air. Due to its strong vertical gradient and longevity in the polar winter vortex, CO is commonly used as a tracer of vortex air originating from the upper mesosphere and lower thermosphere. Hence, it can be used to estimate the vortex edge. We use a CO vmr threshold (discriminating mesospheric air from the background) as a vortex criterion. An altitude independent criterion is needed to differentiate entire profiles. And our short time period (a few days) allows for a time-independent definition. A chemical vortex definition (via CO) is also widely used in the

mesosphere ((Harvey et al., 2015)). For the chemical species and the SPE responses discussed here, the relevant altitude range is more in the stratosphere. In the stratosphere, the vortex might be considerably smaller and is commonly determined from the potential vorticity. Figure 4.5 shows volume mixing ratios of CO versus latitude in the Northern Hemisphere for different longitude bins of size 20 (as shown by different colours) and averaged over latitude bins of size 5 from 27 October (day 300) to 3 November 2003 (day 307) separated by daytime and night-time. A threshold of 0.5 ppmv of CO was chosen at an altitude of 68 km to determine the polar vortex boundary from the corresponding x-axis, where an increase in the volume mixing ratios start to occur. An increase is observed starting at a latitude of approximately 55°N for the different days. The estimation of the polar vortex boundary helps to choose the MIPAS sampling of the zonal averages for a better inter-comparison. One can also check the vortex boundary by looking at CH_4 zonal means, e.g. Figure 9 of Funke et al. (2011). From that figure, and as also discussed in Funke et al. (2011), the boundary is around 60°N, which also works well for the stratosphere. The latitude 57°N was chosen as where the vortex begins and defined the latitude bands 57-77°N as "the edge region of the vortex" and the high-latitude bands 70-90°N as "deep in the vortex".

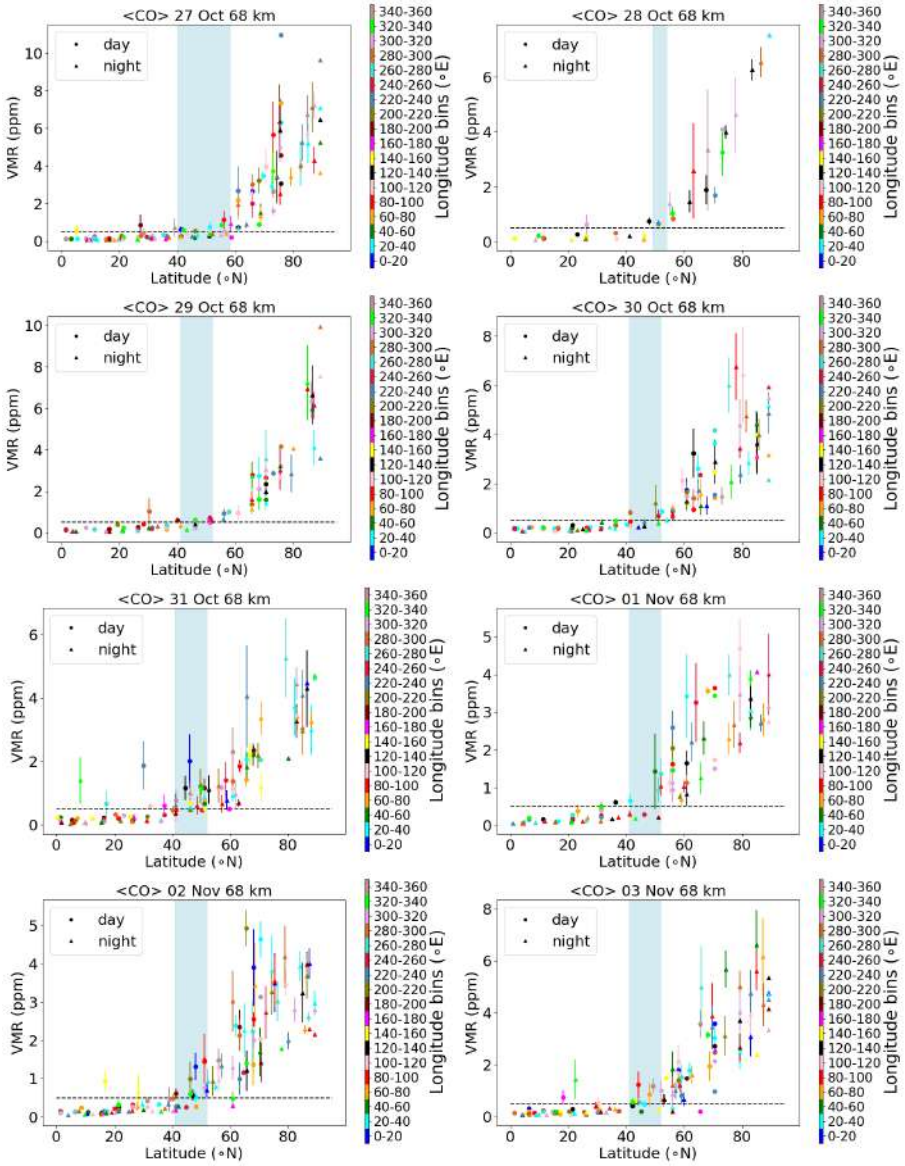

Figure 4.5: MIPAS daily averaged CO (ppm) as a function of latitude (°N) for longitude bins of size 20 and averaged over latitude bins of size 5 for 27th October-3rd November 2003 (day and night) at 68 km altitude. Colors mark the longitude bins from 0-20°E to 340-360°E running from blue to rosybrown. The error bars mark the standard error of mean. The light-blue shaded region marks the latitude range of the vortex edge and the dashed horizontal line is the CO threshold of 0.5 ppm.

4.3.2 Application of MIPAS averaging kernels to the model profiles

Due to the difference in vertical resolutions between the model and MIPAS observations, averaging kernels were applied. The averaging kernels were applied after samplig the model data in the MIPAS altitude grid. The vertical resolution of ExoTIC is 2.7 km, whereas MIPAS has different vertical resolutions for different species. For example, in case of HOCl, the maximum vertical resolution can be 17 km, and for $ClONO_2$, it can be 13 km at an altitude of 40 km and above, as seen from an example in Figure 4.6 for a specific time point. To remove the discrepancy of different vertical resolutions between

the model and MIPAS observations, the original model profiles have to be convoluted and adjusted to the MIPAS altitude resolution. This adjustment procedure yields new species profiles that MIPAS would see if it were to sound the model atmosphere. Using equation 3.14 and a scheme suggested by Connor et al. (1994) to adjust the better-resolved model profiles to those of MIPAS, and the new adjusted model profiles are calculated.

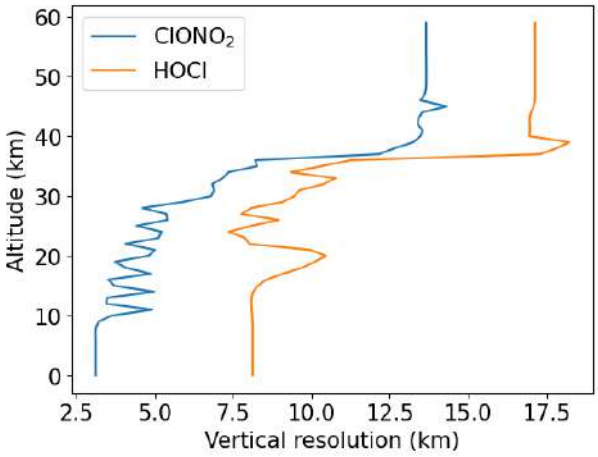

Figure 4.6: Example of typical profiles for the vertical resolution of HOCl and $ClONO_2$.

Since ExoTIC being a 1D column model does not produce the output at the same geo-locations as MIPAS, the application of the MIPAS averaging kernels was based on the temperature criteria. The following procedure was applied for the convolution.

- The model profiles were selected, one at a time, from the entire time series.
- All the profiles from MIPAS within 57.5 and 77.5°N latitude and $\pm$6h of the model profile's time were selected.
- For this obtained MIPAS sample of temperature profiles, the root mean square value was calculated with the model's temperature profile, which is fixed for the entire time series.
- The geo-location for which the root mean square value of the temperature difference profile was minimal was selected, and the averaging kernels for this geolocation were applied to the trace gas profiles from the model.

Using this procedure, the model profiles adjusted to the vertical resolution of MIPAS were obtained. The data were then daily averaged and the absolute or relative differences w.r.t. a day before the event, i.e. 26 October 2003 was calculated.

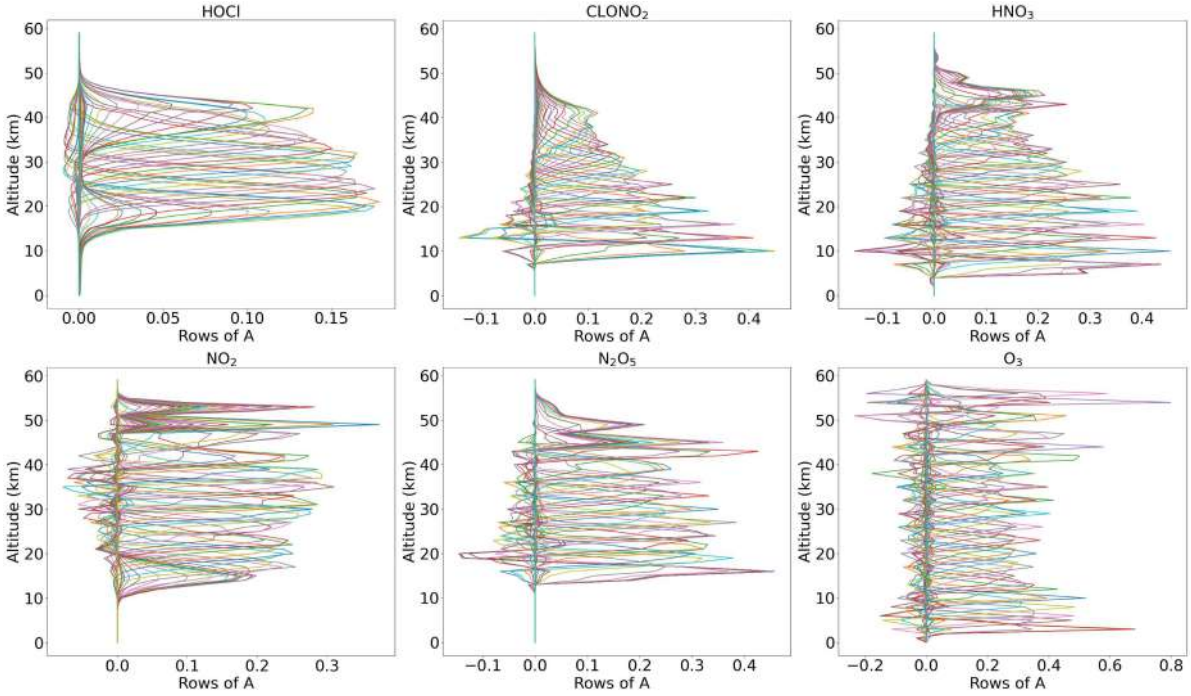

Figure 4.7: Example of rows of MIPAS Averaging Kernels (**A**) for typical MIPAS HOCl, $ClONO_2$, HNO_3, NO_2, N_2O_5 and O_3 at a latitude of 67.5°N on 27 October 2003 at 00:00 UT.

4.3.3 HOCl

A comparison of ENVISAT MIPAS V5 HOCl measurements (von Clarmann et al., 2006) for the polar Northern Hemisphere (57-77°N) and ExoTIC computations with different settings of HOCl simulation is presented in figure 4.9 and 4.11 for daytime and nighttime respectively. The model data is read out in the solar zenith angle range of MIPAS daytime and nighttime observations. The values in both figures 4.9 and 4.11 start on the 26th October 2003 (day 299). MIPAS observations for HOCl showed enhancements with peak values of 0.2 ppb for daytime and 0.24 ppb for nighttime on the 29th of October. The model results with full ion-chemistry, overestimated the observed enhancements for night-time by a factor of 4 (around 1.25 ppb) as shown in figure 4.10. And for day-time, the overestimation was by a factor of 3 (around 0.65 ppb) produced at an altitude of 35-40 km as seen from figure 4.8. HOCl enhancements below 30 km was also observed for both daytime and night-time with full ion-chemistry and a peak producing 0.12 ppb was observed in the mesosphere during night-time. Sensitivity studies were performed setting O(^{1}D) to photo-chemical equilibrium that showed a decrease in the enhancements from 1.25 ppb to 0.55 ppb during nighttime and 0.65 ppb to 0.08 ppb during daytime produced by the model also at 35-40 km during the event. The higher mixing ratios of HOCl below 30 km for both daytime and nighttime also disappeared with this setting. Switching off the chlorine ion-chemistry led to the removal of 0.2 ppb HOCl observed in the mesosphere during nighttime. And similar behaviour was also observed for the parameterised NO_x and HO_x model. However, much lower values were observed during daytime for the model, setting O(^{1}D) to photo-chemical equilibrium, without chlorine ion-chemistry and parameterised

NO_x and HO_x compared to MIPAS observations. Reaction rate constants and photo-chemical data follow in general the JPL-2006 recommendations from Sander et al. (2006).
After the application of averaging kernels the higher mixing ratios produced by the model were smeared out over altitudes and reduced in their peak value. For daytime, the peak value of the full ion-chemistry model decreased from 0.65 ppb to 0.4 ppb. And for the sensitivity studies with $O(^1D)$ in photo-chemical equilibrium, without chlorine ion-chemistry and parameterised NO_x and HO_x, the peak value of 0.08 ppb decreased to 0.03 ppb. This peak value occurs due to the increased availability of chlorine atoms due to the catalytic ozone destruction cycle. The HOCl concentration reaches a peak around 35 km during daytime because this altitude represents the optimal conditions for the ClO-HOCl catalytic cycle (Reactions R38, R39, R40 and R37) to occur. For night-time, full ion-chemistry peak value of 1.25 ppb went down to 0.84 ppb after applying the MIPAS averaging kernels. Setting $O(^1D)$ to photo-chemical equilibrium decreased the peak value from 0.55 ppb to 0.36 ppb which is in better agreement with the MIPAS observations. For the model without chlorine ion-chemistry and parameterised NO_x and HO_x, the enhancements of 0.58 ppb went down to 0.33 ppb that also agrees quite well. Figure 4.12 shows the difference of the model results with MIPAS observations for the different runs, where it can be seen that the difference is lower with averaging kernels applied. Jackman et al. (2008) compared results from the Whole Atmosphere Community Climate Model (WACCM3) with MIPAS observations and applied MIPAS averaging kernels for the Halloween SPE 2003 and found the HOCl peak at an altitude of 48 km on the 29^{th} of October and the MIPAS averaging kernels moved it down to 40 km. ExoTIC however produced the peak around 35-40 km itself for both daytime and nighttime for all the test cases. This is actually quite in agreement with the MIPAS observations and the application of the averaging kernels also didn't shift the peak in terms of altitude. This difference in the peak altitude between the results from Jackman et al. (2008) and ExoTIC might be due to the fact that WACCM3 has fully interactive dynamics, radiation, chemistry and other parameterizations whereas ExoTIC includes only the chemistry. Damiani et al. (2012) considered the SPE of January 2005 where they observed 0.2 ppb increase of HOCl during the event in the polar cap region also using the WACCM model that agreed quite well with Microwave Limb Sounder (MLS) observations. Enhancements of HOCl results from enhanced HO_x constituents. In the middle stratosphere, it is mainly accelerated by odd hydrogen chemistry (via Reaction R37). The morphology of the HOCl distribution and it's temporal variation is a combined effect of photolysis, temperature and availability of ClO, HO_2 and OH, which in themselves show pronounced diurnal variation.

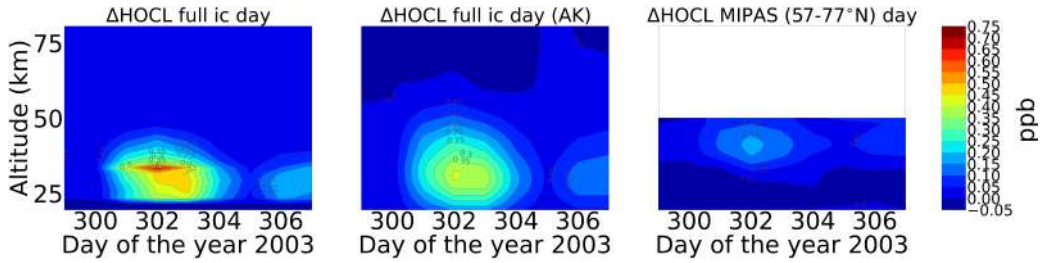

Figure 4.8: Absolute differences of daily averaged data for HOCl w.r.t. a day before the event, i.e. 26th October 2003 for the model setting with full ion-chemistry (day-time).

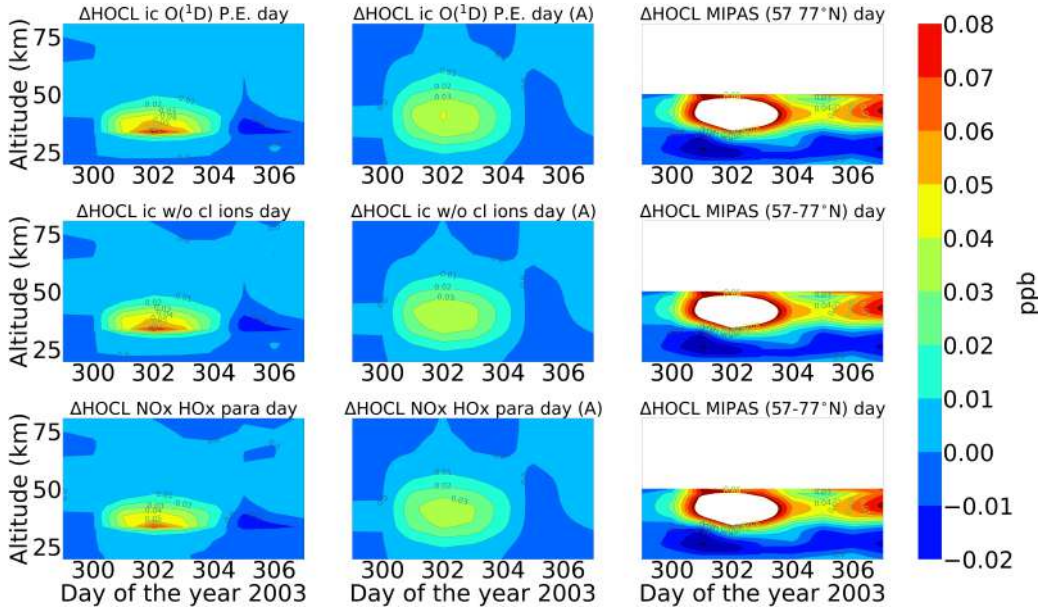

Figure 4.9: Absolute differences of daily averaged data for HOCl w.r.t. a day before the event, i.e. 26th October 2003. Starting point is 26th October 2003 and for the three different model settings (Sensitivity tests (row-wise): ion-chemistry with O(^{1}D) in photo-chemical equilibrium, switching off chlorine ion-chemistry and parameterised NO_x and HO_x); column-wise: without Averaging kernal (A), with Averaging kernel (A) applied and MIPAS observations averaged over 57-77°N for day-time (sza <= 90°). For daytime, the white region below 50 km is the MIPAS peak (0.2 ppb) and the colorbar is adjusted to the lower mixing ratios predicted by the model (first plot). The white region above 50 km for the MIPAS observations represent meaningless data, where the values of Averaging kernal (A) diagonal elements are close to zero (< 0.03) that indicate no sensitivity to the retrieved parameter at the corresponding altitude. Colorbar interval: (-0.02, -0.01, 0.00, 0.01, 0.02, 0.03, 0.04, 0.05, 0.06, 0.07, 0.08)

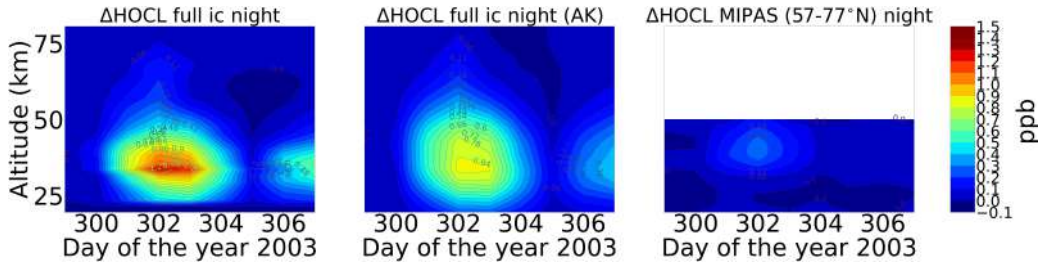

Figure 4.10: Absolute differences of daily averaged data for HOCl w.r.t. a day before the event, i.e. 26th October 2003 for the model setting with full ion-chemistry (night-time).

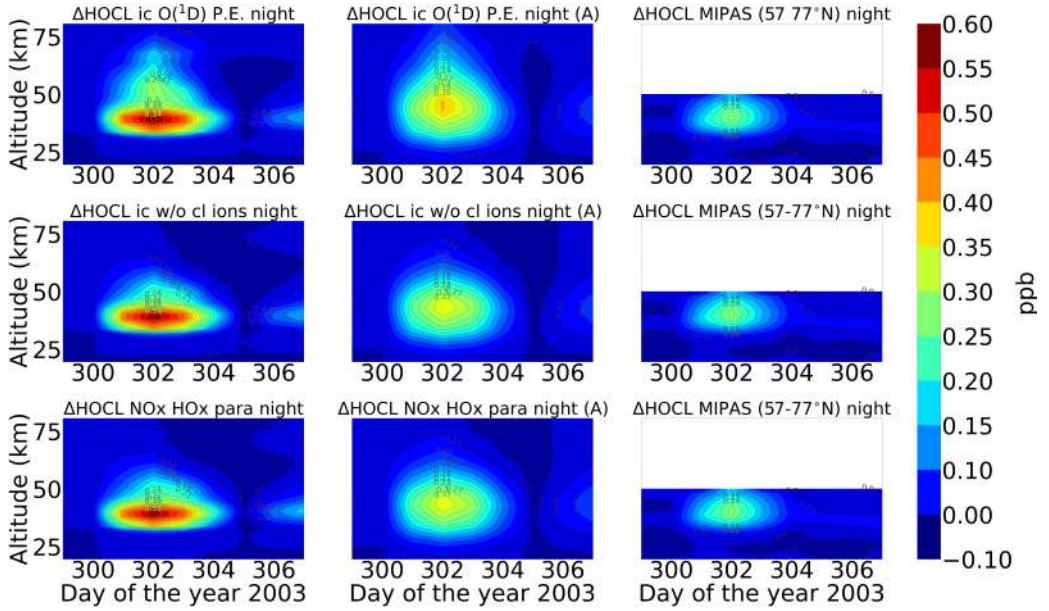

Figure 4.11: Same as figure 4.9 but for nighttime (sza $>$ 98°). Colorbar interval: (-0.10, 0.00, 0.10, 0.15, 0.20, 0.25, 0.30, 0.35, 0.40, 0.45, 0.50, 0.55, 0.60)

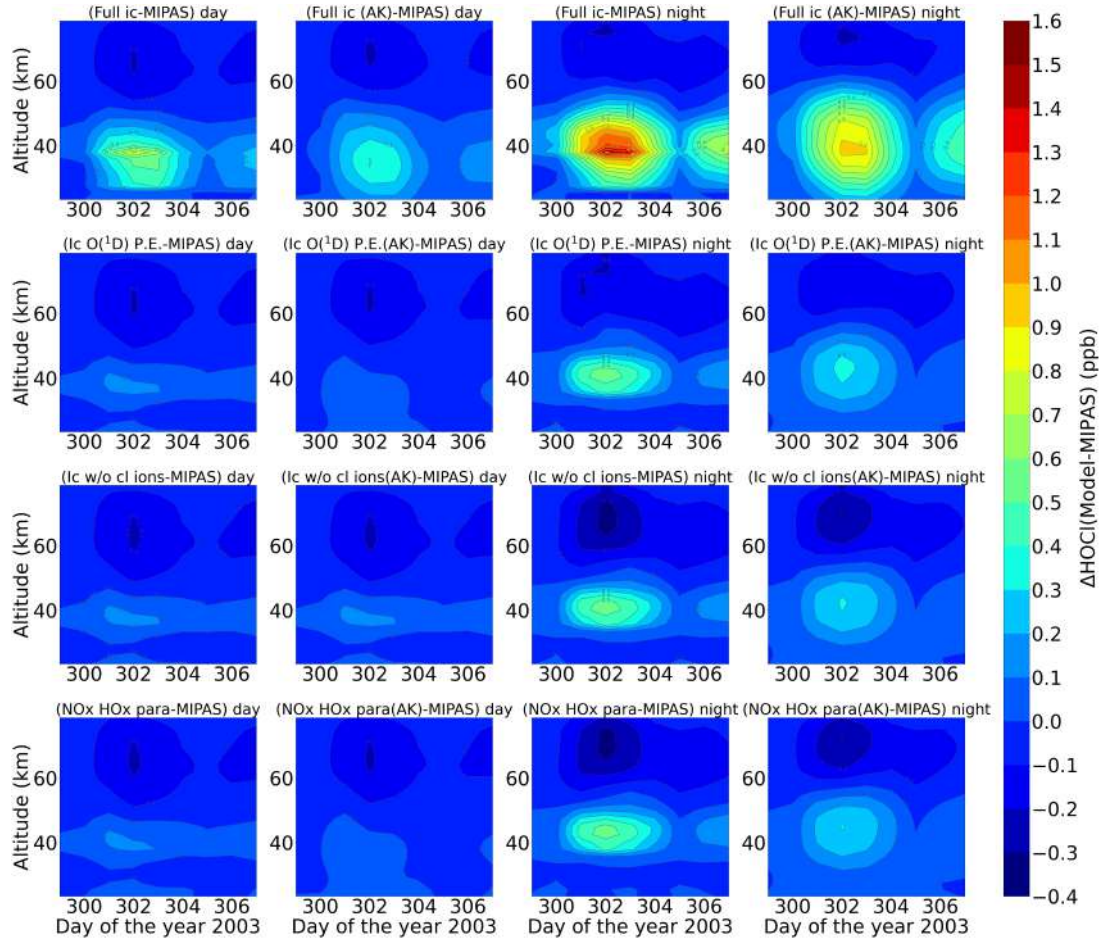

Figure 4.12: (Model-MIPAS) for day-time (sza <= 90°) and night-time (sza > 98°). Row-wise: Differences w.r.t. MIPAS zonal averages for: Full ion-chemistry, full ion-chemistry with O(^{1}D) in photo-chemical equilibrium, sensitivity tests without chlorine ion-chemistry and parameterised NO_x and HO_x model. Column-wise: Daytime, daythime (model with averaging kernel applied), nighttime, nighttime (model with averaging kernel applied).

4.3.4 $ClONO_2$

Figures 4.14 and 4.16 show the daily averaged absolute differences for ENVISAT MIPAS V5 (Höpfner et al., 2007a) and modelled chlorine nitrate w.r.t. 26th October 2003 for day-time and night-time. The zonal average for chlorine nitrate, $ClONO_2$ observations was also taken over a latitude range of 57-77°N, the edge region of the polar vortex. Continuous enhancements of $ClONO_2$ is observed for the full ion-chemistry model with peak values of 0.96 ppb and 1.15 ppb also approximately two days after the event for daytime and night-time respectively starting from the onset of the event on 28th of October (Figures 4.13 and 4.15). The peak was observed around 25 km. In case of the model with ion-chemistry but O(^{1}D) set to photo-chemical equilibrium, a peak value of around 0.18 ppb was observed for both day-time and nighttime which compared much better with the MIPAS observations. Similar results were also observed for the sensitivity study without chlorine ion-chemistry and parameterised NO_x and HO_x model. The increase was seen also approximately two days after the event in the altitude range of 35-40 km. After

the application of averaging kernels the peak value for the full ion-chemistry daytime and night-time decreased down to 0.66 ppb and 0.78 ppb respectively. For the rest, the peak value decreased from 0.12 ppb to 0.09 ppb for daytime and from 0.18 ppb to 0.12 ppb for night-time. Figure 4.17 shows the differences of different model runs with MIPAS observations. As expected, model with averaging kernels applied produces lower values, thereby comparing better. Jackman et al. (2008) observed $ClONO_2$ maximum enhancements of 0.3-0.4 ppb with the peak production at a higher altitude of 40-45 km with WACCM3. The peak however was produced several days later than MIPAS. The application of MIPAS averaging kernels moved the peak down to 40 km and the predicted peak increases are reduced substantially to about 0.2 ppbv, about a factor of 2 less than MIPAS observations. The enhanced $ClONO_2$ production happens due to SPE produced NO_x via Reaction R50. $ClONO_2$ is removed mainly by photolysis in the sunlit atmosphere and, to a lesser extent, by reaction with atomic oxygen. And due to it's pressure dependence, $ClONO_2$ formation by Reaction R50 is more effective at lower altitudes (Funke et al., 2011). The zonal average of MIPAS observations were tested for latitude bands 57-77°N, i.e., at the edge region of the polar vortex and 70-90°N, deep in the polar vortex. The sample of 57-77°N works better for the inter-comparison of $ClONO_2$ compared to 70-90°N. In case the sample is taken deep in the vortex, the model seemed to fairly underestimate the peak values. This can be explained by the Reaction R50, where formation of ClO needs sunlight, which is again available more at the edge region of the polar vortex. But $ClONO_2$ can also photolyse in the presence of sunlight and due to this, there is a balance between the two processes and $ClONO_2$ can form at the edge region which can be transported deep into the vortex and conserved there at high latitudes. This however cannot be reproduced by the 1D model because it is fixed at a certain location and has no transport.

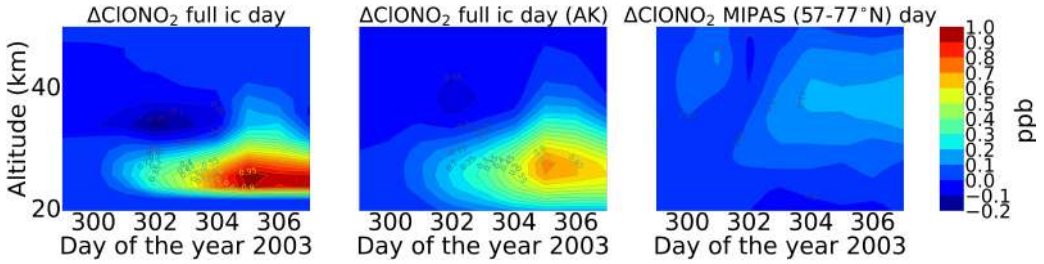

Figure 4.13: Same as figure 4.8 but for $ClONO_2$.

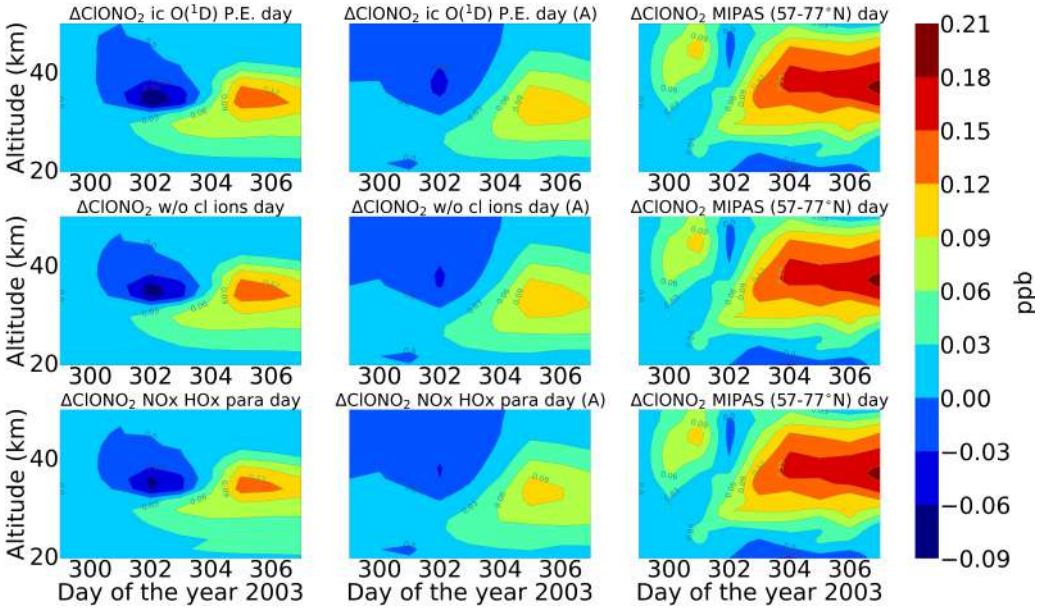

Figure 4.14: Same as figure 4.9 but for $ClONO_2$. Colorbar interval: (-0.09, -0.06, -0.03, 0.00, 0.03, 0.06, 0.09, 0.12, 0.15, 0.18, 0.21)

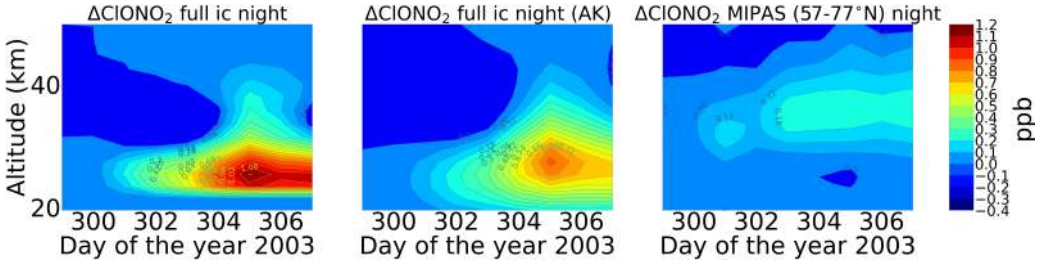

Figure 4.15: Same as figure 4.10 but for $ClONO_2$.

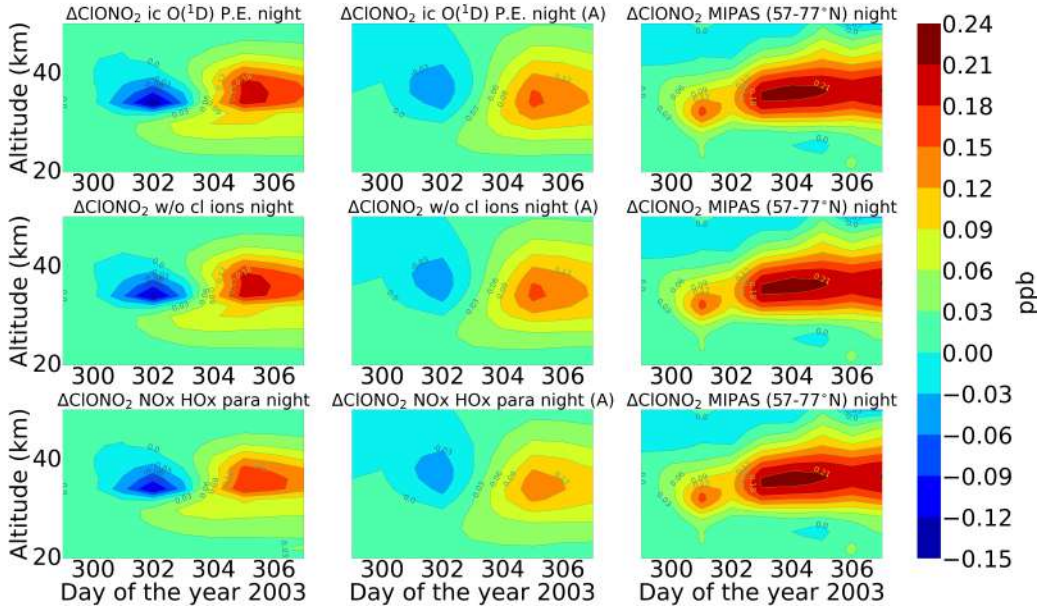

Figure 4.16: Same as figure 4.11 but for $ClONO_2$. Colorbar interval: (-0.15, -0.12, -0.09, -0.06, -0.03, 0.00, 0.03, 0.06, 0.09, 0.12, 0.15, 0.18, 0.21, 0.24)

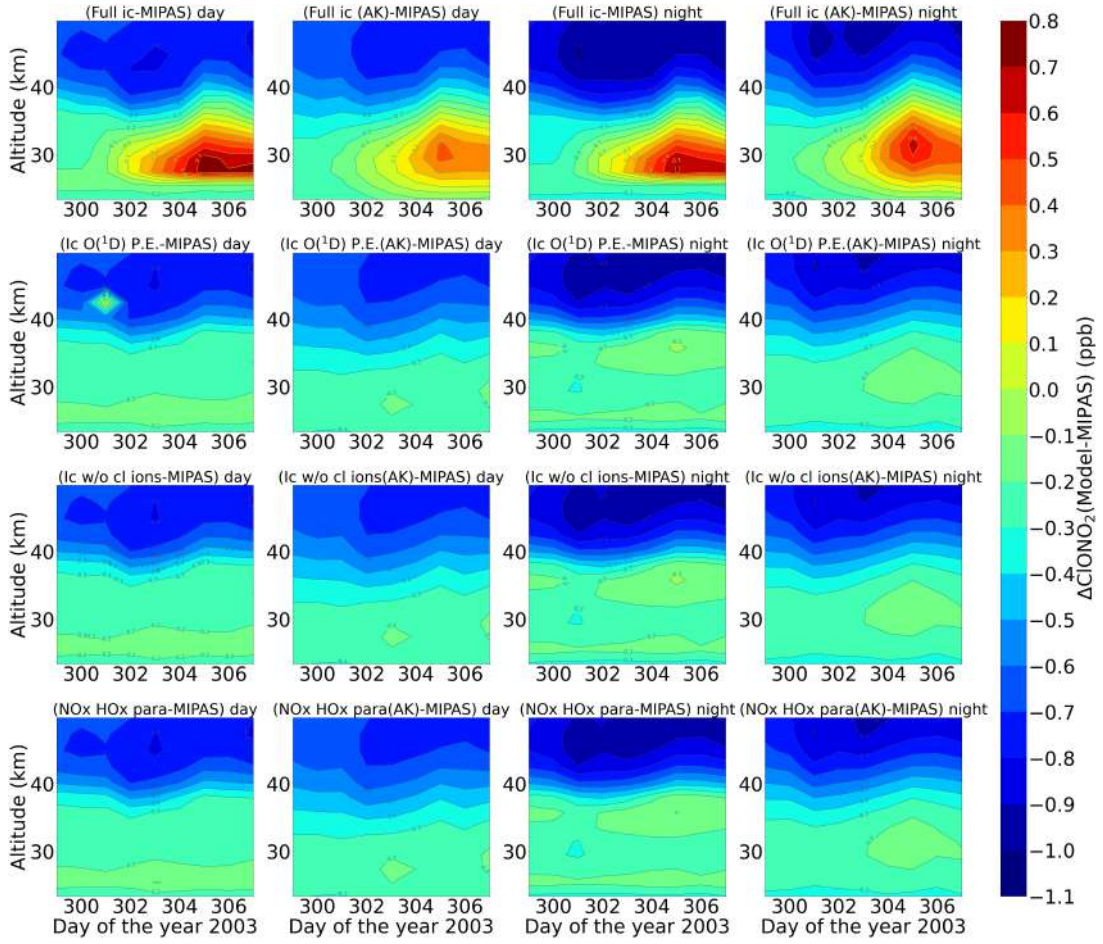

Figure 4.17: Same as figure 4.12 but for $ClONO_2$.

4.3.5 Ozone

Energetic particles in the polar atmosphere enhances the production of NO_x and HO_x in the winter stratosphere and mesosphere. Both NO_x and HO_x are powerful ozone destroyers. An important aspect in the evaluation of the ability of models is the reproduction of the observed ozone destruction caused by the catalytic cycles of NO_x and HO_x during SPE induced chemical composition changes. As inferred from observations, stratospheric ozone decreases due to the indirect effect of EPP by about 10–15 % as observed by satellite instruments (Meraner and Schmidt, 2018). López-Puertas et al. (2005) found HO_x related mesospheric ozone losses upto 70% and NO_x related stratospheric loss of around 30% during the Halloween SPE.

Figures 4.19 and 4.21 show ENVISAT MIPAS V5 (Glatthor et al., 2006) and modelled temporal evolution of the relative ozone changes w.r.t. 26th October, averaged over 70-90°N for daytime and nighttime respectively. For ozone, the long term history of air parcels is more important as air parcels that are ozone depleted gets dispersed into the mid-latitudes if they are at the edge region of the vortex. So a sample deeper in the vortex for ozone is better, the reason we chose 70-90°N here. A loss of 60-75% is observed during the event itself in the mesosphere that is short lived and is related to the HO_x catalytic cycle, where X = H and OH in Reactions R28 and R29, (Funke et al., 2011)(Bates and Nicolet, 1950). The ozone recovers after the event, since HO_x is short-lived. A second peak is observed on the 3rd of November which is related to a weaker coronal mass ejection event. NO_x related loss of 15% is observed in the stratosphere that lasts longer and is also related to the polar winter atmosphere (Reactions R28 and R29 with X = NO). The full ion-chemistry (figures 4.18 and 4.20) shows an ongoing loss of 45% starting from the event day and the sensitivity study with O(^{1}D) in photo-chemical equilibrium confirmed that this loss is due to Reactions like R71 and R68, which produces OH and Cl contributing further to ozone loss. The agreement between the observations and the model results, for night-time, for the three model results except for the full ion-chemistry is excellent in the mesosphere indicating a good ability of the model to reproduce HO_x related ozone loss for SPEs. However, the ozone loss shifted to lower altitudes for both daytime and night-time in all the model settings as compared to MIPAS observations. This could be explained as a result of the AISstorm ionisation rates that was used in the model which could be different to what MIPAS might have experienced during the SPE. AISstorm here uses proton fluxes from GOES 10 and the ionisation rates should be a lower estimate. The SPE ionisation happens in the denser atmosphere, therefore the conversion from particle fluxes into ionisation should be more or less precise in terms of total ionisation and altitude. The main uncertainty of SPE ionisation in AISstorm is the size of the area that is affected by high energetic particle precipitation. This cannot be derived from these channels but is taken from a lower energy channel on another satellite and thus it might be an underestimation of the polar cap size. However if that would be important for the spatial average 70-90°N, we should see an underestimation of the ionisation (and NO_y) as well, which doesn't seem to be the case (and which is unlikely anyway as the equator-ward boundary should be at about 60°N).

Figure 4.22 shows the absolute difference between model runs and MIPAS observations in ppb. In this case, the difference between the model with and without averaging kernels and MIPAS observations is not too big.

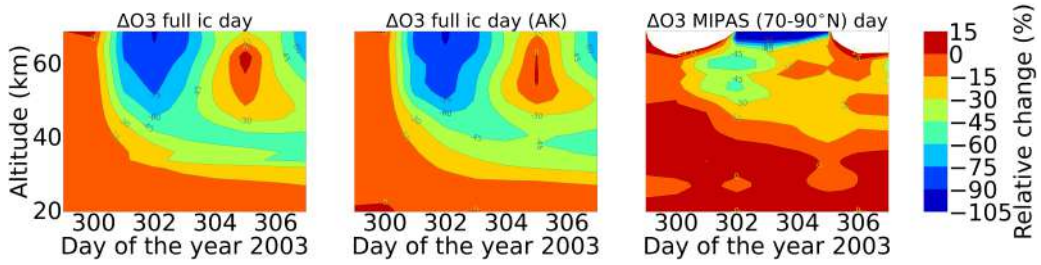

Figure 4.18: Same as figure 4.8 but for O_3.

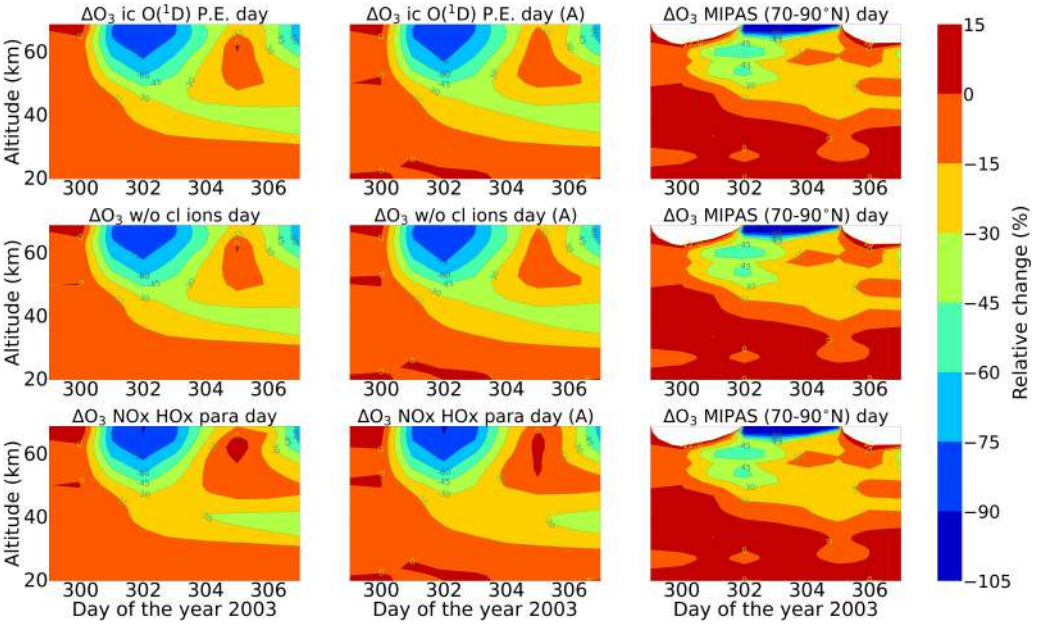

Figure 4.19: Relative difference of ozone w.r.t. 26th October. Rest is same as figure 4.9. Colorbar interval: (-105, -90, -75, -60, -45, -30, -15, 0, 15)

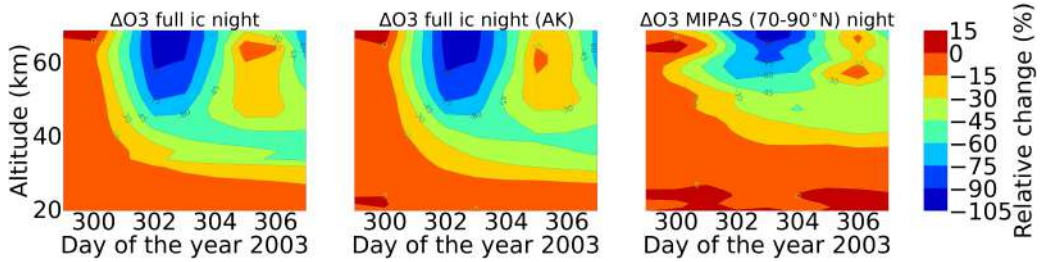

Figure 4.20: Same as figure 4.10 but for O_3.

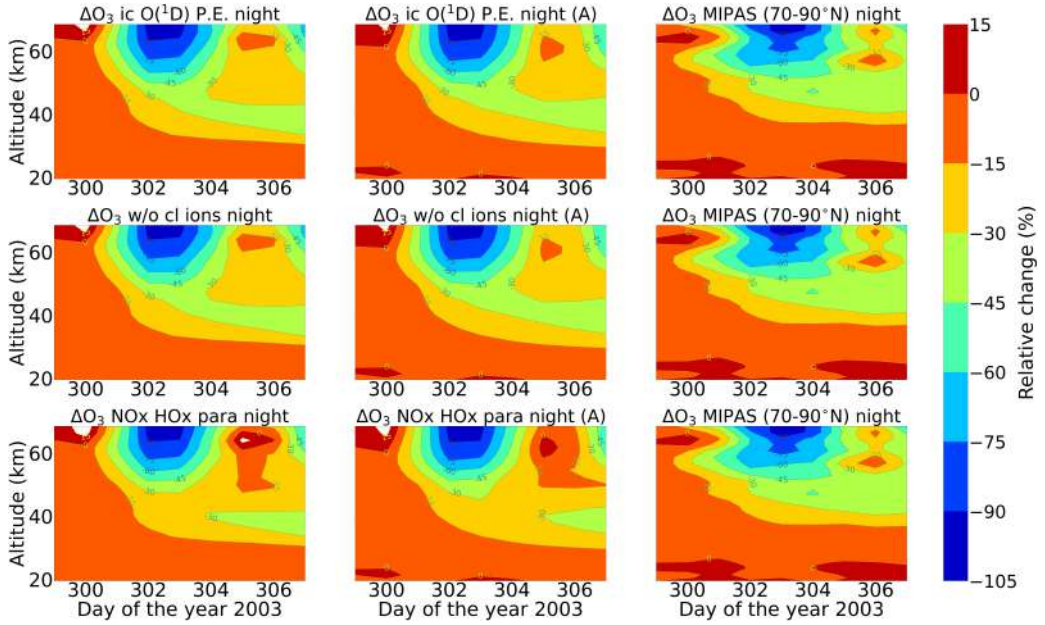

Figure 4.21: Same as figure 4.19 but for night-time. Colorbar interval: (-105, -90, -75, -60, -45, -30, -15, 0, 15)

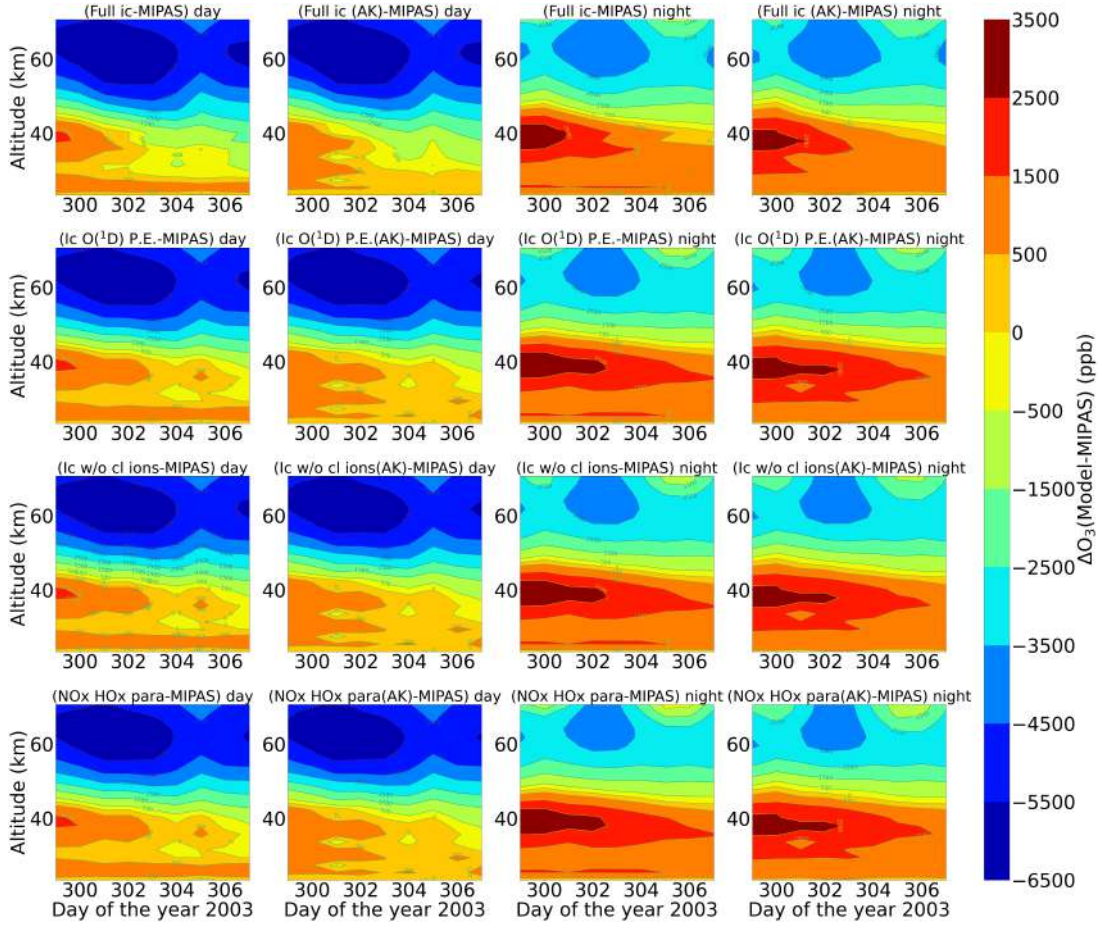

Figure 4.22: Same as figure 4.12 but for ozone.

4.3.6 HNO_3

The retrieval setup of nitric acid, HNO_3 is based on Wang et al. (2007). HNO_3 buildup of about 4.5 ppb during daytime and 8.0 ppb during night-time was observed around 50 km in the full ion-chemistry model during the proton forcing. Further buildup of HNO_3, $\sim$ 3.5-4.0 ppb is observed at slightly lower altitudes as seen from figure 4.23, which is consistent with previous findings from López-Puertas et al. (2005). MIPAS observations reported a peak of 2.0 ppb at 40 km and above for day-time and 4.0 ppb for night-time. As seen from figure 4.24, the model with $O(^1D)$ set to photo-chemical equilibrium compared much better for day-time with a peak of 5.0 ppb at 40 km and above. The parameterised model didn't show a peak during the solar forcing. With averaging kernels, the peak value decreased to 4.5 ppb, still rather overestimated compared to MIPAS peak of 2.0 ppb at that altitude. For night-time, the model results are quite overestimated, showing 10.5 ppb decreasing to 9.5 ppb with averaging kernels compared to MIPAS observations of 3.5 ppb. The second peak on the 3rd of November shows 1.0 ppb for all the model sensitivity runs and MIPAS day-time. And for night-time, it is 2.0-2.5 ppb for models and $\sim$ 1.5 ppb in MIPAS. At 30-35 km, a continuous formation of 0.5-1.0 ppb of HNO_3 is seen. This sudden enhancement is due to the gas-phase chemistry and major gas-phase reactions where HNO_3 is involved:

$$NO_2 + OH + M \longrightarrow HNO_3 + M \quad \text{(R73)}$$

$$HNO_3 + OH \longrightarrow NO_3 + H_2O \quad \text{(R74)}$$

$$HNO_3 + h\nu \longrightarrow NO_2 + OH \quad \text{(R75)}$$

Reaction R73 is the major production process. It is fast enough to produce an HNO_3 enhancement similar to that observed and faster than the loss processes (Reactions R74 and R75). Reaction R74 is slower than reaction R75, some of the HNO_3 enhancements could be caused by an increase of OH, NO_2 or both. The increase of HNO_3 at 35-40 km is caused by Reaction R73 due to an increase of OH in that region. The most important process producing HNO_3 in the stratosphere and mesosphere and creating the direct HNO_3 effect is ion-ion recombination (Aikin, 1997) (Verronen et al., 2008). HNO_3 is produced through reactions of water clusters and nitrate via the following pathway;

$$O_2^+(H_2O) + H_2O \longrightarrow H_3O^+(OH) + O_2 \quad \text{(R76)}$$

$$H_3O^+(OH) + H_2O \longrightarrow H^+(H_2O)_2 + OH \quad \text{(R77)}$$

$$H^+(H_2O)_n + NO_3^-(HNO_3)_m \rightarrow (m+1)HNO_3 + nH_2O \quad \text{(R78)}$$

$$\text{Net} : H_2O + NO_3 \longrightarrow HNO_3 + OH \quad \text{(R79)}$$

with n = 0-8 and m = 0-2 and HNO_3 being produced under dark conditions. Solomon et al. (1981) gave a detailed description of how SPEs lead to the formation of OH and $H^+(H_2O)_n$ water cluster ions and discussed the subsequent production of H resulting from electron-ion recombination. They pointed out that in the lower mesosphere ion-ion recombination with NO_3^- ions, i.e. reaction R78, was more likely,

leading to formation of HNO_3 instead of H. This also requires production of the nitrate ion NO_3^- and the dominant process for that in the stratosphere is through (Brasseur and Solomon, 1984),

$$CO_3^- + NO_2 \longrightarrow NO_3^- + CO_2. \tag{R80}$$

For night-time in the polar regions, HNO_3 has a longer chemical lifetime ($\sim$ months). And after the SPE, HNO_3 can serve as a reservoir of HO_x in polar night and be transported from the original location of the proton forcing. This can lead to more effective ozone depletion in the mesosphere because rapid photo-dissociation of built-up HNO_3 releases HO_x in conditions where atomic oxygen is available for catalytic depletion cycles (Verronen et al., 2006). Studies by Verronen et al. (2008) also showed overestimated amounts of HNO_3 by SIC model compared to MIPAS observations. The model overestimation arises from inaccuracies in the reaction rate constants in the SIC model. We believe that a similar reason is responsible for over-estimations seen in the ExoTIC model.

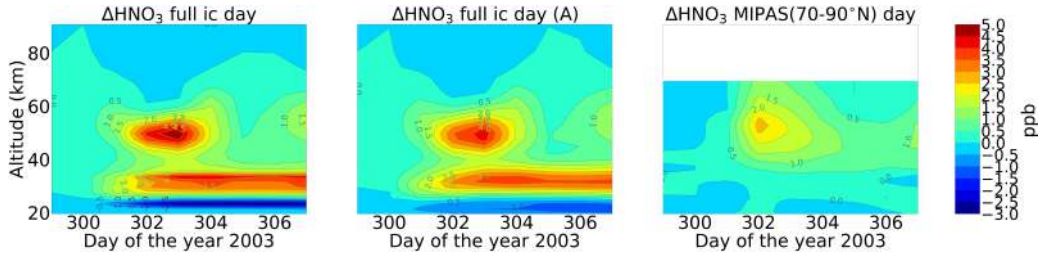

Figure 4.23: Same as figure 4.8 but for HNO_3.

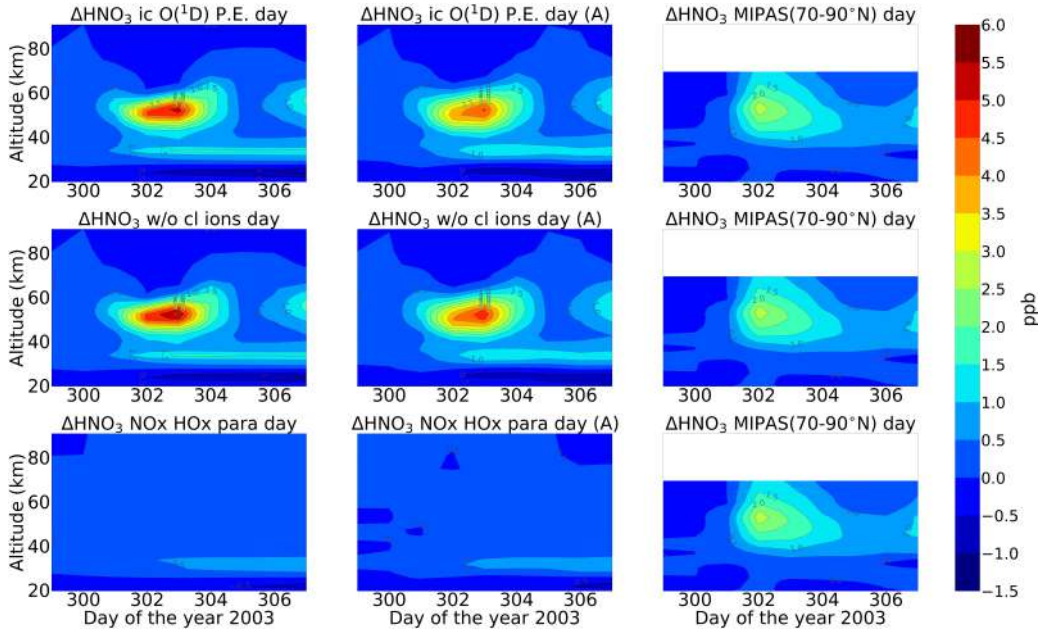

Figure 4.24: Same as figure 4.9 but for HNO_3.

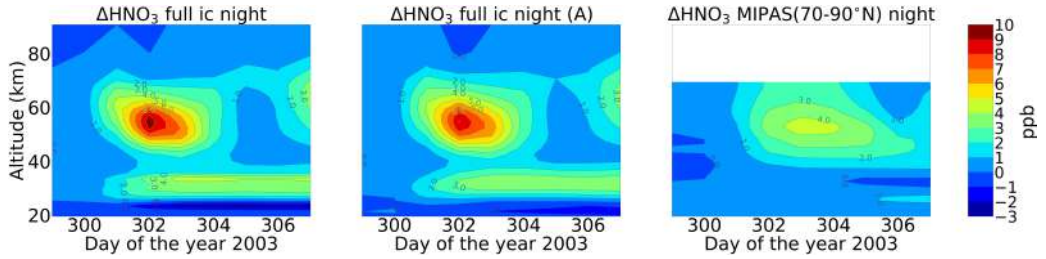

Figure 4.25: Same as figure 4.10 but for HNO_3.

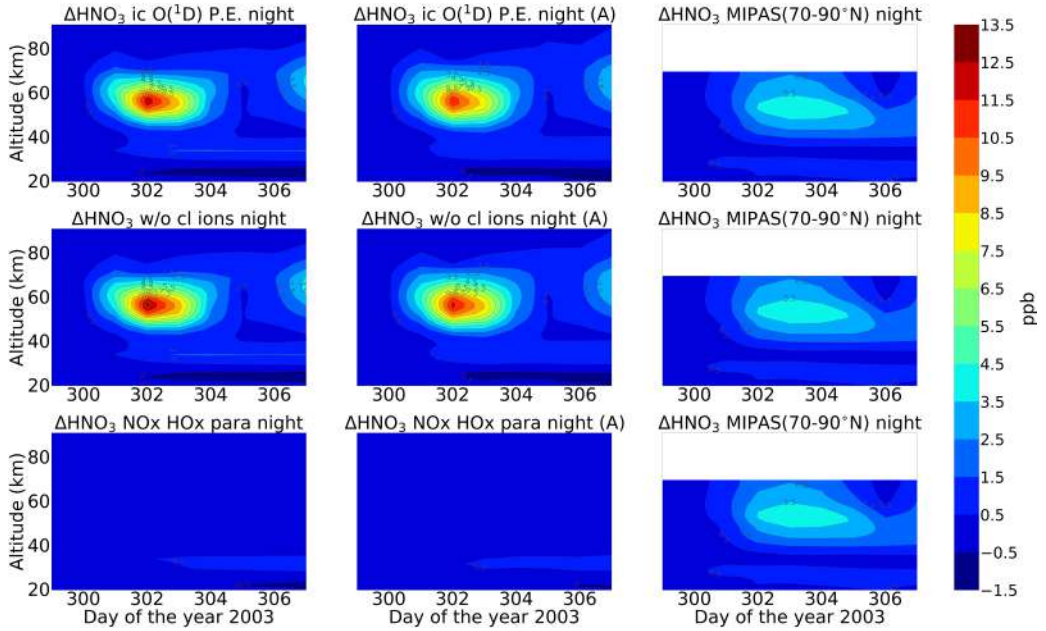

Figure 4.26: Same as figure 4.11 but for HNO_3.

4.3.7 N_2O_5

Nitrogen pent-oxide (N_2O_5) showed enhancements upto 1.4 ppb on the event day, below 30 km with full ion-chemistry. At 40 km, enhancements of 0.3 ppb and 0.8 ppb was found during day-time and night-time respectively. Model values are overestimated for both day and night with full ion-chemistry. The sensitivity run with $O(^1D)$ set to photo-chemical equilibrium showed a peak of 0.25 ppb for day-time and 0.55 ppb for night-time on the event day. This peak at 40 km was not seen by MIPAS. However, the secondary peak on the 3rd of November with 0.3 ppb was reproduced for night-time and a continuous formation of 0.15-0.25 ppb was formed at 25 km which was in agreement with MIPAS observations. For day-time, continuous formation of 0.15-0.2 ppb after the event was seen at 20-25 km. MIPAS observations showed 0.15 ppb for daytime at 40 km on the 3rd of November. N_2O_5 is expected to increase after the NO_x enhancement, but the subsequent partial conversion of NO_x to N_2O_5 through,

$$NO_2 + NO_3 + M \longrightarrow N_2O_5 + M \tag{4.2}$$

can take days and might happen after the event. An increase in OH gives rise to an HNO_3 enhancement and an NO_2 depletion. The larger amount of HNO_3 in the presence of OH under dark conditions would lead to an increase in NO_3 and hence in N_2O_5.

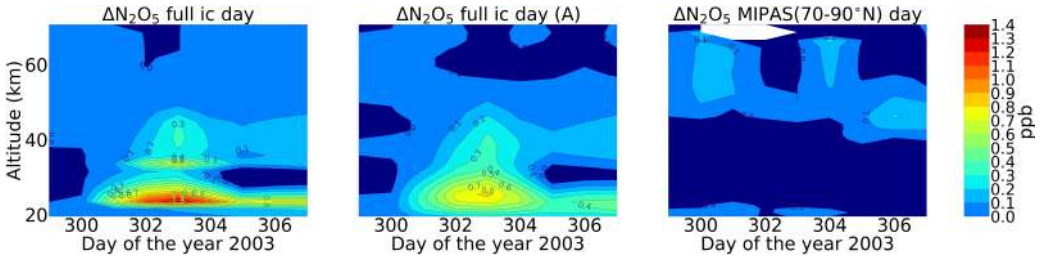

Figure 4.27: Same as figure 4.8 but for N_2O_5.

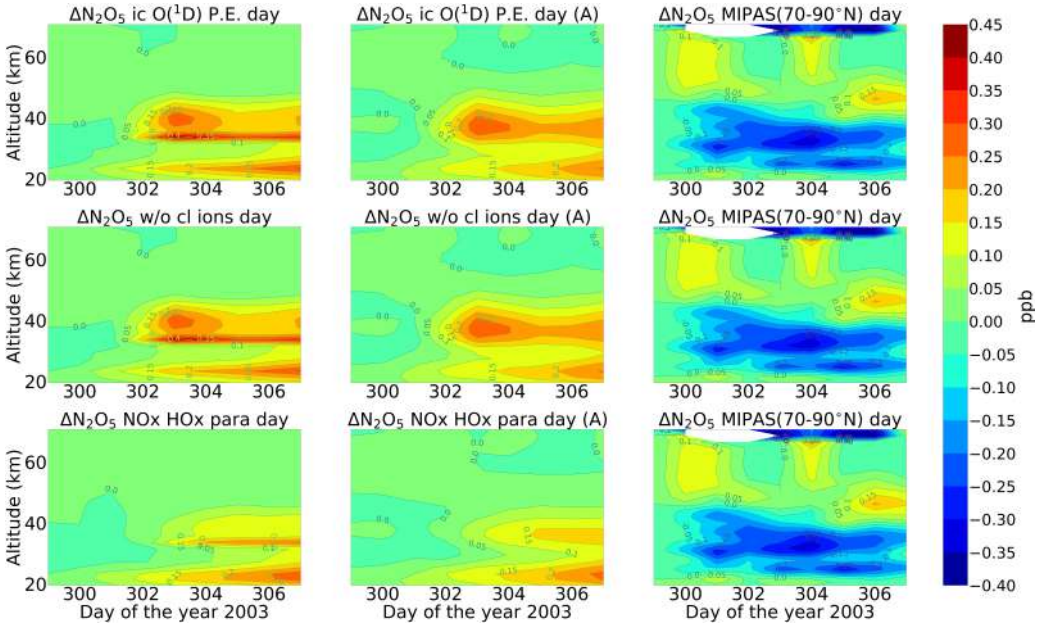

Figure 4.28: Same as figure 4.9 but for N_2O_5.

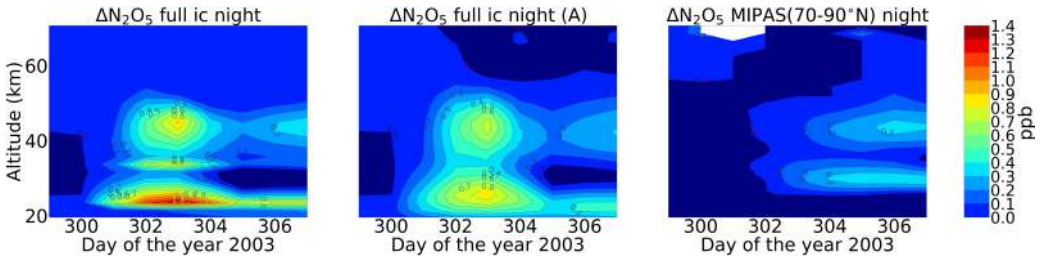

Figure 4.29: Same as figure 4.10 but for N_2O_5.

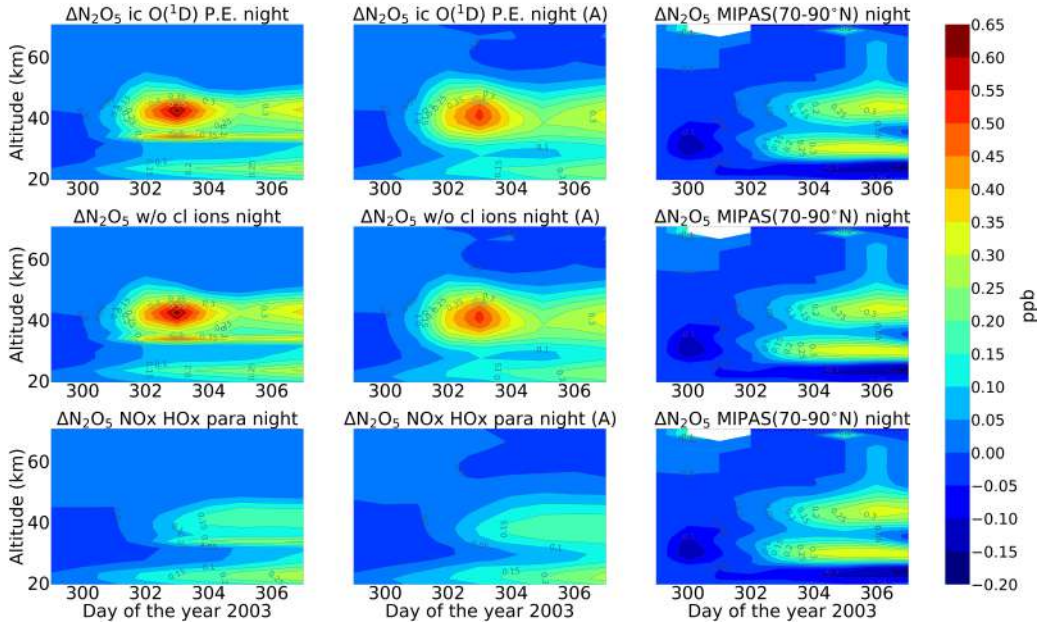

Figure 4.30: Same as figure 4.11 but for N_2O_5.

4.3.8 Total NO_y

An important impact of proton precipitation in the middle atmosphere is the formation of NO_x which happens by the dissociation of molecular nitrogen by ionisation and subsequent recombination with oxygen. In order to assess the agreement of the ENVISAT MIPAS V5 (Funke et al., 2005) and modelled SPE related odd nitrogen enhancements, total NO_y (=NO + NO_2 + HNO_3 + 2*N_2O_5 + $ClONO_2$) is compared. The observed and modelled NO_y enhancements w.r.t. 26th October is shown in figures 4.32 and 4.34 for daytime and night-time conditions respectively. Averaging kernels are also applied to the model profiles for the different NO_y species for the different model settings and then added, except for NO. In case of MIPAS NO and NO_2 data, there is a complication which is, that instead of mixing ratios the logarithms of the mixing ratios are retrieved; also the averaging kernels refer to the logarithms of the mixing ratios. The application of MIPAS averaging kernels to a better resolved profile on the basis of the coarse-grid averaging kernel **A** of the logarithm of the mixing ratio then is (Stiller et al., 2012):

$$x_{\text{new}} = \exp(\mathbf{A}\log(x_{\text{orig}}) + (\mathbf{I} - \mathbf{A})\log(x_{\text{a}})) \tag{4.3}$$

There is a general issue with logarithmic retrievals, because regularization is self-adaptive and depends on the actual state of the atmosphere. For an SPE response, if the NO peaks around 50-60 km and if there is a better sensitivity at this altitude the Jacobian and the averaging kernels scale with the volume mixing ratio. For NO_2 however, the logarithmic averaging kernels behave well and are not dependent on the actual conditions (a deeper discussion of the problem of time and state dependent averaging kernels is given in von Clarmann et al. (2020)). Due to this complication, for the total NO_y in the second column of figures 4.32 and 4.34 for both daytime and nighttime, NO is added without the application of the

averaging kernels as compared to the rest of the species. The magnitude of NO_y enhancements is found to be larger for the ExoTIC model with ion-chemistry settings compared to the MIPAS observations for both daytime and night-time. However the SPE induced NO_y layer is reproduced well in terms of vertical distribution. The MIPAS observations showed a production of 30-40 ppbv in the upper stratosphere during nighttime and 20-30 ppbv during day-time. The MIPAS observations show much higher dynamics than ExoTIC for both day-time and night-time. The nighttime values show stronger dynamics with decreased ionisation rates on day 305-306 and connected to this less ΔNO_y reaches a constant state after the maximum of the first SPE on day 303. This could be an indication that some of the NO_y recombination speeds are faster than expected. The results are shown upto 50 km since above 50 km, NO is the largest contributor (Funke et al., 2011) and averaging kernels are not applied to NO. Another reason is that large uncertainties of small vmr values of $ClONO_2$ (Höpfner et al., 2007b) will spoil the NO_y sum and it's uncertainty. The nighttime results compare better with the observations, specially for the parameterised NO_x and HO_x model. For day-time, the model with and without averaging kernel (**A**) didn't make too much of a difference because NO was added without averaging kernel (**A**) and was abundant during daytime.

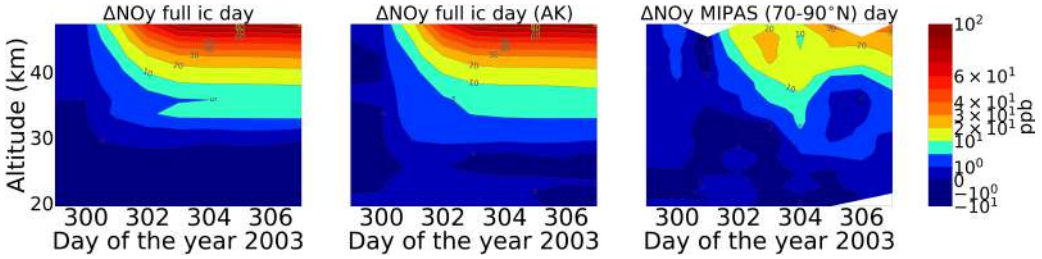

Figure 4.31: Same as figure 4.8 but for NO_y.

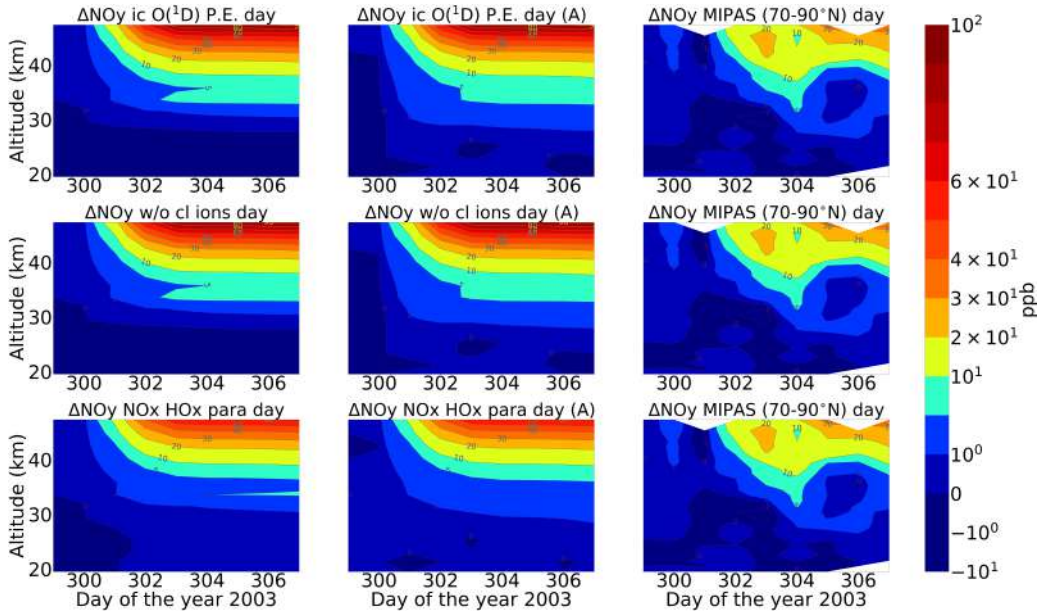

Figure 4.32: Same as figure 4.9 but for NO_y species. Colorbar interval: (-10^{-1}, -10^0, 0, 10^0, 10^1, 2*10^1, 3*10^1, 4*10^1, 6*10^1, 10^2)

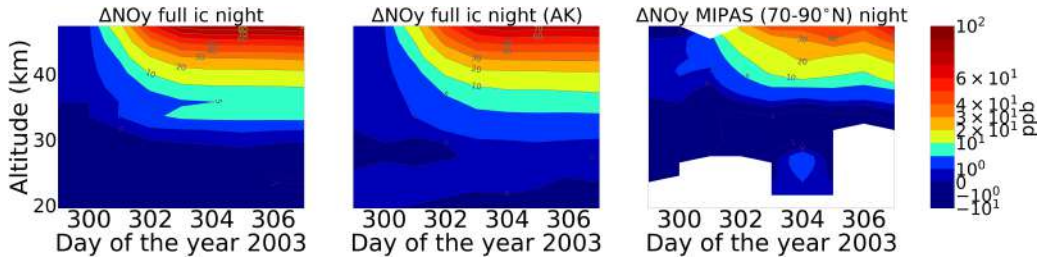

Figure 4.33: Same as figure 4.10 but for NO_y.

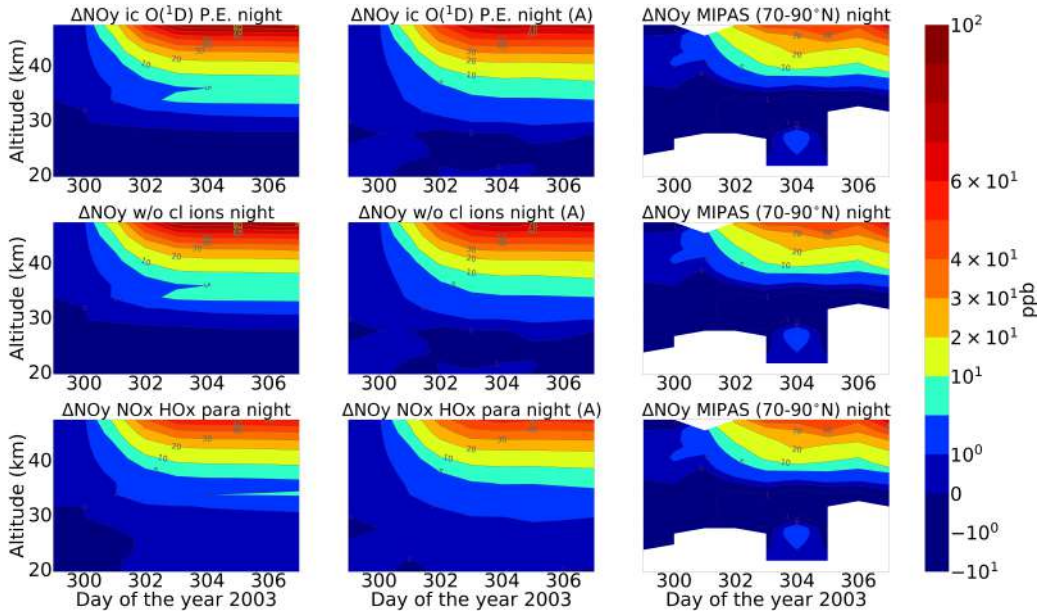

Figure 4.34: Same as figure 4.11 but for NO_y species. Colorbar interval: (-10^{-1}, -10^0, 0, 10^0, 10^1, $2*10^1$, $3*10^1$, $4*10^1$, $6*10^1$, 10^2)

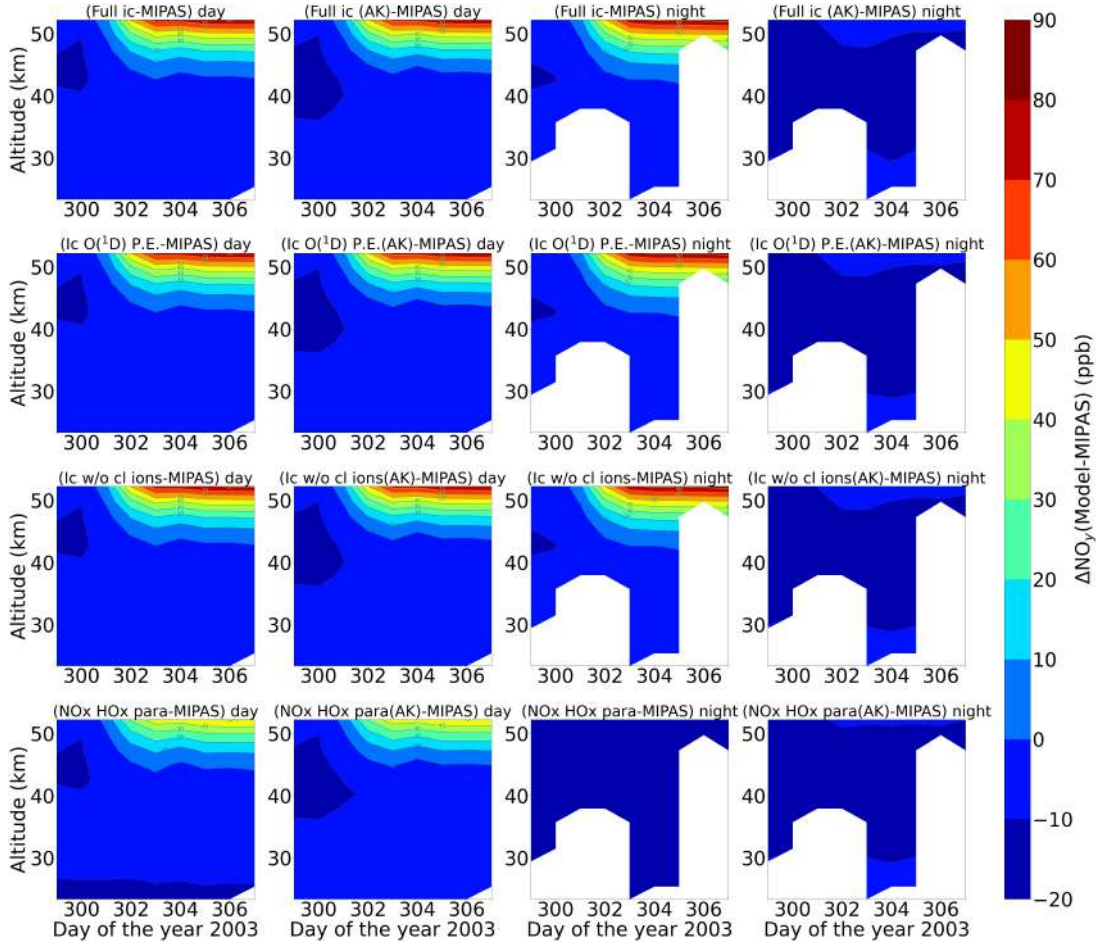

Figure 4.35: Same as figure 4.12 but for NOy.

5 ExoTIC model studies of chlorine activation and ozone loss during extremely large atmospheric ionisation events

5.1 Introduction

Solar energetic particle events affect the Earth's atmosphere and environment, in particular leading to depletion of the protective ozone layer in the Earth's atmosphere, and pose potential technological and life hazards. In this chapter, model studies have been carried out to observe the NO_y and HO_x formation, chlorine activation and ozone loss in the polar cap region and the auroral oval. Two solar proton events, the Halloween SPE of 2003 and an extreme solar event of 775 A.D. was considered for the model studies. Another energetic electron precipitation event was considered whose ionisation rates (IRs) were locally comparable to a solar proton event.

5.2 A worst-case scenario for a solar proton event: Extreme solar event of 774/775 A.D. and comparison with the Halloween SPE 2003

In this section, a comparison study between the Halloween storm of 2003 and the extreme event of A.D. 775 is presented. The greatest solar energetic storm known for the last 11 millennia (the Holocene) occurred in 774-775 A.D., serving as a likely worst case scenario being 40-50 times stronger than any directly observed one. A systematic analysis of the impact that such an event can have on the earth's atmosphere is presented. This exceptionally strong cosmic ray event of 774-775 A.D. was discovered recently in radiocarbon ^{14}C measured in annually dated tree rings and confirmed by ^{10}Be and ^{36}Cl cosmogenic isotope measurements. The event was short in duration, including several pulses, with a very hard energy spectrum, as estimated using the ratio of different cosmogenic isotopes. It was 40-50 times stronger than the largest directly observed event on 23rd February 1956, making the event the strongest known during the last 11 millennia.

5.2.1 Ionisation Rates

The ionisation rates used for the Halloween SPE were obtained from the AISstorm model, an enhanced version of the AIMOS model (Wissing and Kallenrode, 2009). The AIMOS model computes ionization rates by precipitating electrons, protons and alpha particles for the whole atmosphere based on particle flux measurements from Polar Operational Environmental Satellites (POES), Meteorological Operational Satellites (MetOp), and Geostationary Operational Environmental Satellites (GOES). For the extreme

event, integrated ionisation rates were taken from an extreme SPE of 23 February 1956 (SPE 56) (Meyer et al., 1956), which was the strongest observed event with ground-level enhancement (GLE), > 4000%. Cliver et al. (2022) estimated this factor to be 70 times the particle influence compared to the 1956 event and the ionisation rates were scaled accordingly. This factor was a rough estimate to scale the fluxes of particles and excess radiation such that the energy spectrum of SPE 56 was comparable to the isotope signals of the extreme event. The profiles for the Halloween SPE show the average ionisation rates (IRs) for 27 October (day 301) and 28 October (day 302) before the SPE (in blue) and the average IRs for 28 and 29 October during the main SPE phase (in green). It can be observed that the ionisation rates for the stratosphere and lower mesosphere in the case of extreme event are about 1-2 orders of magnitude higher compared to the Halloween SPE main phase. This is because the extreme event contained protons of energies up to a few giga-electron-volt protons compared to about only a few mega-electron-volt protons for the Halloween SPE, and the ionisation rates for the same can be seen to reach much further down to the surface.

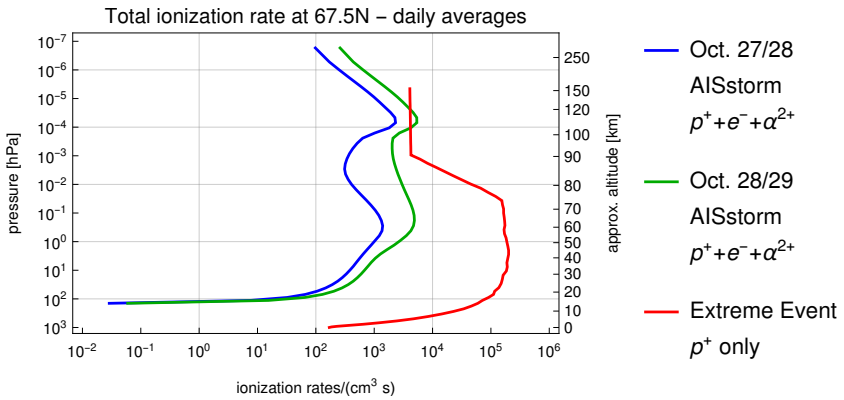

Figure 5.1: Mean ionisation rates (IRs) before the SPE (27-28 October) and in the SPE main phase (28-29 October) obtained from AISstorm and mean IRs of the extreme event for the same latitude of 67.5°N

5.2.2 $N\tilde{O}_y$ and HO_x species

Figure 5.2 shows the formation of $N\tilde{O}_y$ during the Halloween SPE and the extreme scenario with different settings of the ion-chemistry. $N\tilde{O}_y$ consists species of odd nitrogen as shown in equation 5.1:

$$NO_y = NO + NO_2 + N + HNO_3 + 2N_2O_5 + NO_3 + ClONO_2 \tag{5.1}$$

After the onset of the event, $N\tilde{O}_y$ starts accumulating over time in the stratosphere and lower mesosphere. For the extreme scenario, the volume mixing ratio (VMR) of $N\tilde{O}_y$ is about one order of magnitude larger compared to the Halloween SPE in the upper stratosphere and lower mesosphere. For example, the amount of $N\tilde{O}_y$ at 60 km is found to be 50 ppb for the Halloween event compared to 500 ppb for the extreme event. Additionally for the extreme event, $N\tilde{O}_y$ is seen to be formed even in the lower stratosphere (below 30 km). This is because of the high values of ionisation rates that reached further down

in altitude in this case. A small difference was observed between the sensitivity study without the chlorine ion-chemistry and the model setting of ion-chemistry with O(^{1}D) in photo-chemical equilibrium around 75 km. The full ion-chemistry and the ion-chemistry setting O(^{1}D) to photo-chemical equilibrium didn't show much of a difference. For the parameterised model, N$\tilde{O}_y$ enhancements are observed in the mesosphere and lower thermosphere with higher values seen for the extreme scenario compared to the Halloween event. NO_y enhancements of 1100 ppm is produced in the parameterised model for the extreme scenario. For the Halloween event, enhancements of $\sim$ 500 ppm and above was observed in the MLT region. Since only N, NO and NO_2 are present for the parameterised NO_x, the impact of the scavenging reaction, R12 is stronger and the partitioning between N and NO is different compared to the ion-chemistry which also contains other N$\tilde{O}_y$ species like HNO_3 etc. R12 drives the NO_x parameterisation and makes the main difference w.r.t. the ion-chemistry. In contrast to our results, which show the total NO_y that includes NO_x=N+NO, Andersson et al. (2016) showed that WACCM-D with the D-region ion-chemistry predicts more NO_x in the mesosphere compared to WACCM with the standard parameterisation of NO_x and HO_x production for the northern polar cap region, latitude > 60°N during the SPE of January 2005. Kalakoski et al. (2020) also reported the same when considering SPEs using proton flux data from satellite-based GOES observations. They considered an event in which the peak proton flux exceeded 100 particle flux units (pfu), with pfu defined as the 5 min average flux in units of particles $cm^{-2}s^{-1}sr^{-1}$ for protons with energy larger than 10 MeV. The rate of formation of NO_x=N+NO is indeed higher in the mesosphere when full ion-chemistry is considered, but the partitioning between the formation of N and N(^{2}D) forming NO is also increasingly in favour of N, meaning that the rate of loss of NO is also faster in this altitude range when full ion-chemistry is considered. This can lead to less NO depending on the absolute rate of NO_x formation, and the partitioning between N and NO in this formation. The HO_x parameterisation doesn't make much of a difference for N$\tilde{O}_y$.

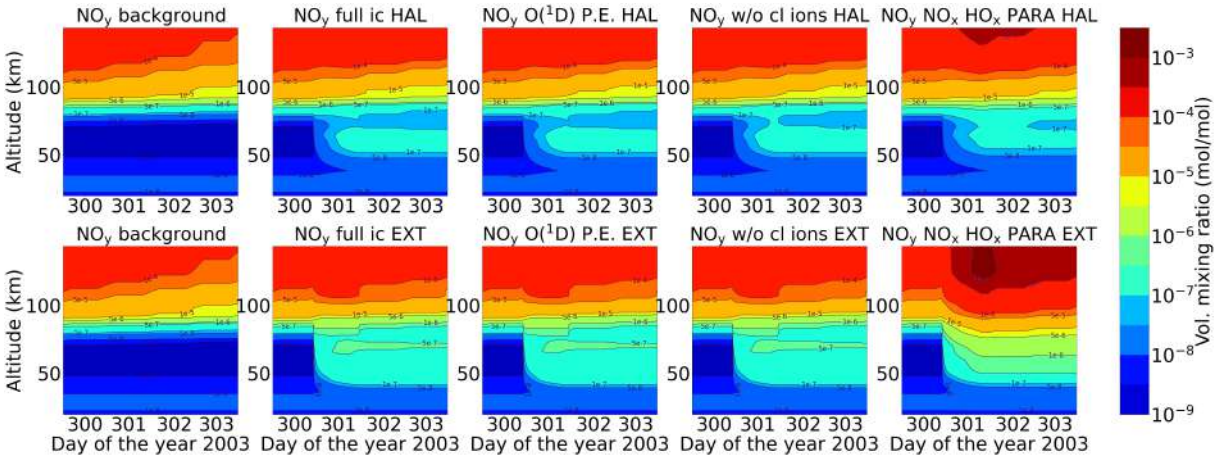

Figure 5.2: Comparison of the Halloween SPE and the extreme scenario (row-wise) for N$\tilde{O}_y$: Reference run (background atmosphere) and full ion chemistry with O(^{1}D) set to photo-chemical equilibrium, without chlorine ions and the parameterized NO_x and HO_x model (column-wise) for a high latitude of 67.5°N.

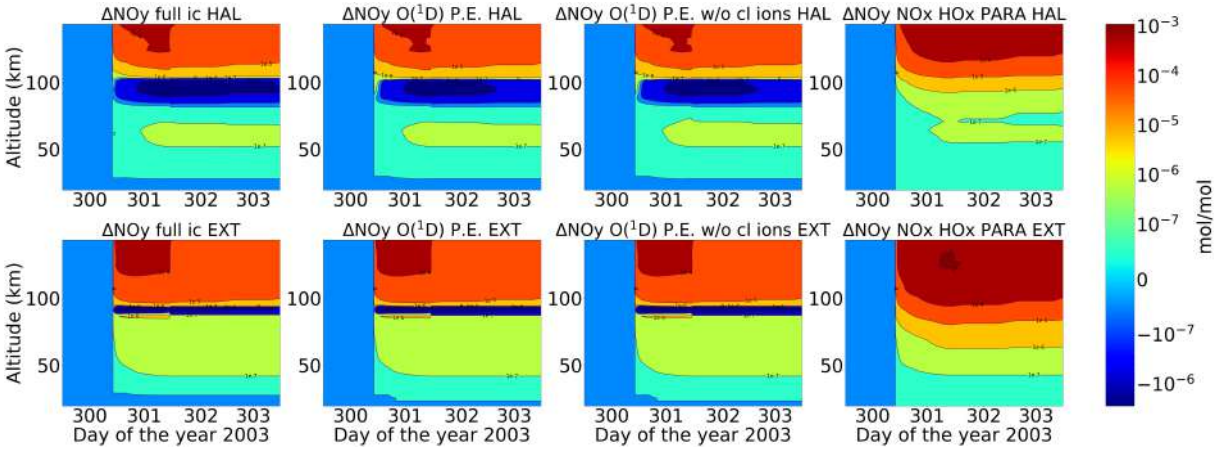

Figure 5.3: Absolute differences of NO_y sensitivity runs w.r.t reference run.

Figure 5.4 shows the temporal evolution of HO_x for the Halloween SPE and extreme scenario that consists of odd hydrogen species (equation 5.2);

$$HO_x = H + OH + HO_2 + 2H_2O_2 \tag{5.2}$$

HO_x was not shown for the MIPAS comparison due to the fact that H and OH are not provided by MIPAS. HO_x enhancements are seen during the event. For the Halloween SPE, HO_x enhancements of 0.1 ppm were observed in the mesosphere during the event whereas for the extreme scenario these enhancements were seen to penetrate deep down. However after the event stops, the HO_x disappears at higher altitudes, since it is short-lived up there. But at lower altitudes, around 25-40 km, HO_x enhancements of around 1 ppb was found to be continuous and more persistent, specially for the extreme scenario. The full ion-chemistry shows HO_x enhancements below 30 km which is due to the presence of $O(^1D)$, that can react with water vapour, hydrogen and methane via Reactions R68, R69 and R70. However with $O(^1D)$ set to photo-chemical equilibrium, the HO_x enhancements below 30 km disappeared for both the events. The impact of chlorine ion-chemistry is seen to be rather small. For the parameterised model, the recovery of HO_x after the event was found to be slower compared to the ion-chemistry model. The high values of HO_x are balanced by the continuous destruction of water vapour and when it is completely destroyed, the HO_x formation breaks down. So the full parameterisation with both NO_x and HO_x is different but the water vapour is a limiting factor for both. The ion-chemistry with more HO_x can also lead to a faster reaction between OH and NO_2 (R81), which can produce HNO_3 contributing a difference to the recovery of HO_x.

$$OH + NO_2 \longrightarrow HNO_3 \tag{R81}$$

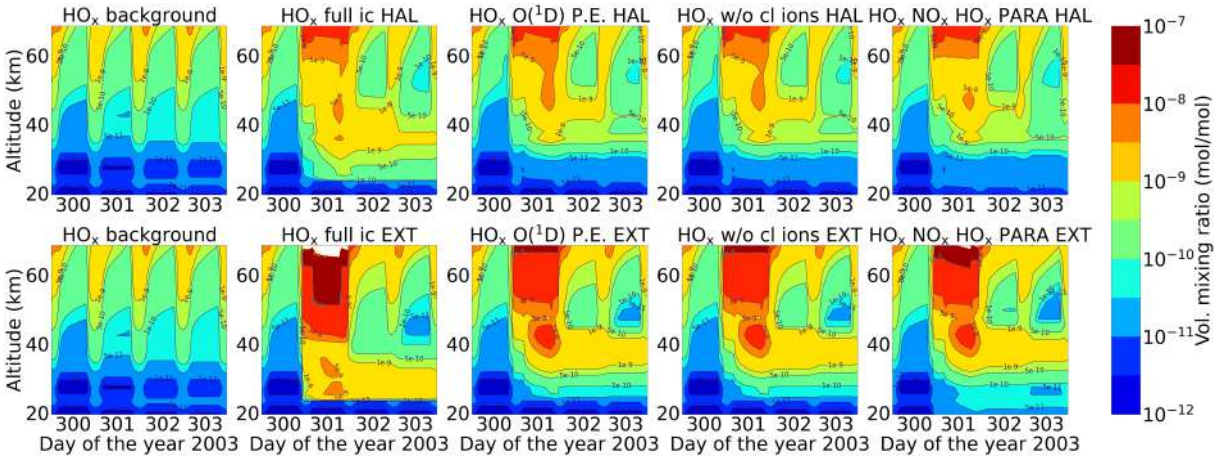

Figure 5.4: Same as figure 5.2 but for odd hydrogen species (HO_x)

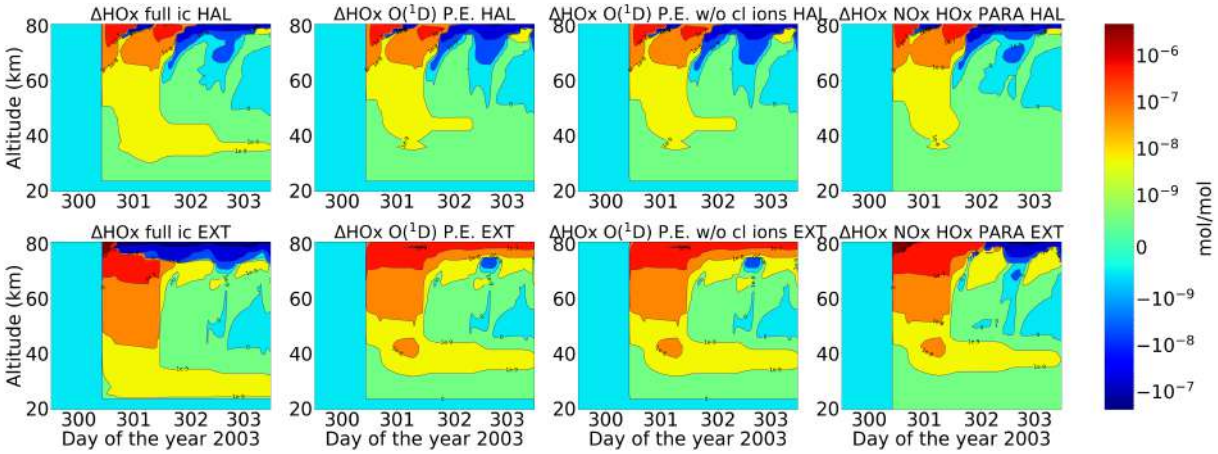

Figure 5.5: Absolute differences of HO_x sensitivity runs w.r.t reference run.

5.2.3 Chlorine species

Figure 5.6 shows the volume mixing ratios of HCl for the two events. Loss of HCl, which can occur via transformation into reactive chlorine as it is taken up from the gas phase into negative ions, is seen during the event in both cases, pronounced more for the extreme scenario. This occurred both in the stratosphere and the mesosphere for full ion-chemistry. Negative ions upon reaction with HCl can form Cl^- ions, which forms large cluster ions thereby releasing Cl upon recombination (Sinnhuber et al., 2012),

$$HCl + X^- \longrightarrow Cl^- + HX \quad \text{(R82)}$$

$$Cl^- + Y \longrightarrow Cl^-Y \quad \text{(R83)}$$

$$Cl^-(Y) + Z^+ \longrightarrow Cl + Z + Y \quad \text{(R84)}$$

where X = O, O_2, CO_3, OH, NO_2, NO_3; Y = HCl, H_2O, CO_2 and Z = positive ions (Kopp and Fritzenwallner, 1997). Cl^- and Cl^- cluster ions like $Cl^-(H_2O)$ can also release HCl via reaction with H (Kopp and Fritzenwallner, 1997). HCl can react with $O(^1D)$ via Reaction R71 resulting in an enhanced loss of HCl below 40 km but that disappears when $O(^1D)$ is set to photo-chemical equilibrium. Around 60 km and above, ExoTIC with full ion-chemistry observed a loss of 55% during the event for the Halloween SPE and a continuous loss of around 15% below 40 km. A loss of 75-80% during the event at 50 km and above and a continuous loss of around 75% below 40 km is observed for the extreme event. With the $O(^1D)$ correction, 5-15% HCl loss for the Halloween SPE and 20-45% HCl loss for the extreme event was observed. From the sensitivity study without the chlorine ions, it is evident that the huge loss of HCl, around 75% observed in the mesosphere is due to the chlorine ion-chemistry. The parameterised model underestimates the loss of HCl which was also found in studies by Winkler et al. (2009). The primary neutral reaction that leads to the decrease in HCl below 50 km is a series of reactions involving HO_x species that are part of the catalytic ozone destruction cycle (Reactions R28 and R29, with x = OH). The decrease in ozone concentration has a secondary effect on the concentration of HCl. In the absence of an SPE, ozone plays a role in the conversion of ClO back to HCl. However, during an SPE, the enhanced ionisation and subsequent formation of ions disrupt this ozone destruction and formation cycle. This leads to an increase in the concentration of ClO and a subsequent reduction in the concentration of HCl. The excess ClO can further participate in additional ozone depletion cycles, leading to a decline in ozone levels during the event. Andersson et al. (2016) reported daily averaged anomalies of HCl in both hemispheres for the latitudinal band 60–82.5°N at altitudes between 40 and 52 km. They compared WACCM-D consisting of the D-region ion-chemistry and WACCM consisting of the standard NO_x and HO_x parameterisation with MLS observations. They found a rapid HCl decrease of about 2-6% during the January 2005 SPE in both hemispheres. With WACCM-D, a loss of around 4% was found compared to a loss of 3% in standard WACCM in the Northern Hemisphere. They also showed that WACCM-D showed better agreement with MLS observations.

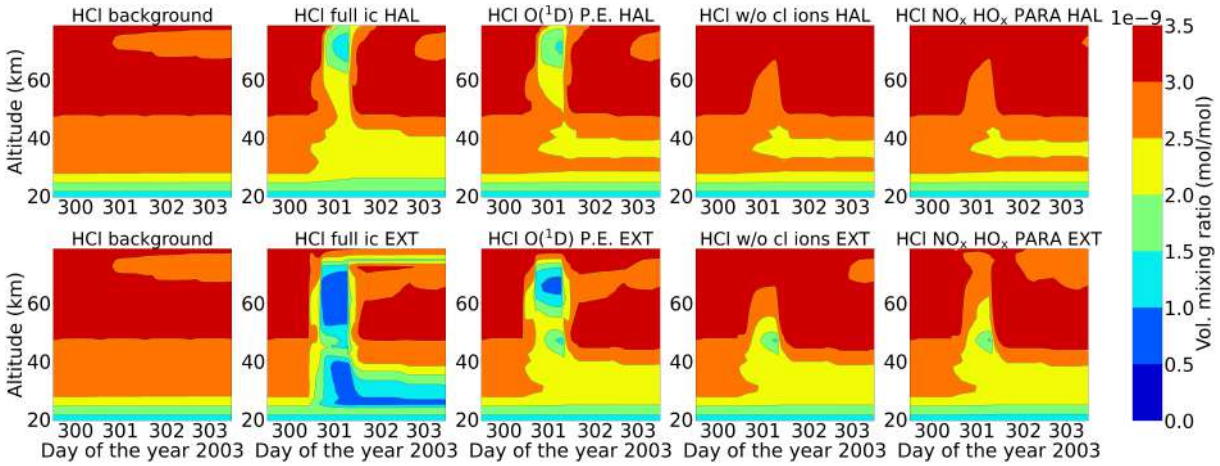

Figure 5.6: Same as figure 5.2 but for HCl

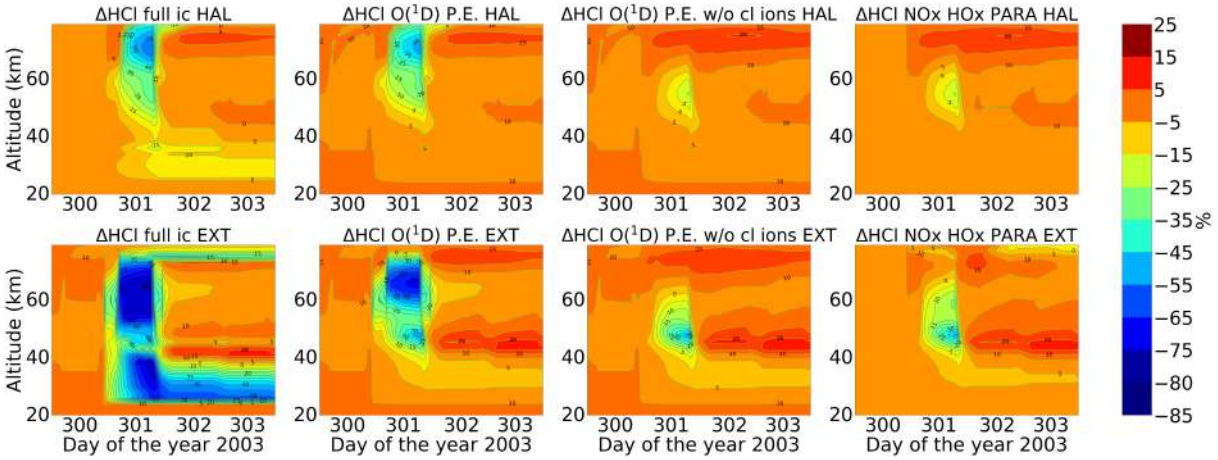

Figure 5.7: Percentage decrease ($100 * \frac{\text{Sensitivity run} - \text{reference run}}{\text{reference run}}$) of HCl calculated w.r.t the reference run.

Since $N\tilde{O}_y$ and HO_x production is enhanced during SPEs, which is evident from figures 5.2 and 5.4, they can react with reactive chlorine species like ClO. ClO can either react with HO_x producing short term enhancement in HOCl (R37), or with NO_x slowly producing $ClONO_2$ (R50). ClO is formed from the reactive Cl via Reaction R39 by neutral gas phase reactions of Cl with ozone in the altitude range of 35-40 km.

From figure 5.8, it can be seen that ClO decreases during the event for the same altitude range but recovers straight after the event stops. ClO can react with HO_x species during SPEs, particularly HO_2 to produce HOCl (R37), which is also a short-lived species. Therefore, a short term enhancement of HOCl is seen during both the events (figure 5.10) which was also observed by von Clarmann et al. (2005) for the Halloween SPE. However, for the extreme scenario, loss of ClO continues specially around 30-40 km even after the event stops. This is because of the excess NO_x available for the extreme event due to which R50 can happen continuously which is supplemented by an increase in $ClONO_2$ after the extreme event as seen from figure 5.12. Loss of HOCl seen after the extreme event is due to excess HO_x as well. HOCl can react with OH to form ClO (R42) and then ClO can react back with HO_2 and this catalytic cycle thereby results in the loss of both species due to excess HO_x.

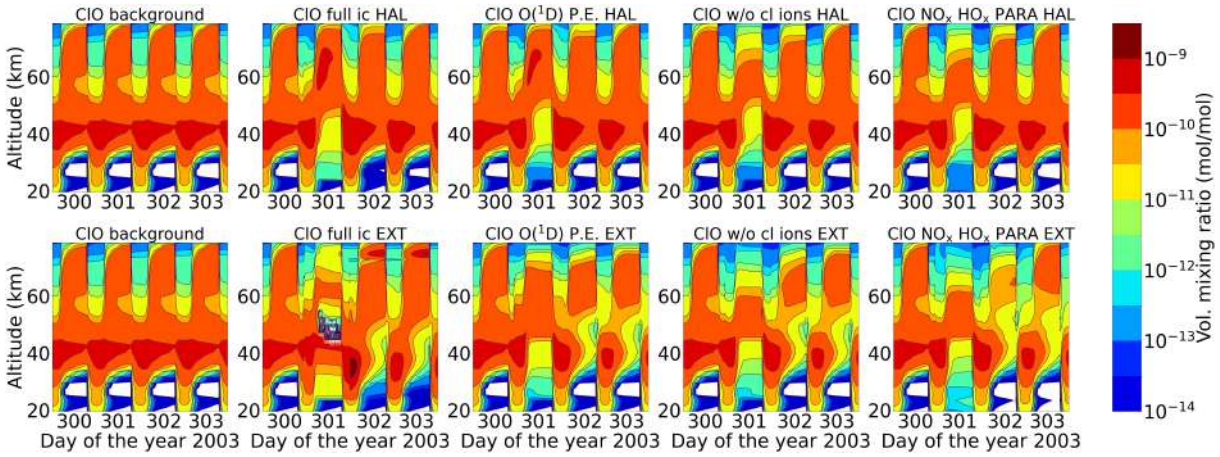

Figure 5.8: Same as figure 5.2 but for ClO

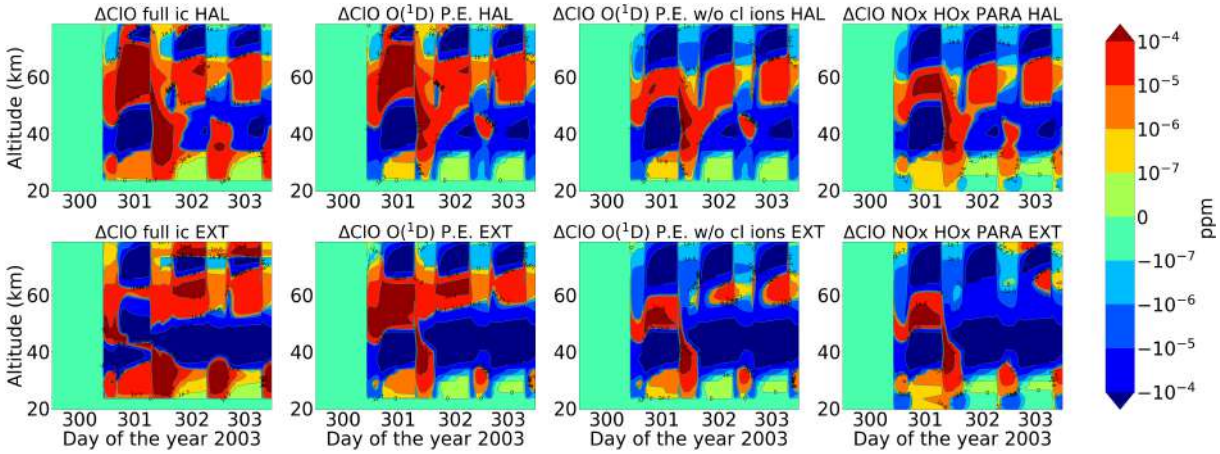

Figure 5.9: Absolute differences of ClO sensitivity runs w.r.t reference run.

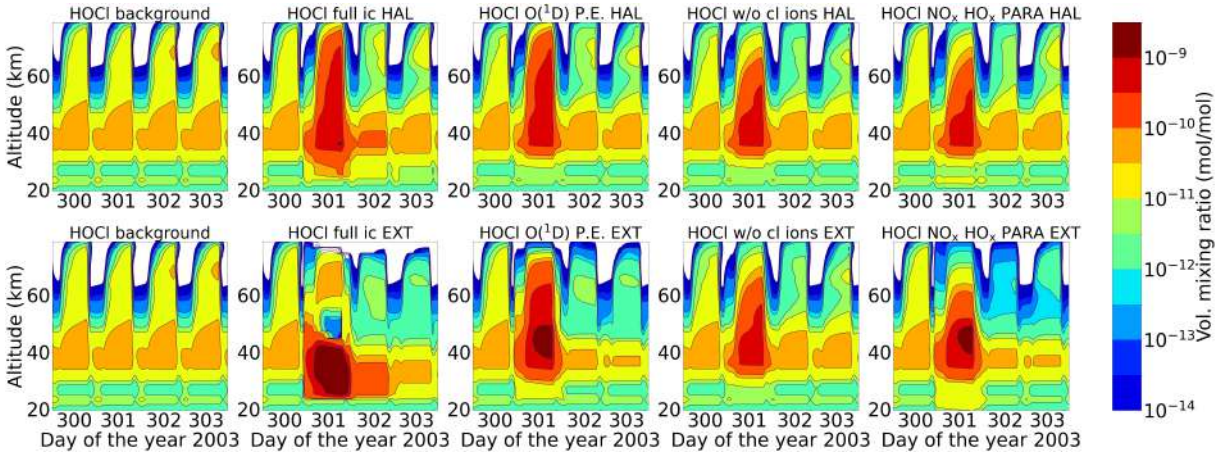

Figure 5.10: Same as figure 5.2 but for HOCl

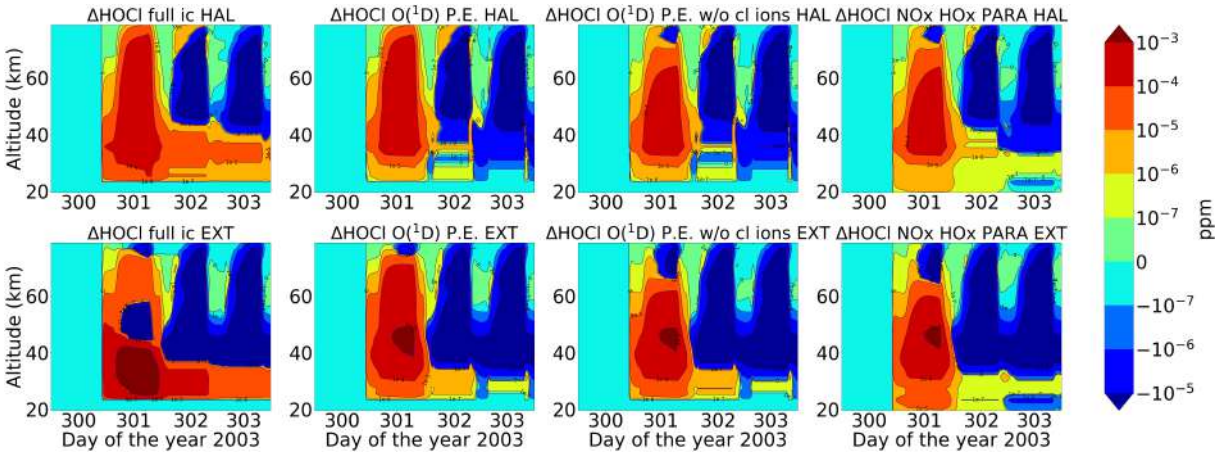

Figure 5.11: Absolute differences of HOCl sensitivity runs w.r.t reference run.

An increase in $ClONO_2$ is also observed during both the events at an altitude of 60 km (figure 5.12). Solomon et al. (1981) pointed out that the increasing NO_x concentrations after a SPE interact with chlorine species, forming chlorine nitrate at the expense of reactive radicals. This reaction is of importance in the lower and middle stratosphere around 40 km, (Jackman et al., 2000) but not so important at higher altitudes. It can be seen from figure 5.12 that at an altitude of 40 km, $ClONO_2$ increases after the event has stopped. This is because after the event ClO is lost via Reaction R50 since NO_x is formed slowly accumulating over time. So the formation of $ClONO_2$ via R50 is slow, hence leading to high production after the event in the lower and middle stratosphere. The chlorine ion-chemistry plays a small role for $ClONO_2$ around 45-50 km specially during night-time on day 301. The production of $ClONO_2$ when the chlorine ion-chemistry is switched off is comparatively higher at that altitude.

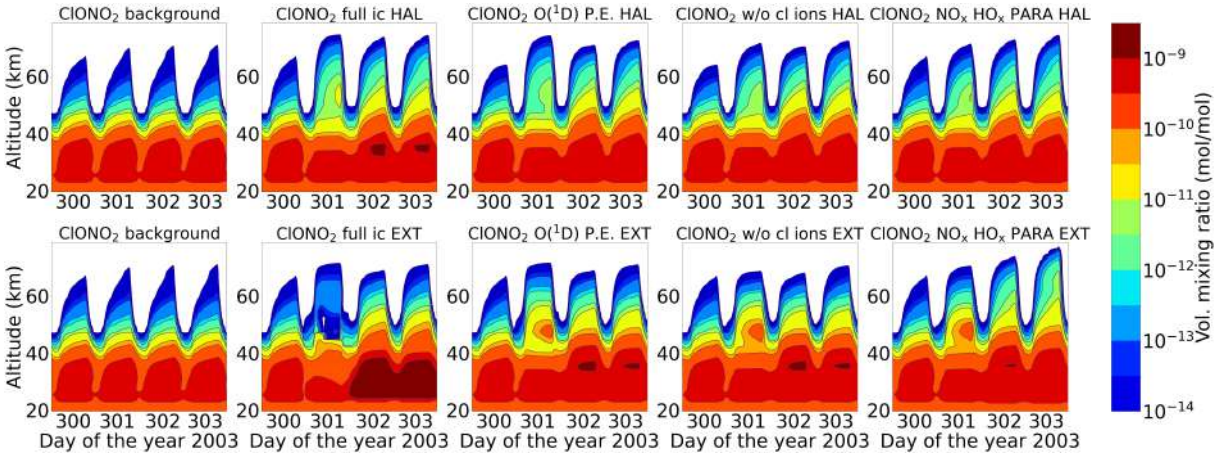

Figure 5.12: Same as figure 5.2 but for $ClONO_2$

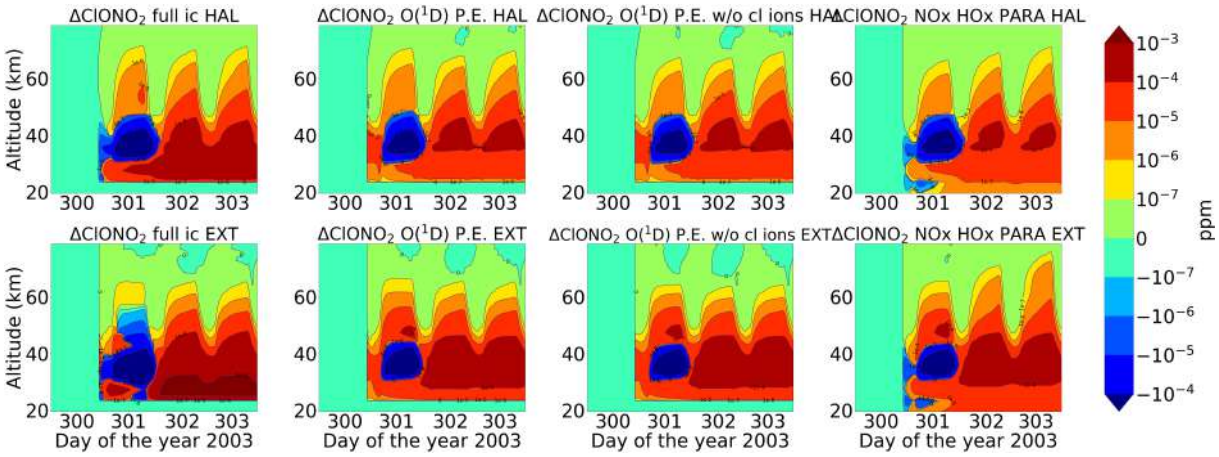

Figure 5.13: Absolute differences of $ClONO_2$ sensitivity runs w.r.t reference run.

Figure 5.14 shows the chlorine species at an altitude of 40 km for the various model set-ups. There is a small impact of chlorine ion-chemistry on the loss of HCl, whereas the parameterised NO_x and HO_x underestimates it. ClO decreases during the event and transfers to HOCl via Reaction R37. After the event, it recovers and the HOCl enhancements also decrease. For the extreme event however, ongoing loss of ClO during nighttime is observed which is due to the excess HO_x produced during the extreme event. Reformation of HCl after the event is observed that happens via Reactions R44 and R45.

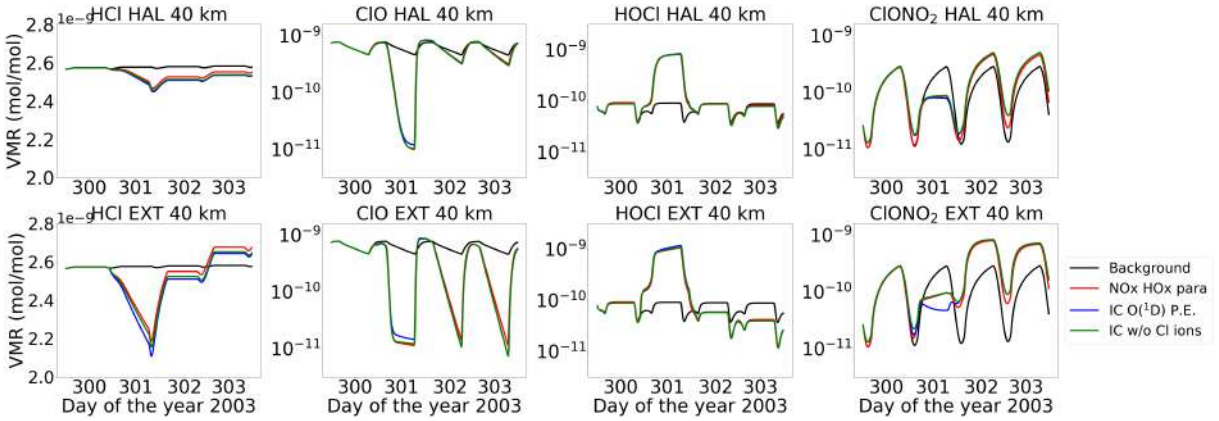

Figure 5.14: Comparison of the Halloween SPE and the extreme scenario for (column wise): HCl, ClO, HOCl and $ClONO_2$ at 40 km.

An interesting observation for HCl can be seen from the figure 19 for the extreme scenario, where the recovered HCl after the event shows a positive excursion. This depends on the diurnal cycle of ClO and happens mainly during night time. The reformation of HCl can happen via Reactions R44 and R45 during night time because during daytime HO_2 and H_2O_2 photolyses. This can be seen from the figure 5.15 where HO_2 and H_2O_2 production increases during the event mainly at night time. A steep increase in HCl is observed during the transition from day to night where Cl, HO_2 and H_2O_2 increases which is constant over the night and increases again afterwards at the beginning of the day. This is due to the

fact that during nighttime the concentration of free chlorine atoms is typically low since the primary source of these atoms is the dissociation of chlorine-containing reservoir species, such as chlorine nitrate ($ClONO_2$). $ClONO_2$ occurs predominantly during daytime due to the presence of sunlight, where it is photolysed to release chlorine atoms and hence at sunrise this renewed increase in chlorine atoms results in a subsequent increase in HCl levels.

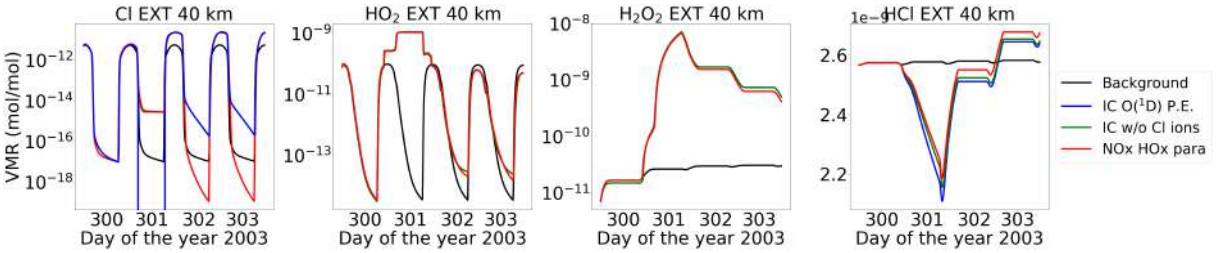

Figure 5.15: Volume mixing ratios of species (Cl, HO_2, H_2O_2 and HCl) at 40 km for the extreme event. The different lines are for the model settings: reference (black), ion-chemistry with O(^{1}D) in photo-chemical equilibrium (blue), without chlorine ions (green) and parameterised NO_x and HO_x (red)

5.2.4 Ozone

Figure 5.16 shows ozone loss during the two events and ozone recovery afterwards. The different sensitivity tests for the Halloween SPE didn't show too much of a difference in the ozone loss and recovery. But for the extreme scenario, the ozone production afterwards is seen to be quite high, $\sim$ 134 ppb above 75 km with full ion-chemistry. The sensitivity tests showed differences mainly in ozone recovery for the extreme scenario.

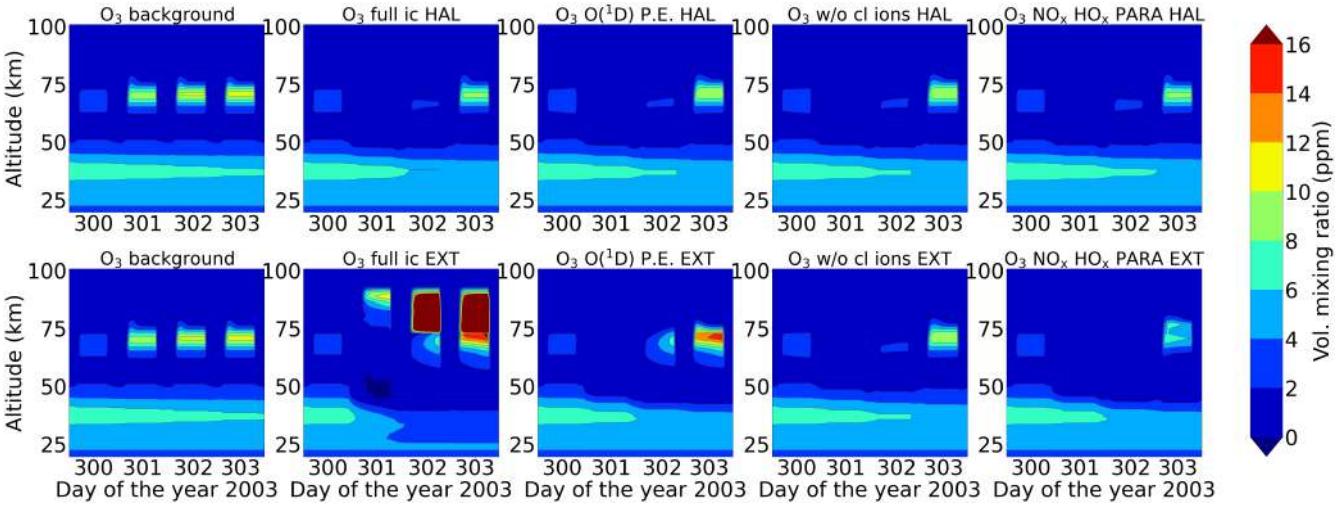

Figure 5.16: Same as figure 5.2 but for ozone

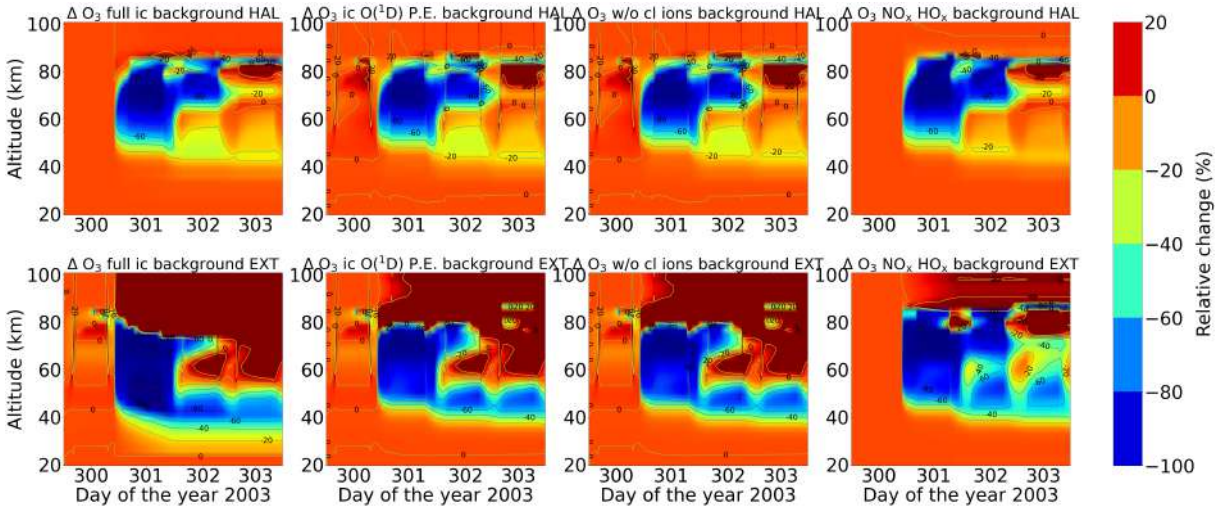

Figure 5.17: Percentage difference ($100 * \frac{\text{Sensitivity run} - \text{reference run}}{\text{reference run}}$) of ozone for the different model runs w.r.t. the reference run (row-wise): Halloween event and extreme scenario; (column-wise): full ion-chemistry, ion-chemistry with O(^{1}D) in photo-chemical equilibrium, without Cl ions and parameterised NO_x and HO_x.

Figure 5.17 shows the percentage difference of ozone for the two events for the different model runs calculated w.r.t. the reference run. It is seen that with the onset of the event, ozone is completely lost which is due to HO_x enhancements in the mesosphere above 55 km. This net ozone loss in the upper stratosphere and mesosphere is mainly due to odd hydrogen (HO_x) catalytic destruction cycles (Reactions R28 and R29, with x = OH) (Jackman et al., 2005) and is short-lived. Since HO_x species have a shorter lifetime, the recovery of ozone is faster. For the extreme event, after the event stops, ozone enhancements upto 25% is observed in the mesosphere and above 80 km.

NO is quite long lived down at 60 km altitude and below so the ozone loss due to the NO_x catalytic cycle seems to be persistent. The ozone loss occurs during day time when NO reacts with ozone to form NO_2, which is then photolysed back to NO and this catalytic cycle between NO and NO_2, related to daytime continues (Reactions R28 and R29, with x = NO). In the beginning, the amount of $N\tilde{O}_y$ was not enough for ozone loss but at the end of the event, the accumulation is large enough for significant ozone depletion which stays on and produces a diurnal cycle between 40 km and 80 km due to NO_x/HO_x cycles as seen from the figure 5.17. The magnitude of depletion with respect to the diurnal cycle and altitude has some considerable variation. Verronen et al. (2005) used a one dimensional chemical model, Sodankylä Ion and neutral Chemistry model (SIC) for ionospheric D-region studies. They studied the effects of ion-chemistry on the neutral atmosphere and also the diurnal variation of NO_x/HO_x increases, as well as ozone depletions. This diurnal variation during a solar proton event or an energetic particle precipitation (EPP) event has been previously reported by Aikin and Smith (1999). Verronen et al. (2005) observed the diurnal cycle of O_x=O+O_3 depletion between 40 and 85 km. They found substantial ozone loss at sunset of 28 October and even greater loss at sunrise of 29 October followed by a recovery at 55–75 km during the noon and afternoon hours. The maximum depletion is reached just after sunset, with a 95% reduction in the O_x values at 78 km. During daytime on 30 October, O_x partly recovers but is again depleted during

sunset. Rohen et al. (2005) also studied the Halloween SPE using SCHIAMACHY observations and considered 60°N magnetic latitude, which compares quite well to our 67.5°N geographic latitude. Since SCHIAMACHY measures only during daytime, they don't see a diurnal cycle in their results. With SCHIAMACHY, they reported a 20-30% ozone loss at 40-50 km in the Northern Hemisphere during the event and a 20-40% ozone loss, also during the event at 40-55 km observed by a photochemical model. This is related to the NO_x catalytic cycle that was long lived. Above 50 km and at higher altitudes, ozone recovery was faster after 50-60% loss during the event observed with SCHIAMACHY and the model which was due to the short lifetime of HO_x and photolytical reproduction of ozone. In our case, the continuing ozone loss at 40-55 km, related to the diurnal variation of NO_x is found to be 60-80% for the extreme scenario as compared to the Halloween event which is just around 20%. At 60-80 km, 80-100% ozone loss is observed during the event and also the continuing loss due to the HO_x related diurnal cycle afterwards. Other two examples that provide valuable insights into the significant ozone variations that can occur during extreme space weather events were studied by Calisto et al. (2013) and Rodger et al. (2008). Calisto et al. (2013) investigated the potential effects of a Carrington-like solar event on ozone using a global 3D chemistry-climate model SOCOL v2.0. They found that the enhanced ionisation during the event led to substantial ozone depletion in the polar regions, particularly in the middle atmosphere. Due to the NO_x and HO_x enhancements, ozone depletion was found to be 60% in the mesosphere and 20% in the stratosphere for several weeks after the event started. They also showed total ozone decreased more than 20 DU in the northern hemisphere. Rodger et al. (2008) examined the relationship between SPEs and ozone depletion using ground-based observations and modeling. They used the Sodankylä Ion and Neutral Chemistry (SIC) model and investigated the Carrington event of August/September 1859 and found that SPEs can cause localized ozone depletion in the polar regions, primarily through the production of NO_x. The most important SPE-driven atmospheric response is an unusually strong and long-lived O_x decrease in the upper stratosphere (O_x levels drop by 40%) primarily caused by the very large fluxes of $>$ 30 MeV protons. Considering these studies, it is crucial to recognize that the ion chemistry processes during SPEs can lead to ozone changes that go beyond what is typically captured in fixed parameterizations or standard models. The enhanced ionisation and subsequent chemical reactions can influence ozone concentrations, particularly in the polar regions. Therefore, when studying the impact of SPEs on ozone, it is important to consider the effects of ion chemistry processes and their potential role in generating substantial ozone variations. By incorporating these processes into models, we can better understand the complex interplay between extreme space weather events, ion chemistry, and ozone dynamics, ultimately improving our ability to assess the impacts of such events on Earth's atmosphere.

5.3 An exceptional middle latitude electron precipitation detected by balloon observations over Moscow

An exceptionally strong high-energy electron precipitation event detected by balloon measurements in geomagnetic mid-latitudes on 14 December 2009, with ionisation rates locally comparable to strong solar proton events. This electron precipitation was most probably caused by wave particle interactions in the slot region between inner and outer radiation belts, connected with poorly understood natural phenomena in the magnetosphere. The outer radiation belt of the Earth is located at a distance of 3-6 Re and contains mainly trapped electrons of energies from several keV to MeV, whose fluxes can vary significantly sometimes for as fast as several hours. One of the most important channels for the loss of electrons from the radiation belts is precipitation into the atmosphere, with electrons falling into the loss cone and the adiabatic motions disturbed under action of perturbations mainly wave particle interactions (Millan and Thorne, 2007). Another cause is the escape of electrons into the interplanetary medium. Energetic electron precipitation occurs at high latitudes, in the zone of the auroral oval corresponding to geomagnetic latitudes of $\sim$ 65-70°N. Comprehensive measurements of mid-latitude electron precipitation from a slot between the outer and inner radiation belts at L $\sim$ 2-4 have been made on the Van Allen Probes. Figure 5.18 shows the ionisation rate profile for balloon observations over Apatity. Very high ionisation rates are found for 60 km and above.

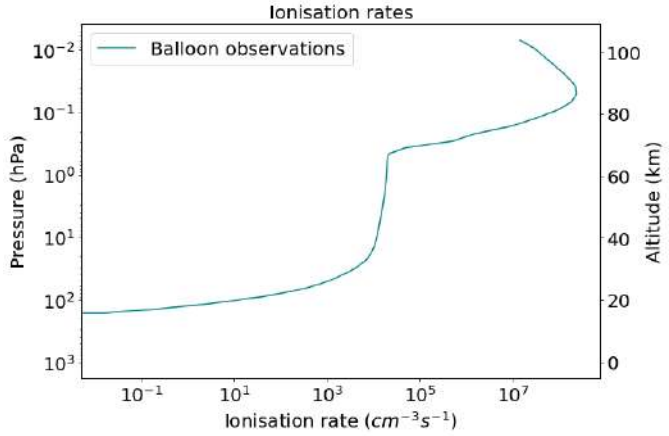

Figure 5.18: Ionisation rate profile as obtained from balloon observations over the latitude of Apatity (67.5°N)

5.3.1 NO_y, HO_x and ozone

The neutral chemistry in the 1D model for this experiment was initialised using temperature, pressure and tracer data from HAMMONIA chemistry climate model (Hamburg Model for the Neutral and Ionized Atmosphere), which is a revised version of the general atmospheric circulation model ECHAM5. It has 109 levels in the vertical direction and covers an altitude up to 112 km. These simulations performed were also for the region of Apatity (67.57°N). Figure 5.19 shows a strong formation of NO_y, around 100 ppb, throughout the middle atmosphere after the onset of the event. Since NO_y is long-lived, its accumulation

continues over the considered time period. The parameterised NO_x and HO_x model showed about 50 ppm around 100 km. The absolute differences show the continuous loss of NO_y observed between 80 and 100 km after the event for the sensitivity studies with full ion-chemistry and switching off the chlorine ion-chemistry. Figure 5.20 shows formation of HO_x during the event, which is around a few ppb in the mesosphere. Switching off the chlorine ion-chemistry didn't make too much of a difference to the full ion-chemistry except that HO_x recovered a little faster without the chlorine ions. The parameterised NO_x and HO_x model showed high HO_x formation about 1.6 ppm, around 80 km in the mesosphere. HO_x formation of about 10 ppb is observed during the event around 40-50 km. And continuous HO_x formation of 1 ppb is observed below 40 km after the event. The enhancements at these low altitudes is due to the presence of $O(^1D)$, which reacts with H_2O, H_2 and CH_4 via Reactions R68, R69 and R70. These seem similar to the results observed for the Halloween SPE 2003 as discussed in Section 4.2.2.

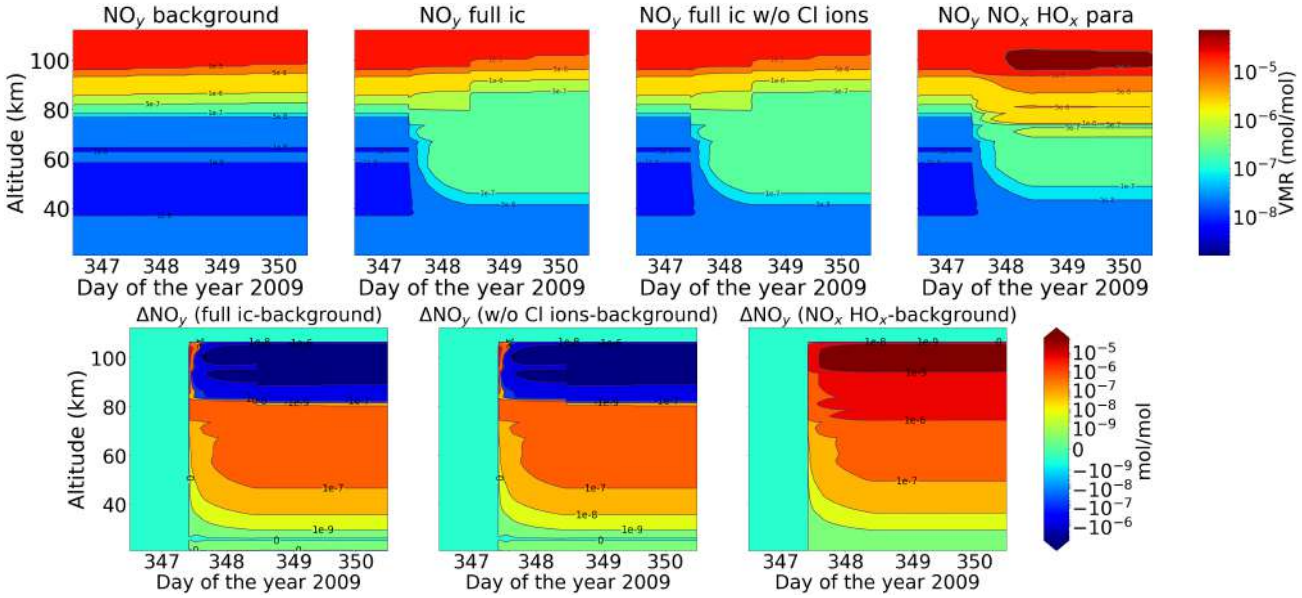

Figure 5.19: Volume mixing ratios of total NO_y (top-row) and the absolute differences of NO_y w.r.t. the reference run (bottom-row) for the different sensitivity tests: reference run, full ion-chemistry, switching off the chlorine ion-chemistry and parameterised NO_x and HO_x.

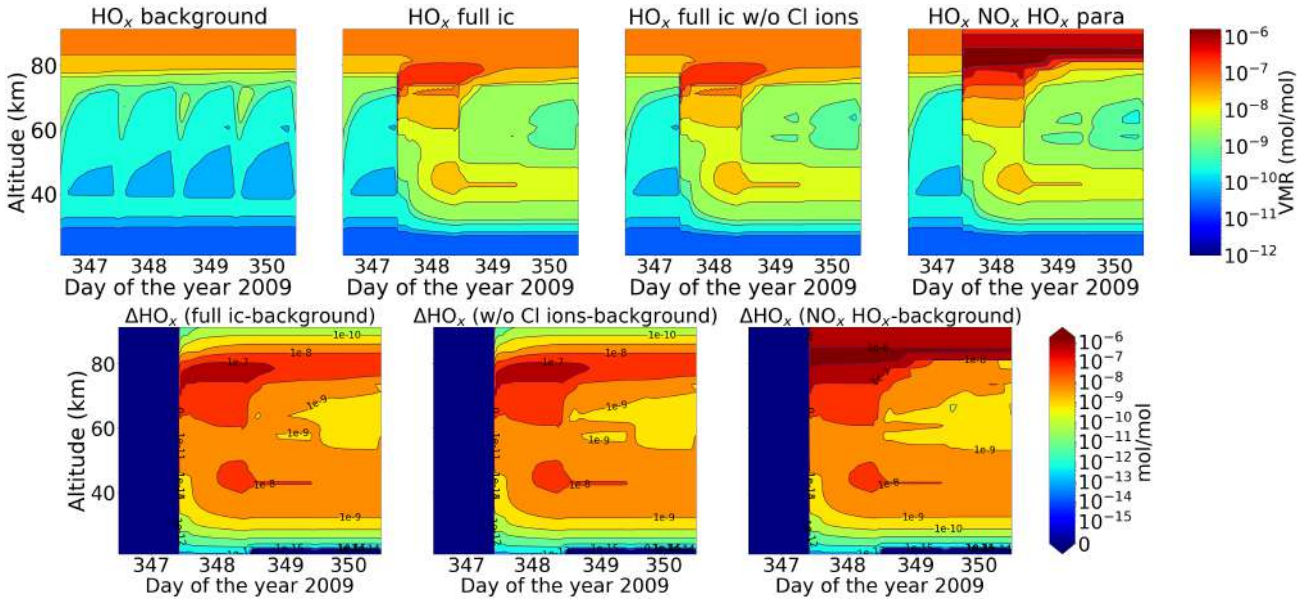

Figure 5.20: Volume mixing ratios of total HO_x (top-row) and the absolute differences of HO_x w.r.t. the reference run (bottom-row) for the different sensitivity tests: reference run, full ion-chemistry, switching off the chlorine ion-chemistry and parameterised NO_x and HO_x.

Figure 5.21 shows ozone and ozone loss observed for the different sensitivity runs. The ion-chemistry sensitivity studies showed 80-100% ozone destruction during the event in the mesosphere and a continuous destruction of 60-80% in the stratosphere and mesosphere. Around 40-50 km, there is a loss of 20% below which is due to photolysis due to the changing ionisation rates. Ozone loss observed during the event is short-lived and is mainly due to the HO_x catalytic cycle. Long lasting ozone loss in the stratosphere is observed, which is due to higher values of NO_x, since the ozone loss due to NO_x is dominant at that altitude. The parameterised NO_x and HO_x showed ozone loss also in the altitude range of 80-100 km which appeared in the form of a diurnal cycle.

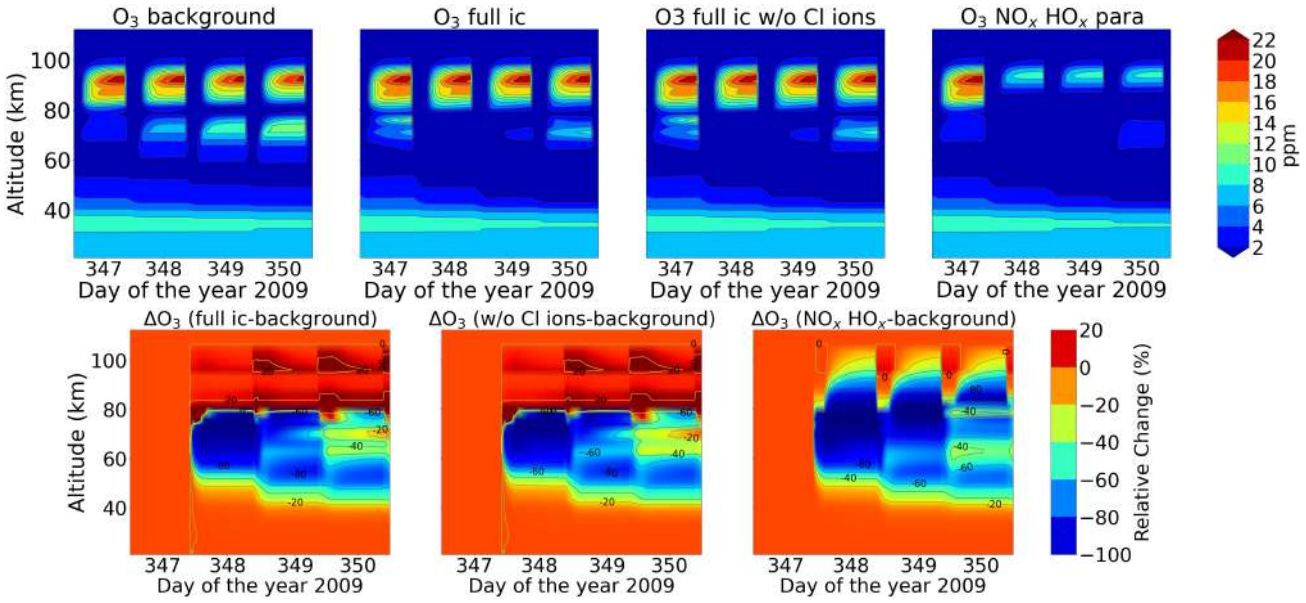

Figure 5.21: Volume mixing ratios of ozone (top-row) and the relative differences of HO_x w.r.t. the reference run (bottom-row) for the different sensitivity tests: reference run, full ion-chemistry, switching off the chlorine ion-chemistry and parameterised NO_x and HO_x.

5.3.2 Chlorine species

Figure 5.22 shows $\sim$ 80% loss of HCl observed during the event with full ion-chemistry above 60 km. In the stratosphere below, loss of 25-55% was found along with a continuous loss of 15% in the middle atmosphere. The loss above 60 km is due to chlorine ion-chemistry following the set of reactions R82, R83 and R84 as discussed in section 4.2.3. The parameterised NO_x and HO_x model underestimates HCl loss which was also found by Winkler et al. (2009) which was seen for the Halloween SPE and the extreme scenario. ClO enhancements of 0.1 ppb have been found during night-time around $\sim$ 60 km and above. And a decrease of 0.1 ppb $\sim$ 50 km and below during the event day. For all the sensitivity runs, after the event ClO recovers below 50 km. Following reactions R37, HOCl enhancements of 1 ppb and above was seen during the event day until $\sim$ 80 km. At $\sim$ 40 km, HOCl continued to form after the event. Loss of ClO continues below 40 km due to reaction R50, thereby forming $ClONO_2$ after the event. Overall this exceptional middle latitude energetic electron precipitation (EEP) event shows similar volume mixing ratio enhancements and losses compared to the Halloween SPE.

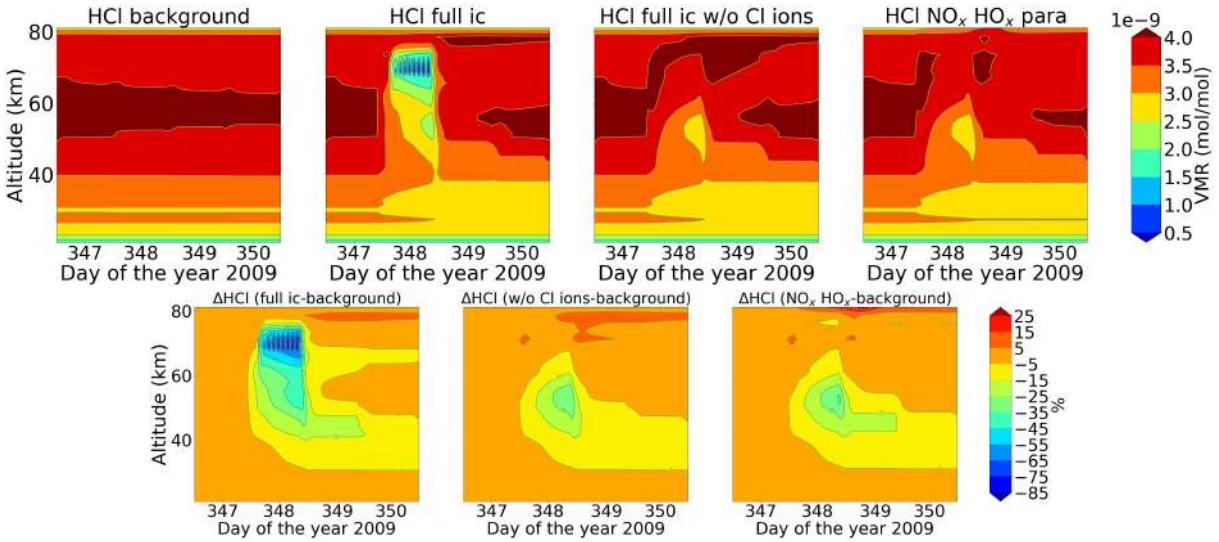

Figure 5.22: Same as figure 5.21 but for HCl

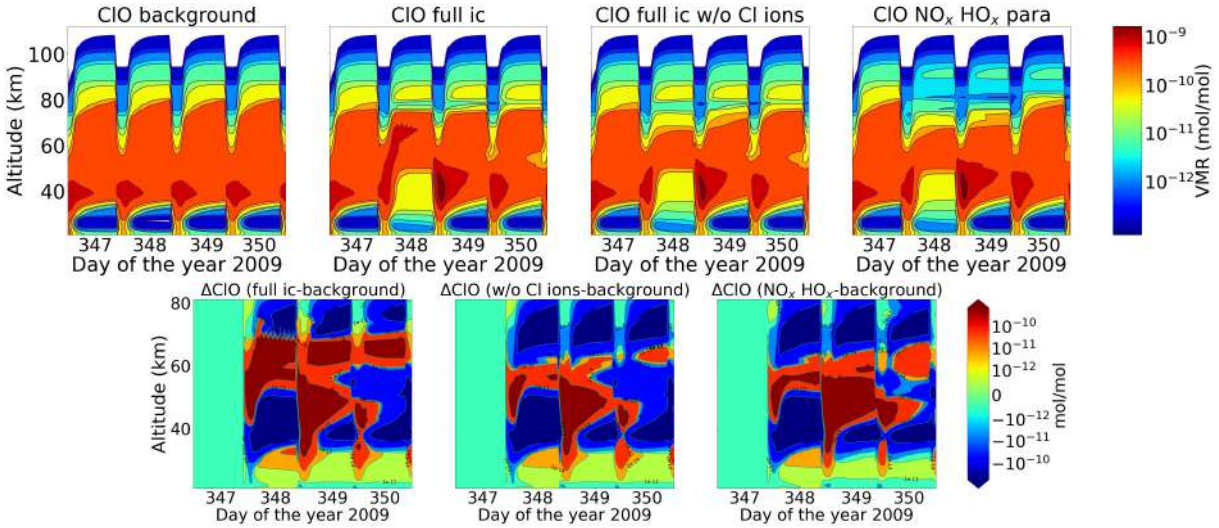

Figure 5.23: Same as figure 5.20 but for ClO.

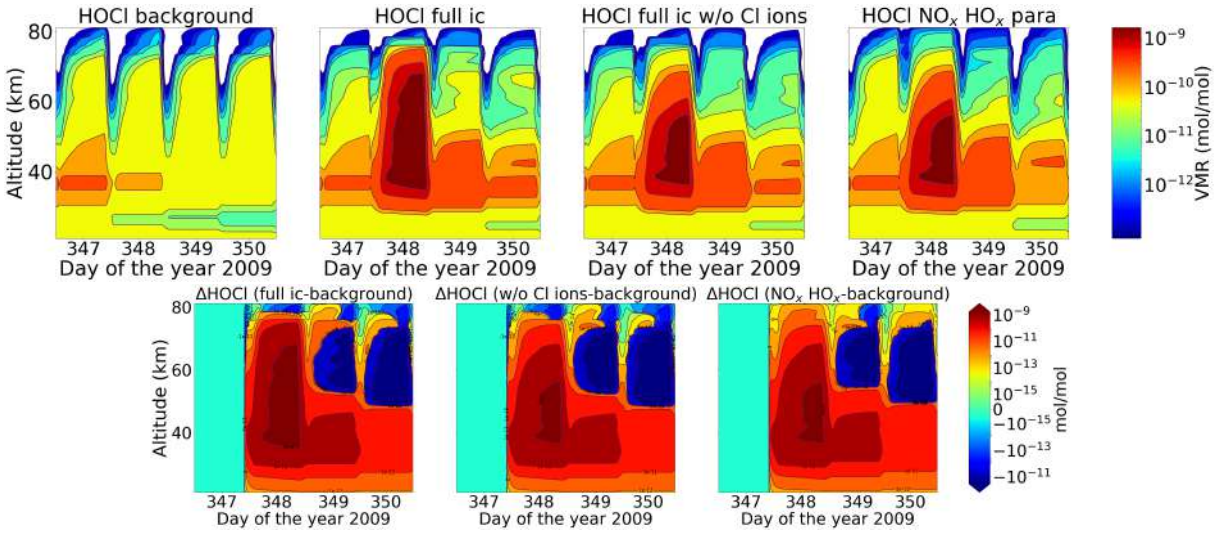

Figure 5.24: Same as figure 5.20 but for HOCl.

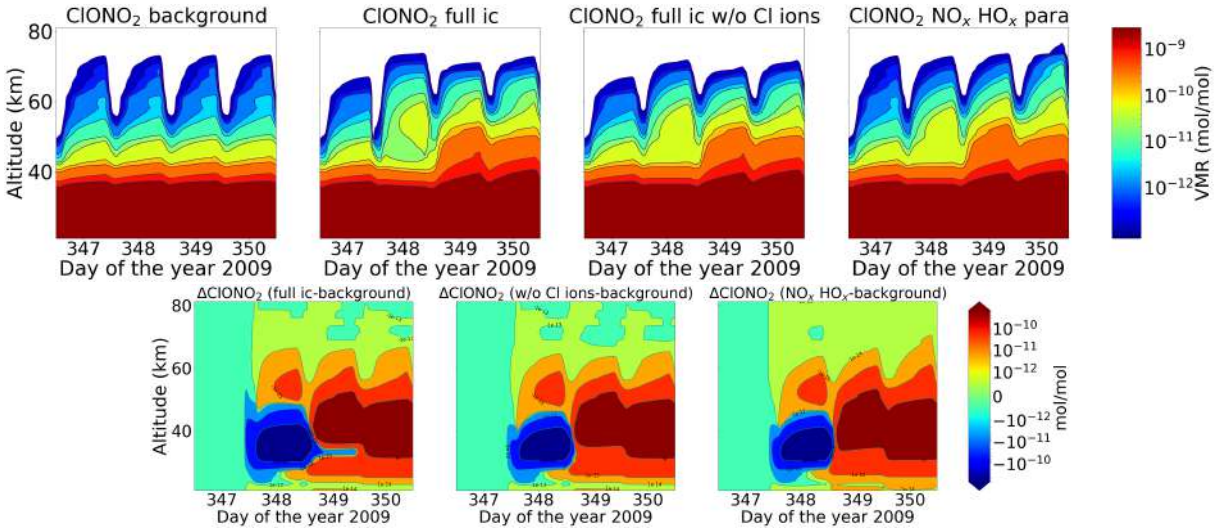

Figure 5.25: Same as figure 5.20 but for $ClONO_2$.

5.4 Impact of chlorine ion-chemistry on ozone loss

With the evaluation of the model results with MIPAS observations, we wanted to assess the impact of chlorine ion-chemistry on ozone loss. The ozone loss in the stratosphere and lower mesosphere during the event has some contribution from chlorine-ion chemistry. Using the model setting that compared best with MIPAS observations, i.e. the ion-chemistry model with $O(^1D)$ in photo-chemical equilibrium, the relative difference was calculated w.r.t. a setting where the chlorine ion-chemistry was switched off. Figure 5.26 shows the same for both daytime and night-time with the time dependent ionisation rates for the 9 days used for the evaluation of the model. The difference here is calculated for daily averaged data for each day. A loss of 2.5% during daytime at an altitude range of 40-60 km and about 10% during

night-time, at an altitude of 50-70 km is observed during the event day. Negative chlorine species directly increase the concentrations of uncharged active chlorine compounds. Through their catalytic cycles, these uncharged chlorine compounds can be responsible for ozone loss at different altitudes which is also dependent on illumination conditions. The ClO_x catalytic cycle (R31 and R63) is responsible for the ozone loss at 40-50 km. There is a slight difference between day-time and nighttime in the loss observed in terms of altitude range, which is expected. This difference can be explained by the difference of the diurnal cycle of ClO during daytime and night-time. The catalytic ozone loss cycles relevant in the stratosphere-mesosphere are the ClO+O (Reactions R31, R63 and R33) and $ClO+HO_2$ (Reactions R36, R39 and R37) that also need solar light, since O is formed by photolysis. During daytime, ClO photolyses in the mesosphere but not in the stratosphere, so ClO is not observed in the mesosphere. The $ClO+HO_2$ cycle produces HOCl which also photolyses during daytime producing Cl through Reaction R38. So during daytime, Cl is more important than ClO. But during nighttime, ClO accumulates in the mesosphere and in the stratosphere, it is mainly $ClONO_2$ due to Reaction R50. As seen from figure 5.27, during the event day on October 28 and also on October 29, the ClO mixing ratios were found to be higher for night-time around 60-70 km compared to daytime. Hence, the ozone loss occurs more in the upper stratosphere-mesosphere around 50-70 km for night-time, thereby producing the difference of the ozone loss in the altitude range. Loss of 0.6% during day-time and 2% during night-time is observed in the altitude range of 30-40 km. The ClO_x cycles with Reactions R46, R47, R48 and Reactions R50, R51, R52 and R53 are responsible at this altitude range for both daytime and night-time. Furthermore, a continuous ozone formation of 2% both during daytime and night-time is observed. This increase is linked to enhanced atomic oxygen production by O_2 photolysis in solar maximum conditions (Marsh et al., 2007). It is observed at an altitude range of 60-70 km for daytime and 50-70 km for night-time.

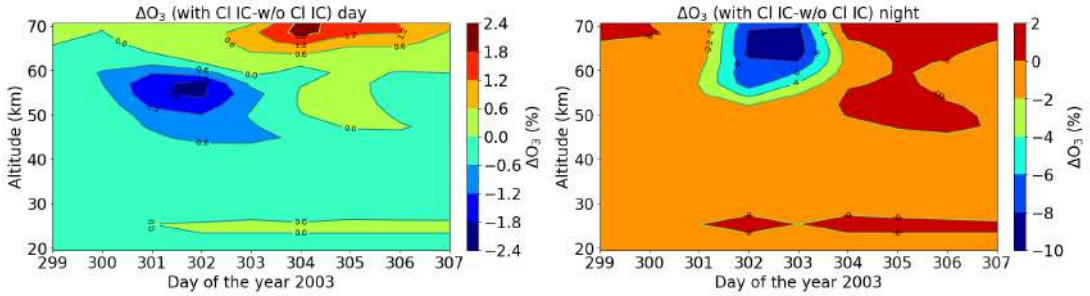

Figure 5.26: Relative difference of the model with full ion-chemistry and $O(^1D)$ in photo-chemical equilibrium including chlorine ions w.r.t. the model without chlorine ion-chemistry for the Halloween SPE: daytime (left) and nighttime (right). The difference here is calculated for daily averaged data.

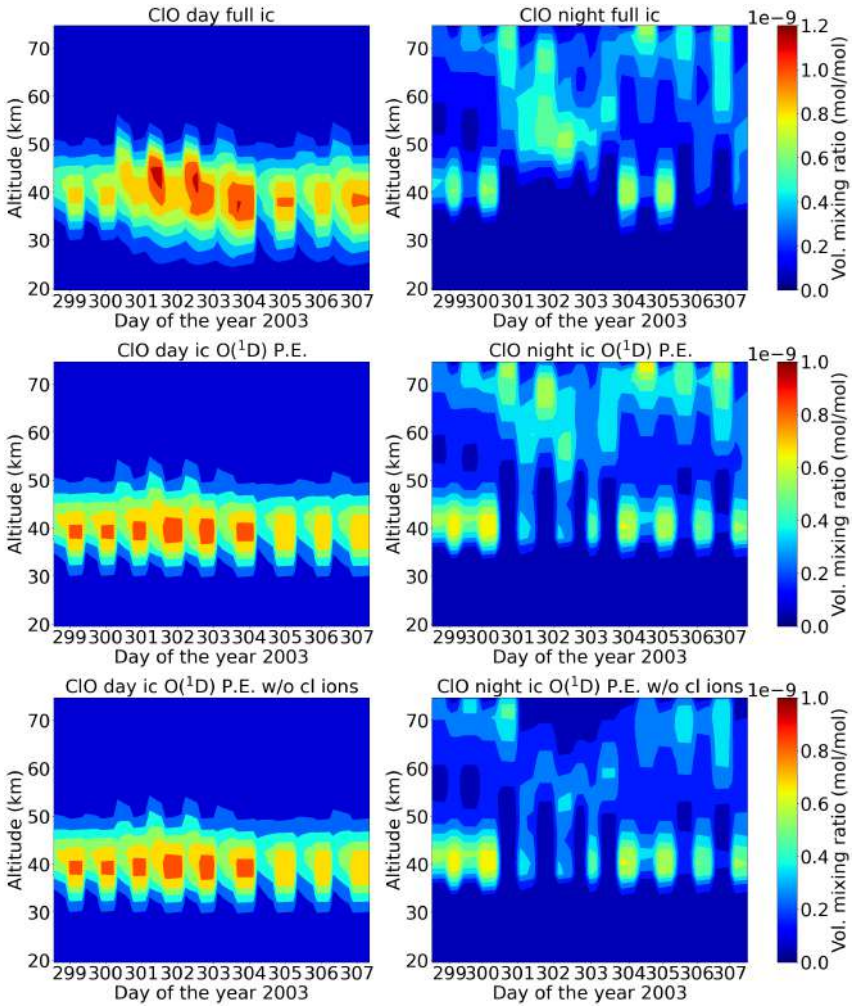

Figure 5.27: Diurnal cycle of ClO with temporal ionisation rates for the Halloween SPE for the sensitivity studies of: full ion-chemistry, ion-chemistry with O(^{1}D) in photo-chemical equilibrium and the one without chlorine ions.

Figure 5.28 shows the relative differences of the model setting with ion-chemistry and O(^{1}D) in photo-chemical equilibrium w.r.t. the model setting without chlorine ion-chemistry comparing the Halloween SPE and the extreme event in order to assess the impact of chlorine ion-chemistry on ozone loss during the event day. An impact of the chlorine ions around 10-20% is observed on the event day. Qualitatively, it was a bit more for the extreme event compared to the Halloween SPE that could be more important for higher forcing. An increase of around 5% for ozone is also seen after the event stops for the extreme scenario. The extreme run doesn't show any impact of chlorine ion-chemistry on ozone loss at 70-75 km while the Halloween SPE does. This can be explained by the ClO and HOCl responses to SPEs and due to the ClO_x catalytic cycle. At an altitude of 70-75 km, ClO decrease for the sensitivity runs for both ion-chemistry with O(^{1}D) in photo-chemical equilibrium and without chlorine ions is larger for the extreme event compared to the Halloween SPE (figure 5.8). This is one contributing factor as to why we don't see an impact on ozone loss at these altitudes. Kalakoski et al. (2020) used WACCM-D to investigate ozone depletion around 50-60 km after the onset of the SPE as explained in Sect. 4. They studied the

effect in both the hemispheres and the duration and altitude range of this extra ozone loss correspond to NO_x and enhanced Cl_x(=Cl+ClO) mixing ratios. An ozone loss of 0.2 ppm in both the hemispheres was observed after the event. Around 70 km, the ozone loss was due to short lived HO_x. And around 50 km, it is driven by NO_x and Cl_x that lasts longer with maximum ozone decrease seen about 30 days after the event onset. Since HCl response to SPEs is partly due to chlorine ion-chemistry which converts it to Cl, ClO and HOCl (Winkler et al., 2009), this is also indirectly an effect of the chlorine ion-chemistry. They also see an increase in ozone, around 0.2 ppm throughout the period near the secondary ozone maximum above 80 km, which is also due to O_2 photolysis as discussed above. We observe a continuous increase of O_3 after the event, which is about 5%. This increase was seen around 50-60 km for the Halloween SPE and 50-75 km for the extreme scenario.

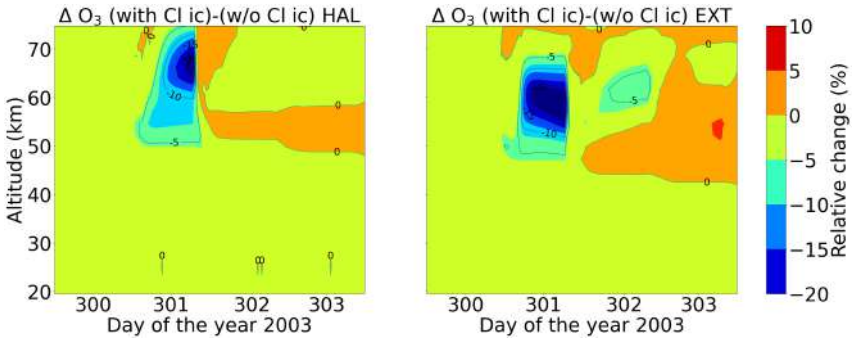

Figure 5.28: Relative difference of the model simulations: full ion-chemistry with O(^{1}D) in photo-chemical equilibrium and with chlorine ions w.r.t. the model setting without chlorine ion-chemistry comparing the Halloween SPE (left) and extreme scenario (right). The data shown here is not daily averaged but the real model time step.

Figure 5.29 shows the impact of chlorine ion-chemistry on ozone loss for the energetic electron precipitation (EEP) over Moscow detected by the balloons which is 15-20% during the event day and a continuation of 10-15% that was found in the upper stratosphere and mesosphere around 60 km.

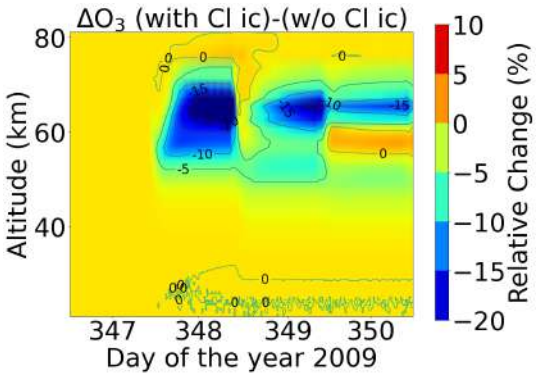

Figure 5.29: Relative difference of ozone for full ion-chemistry w.r.t. the run with switching off the chlorine ion-chemistry

6 Studies of dynamical coupling with atmospheric ionization using EMAC

In this chapter, studies of dynamical feedback to the chemistry of the atmosphere and the response of atmospheric ionisation is investigated with a focus on Sudden Stratospheric Warmings (SSWs). They are produced by the disruption of the polar vortex and planetary wave forcings from the troposphere. According to different studies, the polar vortex after the SSW follows a remarkably regular evolution. The lower stratosphere is warm and an elevated stratopause that descends over the course of the vortex recovery is separated by an extremely cold mid-stratosphere.

6.1 Description of Model Experiments: Specified dynamics and free-running ensemble simulations for the large sudden stratospheric warming of 2009

The impact of two different solar forcings from the top on the middle atmosphere is compared using the EMAC model. First, the extreme ultra-violet (EUV) photo-ionisation is varied to calculate its impact on the SSW 2009 by doubling and halving the rates of the most important ions in the upper atmosphere, i.e., O_2^+, $O(^4S)^+$, $O(^2D)^+$, $O(^2P)^+$, N_2^+ and N^+. Secondly, the impact of solar particles was calculated by synchronising the SSW event on the 22nd January 2009. This was a remarkable major sudden stratospheric warming (SSW) that occurred during the boreal winter 2008/09. Two days for an extreme scenario was chosen and compared to a background with AISstorm ionisation rates that calculates ionisation rates for protons, electrons and alphas based on POES and GOES fluxes from their energy channels with proton and electron detectors. We use a geomagnetic storm, which mainly consists of electrons (few keV-MeV) that mostly affects the mesosphere and lower thermosphere (MLT) region. Around 80 km ($\sim 10^{-3}$ hPa), the geomagnetic storm shows the maximum ionisation rates. The geomagnetic storm has been synchronised with the SSW 2009. Protons were also added and were taken from an extreme solar event that occurred in 775 A.D. whose ionisation rates were derived by scaling the fluxes from an SPE that occurred in 1956 with a very high ground level enhancement (GLE). The particle fluxes were scaled by a factor of 70 as discussed in Chapter 4 so that the spectrum fits the ice core records of the 775 A.D. event. Figure 6.1 shows the latitude-height cross sections of the ionisation rates for the reference (background ionisation rates from AISstorm), a day with low activity (Day 2) and an extreme geomagnetic storm (Day 3). Higher values are seen in the MLT region and at the polar caps at high latitudes for Day 2 and Day 3.

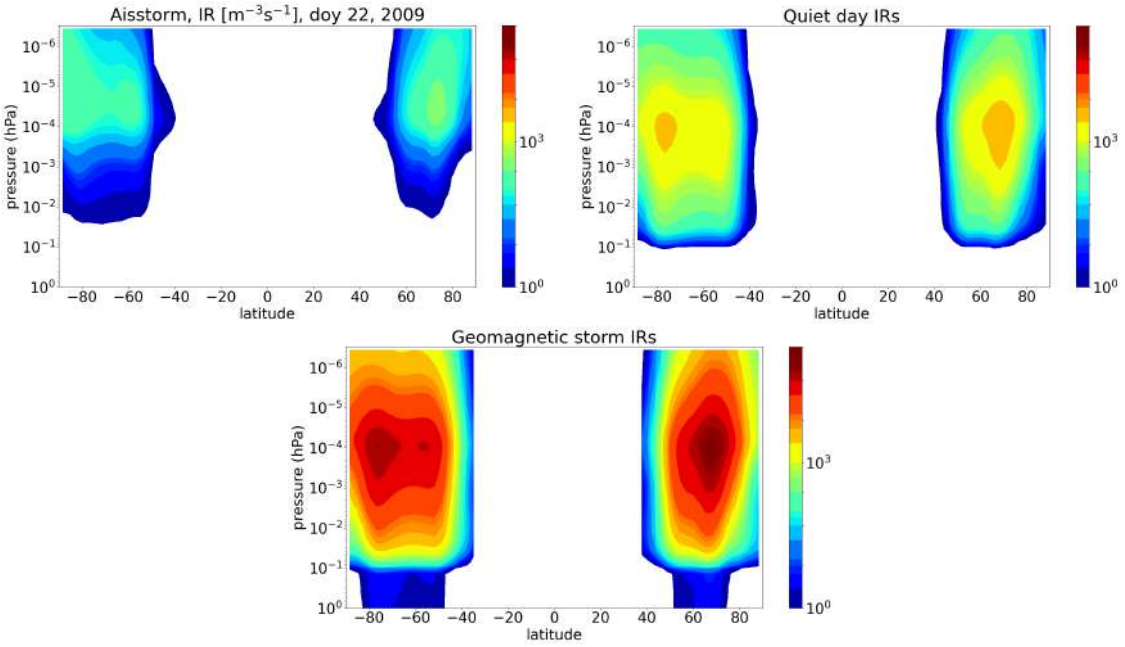

Figure 6.1: Latitude-pressure cross sections of the ionisation rates with AISstorm model (background), day with low activity (Quiet day) and the extreme geomagnetic storm. The colorbar is $m^{-3}s^{-1}$.

Effects on the polar vortex breakdown and its after effects using temperature, ozone, NO_y and zonal mean zonal wind for the Reference (with just AISstorm IRs), a day with low activity (Day 2) and the extreme geomagnetic storm (Day 3) were compared. The focus is mainly on the Northern Hemisphere, polar cap region. Different onset dates were tested for the simulations to get closer to the SSW event and January 13th was chosen. Table 6.1 shows the names of the different model experiments and the different solar forcings. The experiments were conducted for a NO_x based parameterisation and with ion-chemistry containing five important ions in the upper atmosphere. The results shown in the following sub-sections are the ones with NO_x based parameterisation and the ones with five ion-chemistry are shown in the Appendix B. Ensemble simulations were performed with 20 members for each case. For both parameterised NO_x and five ion-chemistry, the simulations with different cases were performed.

Model experiments	**EUV-Cases**	**Particle forcings**	**Cases**
Specified Dynamics and Free Running	EUV*2	Background (AISstorm)	Parameterised NOx
	EUV*1	Low activity	Five ion-chemistry
	EUV/2	Geomagnetic storm (GMS)	(O_2^+, $O(^4S)^+$, $O(^2P, ^2D)^+$, N_2^+, N^+)

Table 6.1: Different model experiments with the different forcings: EUV and solar particles.

6.2 Can we simulate sudden stratospheric warmings (SSWs) with a free-running model?

In this section, simulation results with specified dynamics (S.D.) and free-running (F.R.) for the different solar forcings are shown focusing on the temperature and zonal mean zonal wind. Dynamical radiative feedback due to the changes in chemistry on ozone was studied.

6.2.1 Temperature

Figure 6.2 shows the evolution of temperatures for the time period of January 13, 2009 - February 28, 2009 with the parameterised NO_x model with specified dynamics nudged upto 10 Pa (80 km) and free-running above in the upper mesosphere and thermosphere. The figures are shown for (row-wise): EUV*2, EUV*1 and EUV/2 and column-wise for the reference run with AISstorm ionisation rates for the background, a day with low activity (Day 2) and an extreme geomagnetic storm (Day 3). Initial cooling is observed in the MLT region which breaks down after the SSW. The temperature goes down to 160 K. After the SSW, the temperature goes up to 200 K in the MLT region. The vortex and temperature breakdown occurs in the stratosphere around January 27 and its recovery is way later, around February 10 with the elevated stratopause observed around 75 km. The altitude in the stratopause increases by 12.5 km for all cases in case of specified dynamics. The variation among the different cases is not too much. Figure 6.3 shows the time evolution of the temperatures for the same cases as figure 6.2 but free-running in the whole altitude region. The reformation of the polar vortex here after the SSW is earlier, around February 3rd as compared to specified dynamics. It is observed that upon doubling and halving the EUV, the temperature increases after the polar vortex reformation compared to EUV*1 around 75 km. This is the case for both the particle forcings. In case of EUV/2, and for day 2 and day 3, a second SSW is observed on February 24 with a temperature increase of 270 K in the stratosphere.

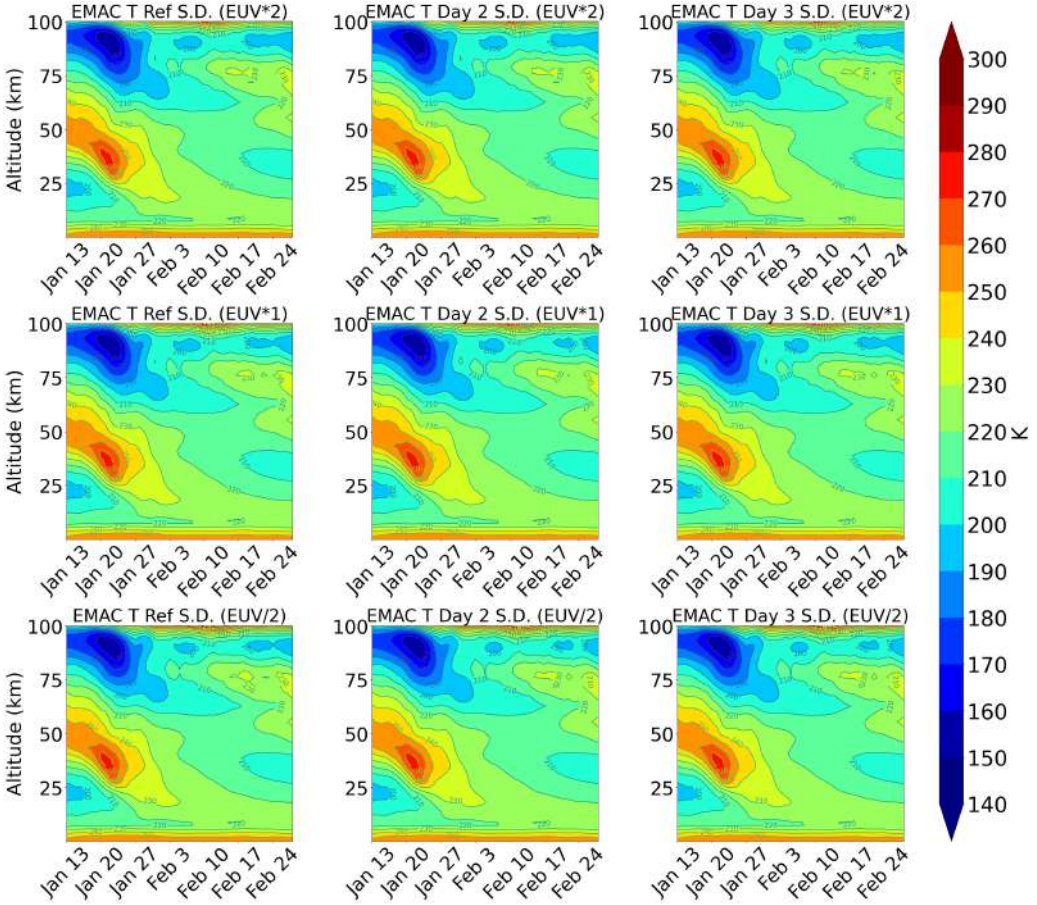

Figure 6.2: Daily averages of zonally averaged temperatures over 60-90°N for parameterised NO_x specified dynamics (column-wise): with the background AISstorm, Day 2 with low activity and Day 3 with the extreme geomagnetic storm synchronised on 22nd January 2009. The time series is shown for: Jan 13, 2009-Feb 28, 2009. Row-wise: EUV*2, EUV*1 and EUV/2

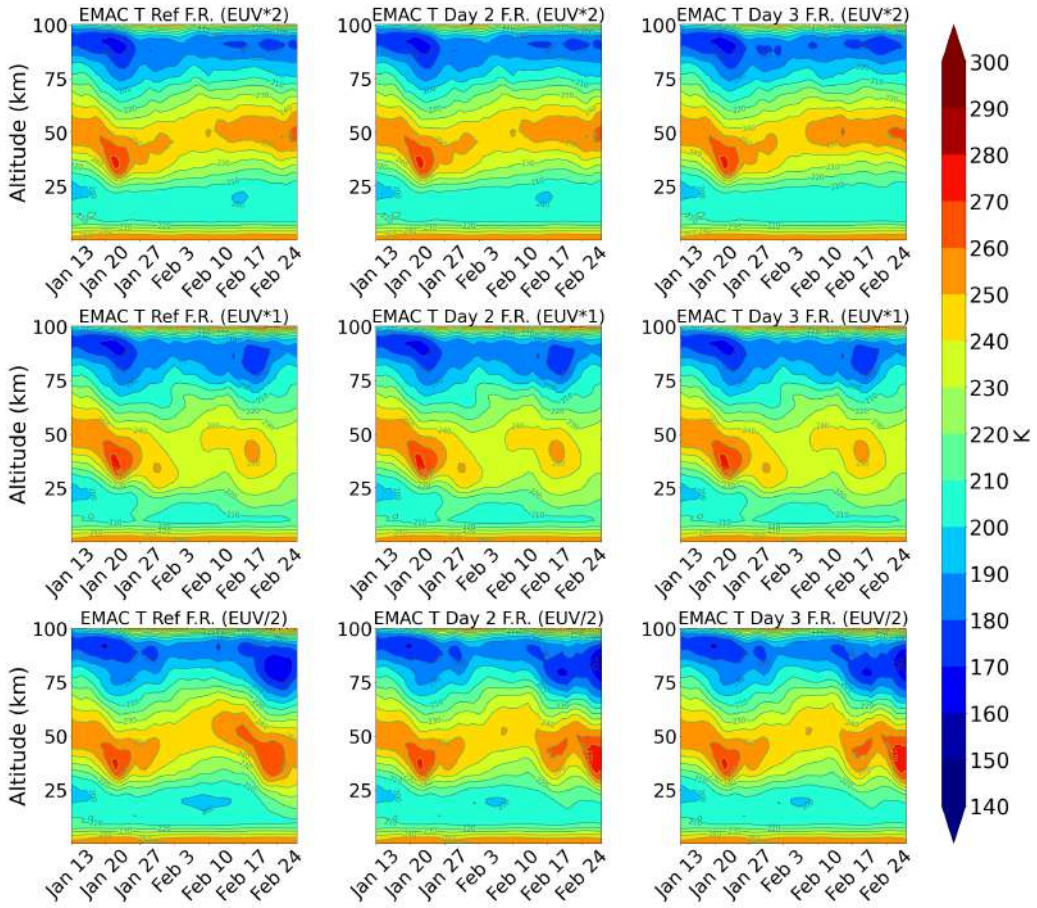

Figure 6.3: Daily averages of zonally averaged temperatures over 60-90°N for the parameterised NO_x (column-wise): with the background AISstorm, Day 2 with low activity and Day 3 with the extreme geomagnetic storm synchronised on 22nd January 2009. The time series is shown for: Jan 13, 2009-Feb 28, 2009. Row-wise: EUV*2, EUV*1 and EUV/2

Figure 6.4 shows latitude height cross-sections of temperature taking an example of one EUV case (EUV*1), for the background ionisation rates with AISstorm, Day 2 with low activity and day 3 with the the extreme geomagnetic storm (GMS). A warm stratosphere and a cold mesosphere is observed for the southern hemisphere before the SSW for all cases. On the day of the SSW, i.e., 23rd January 2009, the temperature increases in the stratosphere in the Northern Hemisphere to 260 K and 280 K in the North pole. Enhanced mesospheric cooling is observed as well. Both the stratospheric warming and mesospheric cooling disappears after the SSW, i.e., on the 3rd of February.

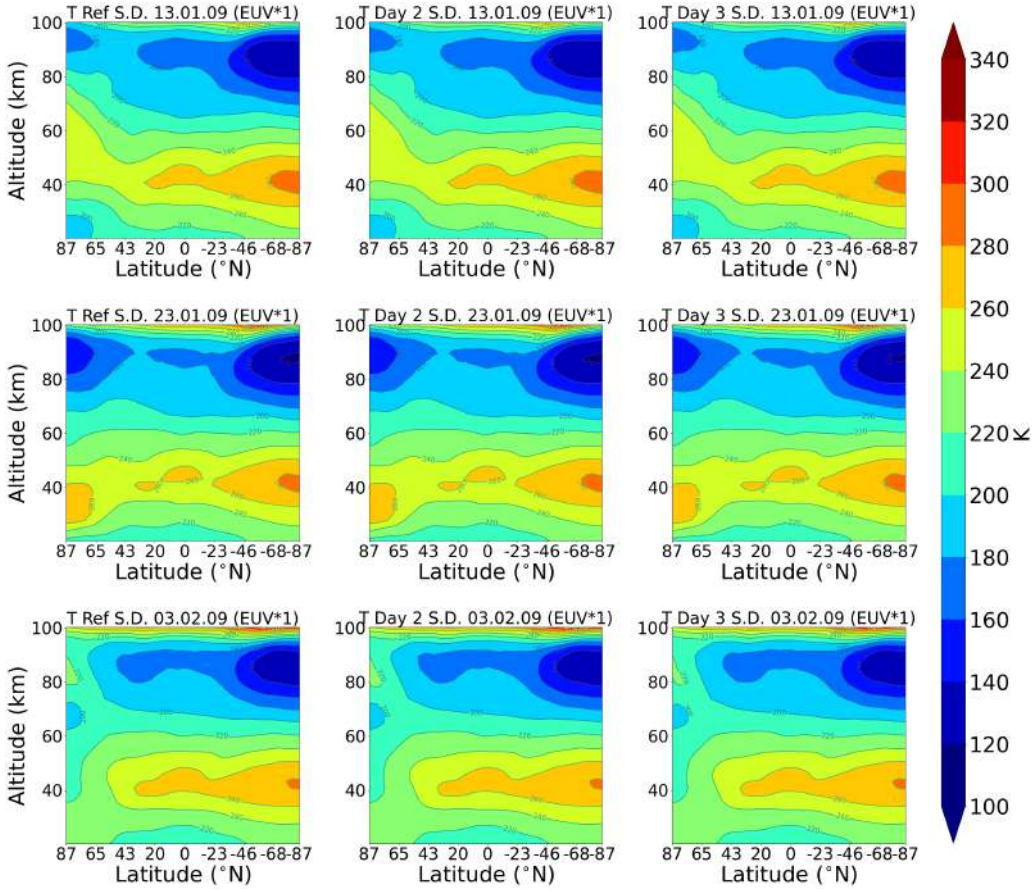

Figure 6.4: Latitude-height cross-sections of temperature averaged over the longitudes for EUV*1 (column-wise): with the background AISstorm, Day 2 with low activity and Day 3 with the extreme geomagnetic storm. Row-wise: Jan 13th, Jan 23rd and Feb 3rd

Zonal mean zonal wind

Figure 6.5 shows the zonal mean zonal wind time evolution for simulations with specified dynamics for the different cases. A reversal or deceleration of zonal mean zonal wind, where it changes direction from westerly to easterly, is seen on the day of the SSW, i.e. 22nd January 2009. In this case, the depth of the wind reversal goes below 25 km. The wind recovers after that in the stratosphere. The wind speed shows an increase upto 60 m/s in the stratosphere towards the end of February for all the cases. Figure 6.6 shows the simulations of zonal mean zonal wind for all the cases with the free running model. The wind reversal is seen on the day of the warming in each case and a second reversal is also seen for all cases on January 27 after which a decrease in the circumpolar westerly wind speeds occur but the reversal of westerly to easterly don't. They occur more frequently in the upper stratosphere and also in both the hemispheres. A third reversal is seen in case of EUV*1 and EUV/2 around February 17, 2009.

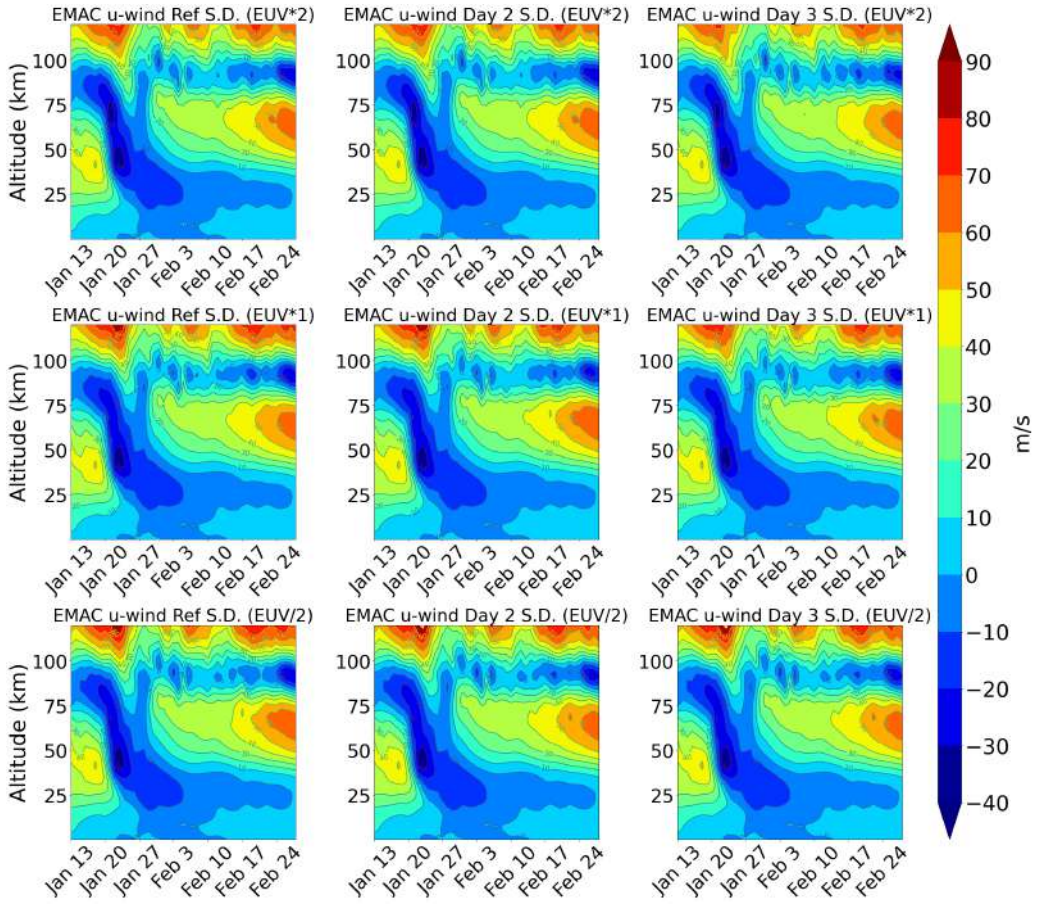

Figure 6.5: Daily averages of zonally averaged zonal mean zonal wind (u-wind) over 60-90°N for parameterised NO_x specified dynamics (column-wise): with the background AISstorm, Day 2 with low activity and Day 3 with the extreme geomagnetic storm synchronised on 22nd January 2009. The time series is shown for: Jan 13, 2009-Feb 28, 2009. Row-wise: EUV*2, EUV*1 and EUV/2

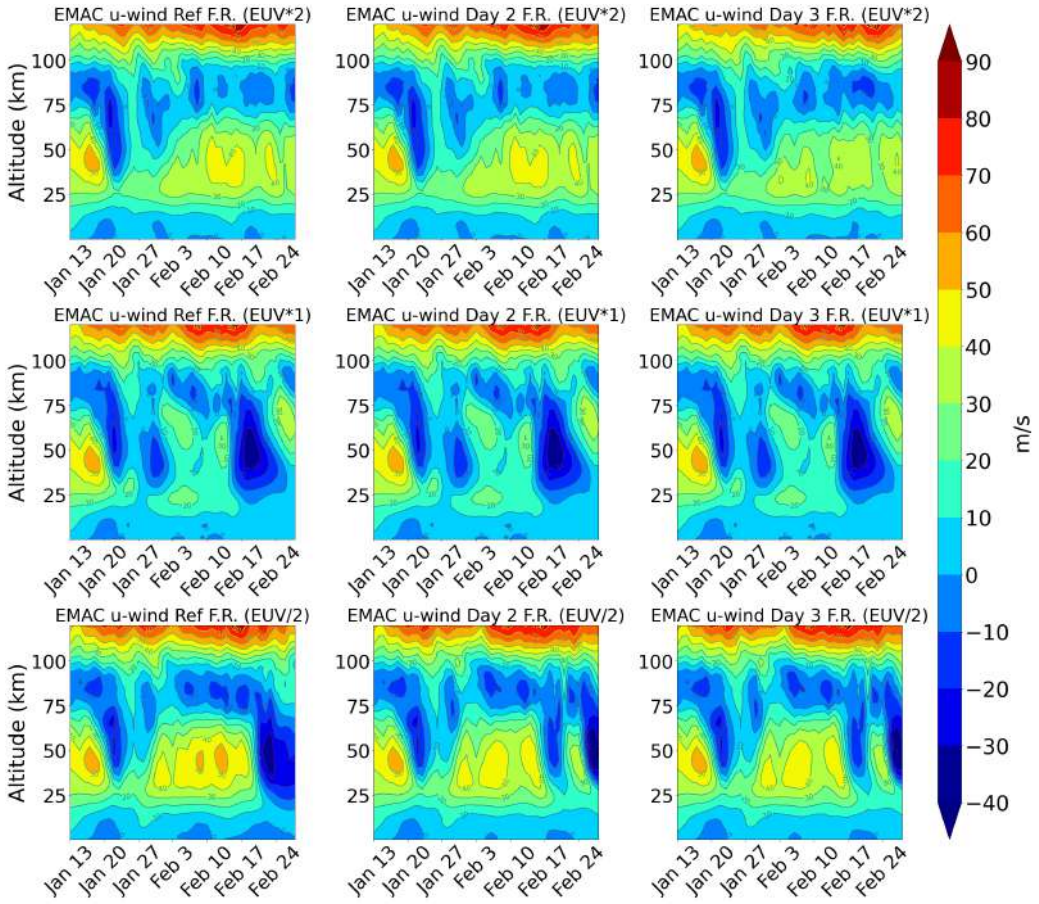

Figure 6.6: Daily averages of zonally averaged zonal mean zonal wind (u-wind) over 60-90°N for the parameterised NO_x (column-wise): with the background AISstorm, Day 2 with low activity and Day 3 with the extreme geomagnetic storm synchronised on 22nd January 2009. The time series is shown for: Jan 13, 2009-Feb 28, 2009. Row-wise: EUV*2, EUV*1 and EUV/2

Figure 6.7 shows the latitude-height cross-sections for the reference run with AISstorm IRs, day 2 with low activity and day 3 with the extreme geomagnetic storm for EUV*1 case for the specified dynamics runs as an example. An accelerated zonal mean zonal wind is seen in the Northern Hemisphere (NH) with winds upto 70 m/s in the stratosphere combined with a deceleration with values -70 m/s in the Southern Hemisphere on the 13th of January 2009. On the day of the SSW, i.e., on the 23rd of January 2009, winds decelerate to -70 m/s in the Northern Hemisphere in the stratosphere and accelerate above $\sim$ 100 km in the mesosphere to 90 m/s. And then accelerate again upto 50 m/s in the stratosphere and Northern Hemisphere (NH).

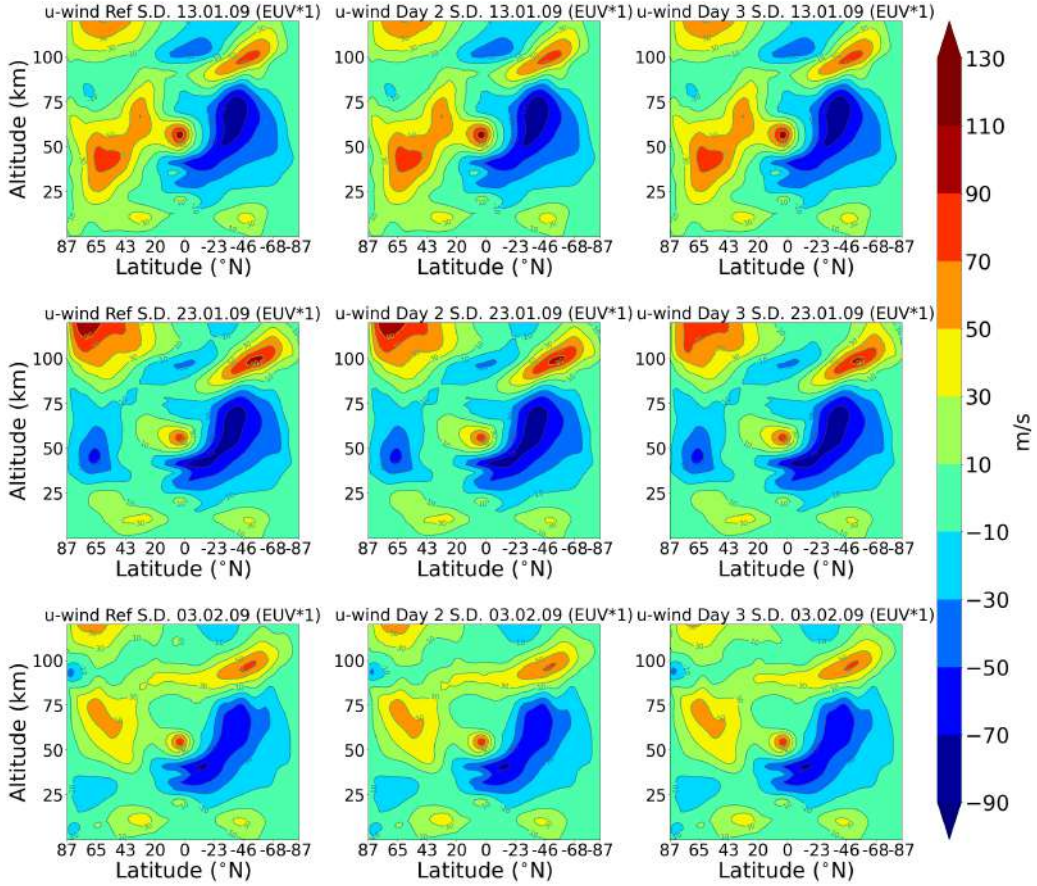

Figure 6.7: Latitude-height cross-sections of zonal mean zonal wind for specified dynamics averaged over the longitudes for EUV*1 (column-wise): with the background AISstorm, Day 2 with low activity and Day 3 with the extreme geomagnetic storm. Row-wise: Jan 13th, Jan 23rd and Feb 3rd

6.3 Effects on the chemistry of the middle atmosphere due to different forcings from the upper atmosphere

To look at the effects on the chemistry of the middle atmosphere during the SSW with particle and EUV impacts, total NO_y and ozone are considered particularly in the MLT region. Ensemble simulations have been performed with January 13th as the onset. The ensembles were generated by changing the initial temperatures by 0.3% and keeping the global mean temperature in EMAC constant.

6.3.1 Total NO_y

Figure 6.8 shows the total NO_y for 20 individual ensemble members for the normal EUV forcing with NO_x based parameterisation. The MLT peak on the event day is observed for all the ensemble members and the NO_y enhancements afterwards. So basically, all the ensemble members predict the SSW. The timing and the onset of the enhanced descent post-SSW in the stratosphere and mesosphere varies among the ensembles. However, the enhanced NO_y in the mid-thermosphere region above 150 km which is driven by EUV seems to have a similar variability.

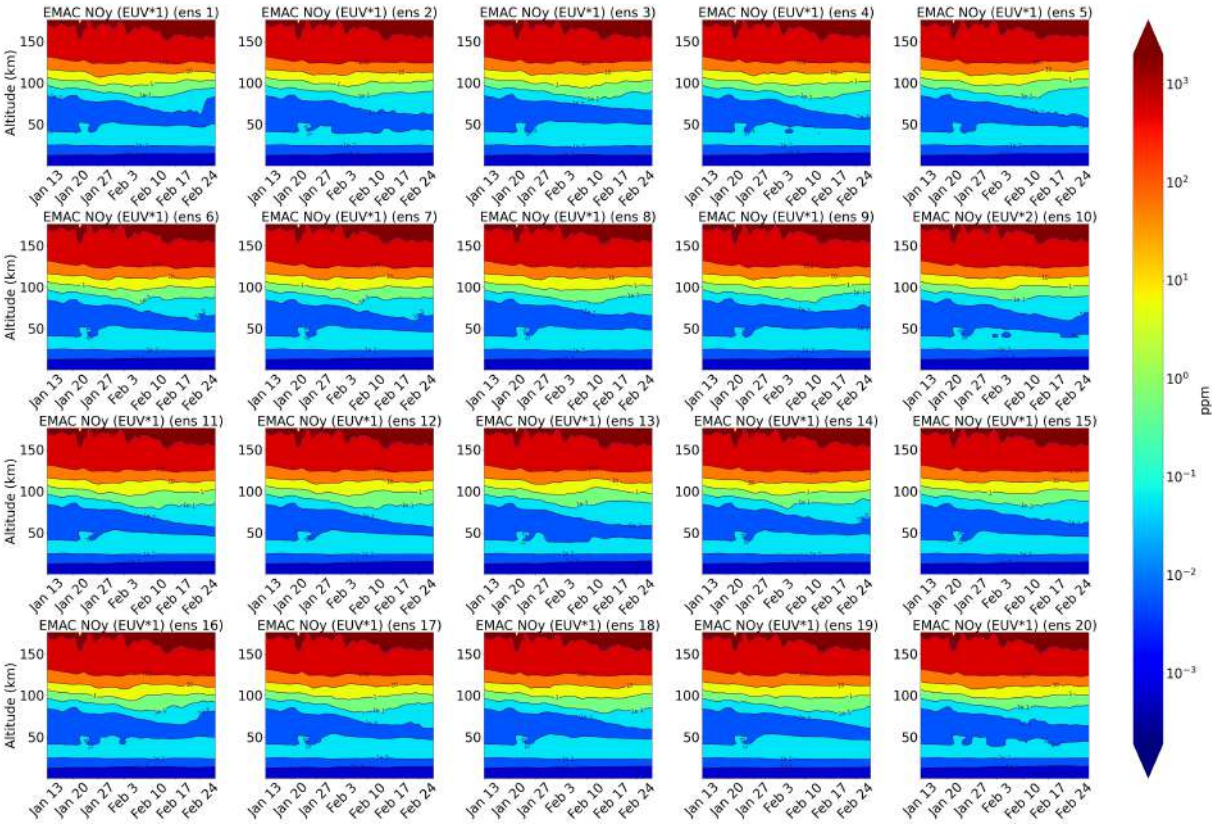

Figure 6.8: An example of 20 different ensemble members of total $NO_y = N + NO + NO_2 + NO_3 + HNO_2 + HNO_3 + HNO_4 + ClONO_2 + 2 * N_2O_5 zonallyaveragedover 70 - 90°N$ calculated for the geomagnetic storm (Day 3) and EUV (EUV*1): Free-running (F.R.) simulations calculated with a NO_x based parameterisation.

Figure 6.9 shows the mean of 20 ensemble members for the different forcings. In the MLT region, above 150 km, NO_y enhancements upto 10000 ppm is seen on the day of the event, which propagates downwards after the SSW. This seems to decrease with lower EUV and higher particle forcing after January 22nd. For the higher particle forcings, the peak produced is more pronounced compared to the background, with enhancements reaching much far below. For example, in case of the geomagnetic storm, the peak on the day of the SSW goes down to 150 km for EUV*2, $\sim$ 140 km for EUV*1 and to $\sim$ 125 km for EUV/2. The NO_y contribution is mainly dominated by N and NO. Ground and excited states of N are produced during the event that can react with O_2 to form NO in the thermosphere (Reactions R10 and R11). The scavenging reaction that destroys NO also takes place simultaneously. Higher production of NO_y, i.e., N and NO is observed for the geomagnetic storm. Down-welling is observed below 100 km for all cases which is due to adiabatic heating (Funke et al., 2017). In the pre-SSW phase (Jan 13-Jan 20), as seen from figure 6.10, a very small down-welling of about 0.01 ppm is observed around 65 km. And around 90-100 km, down-welling of 0.1 ppm is observed. Funke et al. (2017) studied the SSW 2009 with different high-top models and with observations, for example, with MIPAS. From figure 12 of Funke et al. (2017), in the pre-SSW phase with MIPAS observations, odd nitrogen, (NO_x = NO + NO_2) enhancements of 0.01 ppm around 65 km and 0.1 ppm around 100 km which is known as down-welling.

The SSW main phase, i.e, Jan 20-Jan 24, starts with the breakdown of the polar vortex and dilution of the mesospheric NO_x by upwelling and increased horizontal mixing as a decrease of NO_x from 0.01 ppm to 0.001 ppm. This is later followed in the post-SSW phase (Jan 20-Feb 28) by a strong down-welling of NO_y leading to a pronounced increase in the mesosphere and an upwelling afterwards. Figure 6.11 shows the ensemble means for all cases with the five ion-chemistry. The geomagnetic storm on the event day, i.e., 22nd January, showed a very high production upto 10000 ppm with the peak going below 150 km in altitude. And enhancements in the MLT region after the event is seen but for higher altitudes compared to the parameterised NO_x.

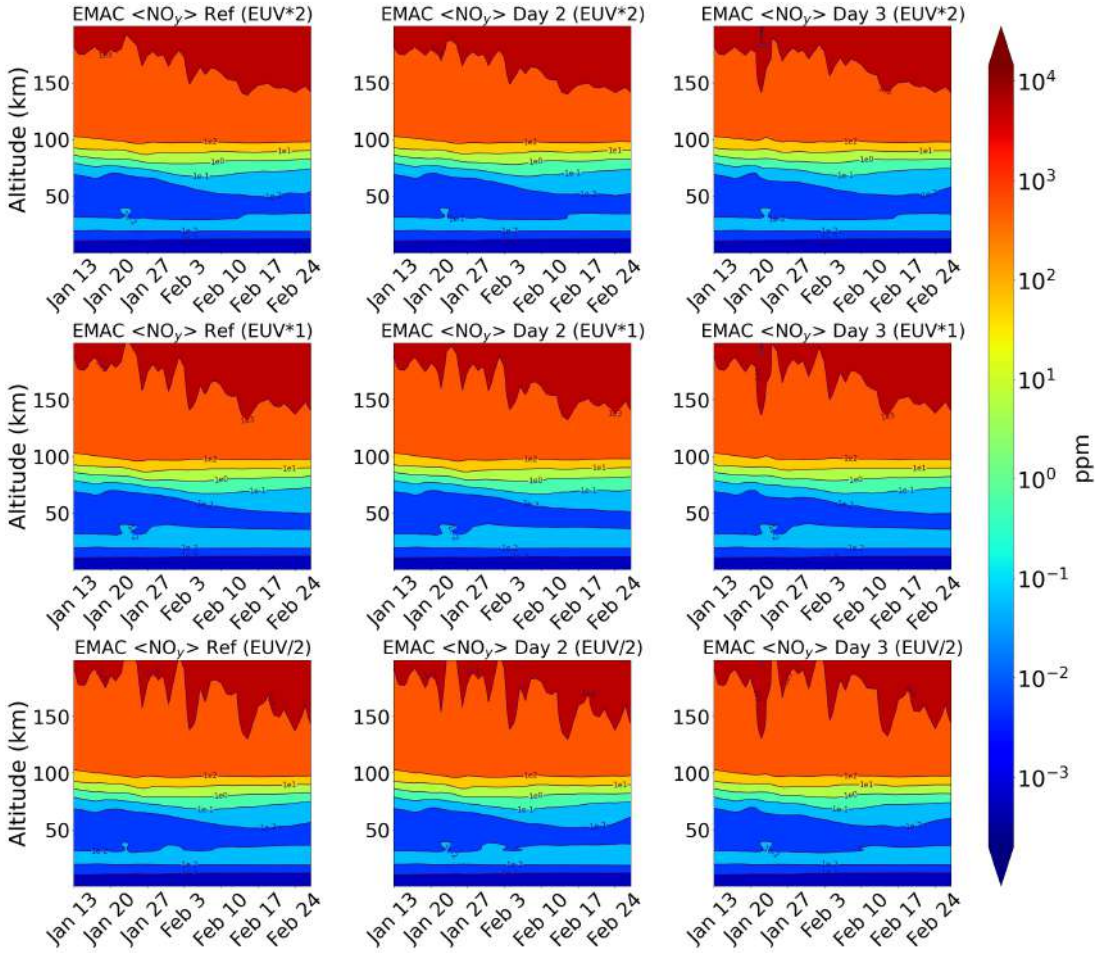

Figure 6.9: Mean of 20 different ensemble members of total NO_y zonally averaged over 70-90°N calculated for the reference (AISstorm), low activity (Day 2) and geomagnetic storm (Day 3) for all the EUV forcings and the particle forcings with a NO_x based parameterisation.

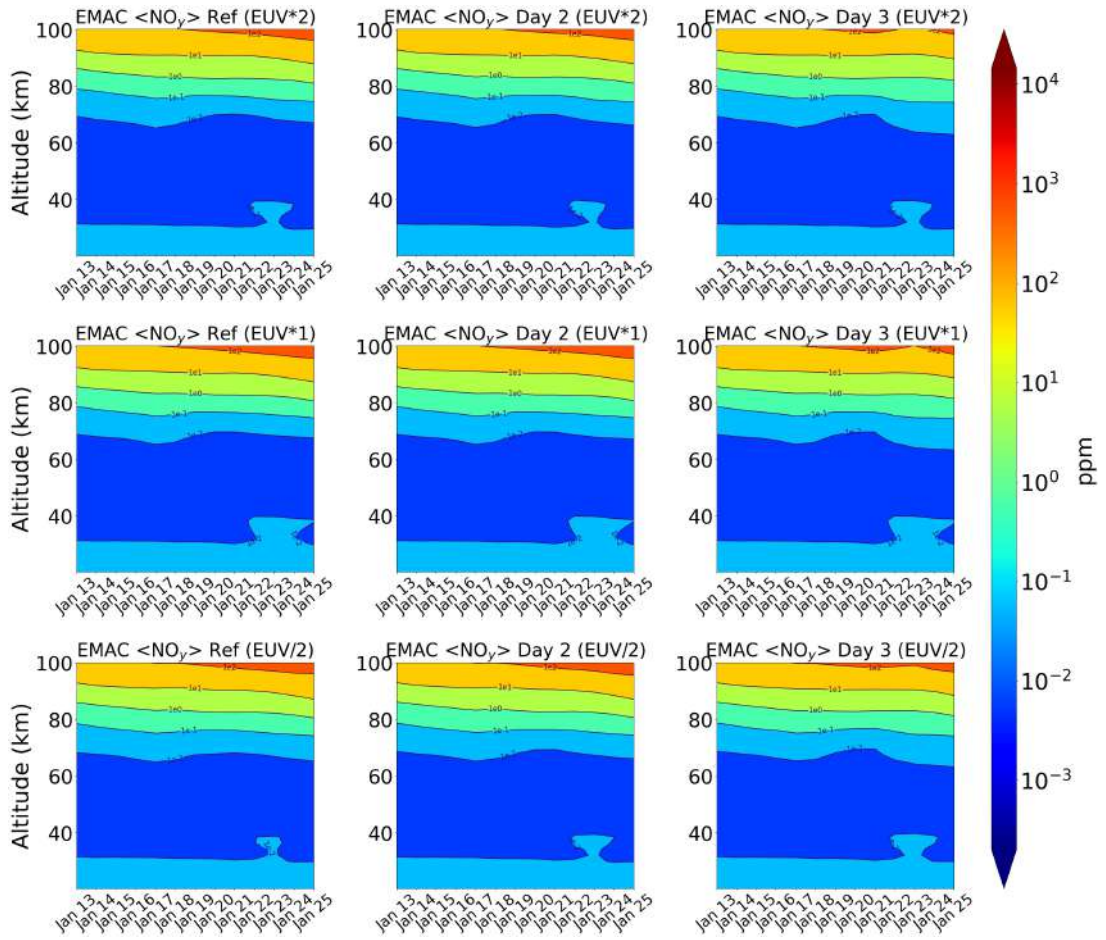

Figure 6.10: Same as figure 6.9 but zoomed from January 13-January 25.

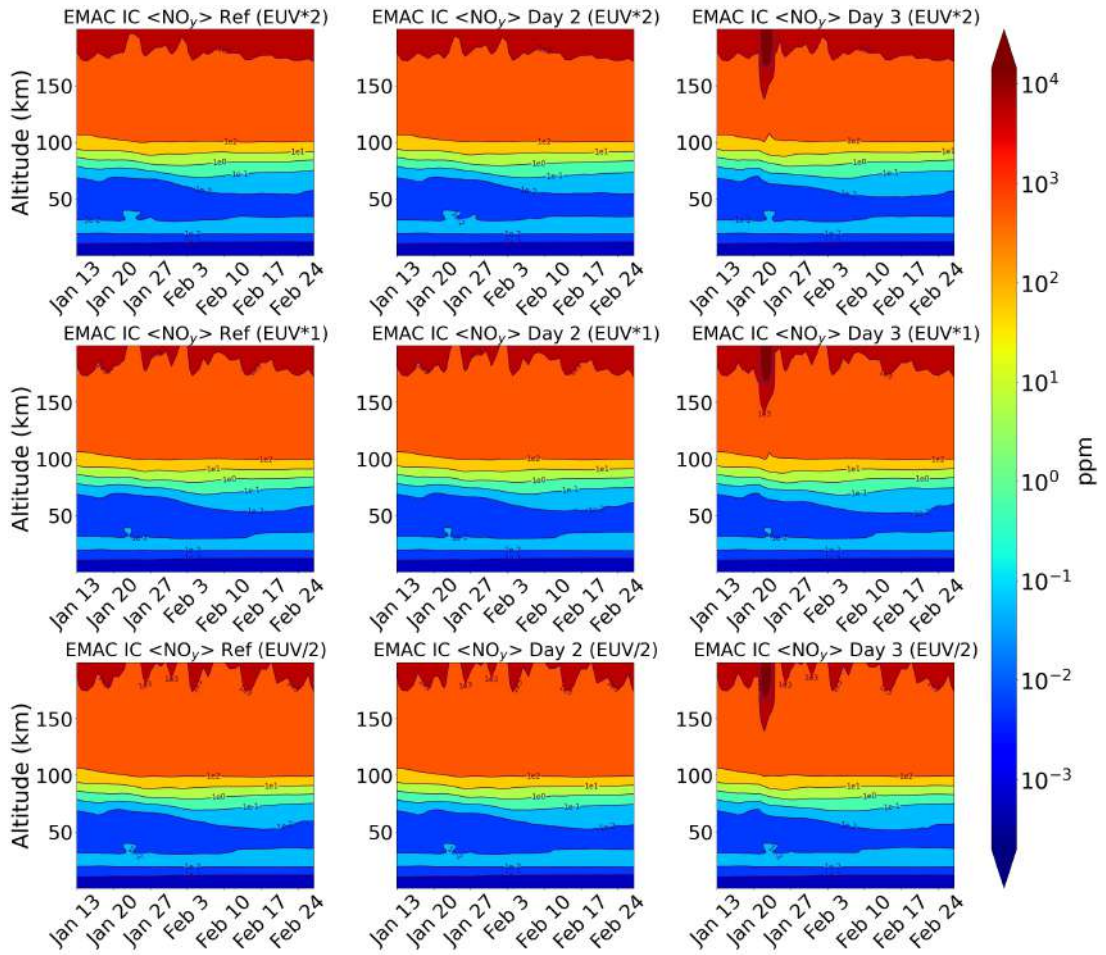

Figure 6.11: Mean of 20 different ensemble members for total NO_y calculated for the reference (with AISstorm), day 2 with low activity and the geomagnetic storm (Day 3) for all the EUV forcings and particle forcings with the five ion-chemistry.

The results between NO_x based parameterisation and five ion-chemistry show a small difference. Figure 6.12 shows the difference of ion-chemistry to the parameterised NO_x based simulations. For the geomagnetic storm, above 150 km, on January 22nd, the five ions produced 10000 ppm more NO_y.

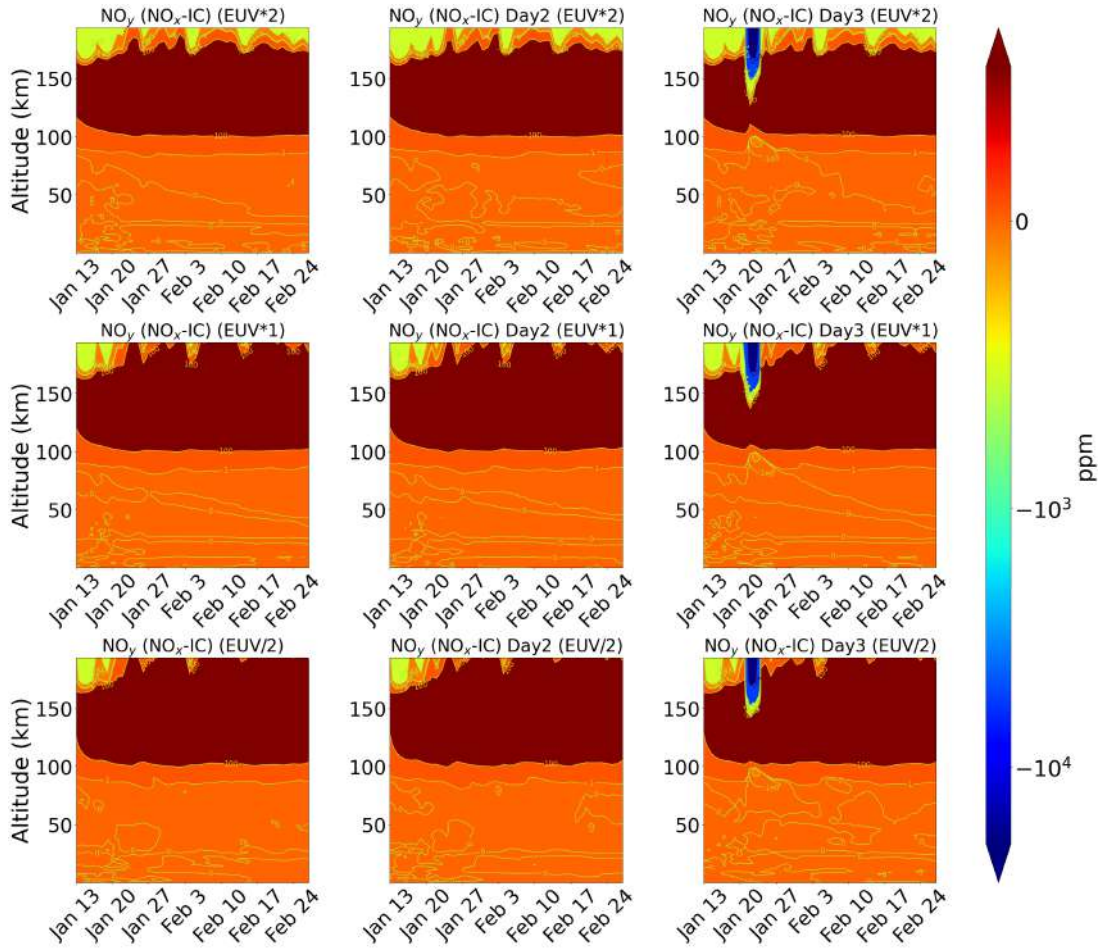

Figure 6.12: Absolute differences of total NO_y for the parameterised NO_x w.r.t. five ion-chemistry.

EUV impact and particle impact

Figure 6.13 shows the absolute differences of the ensemble means for EUV/2 and EUV*2 w.r.t. EUV*1 for the three cases of particle forcings. EUV*2 shows higher NO_y enhancements $\sim$ 240 ppm on the day of the event in the MLT region for all cases compared to EUV*1. But comparing EUV/2 to EUV*1, EUV*1 shows 160 ppm enhancements going below to 120 km. For the extreme geomagnetic storm, Day 3, EUV/2 shows more NO_y, i.e., 240 ppm in the altitude range of 100-150 km and the EUV*2 shows a decrease of 160 ppm compared to EUV*1 on the event day, January 22nd. Above 150 km, for the same day, there is a decrease of 160 ppm for EUV/2 and an increase of 260 ppm for EUV*2. Down-welling of 40 ppm is observed for all cases below 100 km. Calculating the significance for the EUV impact using:

$$\text{Significance} = \left| \frac{\text{Ensemble mean (EUV/2, EUV*2)} - \text{Ensemble mean (EUV*1)}}{\text{Standard error (EUV*1)}} \right| \tag{6.1}$$

where N is the number of ensembles and standard error is:

$$\text{Standard error} = \frac{\text{Standard Deviation of ensembles}}{\sqrt{\text{N}}} \tag{6.2}$$

where $\sigma \geq 3$, means the change is significant and $\sigma \leq 3$ means not significant. Figure 6.13 shows the absolute differences of EUV/2 and EUV*2 w.r.t. EUV*1 in the top and bottom rows respectively. Along the columns is the reference run, day 2 with low activity and day 3 with geomagnetic storm. Above 150 km, NO_y decreases by 25 ppmv for the entire time period for all the particle forcings for EUV/2. Around 150 km, NO_y increases by 25 ppm. For EUV*2, NO_y increases by 25 ppm. And below 150 km, NO_y decreases by 25 ppm. And between 50-100 km, a down-welling of 5 ppm is seen for both EUV cases and all the particle cases, which, is quite significant. With five ion-chemistry, from figure 6.14 instead of small structures of increased NO_y, a continuous increase around 150 km and a decrease of 25 ppm above 150 km for EUV/2. For EUV*2, around 150 km, NO_y decreases by 25 ppm that appears as a layer. ΔNO_y for EUV/2 and EUV*2 is anti-correlated in the thermosphere.

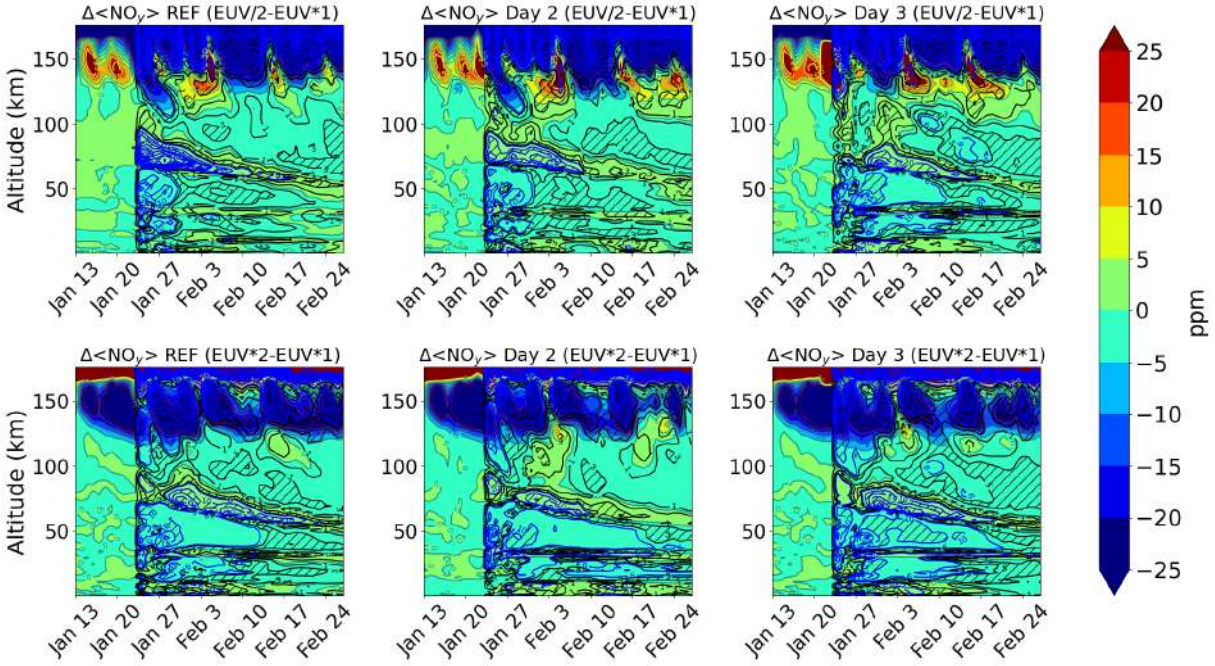

Figure 6.13: Absolute differences of NO_y for different EUV forcings (column-wise: Reference, Day 2 and Day 3) w.r.t. EUV*1 (row-wise: EUV/2 and EUV*2) for free-running (F.R.) ensemble means. The blue lines denote significance, $\sigma \geq 3$ and the black lines denote $\sigma \leq 3$. The significance is not plotted for SEM < 0.1.

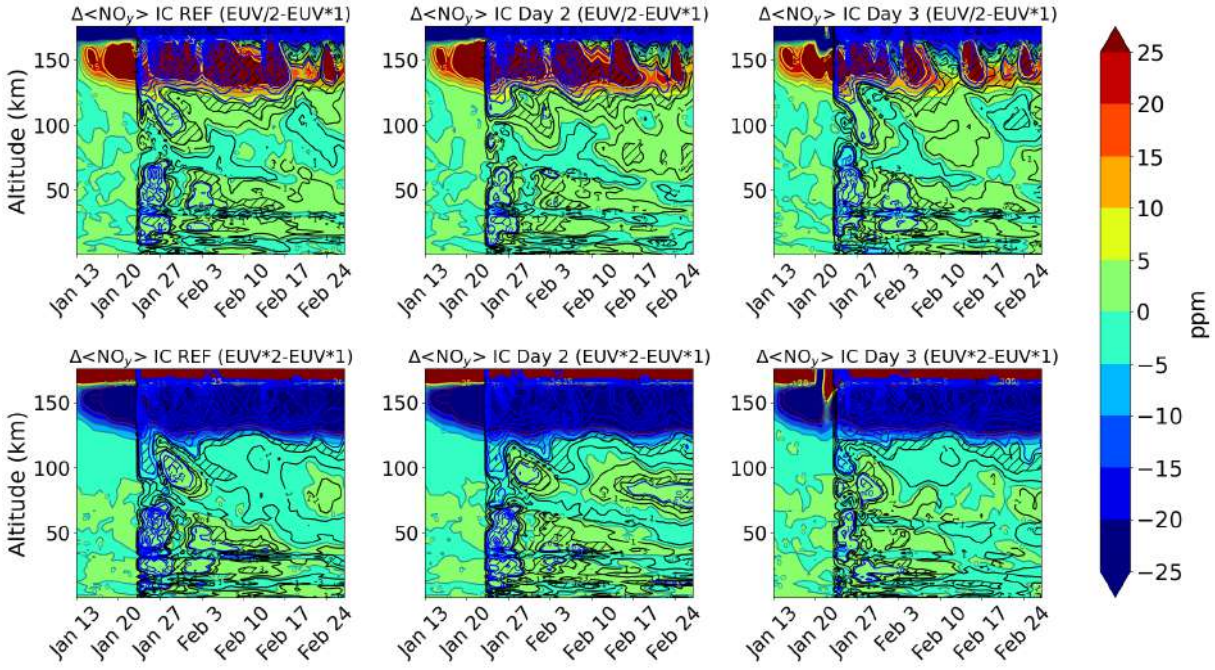

Figure 6.14: Absolute differences for the EUV impact of the ensemble means for the three cases with AISstorm ionisation rates, Day 2 with low activity and day 3 (extreme geomagnetic storm) with five ion-chemistry. The blue lines denote significance, i.e., $\sigma \geq 3$. The black lines denote $\sigma \leq 3$.

Instantaneous NO_y enhancements of a 1000 ppm was observed on the event day for day 2 and 10000 ppm for day 3 for both specified dynamics (S.D.) and free-running (F.R.) ensemble means as seen from figure 6.15. The production of NO_y is higher on the day of the event and decreases afterwards. Higher production of NO_y i.e., N and NO is observed for the geomagnetic storm (GMS). Down-welling is observed at 100 km for day 2, and lower EUV corresponds to higher NO_y and the impact of NO_y on the SSW is higher. NO_y increase after the event is seen for day 2 which is due to background NO. 10000 ppm of NO_y was produced during the event for the geomagnetic storm for both specified dynamics and free-running ensemble simulations. For day 2, the NO_y produced is lower compared to day 3. Larger down-welling upto $\sim$ 100 km is observed for the lowest EUV forcing. Figure 6.16 shows the differences of the particle forcings with specified dynamics and ensemble means with five ion-chemistry. Due to more background NO, there is more NO_y produced after the event for day 2 and day 3 for both specified dynamics and free-running with EUV*2 and EUV*1. For EUV/2, that increase was not seen.

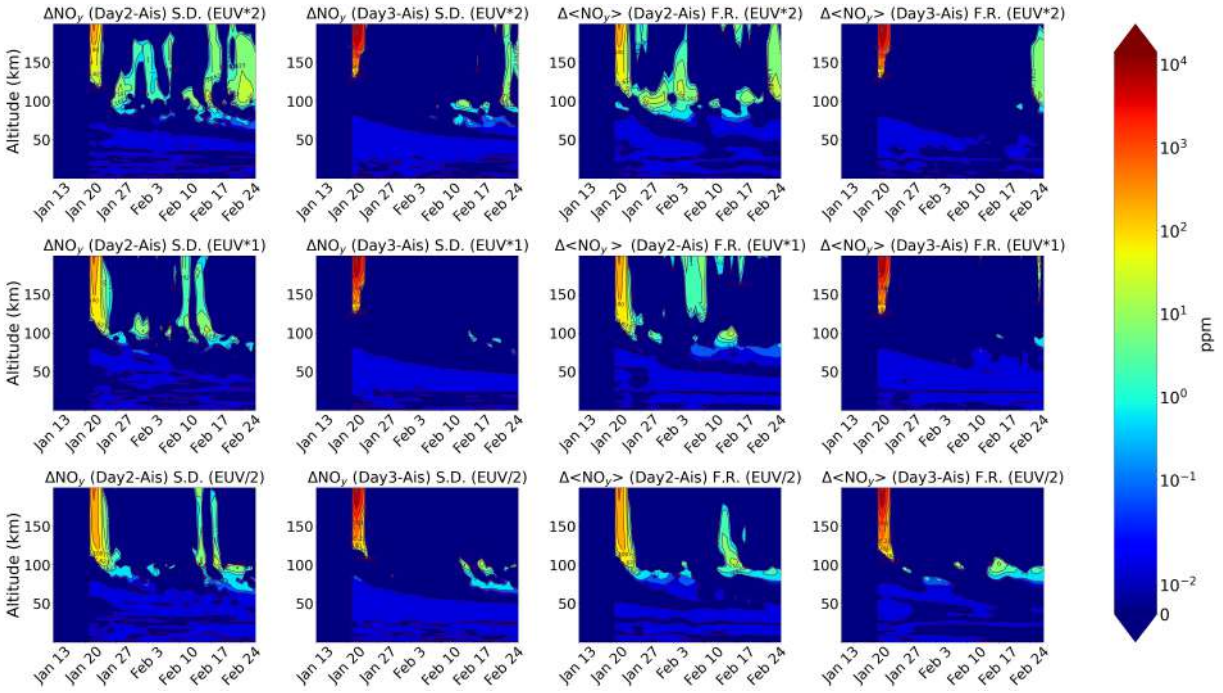

Figure 6.15: Absolute differences of total NO_y for different particle forcings (column-wise: Day 2 and Day 3) w.r.t. reference run (with AISstorm) for specified dynamics (S.D.) and free-running (F.R.) ensemble means for EUV*2, EUV*1 and EUV/2 (row-wise).

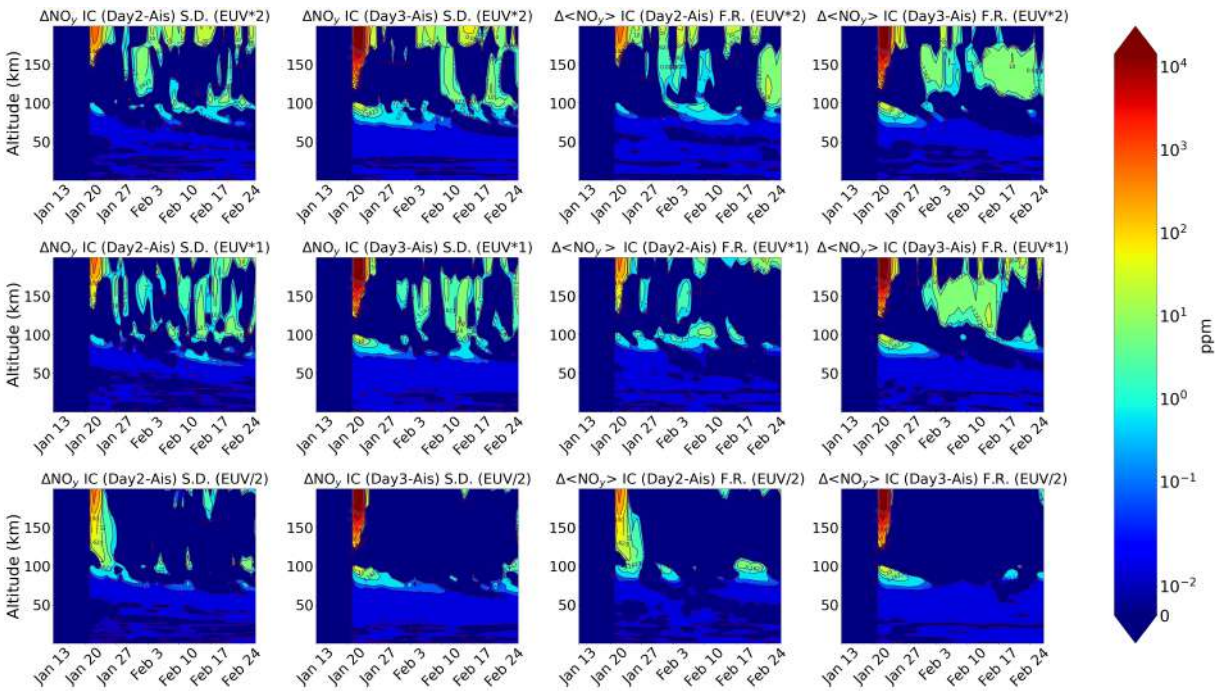

Figure 6.16: Same as figure 6.15 but with five ion-chemistry.

6.3.2 Ozone

Figure 6.17 shows the daily mean ensemble mean for ozone that is zonally averaged over 70-90°N. The differences among the cases are not too high. After the event starts on the 22nd of January, ozone enhancements of $\sim$ 7 ppm are observed which continues until February 3rd. Above 75 km, there is O_3 production of 2.0 ppm in all cases due to enhanced down-welling of O from the thermosphere. Figure 6.18 show the daily mean ensemble mean for ozone that is zonally averaged over 70-90°N with the five ion-chemistry. It doesn't show too much of a difference to figure 6.17. Around 25-50 km, upto 7 ppm of ozone is found during the event.

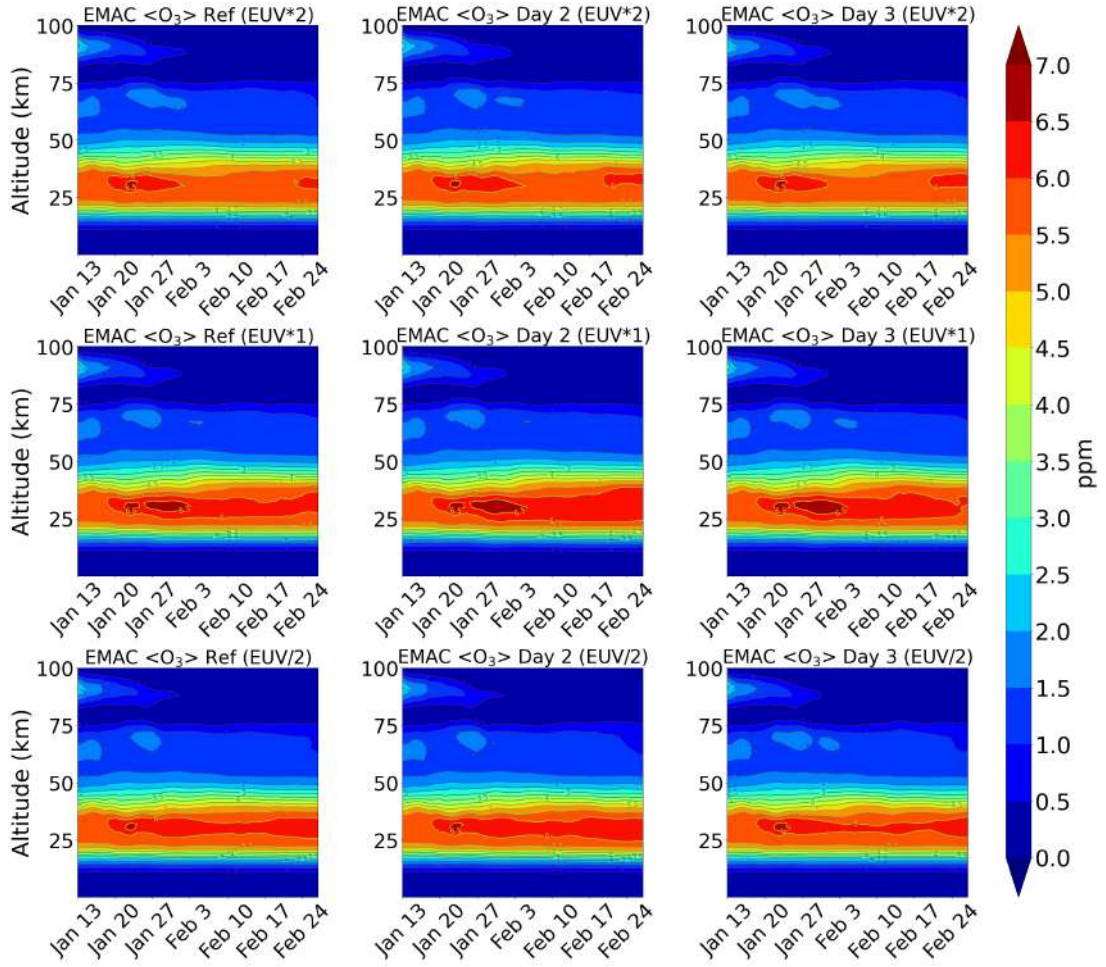

Figure 6.17: Same as figure 6.9 but for ozone.

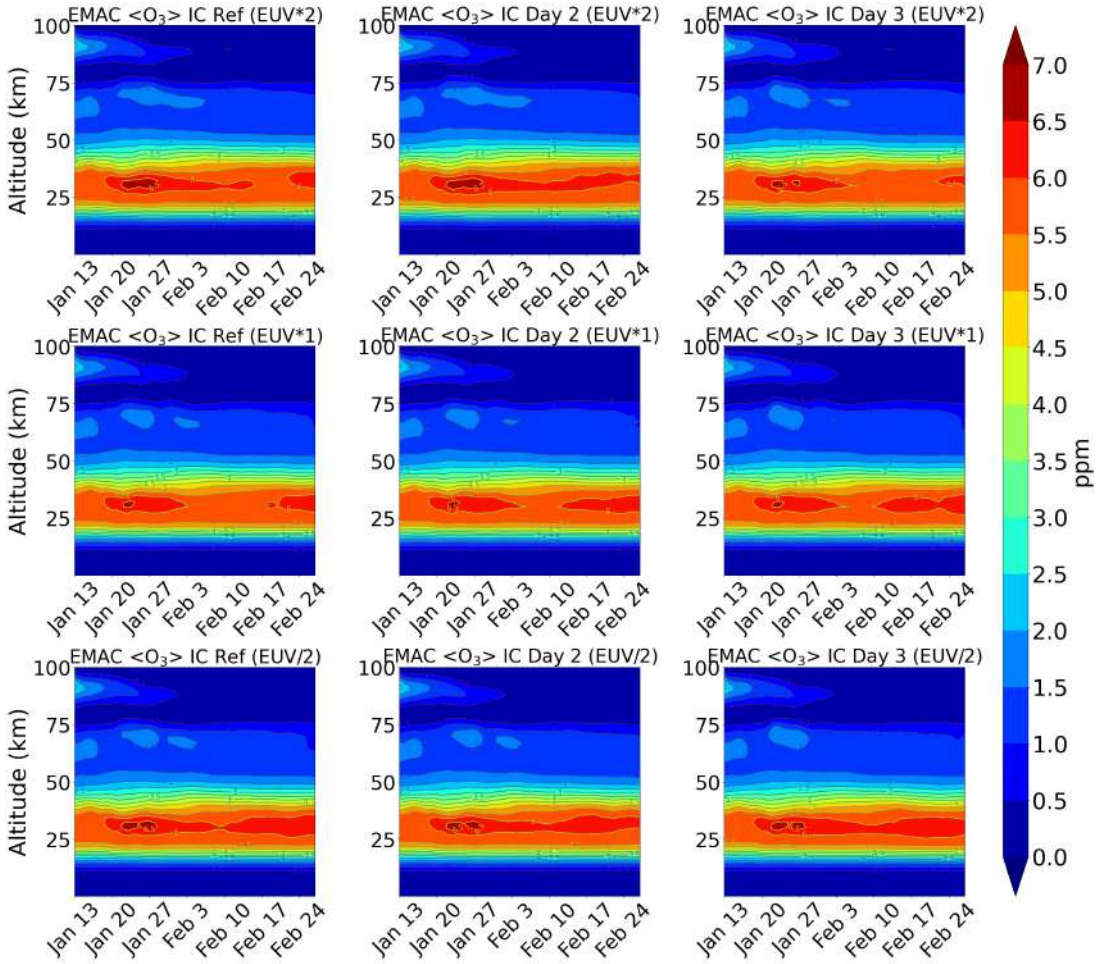

Figure 6.18: Same as figure 6.17 but with five ion-chemistry.

Figure 6.19 shows the difference of parameterised NO_x w.r.t. five ion-chemistry. Below 50 km, there is a difference in all cases. There is an increase of 0.4-0.6 ppm after January 27th and 1.2 ppm after February 10th at 50 km. For EUV/2, there is an increase of 0.2 ppm below 50 km which appears for day 2 and disappears for the geomagnetic storm for day 3.

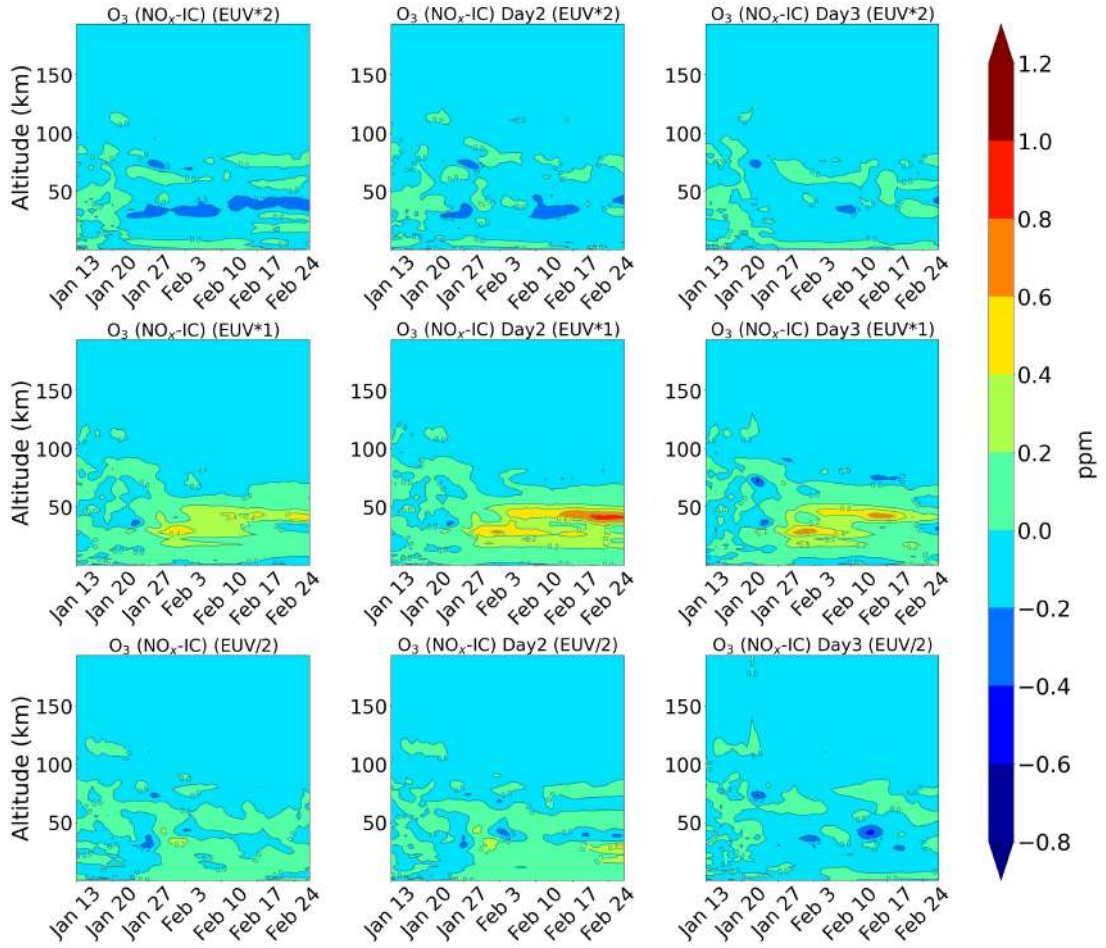

Figure 6.19: Absolute differences of total O_3 for the parameterised NO_x w.r.t. five ion-chemistry.

EUV impact and particle impact

The EUV impact is calculated through equation 6.1. From figure 6.20, the impact of EUV is seen. So, ozone loss of 5-10% is seen at 25-50 km for the reference run after January 27th which continues until February 24th at 50 km. This is also seen for day 2 and day 3 which appears below 25 km as well and is more pronounced. Ozone enhancements upto 45% are seen around 100 km for EUV/2, after February 3rd for the reference run, and also for Day 2 and Day 3. For EUV*2, above 100 km, enhancements of 45% were found for the entire duration which appears as a layer. This layer seems to suggest a dynamical feature rather than a direct impact of the EUV ionisation. This layer forms due to the dissociation of O_2 by the extreme ultra-violet, so less EUV means less O_2 and less O and therefore, less O_3. This is mainly above 90 km but dissociation of O_2 by EUV above is not so efficient below. Below 70 km, after January 22nd, there is ozone loss observed, which is higher for higher EUV and higher particle forcings. Below 25 km, there is some loss of ozone observed, which might be related to polar stratospheric clouds. Figure 6.21 shows the EUV impact for ozone with five ions. Ozone increase of 25-45% is observed on the event day at 80-100 km for EUV/2 and then a loss of 15-35% afterwards, which increases afterwards and then

decreases again. In case of EUV*2, ozone decrease of $\sim$ 15-25% is found above 100 km for the entire time period. For the geomagnetic storm, on the day of the event, ozone decrease is observed from the top of the atmosphere which goes down to 55 km. For EUV*2, a decrease of 15-25% of O_3 is also found after February 3rd at 80 km. After the SSW event, on January 27th, there is an increase of 45-65% which decreases to 55% afterwards. Above 100 km, an increase of 25% for EUV*2 is found which appears as a layer. At 75 km and below, 5-10% increase is seen which is anti-correlated to what was observed for parameterised NO_x.

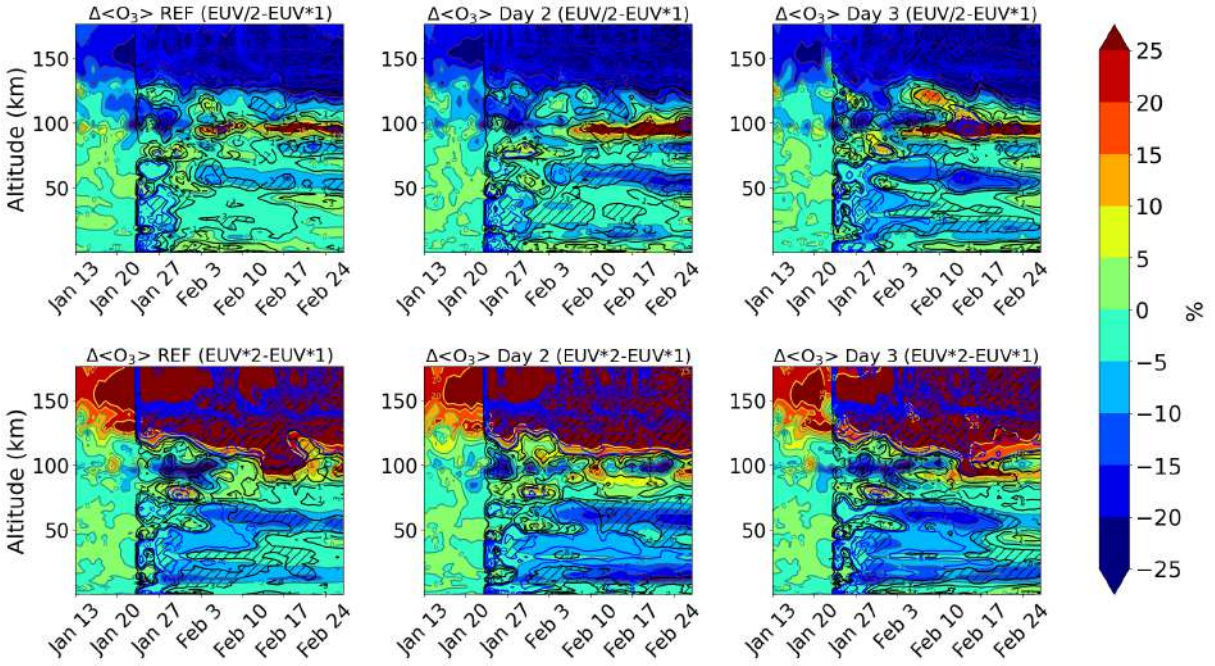

Figure 6.20: Percentage differences of EUV forcings (row-wise: EUV*2 and EUV/2) for O_3 for the different particle forcings (column-wise: reference, day 2 and day 3) w.r.t. background EUV for free-running (F.R.) ensemble means. The blue lines denote significance, i.e., $\sigma \geq 3$. The black lines denote $\sigma \leq 3$. The significance is not plotted for SEM < 0.1

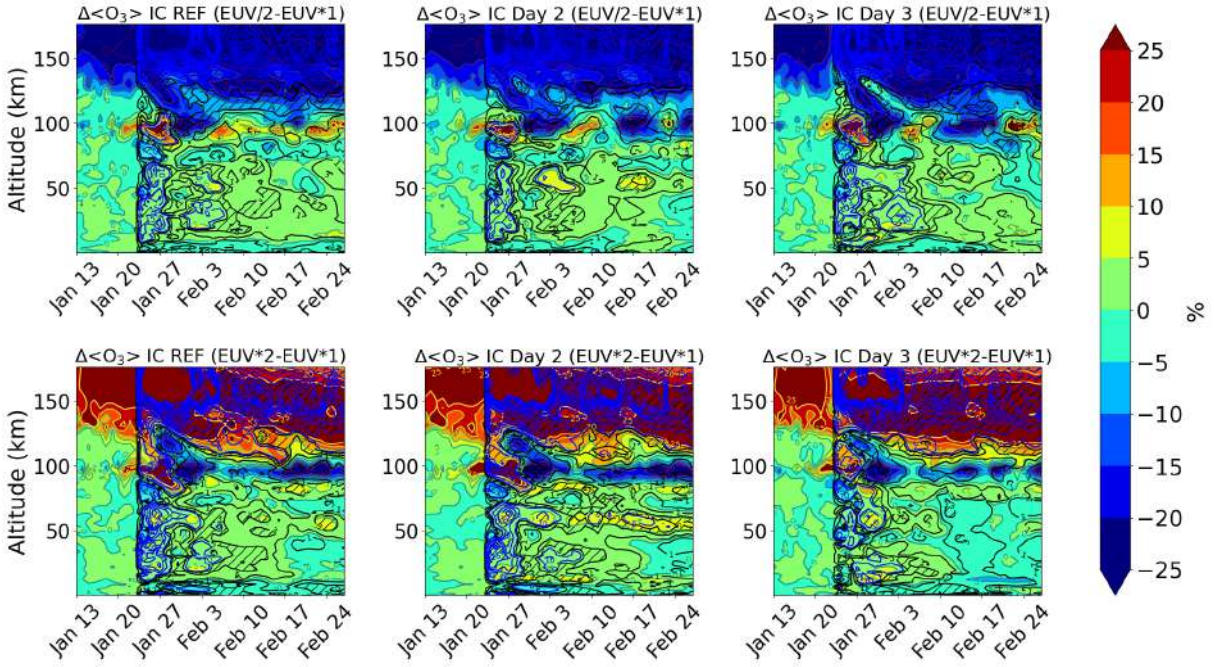

Figure 6.21: Same as figure 6.20 but with five ions.

Figure 6.22 shows percentage differences of ozone to look at the particle impact. For specified dynamics, there is a 15% increase of O_3 for both day 2 and day 3 on the event day for EUV*1. And 35% increase for EUV*1 and 65% increase for the lowest EUV, EUV/2 on the event day which propagates down until 100 km as seen for both specified dynamics (S.D.) and the free-running ensemble means. This is again due to the dissociation of O_2 by the ionisation, which then leads to enhanced O_3 formation. There's a ozone layer at 75 km with 25-35% of ozone and 35% decrease after February 10 which is seen for day 3. There is a secondary peak after the SSW with 25% ozone increase until February 3rd from 125 km upto above which was seen in both specified dynamics (S.D.) and in free-running (F.R.) ensemble mean for EUV*1 and EUV/2. In case of specified dynamics (S.D.), ozone production of 5-15% continued until February 24, whereas for free-running (F.R.) ensemble mean, this production stopped on February 10th. There's also some ozone loss (5-25%) produced around 75-100 km for day 3 and for the lowest EUV. This increases to 55% after February 10th. This is due to the transport of atomic oxygen at 75 km. Figure 6.23 shows the particle impacts with five ions. For day 3, with specified dynamics, the ozone loss during the event day, is 35%. With decreasing EUV, ozone formation occurs during the event which increases below 100 km. There is ozone produced around 75 km for the entire time period. And the ensemble means show the same. Ozone forms at a lower altitude which is stronger with lower EUV. Continuous ozone formation of 5-15% until February 10 is seen after the event day above 125 km for day 3 with EUV/2 and around 100 km, 5-15% loss of ozone is seen. There is a secondary peak observed for the ensemble mean. There is a decrease of 35% observed at 100 km and below which is more pronounced for the ensemble mean and with lower EUV and higher particle forcing. This difference wasn't captured by the specified dynamics which means there is a dynamical feedback captured only by the free-running.

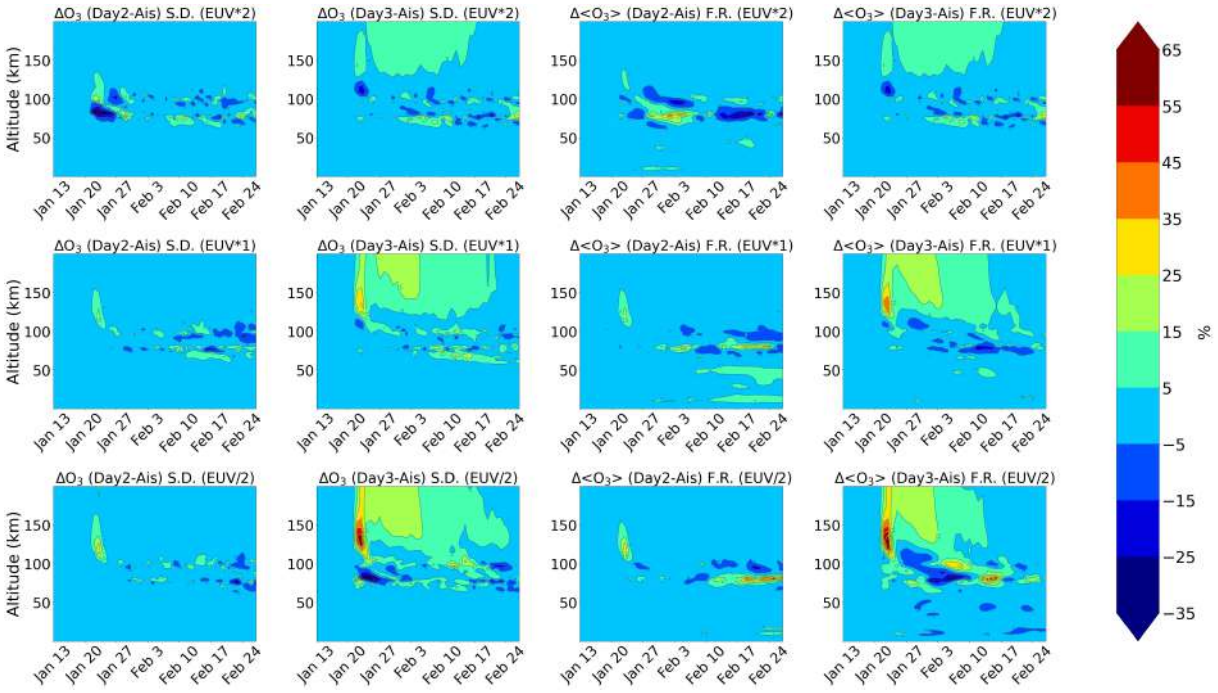

Figure 6.22: Absolute differences of ozone for different particle forcings (column-wise: Day 2 and Day 3) w.r.t. background for specified dynamics (S.D.) and free-running (F.R.) ensemble means for EUV*2, EUV*1 and EUV/2 (row-wise).

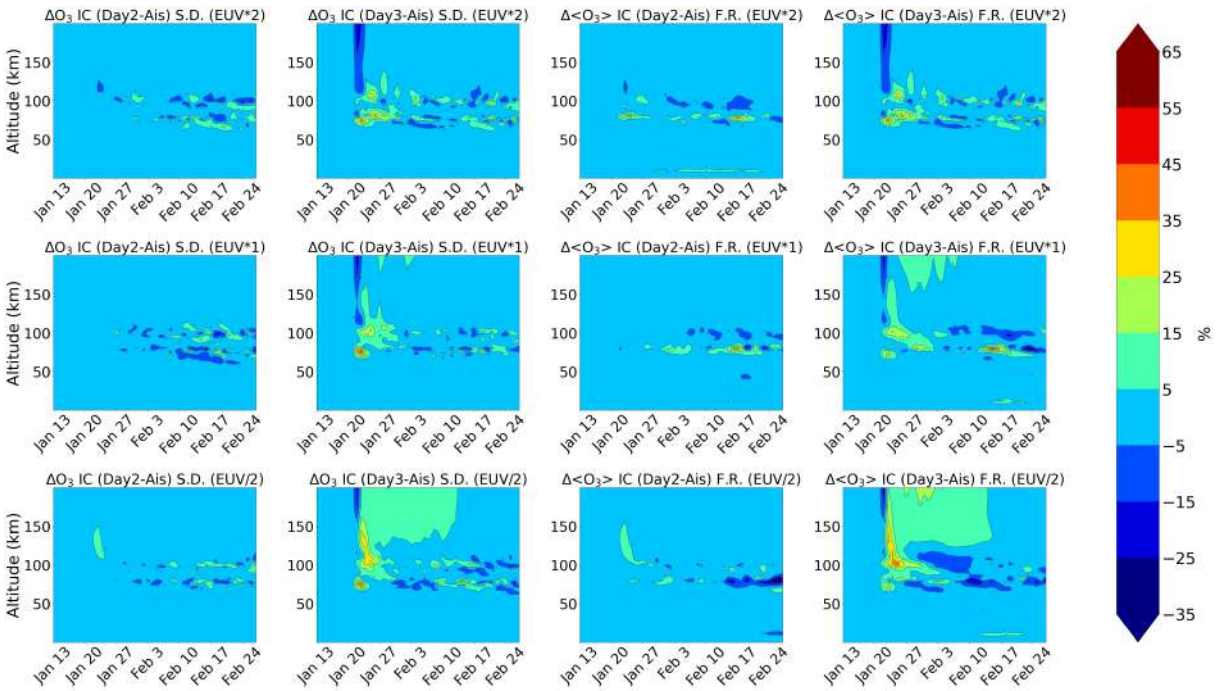

Figure 6.23: Same as figure 6.22 but with five ion-chemistry.

6.4 Dynamical feedback from chemistry

6.4.1 Temperature

Figure 6.24 shows 20 different ensemble members generated from EMAC with the different temperature perturbations. Although temperature is not a tracer for vertical motion, during strong descent, changes are observed in the thermal structure due to adiabatic warming. The elevated stratopause (ES) is observed on February 3rd for most ensembles and then the altitude stays constant afterwards. For ensemble 1, the elevated stratopause (ES) went down to its original climatological height after February 17. After the polar vortex reformation, the temperatures increase and the onset of this increase varies across the ensembles. MIPAS observations showed the elevated stratopause around February 1st for the January 2009 event at a much higher altitude (Funke et al., 2017).

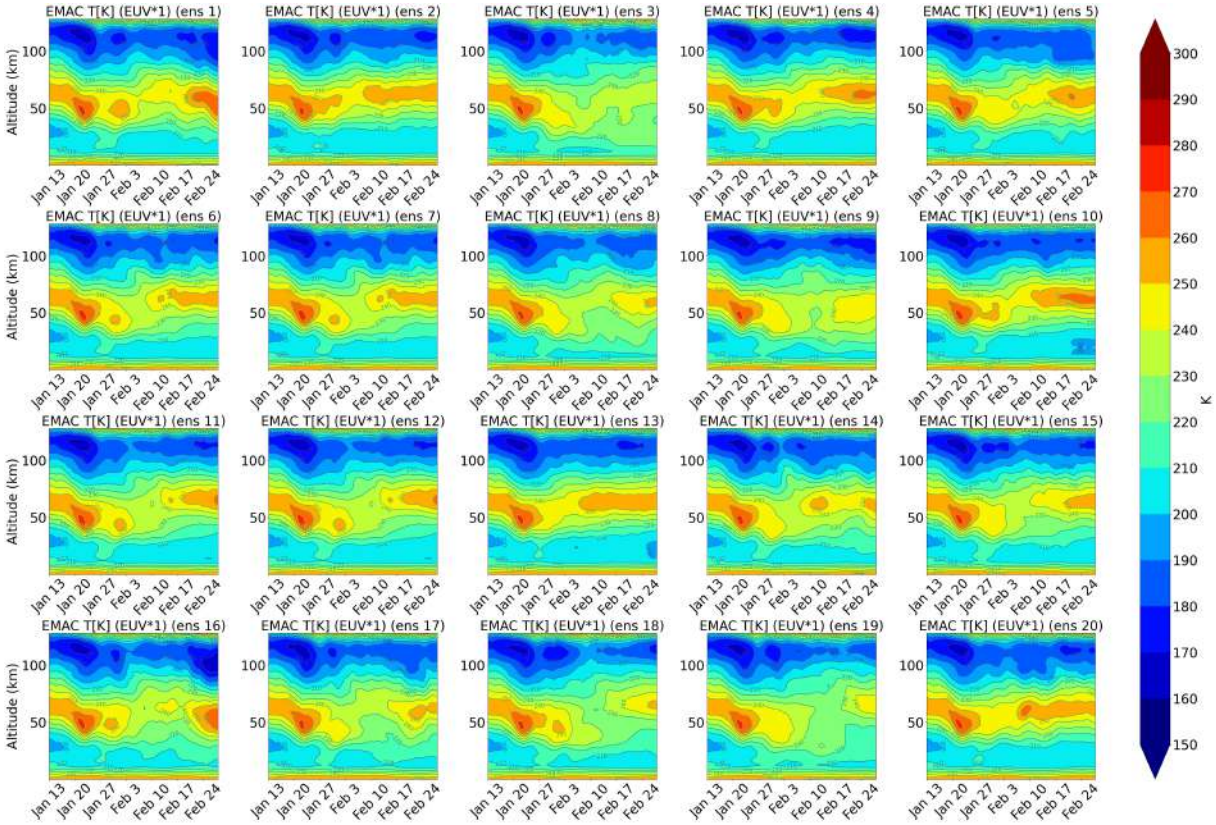

Figure 6.24: 20 different ensemble members of temperature zonally averaged over 70-90°N calculated for the geomagnetic storm (Day 3) and EUV (EUV*1): Free-running (F.R.) simulations calculated with a NO_x based parameterisation.

Figure 6.25 shows the mean of the ensembles for the different forcings, i.e., EUV and particle forcings. For EUV*2, the elevated stratopause (ES) starts on January 27th and goes on until February 3rd and stays at a constant height afterwards until February 24th. An increase in temperature of 250 K after the elevated stratopause (ES) is observed on February 3rd that continues until February 24th as well. Mesospheric cooling is observed for all the cases, background, Day 2 and Day 3. The elevated stratopause looked

similar for EUV/2, i.e., ascended on January 27th until February 3rd and stayed at a constant height afterwards. The temperature increases upto 250 K for EUV*2 and EUV/2 after February 3rd at 50 km. For EUV*1, temperature increase of 220 K is observed below 25 km after 2-3 the event. The elevated stratopause (ES) begins on January 27th but the temperature increase of 250 K was found way later. The temperature increased to 260 K after February 3rd for EUV*2 at 50 km. For EUV/2 as well, increase of 260 K is observed after February 10. However, for EUV*1, the temperature increases by 260 K after February 17th. Figure 6.26 shows the ensemble means due to five ion-chemistry. The temperature increase upto 220 K below 25 km doesn't show up with five ions. The temperature increase here starts earlier compared to the results with parameterised NO_x on February 3rd for EUV*1. The EUV*2 and EUV/2 with five ions doesn't show too much of a difference.

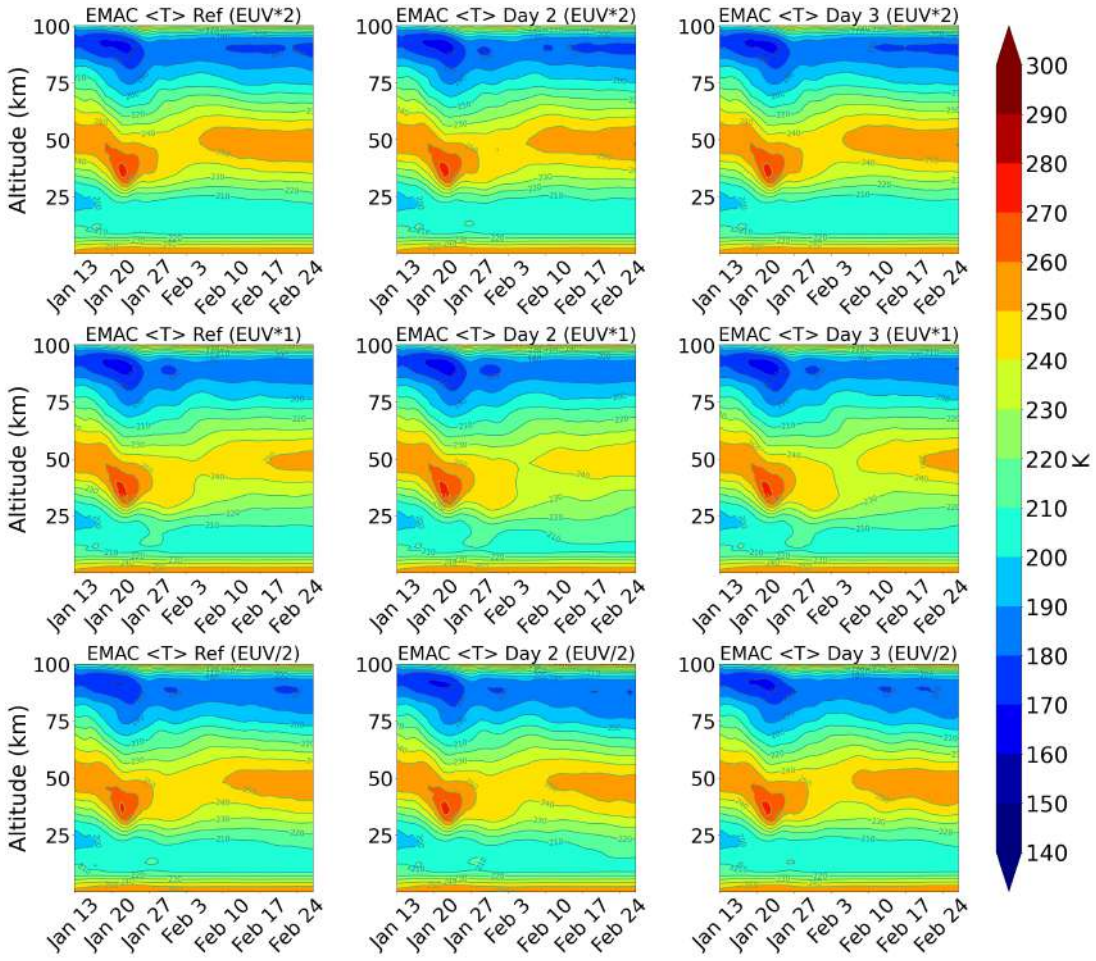

Figure 6.25: Mean of 20 different ensemble members for temperature zonally averaged over 70-90°N calculated for the reference (AISstorm), day 2 with low activity and the geomagnetic storm (Day 3) for all the EUV forcings and particle forcings with the NO_x based parameterisation.

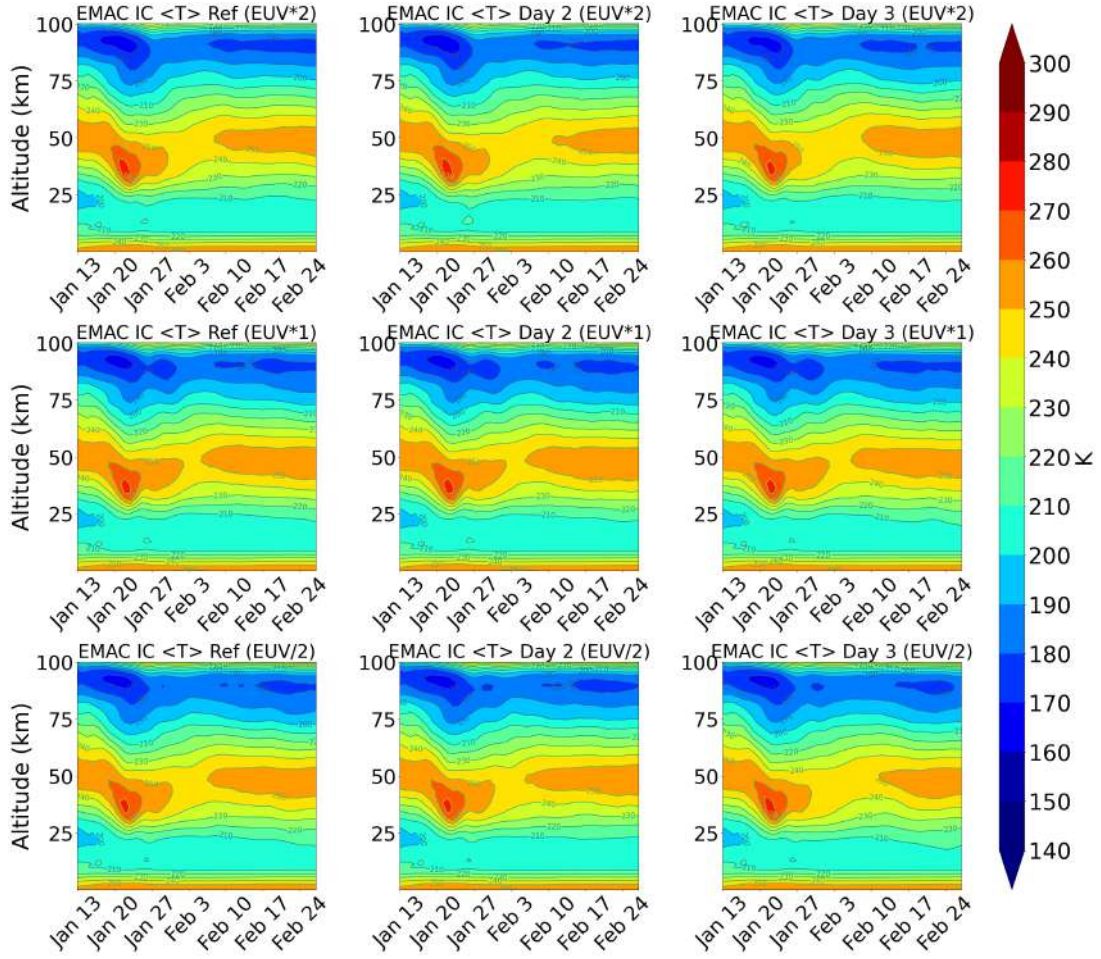

Figure 6.26: Same as figure 6.25 but with five ion-chemistry.

EUV and particle impact

The EUV impact for temperature shows maximum increase for both the particle forcings, i.e., the day with low activity (Day 2) and the geomagnetic storm (Day 3) which is around 12 K for both EUV/2 and EUV*2 in the stratosphere and lower mesosphere around 50-75 km as seen from figure 6.27. Temperatures more than 25 K is observed above 150 km for EUV/2. There is a temperature decrease at 100 km, from February 17th for all the three particle forcings. Above 50 km, in the stratosphere after January 27, a temperature increase of 5-10 K is seen which is until February 3rd for the reference run. For day 2, the temperature increase continues and increases after February 17th upto 25 K. In case of the geomagnetic storm, the temperature increases after January 27th by 10-15 K. Below 50 km, the temperature decreases and goes down to 20 K after January 27. Temperatures below 50 km decrease until February 10th and the decrease is the most for the geomagnetic storm until February 5th. With EUV*2, in the thermosphere, above 150 km, the temperature decreases by 25 K. In the stratosphere, between 50-100 km, there is a 10-15 K increase and that increases by 25 K on February 3rd. Basically, temperature increase is higher for higher particle forcing. Below 50 km temperature decreases by 25 K after the

event and is more pronounced and continues over time. This can be related to ozone loss below 50 km as seen above. Temperature decreases above 125 km as a layer for the entire time period. There is a temperature decrease observed at 100 km after February 10th. Figure 6.28 shows an increase in temperature upto 25 K above 150 km for EUV/2 and decrease in temperature upto 25 K. For the geomagnetic storm, at 150 km, for EUV*2, on the day of the warming, there is a sharp decrease until 50 km. With the ion-chemistry, the structures of increase and decrease are not as pronounced as the NO_x based parameterisation. Higher EUV in the thermosphere tends to lower temperatures, presumably due to higher NO and radiative cooling. Anomalies after the event in 30-100 km likely show a dynamical feedback to ozone. These anomalies are quite significant in most cases. The changes in the middle atmosphere are similar for EUV*2 and EUV/2 cases, while they are anti-correlated in the thermosphere.

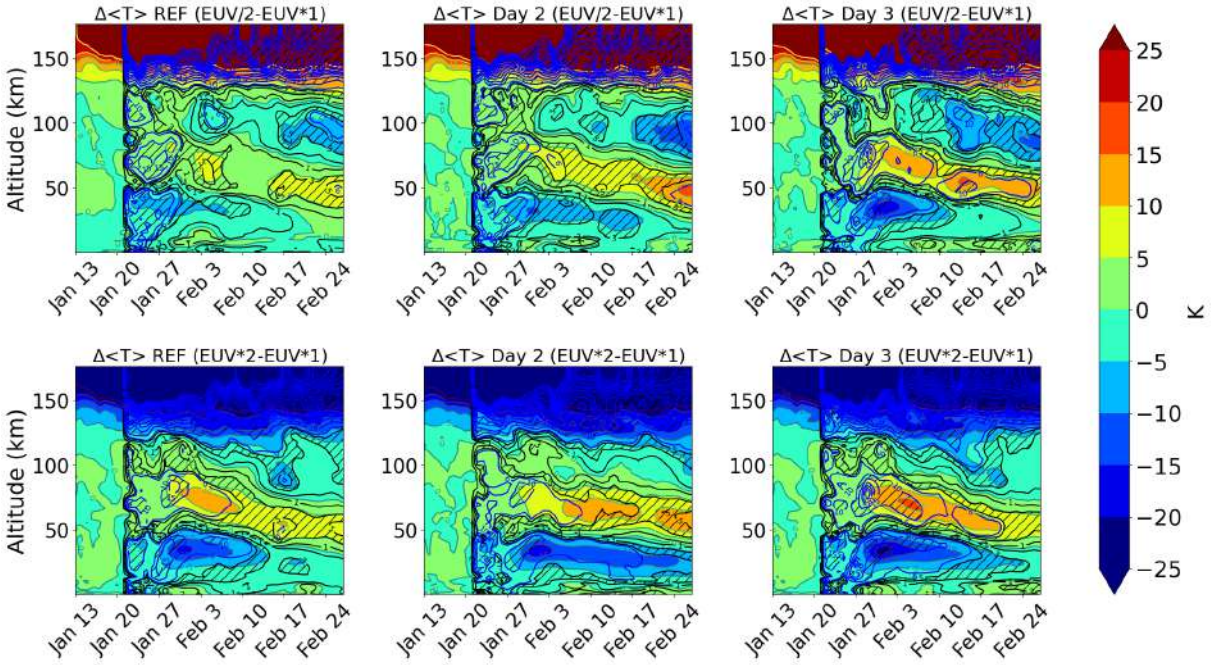

Figure 6.27: Same as figure 6.13 but for temperature.

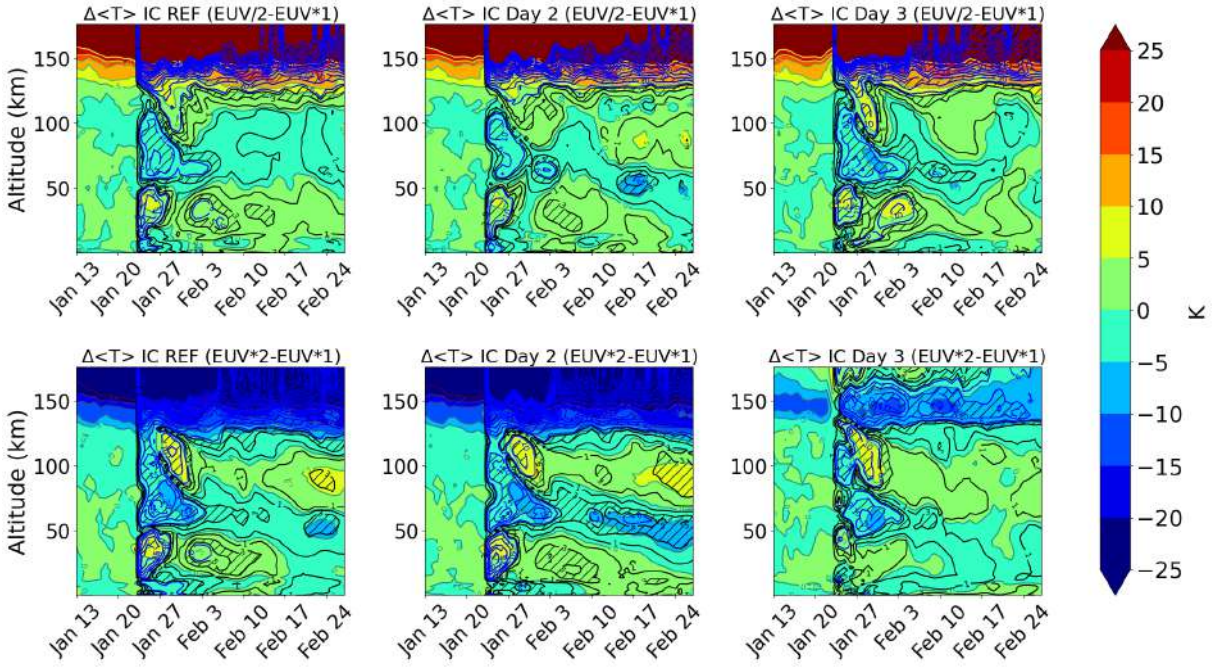

Figure 6.28: Same as figure 6.13 but with ion-chemistry.

The impact from the different particle forcings can be seen from figure 6.29 for both the days and for specified dynamics (S.D.) and free-running (F.R.) ensemble means. For day 2, a very small decrease of 5-10K is observed on the day of the event for both specified dynamics (S.D.) and free-running (F.R.) ensemble mean. For day 3, there is a sharp decrease in temperature on January 22nd. Cooling effect is observed with decreasing EUV. For EUV*2, there is a decrease of 10K, 30K for EUV*1 and 50K for EUV/2. And an increase of 10K around 100 km, observed for EUV*2. Another secondary peak is also seen for EUV*1 and EUV/2 in the MLT region for both specified dynamics and free-running ensemble means. Figure 6.30 shows particle impact with the five ions. With lower EUV forcing, the cooling peak appears to be stronger and this cooling continues above 150 km which is seen for both specified dynamics and the ensemble mean. Figure 6.31 shows the difference of the parameterised NO_x model w.r.t. five ion-chemistry for temperature. The temperature for all EUV and particle forcings decreases when the ion-chemistry is on. Above 125 km, in the thermosphere, there is a layer of increased temperatures of 75-85 K and a peak of 115 K. For day 3, on the event day, there is a decrease of temperature $\sim$ 5 K above 100 km.

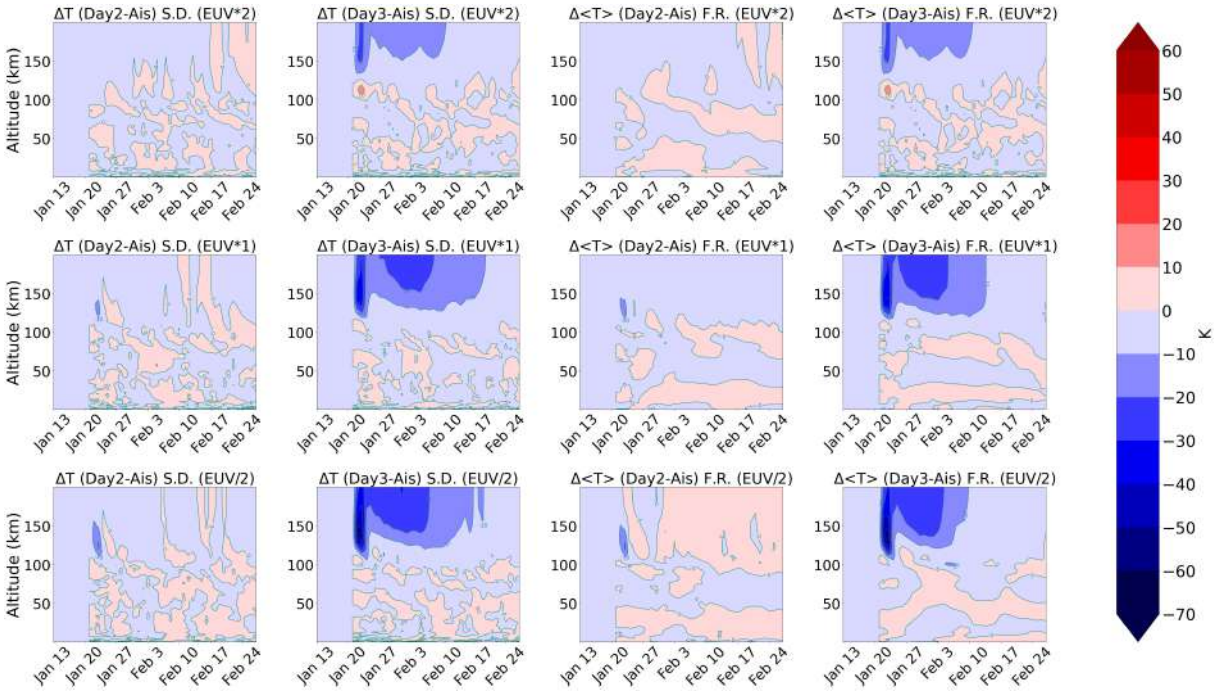

Figure 6.29: Absolute differences of temperature for different particle forcings (column-wise: Day 2 and Day 3) w.r.t. background for specified dynamics (S.D.) and free-running (F.R.) ensemble means for EUV*2, EUV*1 and EUV/2 (row-wise).

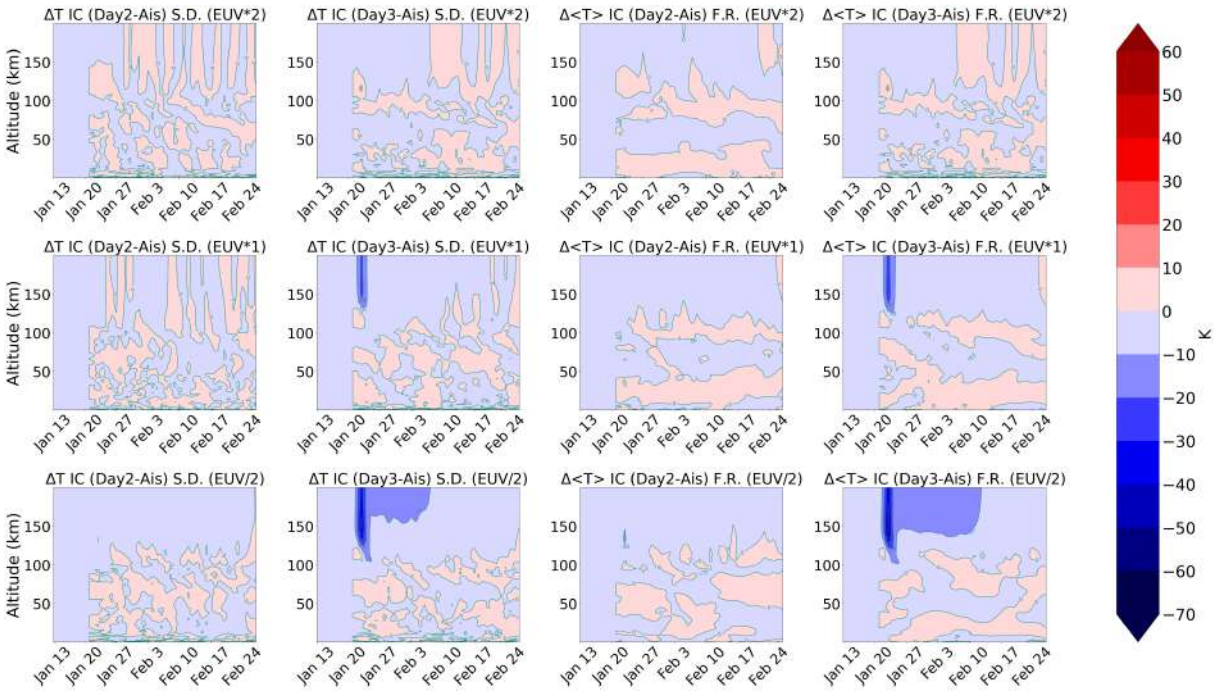

Figure 6.30: Same as figure 6.29 but with ion-chemistry.

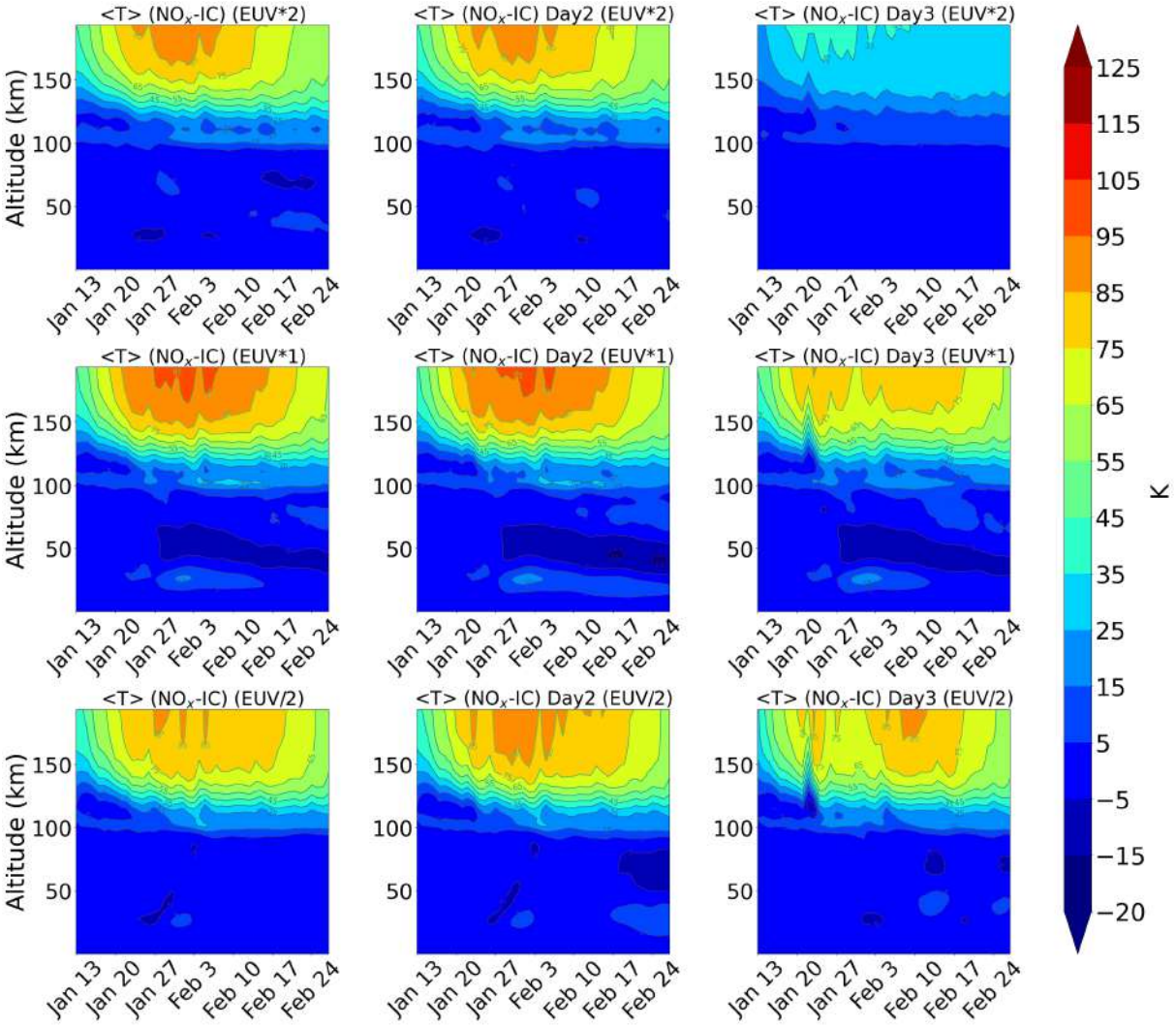

Figure 6.31: Absolute differences of temperature for the parameterised NO_x w.r.t. five ion-chemistry.

6.4.2 Zonal mean zonal wind

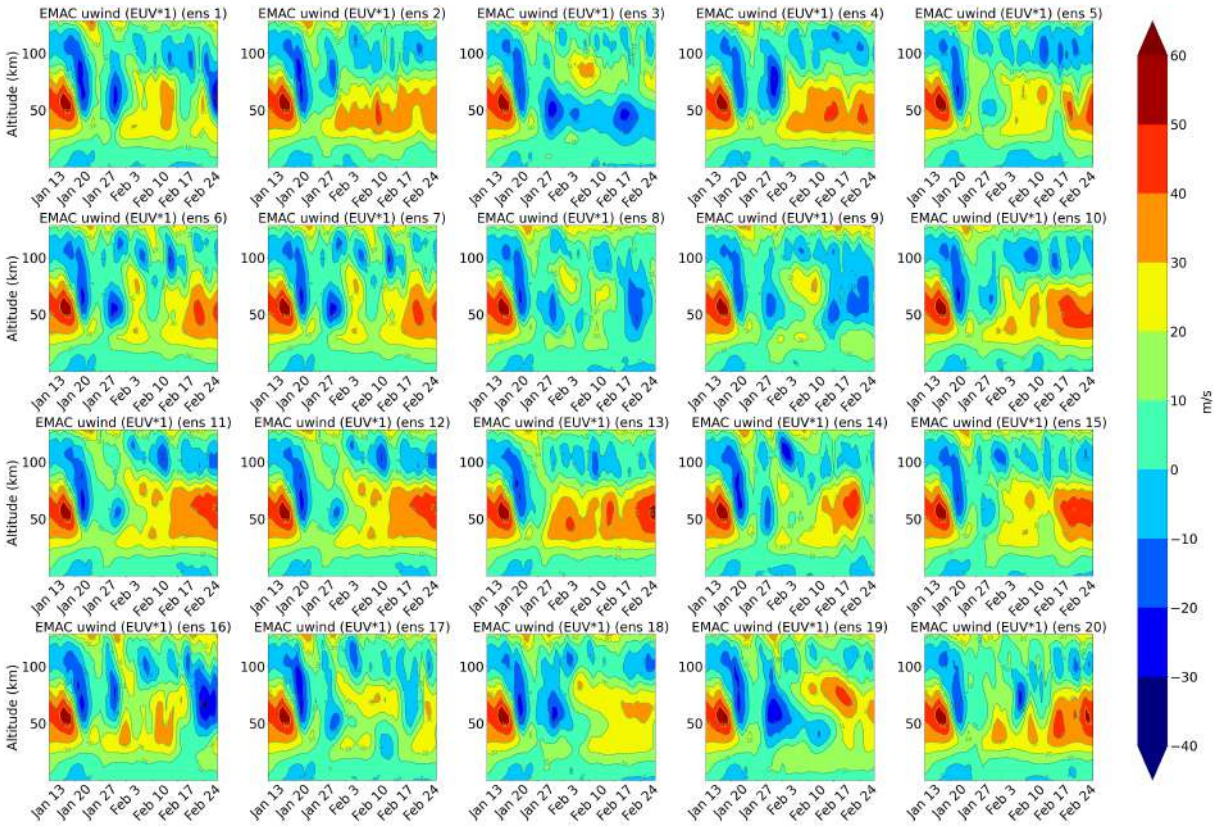

Figure 6.32: An example of 20 different ensemble members of zonal mean zonal wind zonally averaged over 70-90°N calculated for the geomagnetic storm (Day 3) and EUV (EUV*1): Free-running (F.R.) simulations calculated with a NO_x based parameterisation.

Figure 6.32 shows an example of 20 different ensemble members of zonal mean zonal wind averaged over 70-90°N. A wind reversal during January 22nd is seen which goes down to 50 km. And a second reversal is also seen on January 27th for most members. The zonal mean zonal wind changes direction after the SSW in the stratosphere and the mesosphere and then accelerates again. For some members, a third warming is observed on February 24 characterised by a wind reversal. The ensemble means show a wind reversal on January 22nd which goes below 50 km. A second reversal is seen on January 27th for all cases. Wind recovery is seen after January 27th for nearly all the members, sometimes upto 60 m/s. In the upper stratosphere and mesosphere, the wind has negative values and a deceleration of 5-15 m/s. That can be seen from the members and also from the ensemble mean from figure 6.33. Above 100 km, the zonal mean zonal wind accelerates to 95 m/s during the SSW and continues with the same value for the whole time series. In the stratosphere, after the reversal, the circumpolar winds decelerate compared to before the SSW but does not change direction for all EUV and particle forcings. For lower EUV, the acceleration of the zonal mean zonal wind on January 22nd above 150 km is quite high mainly for the geomagnetic storm. Below 100 km on January 20th, there is a wind reversal which continues above 50

km until February 24th. Below 50 km, the zonal mean zonal wind accelerates again to 25-35 m/s. With changing EUV, the wind acceleration is more after the wind reversal below 50 km, compared to normal EUV.

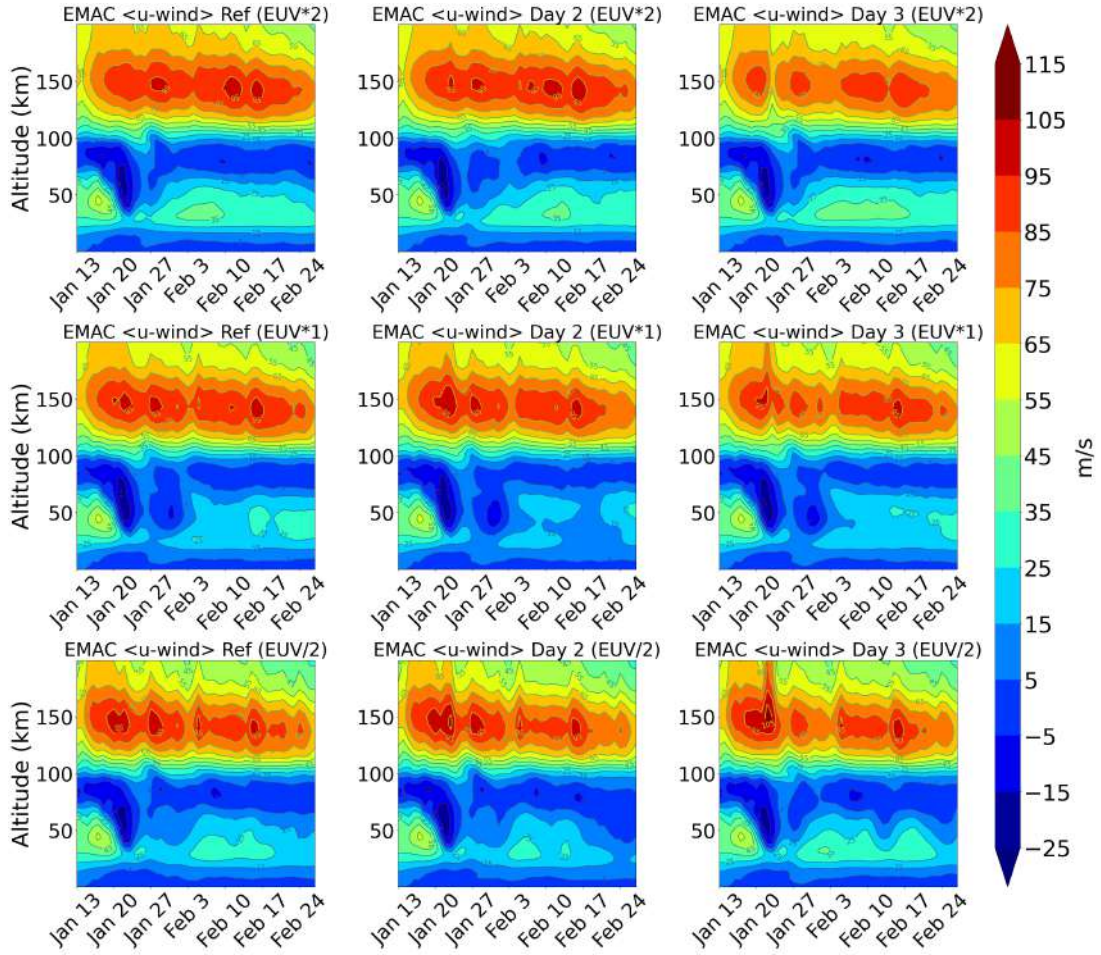

Figure 6.33: Mean of 20 different ensemble members for zonal mean zonal wind calculated for the reference (AISstorm), Day 2 with low activity and the geomagnetic storm (Day 3) for all the EUV forcings and particle forcings with the NO_x based parameterisation.

Figure 6.34 shows the ensemble mean with five ion-chemistry. The wind reversal at 100 km continues after the SSW event for all cases. Below 50 km, the wind acceleration after the reversal is higher upto 35 m/s. For day 3, above 100 km, during the event, there is a deceleration of u-wind. The wind acceleration in the thermosphere above 100 km increases with lower EUV upto 75-80 m/s whereas for the parameterised NO_x, the values appeared the same. Figure 6.35 shows the difference between parameterised NO_x and five ion-chemistry. On the day of the event, there is an acceleration of the zonal mean zonal wind for day 2 and day 3 which increases with decreasing EUV. Above 100 km, the increased zonal mean zonal wind appears as a layer which decreases with decreasing EUV for the three particle forcings. For normal EUV, EUV*1, there is a decrease below 50 km, which appears to go down to 35 m/s on January 27th and continues with time. With EUV*2 and EUV/2, the u-wind doesn't decrease below 100 km.

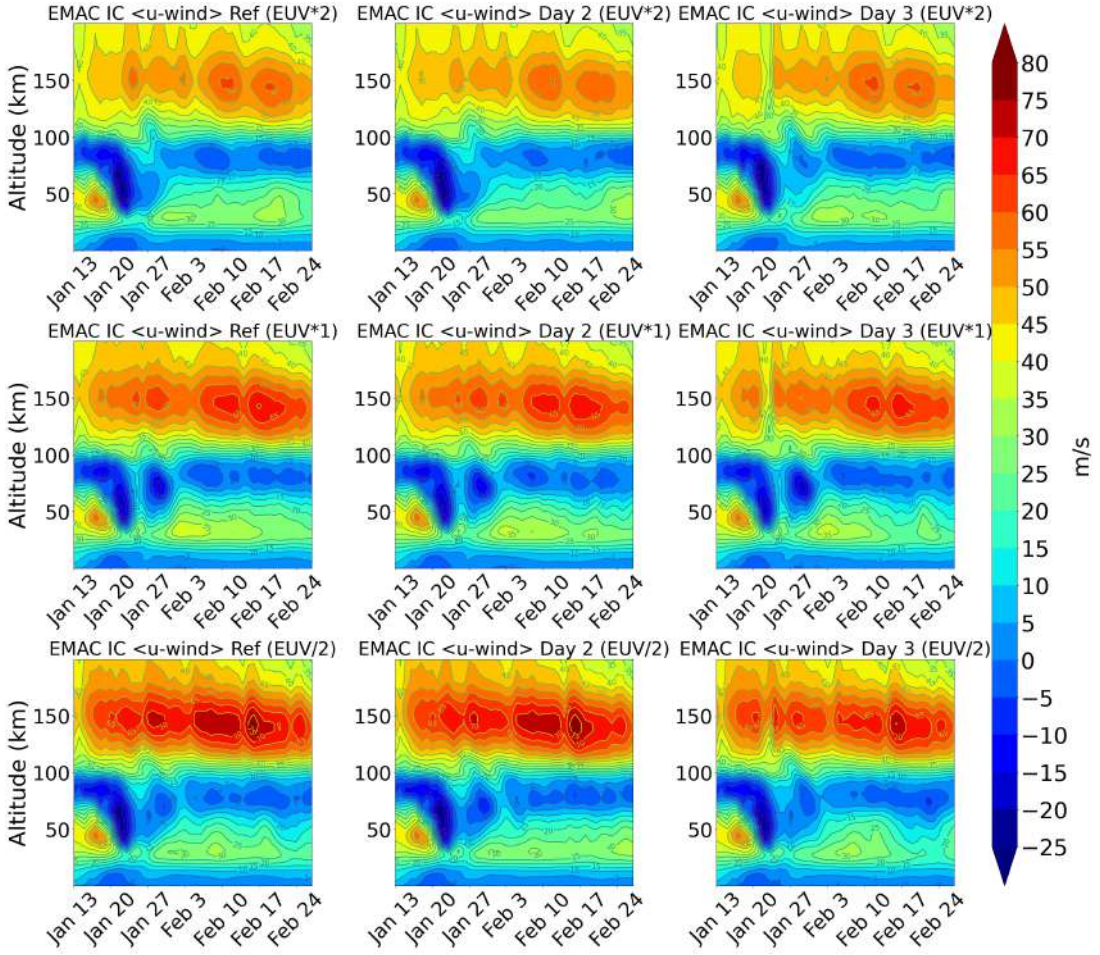

Figure 6.34: Same as figure 6.33 but with five ion-chemistry.

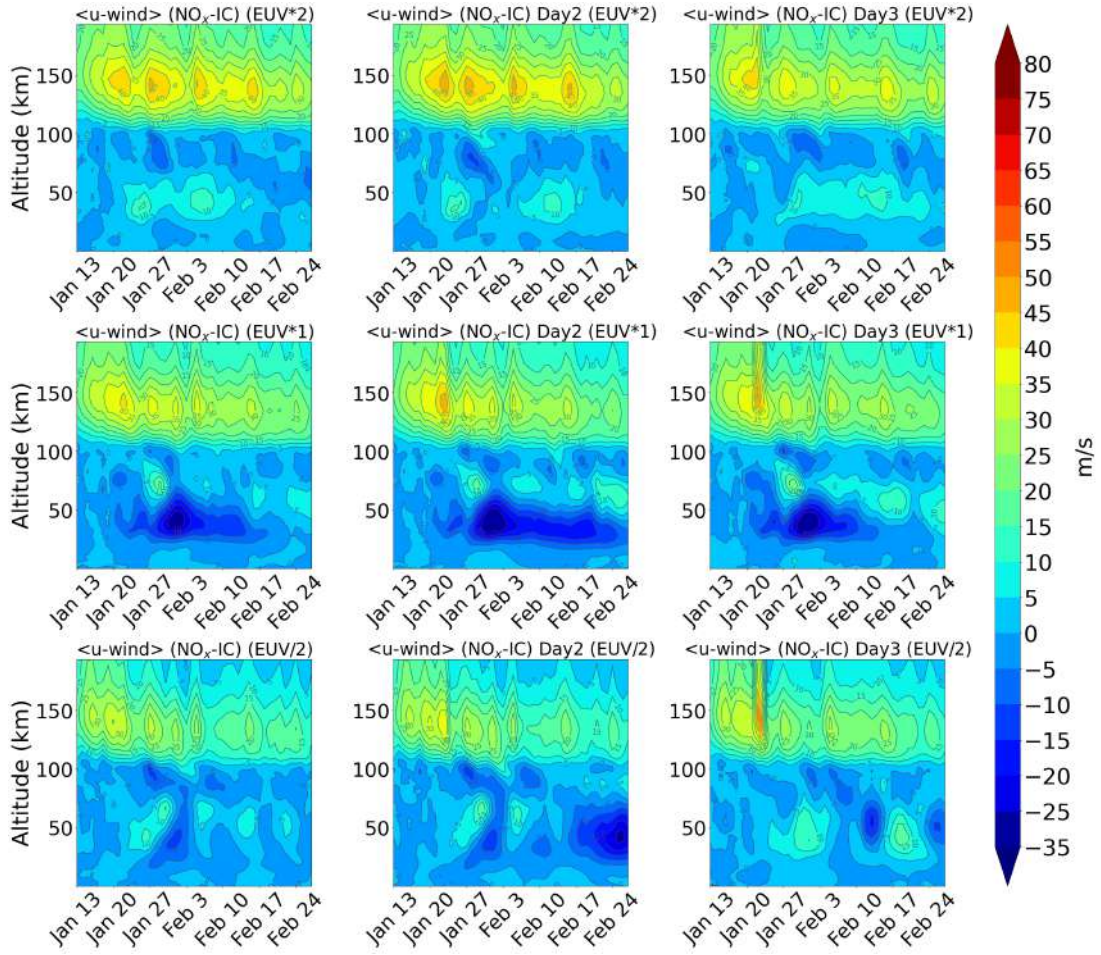

Figure 6.35: Absolute differences of zonal mean zonal wind for the parameterised NO_x w.r.t. five ion-chemistry.

EUV and particle impact

Figure 6.36 shows EUV/2 increases of zonal mean zonal wind upto 15 m/s after the SSW on January 27th over the altitude range of 25-75 km. And an increase of 10 m/s after February 3rd. After February 10th, there is an increase of the zonal mean zonal wind to 10 m/s at 25-50 km for day 2 with low activity. And after February 17th, the wind decreases by 20 m/s in the range of 25-75 km. And for day 3, after a couple of days of the SSW event after January 27th, the zonal mean zonal wind increases to more than 25 m/s over the same altitude range for the time period from January 27th to February 17th. For EUV*2, and day 2 with low activity, the increase is of 25 m/s in an altitude range of 25-75 km on January 27th with a significance of 10. For EUV*2, for all the particle forcings, after January 27th, there is an increase upto 25 m/s and 20 m/s after February 10th. For the geomagnetic storm, on the event day at 150 km in the thermosphere, there is an increase of 25 m/s and a decrease of 10 m/s until February 24th with EUV*2. For EUV*2, a decrease of 15 m/s is seen on the event day. Figure 6.37 shows an increase around 100 km for all cases on the event day for both EUV forcings. And a decrease of 20 m/s just above at 125 km is seen for EUV/2 which is more pronounced for the reference run compared to day 2 and day 3. Around

150 km, zonal mean zonal wind increases by 10 m/s for EUV/2. For EUV*2, the acceleration of 25 m/s at 100 km on the day of the event and deceleration from about 150 km is observed which reaches further down in altitude for the reference compared to day 2 and day 3. And a decrease of 10 m/s is seen at 150 km which continues for the entire time series. Around 50 km, the wind decreases to 20 m/s for both EUV forcings.

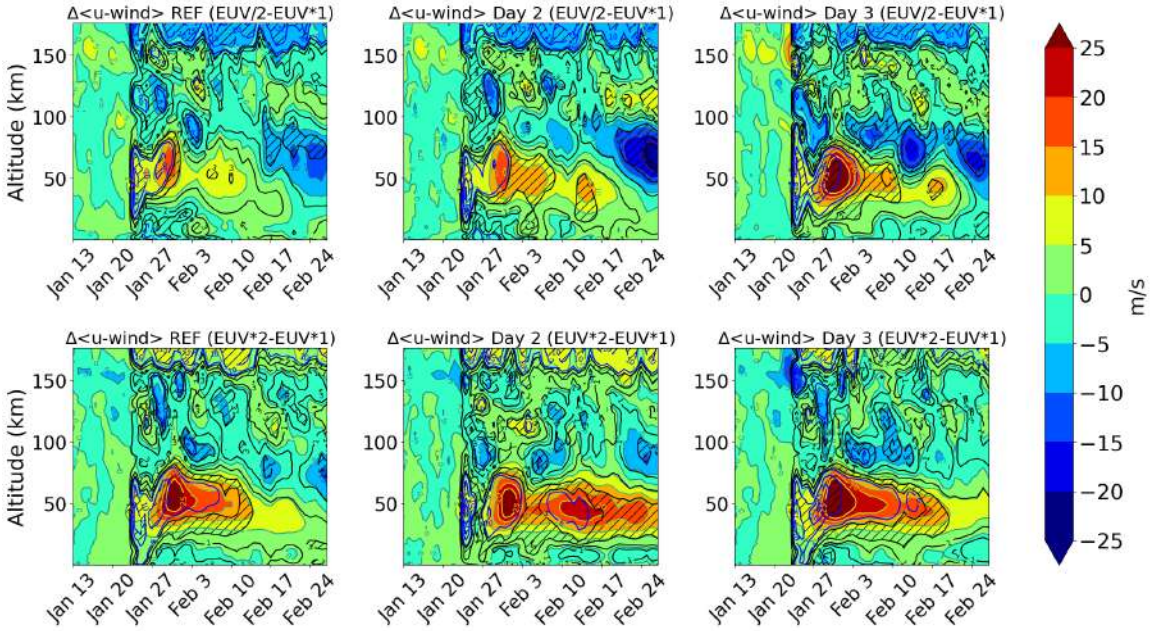

Figure 6.36: Same as figure 6.13 but for zonal mean zonal wind.

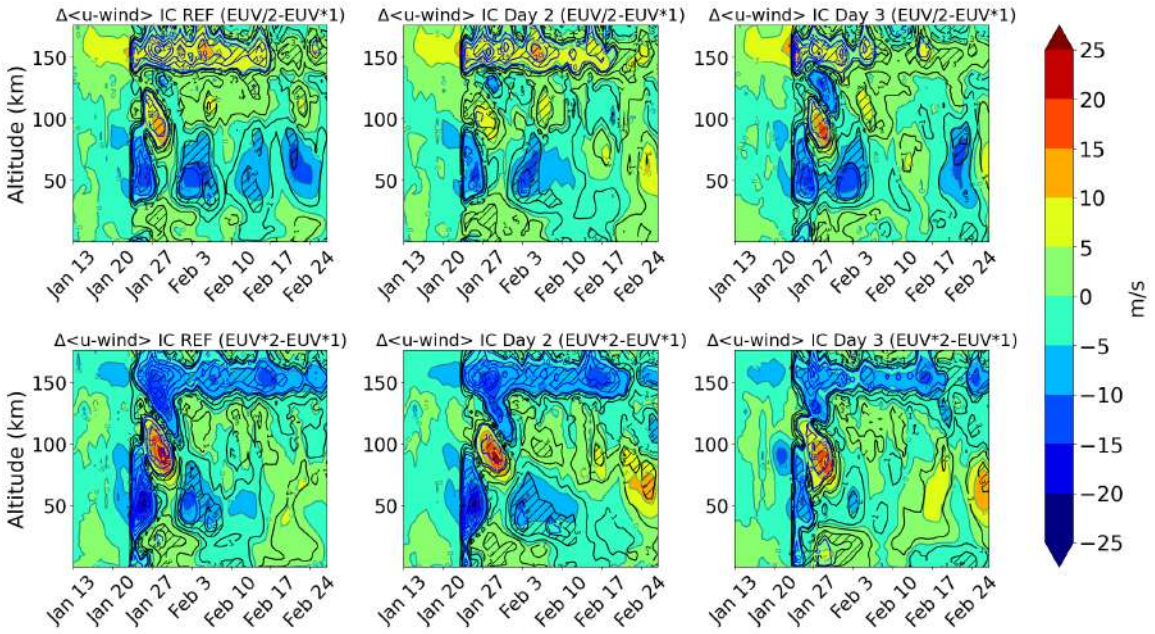

Figure 6.37: Same as figure 6.36 but with ion-chemistry.

Figure 6.38 shows the absolute differences of zonal mean zonal wind with the different particle forcings for day 2 and day 3. For low activity, acceleration of the zonal mean zonal wind upto 25 m/s is observed in the MLT region which increases with lower EUV for the day of the event. For day 3, deceleration of the zonal mean zonal wind on January 22nd is seen which accelerates later with EUV/2. Above 150 km, an acceleration is seen. With the ensemble mean, deceleration of the zonal mean zonal wind is seen afterwards from 100 km. On the day of the event, wind acceleration observed is higher for day 3 in the MLT region. The deceleration is observed after the event day which continues until February 10 and goes down to 50 km after a couple of days of the SSW. For the geomagnetic storm, day 3, in the MLT region, there is a wind reversal during the event and that goes down to a 100 km and continues until February 3rd which is seen for both the specified dynamics (S.D.) and free-running (F.R.) ensemble mean cases. For EUV/2, this reversal goes down to below 50 km and is seen to continue until February 10. Below 100 km just after the event, this wind reversal continues at lower altitudes until January 27th. Then the wind accelerates in the same altitude range, i.e., 20-60 km to 20 m/s until February 3rd. Between February 10th and February 17th, there is a small deceleration and then an acceleration to 10 m/s. Figure 6.39 shows the absolute differences of zonal mean zonal wind for the different particle forcings for both specified dynamics and free-running ensembles. The wind reversal or deceleration is stronger for day 3 on the day of the event, for all the EUV forcings. In this case, the wind trends show a deceleration and not an acceleration for all the particle forcings on the event day. And a wind reversal is seen after the event day for geomagnetic storm.

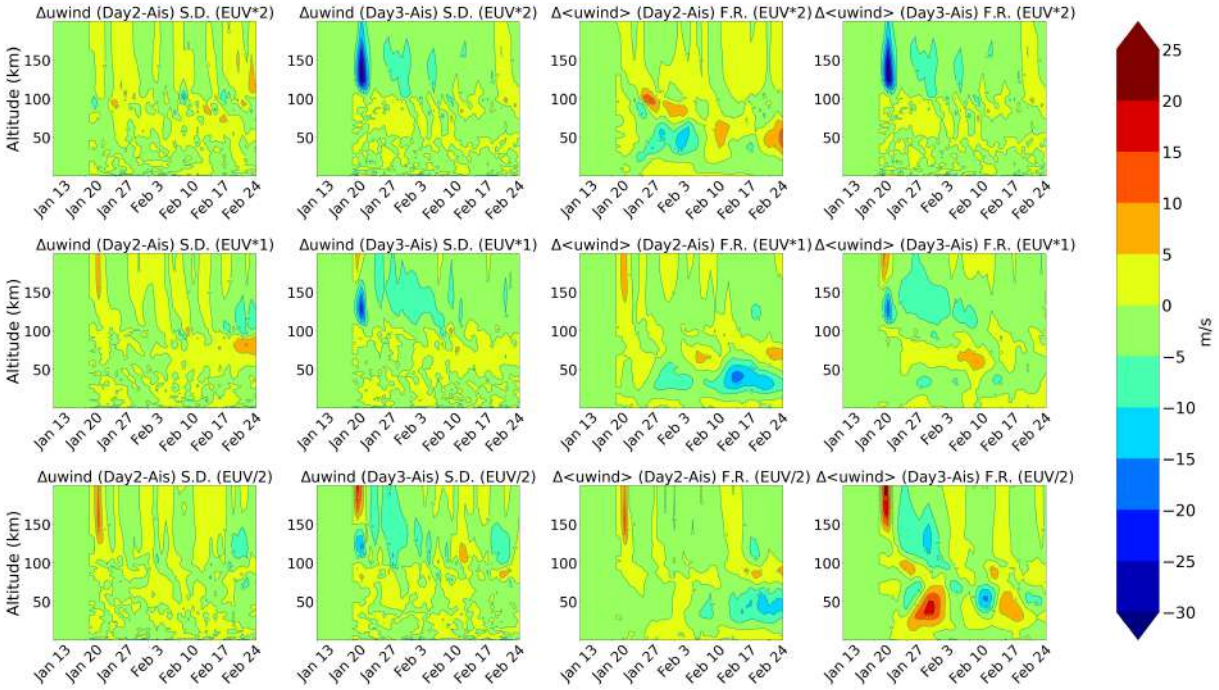

Figure 6.38: Absolute differences of zonal mean zonal wind for different particle forcings (column-wise: Day 2 and Day 3) w.r.t. background for specified dynamics (S.D.) and free-running (F.R.) ensemble means for EUV*2, EUV*1 and EUV/2 (row-wise).

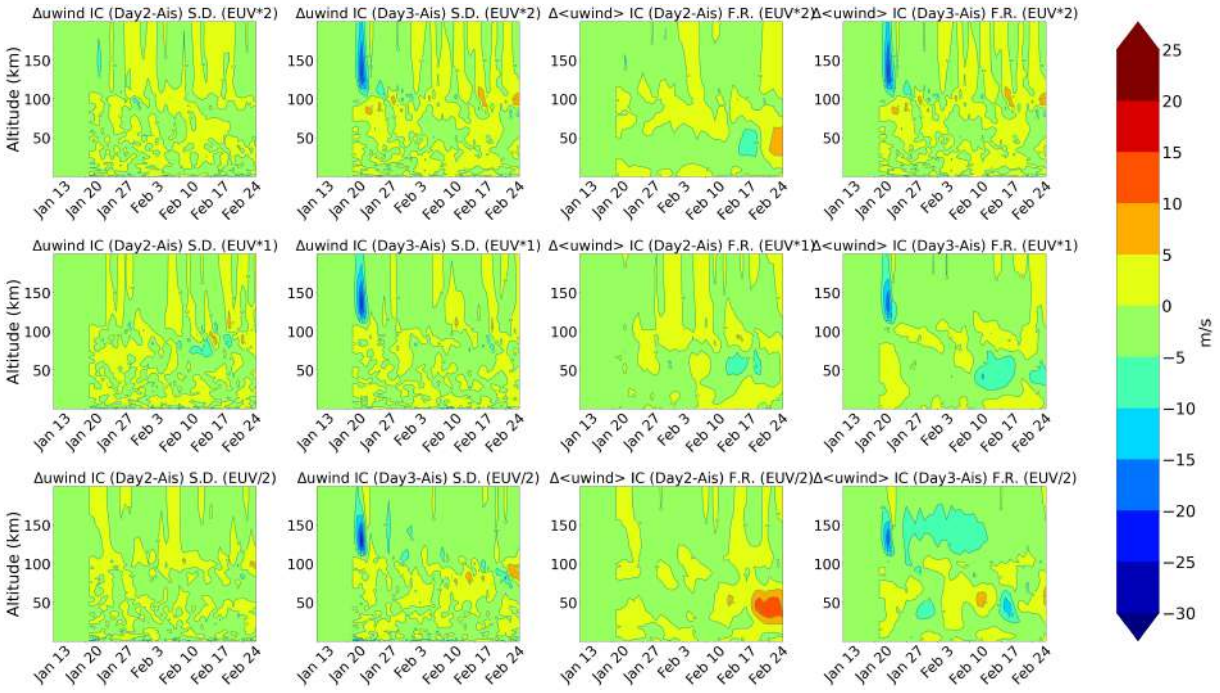

Figure 6.39: Same as figure 6.38 but with ion-chemistry.

6.4.3 Summary

This study focused on dynamical coupling from the upper atmosphere to the stratosphere during sudden stratospheric warmings (SSWs) which were found to be reproduced by a free-running model. The EUV photo-ionisation was varied and particles were added on the day of the SSW. For the simulations with NO_x based parameterisation, ozone levels decreased in the stratosphere that coupled down to the troposphere. The ozone loss was higher for stronger EUV and particle forcings, i.e., Day 3 (extreme Geomagnetic storm). However, with the five ion-chemistry, no stratospheric ozone loss was found. Instead a small formation of 5-10% was seen. In case of the temperatures, the results showed significant increase of 10-20 K after the event with changing EUV in the altitude range of 50-100 km, which was more consistent in time for the extreme geomagnetic storm. With five ion-chemistry, there is a decrease in temperature just after the event between 50-100 km and an increase around 100 km, which continues in time. The zonal mean zonal wind accelerates after the event for Day 3 and is also continuous in time around 50 km. At 100 km, the wind shows a decrease which is stronger for lower EUV with NO_x based parameterisation. But with the five ions, there is an acceleration of wind at 100 km and deceleration above 150 km. The strong zonal mean zonal wind in the stratosphere with changing EUV is due to dynamical feedback from ozone which needs to be further investigated. The changes in the middle atmosphere for all quantities overall were found to be quite significant.

7 Conclusions and Outlook

Focusing on atmospheric chemistry studies, a one dimensional state of the art stacked box model, ExoTIC, has been validated by comparing to satellite data, MIPAS on ENVISAT. Two solar proton events were considered for the model simulations. Chlorine ion-chemistry and its impact on ozone loss was studied in detail. A comparison of stratospheric and mesospheric composition changes observed by MIPAS in the polar cap region are demonstrated. The inter-comparison of the model and MIPAS observations allowed for an evaluation of the overall ability of the ExoTIC model to reproduce observed atmospheric perturbations generated by solar proton events, particularly with respect to changes in the chlorine species, SPE induced NO_y enhancements and ozone depletion. Polar upper stratospheric and lower mesospheric NO_y increased by over 40 ppbv and mesospheric ozone decreased by over 70% during the SPE period. The inter-comparison also tested and identified deficiencies in the chemical schemes, particularly with respect to nitrogen and chlorine chemistry which is relevant for stratospheric ozone. Short-time enhancements of HOCl and $ClONO_2$ were observed by MIPAS and also reproduced in the simulations with different model settings. Application of MIPAS averaging kernels to the ExoTIC output made the inter-comparison much better. HOCl enhancements were reproduced best for the model simulation with ion-chemistry with the $O(^1D)$ correction. An HOCl enhancement of more than 0.2 ppbv occurred roughly during the event as observed by MIPAS. The HOCl enhancements observed after application of averaging kernels and its temporal variation agree quite well with MIPAS. The ozone depletion simulated by the model extends over a large altitude range as compared to MIPAS observations. Jackman et al. (2008) found the opposite from WACCM3 results in the northern hemisphere in terms of altitude range. The encountered differences between the model and observations for $ClONO_2$ enhancements, it's underestimation by the model are related to a smaller availability of ClO in the polar region before the SPE. The $ClONO_2$ peak is observed at the same altitude for both the model and MIPAS, but the enhancements in MIPAS is observed earlier and the peak values seem to agree quite well even without the averaging kernels applied. Jackman et al. (2008) also found the $ClONO_2$ peak at the same altitude with WACCM3 but the values were underestimated by a factor of 2 compared to MIPAS. The comparison of the Halloween SPE and the extreme solar event of 775 A.D. showed long lasting stratospheric ozone loss for the extreme scenario. A long lasting impact was also found for the chlorine species like HOCl and HCl in case of the extreme scenario. Loss of HCl was underestimated by the parameterised model which was also found by Winkler et al. (2009) during the solar proton event in July 2000 in the northern polar region. For the extreme event, the parameterised model showed much higher NO_y enhancements, about a 1000 ppm in the mesosphere and lower thermosphere. HO_x enhancements of 0.1 ppm was found during

the extreme event which went further down in altitude upto 40 km, for all the model case studies. An impact of around 10-20 % on ozone loss was found due to the chlorine ions for the two events, a bit stronger for the extreme scenario that is more important for higher forcing. Ozone formation was observed after the event which is also due to the impact of chlorine ion-chemistry. For the Halloween event with temporal ionisation rates, ozone loss of 2.4 % during day-time and 10 % during nighttime was observed during the event that is also due to the included chlorine ion-chemistry. Ozone formation of 2-4 % was found after the event both during day-time and nighttime. In general, ExoTIC simulations reproduced the impacts of the Halloween SPE quite well, mainly for HOCl and NO_y. However, the initial state of the atmosphere in the simulations could be an important factor for some variability in the model results and MIPAS observations. While previous results with UBIC focused on the solar proton event in July 2000 in the northern polar region and compared to the HCl measurements from Halogen Occultation Experiment instrument (HALOE), we compare with MIPAS observations. Since MIPAS observations provide a better picture of the polar cap region as compared to HALOE observations that are less densely sampled, these results suggest that the validated D-region ion-chemistry setup in the ExoTIC model can be trusted to implement in a global 3D model. The problem of $O(^1D)$ in the ion-chemistry in ExoTIC should be taken into account which was however related to the neutral chemistry model. Considering the impact of chemistry and different solar forcings like extreme ultra-violet and high energetic particles from the upper atmosphere, simulations from different setups of the EMAC (ECHAM5/MESSy) were performed with a focus on sudden stratospheric warmings (SSWs) to look at the dynamical feedback from the chemistry. Setups with a NO_x based parameterisation and five ion-chemistry of the upper atmosphere were used. The results showed polar vortex strengthening after the event which was seen in the temperature increase and the strengthening of the zonal mean zonal wind in the stratosphere with changing EUV which is due to dynamical feedback from ozone. With EUV forcing for the simulations with NO_x based parameterisation and with five ions, ozone levels increase by 5-10% in the stratosphere. The changes in the middle atmosphere is quite significant. Future studies will focus on understanding the relations between temperature and zonal mean zonal wind and more analysis on the dynamical feedback due to the chemical changes from the forcings in the upper atmosphere.

8 Reactions in ExoTIC containing chlorine ions

Table 8.1: T is the temperature in K, and M is the total air density in cm^{-3}

Reactants	Products	Rate coefficient	Source
$Cl^- + Cl_2$	Cl_3^-	$9\times10^{-30}\times(M)$	Amelynck et al. (1994)
$Cl^- + CO_2$	$Cl^-(CO_2)$	$6\times10^{-29}\times(\frac{300}{T})^2\times(M)$	Kopp and Fritzenwallner (1997)
$Cl^- + H_2O$	$Cl^-(H_2O)$	$2\times10^{-29}\times(\frac{300}{T})^2\times(M)$	Turco (1977b)
$Cl^- + HCl$	$Cl^-(HCl)$	$1\times10^{-27}\times(M)$	Kazil et al. (2003)
$Cl^-(CO_2)$	$Cl^- + CO_2$	$2.6\times10^{-5}\times(\frac{300}{T})^3\times e^{\frac{-4000}{T}}\times(M)$	Kopp and Fritzenwallner (1997)
$Cl^-(H_2O)$	$Cl^- + H_2O$	$9.2\times10^{-5}\times(\frac{300}{T})^3\times e^{\frac{-7450}{T}}\times(M)$	Kopp and Fritzenwallner (1997)
$Cl^-(HCl)$	$Cl^- + HCl$	$3.33\times10^{-5}\times(\frac{300}{T})\times e^{\frac{-11926}{T}}\times(M)$	Kopp and Fritzenwallner (1997)
$NO_3^- + HCl$	$NO_3^-(HCl)$	$5.22\times10^{-28}\times(\frac{300}{T})^{2.62}$	Kopp and Fritzenwallner (1997)
$OH^- + HCl$	$Cl^- + H_2O$	$1.5\times10^{-9}\times(\frac{300}{T})^5$	Kopp and Fritzenwallner (1997)
$Cl^- + ClONO_2$	$NO_3^- + Cl_2$	9.2×10^{-10}	Turco (1977b)
$Cl^- + HNO_3$	$NO_3^- + HCl$	2.8×10^{-9}	Huey (1996)
$Cl^- + H$	$e + HCl$	9.6×10^{-10}	Turco (1977b)
$Cl^- + N_2O_5$	$NO_3^- + ClNO_2$	9.4×10^{-10}	Amelynck et al. (1994)
$Cl^-(H_2O) + Cl_2$	$Cl_3^- + H_2$	1.09×10^{-9}	Kopp and Fritzenwallner (1997)
$Cl^-(H_2O) + HCl$	$Cl^-(HCl) + H_2O$	1.30×10^{-9}	Kopp and Fritzenwallner (1997)
$Cl^-(H_2O) + HNO_3$	$NO_3^-(HCl) + H_2O$	2.85×10^{-9}	Kopp and Fritzenwallner (1997)
$Cl^-(H_2O) + H$	$e + H_2O + HCl$	8×10^{-11}	Kopp and Fritzenwallner (1997)
$Cl^-(HCl) + Cl_2$	$Cl_3^- + HCl$	5.3×10^{-10}	Kopp and Fritzenwallner (1997)
$Cl^-(HCl) + HNO_3$	$NO_3^-(HCl) + HCl$	2.48×10^{9}	Kopp and Fritzenwallner (1997)
$Cl^- + NO_2$	$NO_2^- + Cl$	6.0×10^{-12}	Kopp and Fritzenwallner (1997)
$Cl^- + O_3$	$ClO^- + O_2$	5.0×10^{-13}	Turco (1977b)
$Cl_2^- + HNO_3$	$NO_3^-(HCl) + Cl$	4.8×10^{-10}	Amelynck et al. (1994)
$Cl_2^- + NO_2$	$Cl^- + ClNO_2$	4.0×10^{-11}	Kopp and Fritzenwallner (1997)
$Cl_2^- + O_3$	$O_3^- + Cl_2$	2.0×10^{-12}	Kopp and Fritzenwallner (1997)
$Cl_3^- + HNO_3$	$NO_3^-(HCl) + Cl_2$	1.3×10^{-9}	Amelynck et al. (1994)
$CO_3^- + ClONO_2$	$NO_3^- + ClO + CO_2$	2.1×10^{-9}	Kopp and Fritzenwallner (1997)

Reactants	Products	Rate coefficient	Source
CO_3^- + HCl	Cl^- + OH + CO_2	3.0×10^{-11}	Kopp and Fritzenwallner (1997)
CO_4^- + HCl	$Cl^-(HO_2)$ + CO_2	1.2×10^{-11}	Kopp and Fritzenwallner (1997)
NO_2^- + Cl_2	Cl_2^- + NO_2	6.8×10^{-10}	Kopp and Fritzenwallner (1997)
NO_2^- + HCl	Cl^- + HNO_2	1.4×10^{-9}	Kopp and Fritzenwallner (1997)
NO_3^- + HCl	Cl^- + HNO_2	1.0×10^{-12}	Kopp and Fritzenwallner (1997)
$NO_3^-(HCl)$ + HNO_3	$NO_3^-(HNO_3)$ + HCl	7.6×10^{-10}	Amelynck et al. (1994)
O^- + HCl	Cl^- + OH	2.0×10^{-9}	Turco (1977b)
O_2^- + HCl	Cl^- + HO_2	1.6×10^{-9}	Turco (1977b)
O_3^- + Cl_2	Cl^- + ClO + O2	1.3×10^{-9}	Turco (1977b)
ClO^- + NO	Cl^- + NO_2	$2.9\times10^{-11}\times0.5$	Turco (1977b)
ClO^- + O_3	Cl^- + O_2 + O_2	6.0×10^{-11}	Turco (1977b)
ClO^- + O_3	ClO + O_3^-	1.0×10^{-11}	Turco (1977b)
O^- + Cl	Cl^- + O	1.0×10^{-10}	Turco (1977b)
O^- + ClO	Cl^- + O_2	1.0×10^{-10}	Turco (1977b)
O_2^- + Cl	Cl^- + O_2	1.0×10^{-10}	Turco (1977b)
O_2^- + ClO	ClO^- + O_2	1.0×10^{-10}	Turco (1977b)
OH^- + Cl	Cl^- + OH	1.0×10^{-10}	Turco (1977b)
OH^- + ClO	ClO^- + OH	1.0×10^{-10}	Turco (1977b)
CO_3^- + Cl	Cl^- + O + CO_2	1.0×10^{-10}	Turco (1977b)
CO_3^- + Cl	ClO^- + CO_2	1.0×10^{-10}	Turco (1977b)
CO_3^- + ClO	Cl^- + CO_2 + O_2	1.0×10^{-10}	Turco (1977b)
CO_4^- + Cl	Cl^- + O_2 + CO_2	1.0×10^{-10}	Turco (1977b)
CO_4^- + ClO	ClO^- + O_2 + CO_2	1.0×10^{-10}	Turco (1977b)
NO_2^- + Cl	Cl^- + NO_2	1.0×10^{-10}	Turco (1977b)
NO_2^- + ClO	Cl^- + NO_3	1.0×10^{-10}	Turco (1977b)
HCO_3^- + Cl	Cl^- + OH + CO_2	1.0×10^{-10}	Turco (1977b)
HCO_3^- + ClO	Cl^- + HO_2 + CO_2	1.0×10^{-10}	Turco (1977b)
ClO^- + O	Cl^- + O_2	2.0×10^{-10}	Turco (1977b)
H^+ + Cl^-	Cl	$6\times10^{-8}\times(\frac{300}{T})^{0.5}+1.25\times10^{-25}\times(\frac{300}{T})^4\times(M)^*$	Arijs et al. (1987)
H^+ + Cl_2^-	Cl_2		
H^+ + Cl_3^-	Cl_2 + Cl		
H^+ + Cl^-(HCl)	Cl + HCl		
H^+ + $Cl^-(H_2O)$	Cl + H_2O		
H^+ + $Cl^-(CO_2)$	Cl + CO_2		
H^+ + $Cl^-(HO_2)$	Cl + HO_2		
H^+ + ClO^-	ClO		

* The coefficient is the same for all the reactions below

9 Bibliography

Abraham, J. e. a., 2010: Measurement of the energy spectrum of cosmic rays above 1018 ev using the pierre auger observatory. *Physics Letters B*, **685 (4–5)**, 239–246, URL http://dx.doi.org/10.1016/j.physletb.2010.02.013.

Aikin, A., 1997: Production of stratospheric hno3 by different ion-molecule reaction mechanisms. *Journal of Geophysical Research: Atmospheres*, **102 (D11)**, 12 921–12 925.

Aikin, A. C. and H. J. P. Smith, 1999: Mesospheric constituent variations during electron precipitation events. , **104 (D21)**, 26,457–26,471.

Amelynck, C., D. Fussen, and E. Arijs, 1994: Reactions of nitric acid with di- and trichloride ions, di- and tri-iodide ions and with co−4 in the gas phase. *International Journal of Mass Spectrometry and Ion Processes*, **133 (1)**, 13–28, URL https://www.sciencedirect.com/science/article/pii/016811769403950X.

Anchordoqui, L., T. PAUL, S. REUCROFT, and J. SWAIN, 2003: Ultrahigh energy cosmic rays: The state of the art before the auger observatory. *International Journal of Modern Physics A*, **18 (13)**, 2229–2366, URL https://doi.org/10.1142/S0217751X03013879, https://doi.org/10.1142/S0217751X03013879.

Andersson, M. E., P. T. Verronen, D. R. Marsh, S.-M. Päivärinta, and J. M. C. Plane, 2016: Waccm-d—improved modeling of nitric acid and active chlorine during energetic particle precipitation. *Journal of Geophysical Research: Atmospheres*, **121 (17)**, 10,328–10,341, URL https://agupubs.onlinelibrary.wiley.com/doi/abs/10.1002/2015JD024173, https://agupubs.onlinelibrary.wiley.com/doi/pdf/10.1002/2015JD024173.

Arijs, E., D. Nevejans, and J. Ingels, 1987: Stratospheric positive ion composition measurements and acetonitrile detection: a consistent picture? *International Journal of Mass Spectrometry and Ion Processes*, **81**, 15–31, URL https://www.sciencedirect.com/science/article/pii/0168117687800034.

Baker, D. N., G. M. Mason, and J. E. Mazur, 2012: A small spacecraft mission with large accomplishments. *Eos, Transactions American Geophysical Union*, **93 (34)**, 325–326.

Baldwin, M. P., B. Ayarzagüena, T. Birner, N. Butchart, A. H. Butler, A. J. Charlton-Perez, D. I. Domeisen, C. I. Garfinkel, H. Garny, E. P. Gerber, et al., 2021: Sudden stratospheric warmings. *Reviews of Geophysics*, **59 (1)**, e2020RG000 708.

Barth, C. A., 1992: Nitric oxide in the lower thermosphere. *Planetary and Space Science*, **40 (2)**, 315–336, URL https://www.sciencedirect.com/science/article/pii/003206339290067X.

Bates, D. R. and M. Nicolet, 1950: The photochemistry of atmospheric water vapor. *Journal of Geophysical Research (1896-1977)*, **55 (3)**, 301–327, URL https://agupubs.onlinelibrary.wiley.com/doi/abs/10.1029/JZ055i003p00301, https://agupubs.onlinelibrary.wiley.com/doi/pdf/10.1029/JZ055i003p00301.

Baumgaertner, A. J. G., P. Jöckel, H. Riede, G. Stiller, and B. Funke, 2010a: Energetic particle precipitation in echam5/messy – part 2: Solar proton events. *Atmospheric Chemistry and Physics*, **10 (15)**, 7285–7302, URL https://acp.copernicus.org/articles/10/7285/2010/.

———, 2010b: Energetic particle precipitation in echam5/messy – part 2: Solar proton events. *Atmospheric Chemistry and Physics*, **10 (15)**, 7285–7302, URL https://acp.copernicus.org/articles/10/7285/2010/.

Bazilevskaya, G., M. Kalinin, M. Krainev, V. Makhmutov, Y. Stozhkov, A. Svirzhevskaya, N. Svirzhevsky, and B. Gvozdevsky, 2020: Temporal characteristics of energetic magnetospheric electron precipitation as observed during long-term balloon observations. *Journal of Geophysical Research: Space Physics*, **125 (11)**, e2020JA028 033.

Borthakur, M., M. Sinnhuber, A. Laeng, T. Reddmann, P. Braesicke, G. Stiller, T. von Clarmann, B. Funke, I. Usoskin, J. M. Wissing, and O. Yakovchuk, 2023: Impact of chlorine ion chemistry on ozone loss in the middle atmosphere during very large solar proton events. *Atmospheric Chemistry and Physics*, **23 (20)**, 12 985–13 013, URL https://acp.copernicus.org/articles/23/12985/2023/.

Brasseur, . S. S., G., 2005: *Aeronomy of the Middle Atmosphere: Chemistry and Physics of the Stratosphere and Mesosphere*. Springer.

Brasseur, G. and S. Solomon, 1984: *Aeronomy of the Middle Atmosphere: Chemistry and Physics of the Stratosphere and Mesosphere*. Atmospheric Sciences Library, Springer Netherlands, URL https://books.google.de/books?id=GLV6AAAAIAAJ.

Calisto, M., I. Usoskin, and E. Rozanov, 2013: Influence of a carrington-like event on the atmospheric chemistry, temperature and dynamics: revised. *Environmental Research Letters*, **8 (4)**, 045 010, URL https://dx.doi.org/10.1088/1748-9326/8/4/045010.

Callis, L. B., D. N. Baker, M. Natarajan, J. B. Bernard, R. A. Mewaldt, R. S. Selesnick, and J. R. Cummings, 1996a: A 2-d model simulation of downward transport of noy into the stratosphere: Effects on the 1994 austral spring o3and noy. *Geophysical research letters*, **23 (15)**, 1905–1908.

Callis, L. B., R. E. Boughner, D. N. Baker, R. A. Mewaldt, J. Bernard Blake, R. S. Selesnick, J. R. Cummings, M. Natarajan, G. M. Mason, and J. E. Mazur, 1996b: Precipitating electrons: Evidence for effects on mesospheric odd nitrogen. *Geophysical research letters*, **23 (15)**, 1901–1904.

Callis, L. B., M. Natarajan, D. S. Evans, and J. D. Lambeth, 1998: Solar atmospheric coupling by electrons (solace): 1. effects of the may 12, 1997 solar event on the middle atmosphere. *Journal of Geophysical Research: Atmospheres*, **103 (D21)**, 28 405–28 419.

Chakrabarty, D. and S. Ganguly, 1989: On significant quantities of negative ions observed around the mesopause. *Journal of Atmospheric and Terrestrial Physics*, **51 (11)**, 983–989, URL `https://www.sciencedirect.com/science/article/pii/0021916989900135`.

Charlton-Perez, A., L. M. Polvani, J. Austin, and F. Li, 2008: The frequency and dynamics of stratospheric sudden warmings in the 21st century. *Journal of Geophysical Research: Atmospheres*, **113 (D16)**.

Chipperfield, M. P., 1999: Multiannual simulations with a three-dimensional chemical transport model. *Journal of Geophysical Research: Atmospheres*, **104 (D1)**, 1781–1805, URL `https://agupubs.onlinelibrary.wiley.com/doi/abs/10.1029/98JD02597`, `https://agupubs.onlinelibrary.wiley.com/doi/pdf/10.1029/98JD02597`.

Cleveland, C. J. and C. Morris, 2013: Section 10 - solar. *Handbook of Energy*, Cleveland, C. J. and C. Morris, Eds., Elsevier, Amsterdam, 405–450, URL `https://www.sciencedirect.com/science/article/pii/B9780080464053000103`.

Cliver, E. W., C. J. Schrijver, K. Shibata, and I. G. Usoskin, 2022: Extreme solar events. *Living Reviews in Solar Physics*, **19 (1)**, URL `https://doi.org/10.1007%2Fs41116-022-00033-8`.

Connor, B. J., D. E. Siskind, J. J. Tsou, A. Parrish, and E. E. Remsberg, 1994: Ground-based microwave observations of ozone in the upper stratosphere and mesosphere. , **99 (D8)**, 16,757–16,770.

Damiani, A., B. Funke, D. R. Marsh, M. López-Puertas, M. L. Santee, L. Froidevaux, S. Wang, C. H. Jackman, T. von Clarmann, A. Gardini, R. R. Cordero, and M. Storini, 2012: Impact of january 2005 solar proton events on chlorine species. *Atmospheric Chemistry and Physics*, **12 (9)**, 4159–4179, URL `https://acp.copernicus.org/articles/12/4159/2012/`.

Daniel, J. S., S. Solomon, R. W. Portmann, and R. R. Garcia, 1999: Stratospheric ozone destruction: The importance of bromine relative to chlorine. *Journal of Geophysical Research:*

Atmospheres, **104 (D19)**, 23 871–23 880, URL https://agupubs.onlinelibrary.wiley.com/doi/abs/10.1029/1999JD900381, https://agupubs.onlinelibrary.wiley.com/doi/pdf/10.1029/1999JD900381.

Fischer, H., 1992: Remote sensing of atmospheric trace constituents using fourier transform spectrometry. *Berichte der Bunsengesellschaft für physikalische Chemie*, **96 (3)**, 306–314.

Fischer, H., M. Birk, C. Blom, B. Carli, M. Carlotti, T. von Clarmann, L. Delbouille, A. Dudhia, D. Ehhalt, M. Endemann, J. M. Flaud, R. Gessner, A. Kleinert, R. Koopman, J. Langen, M. López-Puertas, P. Mosner, H. Nett, H. Oelhaf, G. Perron, J. Remedios, M. Ridolfi, G. Stiller, and R. Zander, 2008: Mipas: an instrument for atmospheric and climate research. *Atmospheric Chemistry and Physics*, **8 (8)**, 2151–2188, URL https://acp.copernicus.org/articles/8/2151/2008/.

Fischer, H., C. Blom, H. Oelhaf, B. Carli, M. Carlotti, L. Delbouille, D. Ehhalt, J. Flaud, I. Isaksen, M. Lopez-Puertas, et al., 2000: Envisat-mipas, the michelson interferometer for passive atmospheric sounding; an instrument for atmospheric chemistry and climate research. *ESA SP*, **1229**.

Fischer, H. and H. Oelhaf, 1996: Remote sensing of vertical profiles of atmospheric trace constituents with mipas limb-emission spectrometers. *Applied Optics*, **35 (16)**, 2787–2796.

Friedl-Vallon, F., T. von Clarmann, H. Fischer, C. Fritzsche, H. Oelhaf, C. Piesch, M. Seefeldner, D. Rabus, and W. Völker, 1993: Limb emission spectroscopy with the balloon-borne michelson interferometer for passive atmospheric sounding. *Optical methods in atmospheric chemistry*, SPIE, Vol. 1715, 441–450.

Funke, B., W. Ball, S. Bender, A. Gardini, V. L. Harvey, A. Lambert, M. López-Puertas, D. R. Marsh, K. Meraner, H. Nieder, S.-M. Päivärinta, K. Pérot, C. E. Randall, T. Reddmann, E. Rozanov, H. Schmidt, A. Seppälä, M. Sinnhuber, T. Sukhodolov, G. P. Stiller, N. D. Tsvetkova, P. T. Verronen, S. Versick, T. von Clarmann, K. A. Walker, and V. Yushkov, 2017: heppa-ii model–measurement intercomparison project: epp indirect effects during the dynamically perturbed nh winter 2008–2009. *Atmospheric Chemistry and Physics*, **17 (5)**, 3573–3604, URL https://acp.copernicus.org/articles/17/3573/2017/.

Funke, B., A. Baumgaertner, M. Calisto, T. Egorova, C. H. Jackman, J. Kieser, A. Krivolutsky, M. López-Puertas, D. R. Marsh, T. Reddmann, E. Rozanov, S.-M. Salmi, M. Sinnhuber, G. P. Stiller, P. T. Verronen, S. Versick, T. von Clarmann, T. Y. Vyushkova, N. Wieters, and J. M. Wissing, 2011: Composition changes after the "halloween" solar proton event: the high energy particle precipitation in the atmosphere (heppa) model versus mipas data intercomparison study. *Atmospheric Chemistry and Physics*, **11 (17)**, 9089–9139, URL https://acp.copernicus.org/articles/11/9089/2011/.

Funke, B., M. López-Puertas, T. von Clarmann, G. P. Stiller, H. Fischer, N. Glatthor, U. Grabowski, M. Höpfner, S. Kellmann, M. Kiefer, A. Linden, G. Mengistu Tsidu, M. Milz, T. Steck, and D. Y. Wang, 2005: Retrieval of stratospheric nox from 5.3 and 6.2 m nonlocal thermodynamic equilibrium emissions measured by michelson interferometer for passive atmospheric sounding (mipas) on envisat. *Journal of Geophysical Research: Atmospheres*, **110 (D9)**, URL https://agupubs.onlinelibrary.wiley.com/doi/abs/10.1029/2004JD005225, https://agupubs.onlinelibrary.wiley.com/doi/pdf/10.1029/2004JD005225.

Glatthor, N., T. von Clarmann, H. Fischer, B. Funke, S. Gil-López, U. Grabowski, M. Höpfner, S. Kellmann, A. Linden, M. López-Puertas, G. Mengistu Tsidu, M. Milz, T. Steck, G. P. Stiller, and D.-Y. Wang, 2006: Retrieval of stratospheric ozone profiles from mipas/envisat limb emission spectra: a sensitivity study. *Atmospheric Chemistry and Physics*, **6 (10)**, 2767–2781, URL https://acp.copernicus.org/articles/6/2767/2006/.

Gopalswamy, N., S. Yashiro, Y. Liu, G. Michalek, A. Vourlidas, M. Kaiser, and R. Howard, 2005: Coronal mass ejections and other extreme characteristics of the 2003 october–november solar eruptions. *Journal of Geophysical Research: Space Physics*, **110 (A9)**.

Gulde, T., C. Piesch, C. Blom, H. Fischer, F. Fergg, and G. Wildgruber, 1994: The airborne mipas infrared emission experiment. *Proceedings of the First International Airborne Remote Sensing Conference and Exhibition*, Environmental Research Institute of Michigan Ann Arbor, MI, Vol. 2, 301–311.

Harvey, V. L., C. E. Randall, and R. L. Collins, 2015: Chemical definition of the mesospheric polar vortex. *Journal of Geophysical Research: Atmospheres*, **120 (19)**, 10,166–10,179, URL https://agupubs.onlinelibrary.wiley.com/doi/abs/10.1002/2015JD023488, https://agupubs.onlinelibrary.wiley.com/doi/pdf/10.1002/2015JD023488.

Herbst, K., J. L. Grenfell, M. Sinnhuber, and F. Wunderlich, 2022: Increase: An updated model suite to study the influence of cosmic rays on exoplanetary atmospheres. *Astronomische Nachrichten*, **343 (4)**, e210 072, URL https://onlinelibrary.wiley.com/doi/abs/10.1002/asna.20210072, https://onlinelibrary.wiley.com/doi/pdf/10.1002/asna.20210072.

Herbst, Konstantin, Grenfell, John Lee, Sinnhuber, Miriam, Rauer, Heike, Heber, Bernd, Banjac, Sasa, Scheucher, Markus, Schmidt, Vanessa, Gebauer, Stefanie, Lehmann, Ralph, and Schreier, Franz, 2019: A new model suite to determine the influence of cosmic rays on (exo)planetary atmospheric biosignatures - validation based on modern earth. *A&A*, **631**, A101, URL https://doi.org/10.1051/0004-6361/201935888.

Hersbach, H., B. Bell, P. Berrisford, S. Hirahara, A. Horányi, J. Muñoz-Sabater, J. Nicolas, C. Peubey, R. Radu, D. Schepers, A. Simmons, C. Soci, S. Abdalla, X. Abellan, G. Balsamo, P. Bechtold, G. Biavati, J. Bidlot, M. Bonavita, G. De Chiara, P. Dahlgren, D. Dee, M. Diamantakis, R. Dragani, J. Flem-

ming, R. Forbes, M. Fuentes, A. Geer, L. Haimberger, S. Healy, R. J. Hogan, E. Hólm, M. Janisková, S. Keeley, P. Laloyaux, P. Lopez, C. Lupu, G. Radnoti, P. de Rosnay, I. Rozum, F. Vamborg, S. Villaume, and J.-N. Thépaut, 2020: The era5 global reanalysis. *Quarterly Journal of the Royal Meteorological Society*, **146 (730)**, 1999–2049, URL https://rmets.onlinelibrary.wiley.com/doi/abs/10.1002/qj.3803, https://rmets.onlinelibrary.wiley.com/doi/pdf/10.1002/qj.3803.

Hong, S.-S. and R. S. Lindzen, 1976: Solar semidiurnal tide in the thermosphere. *Journal of Atmospheric Sciences*, **33 (1)**, 135 – 153, URL https://journals.ametsoc.org/view/journals/atsc/33/1/1520-0469_1976_033_0135_sstitt_2_0_co_2.xml.

Höpfner, M., T. von Clarmann, H. Fischer, B. Funke, N. Glatthor, U. Grabowski, S. Kellmann, M. Kiefer, A. Linden, M. Milz, T. Steck, G. P. Stiller, P. Bernath, C. E. Blom, T. Blumenstock, C. Boone, K. Chance, M. T. Coffey, F. Friedl-Vallon, D. Griffith, J. W. Hannigan, F. Hase, N. Jones, K. W. Jucks, C. Keim, A. Kleinert, W. Kouker, G. Y. Liu, E. Mahieu, J. Mellqvist, S. Mikuteit, J. Notholt, H. Oelhaf, C. Piesch, T. Reddmann, R. Ruhnke, M. Schneider, A. Strandberg, G. Toon, K. A. Walker, T. Warneke, G. Wetzel, S. Wood, and R. Zander, 2007a: Validation of mipas clono$_2$ measurements. *Atmospheric Chemistry and Physics*, **7 (1)**, 257–281, URL https://acp.copernicus.org/articles/7/257/2007/.

———, 2007b: Validation of mipas clono$_2$ measurements. *Atmospheric Chemistry and Physics*, **7 (1)**, 257–281, URL https://acp.copernicus.org/articles/7/257/2007/.

Huey, L., 1996: The kinetics of the reactions of cl−, o−, and o2− with hno3: Implications for measurement of hno3 in the atmosphere. *International Journal of Mass Spectrometry and Ion Processes*, **153 (2)**, 145–150, URL https://www.sciencedirect.com/science/article/pii/0168117695043543.

J. C. Farman, B. G. G. and J. D. Shanklin, 1985: Large losses of total ozone in antarctica reveal seasonal clox/nox interaction. *Nature*, **315 (6016)**, 207–210.

Jackman, C. H., M. T. DeLand, G. J. Labow, E. L. Fleming, D. K. Weisenstein, M. K. Ko, M. Sinnhuber, and J. M. Russell, 2005: Neutral atmospheric influences of the solar proton events in october–november 2003. *Journal of Geophysical Research: Space Physics*, **110 (A9)**.

Jackman, C. H., E. L. Fleming, and F. M. Vitt, 2000: Influence of extremely large solar proton events in a changing stratosphere. *Journal of Geophysical Research: Atmospheres*, **105 (D9)**, 11 659–11 670, URL https://agupubs.onlinelibrary.wiley.com/doi/abs/10.1029/2000JD900010, https://agupubs.onlinelibrary.wiley.com/doi/pdf/10.1029/2000JD900010.

Jackman, C. H., D. R. Marsh, F. M. Vitt, R. R. Garcia, E. L. Fleming, G. J. Labow, C. E. Randall, M. López-Puertas, B. Funke, T. von Clarmann, and G. P. Stiller, 2008: Short- and medium-term atmospheric constituent effects of very large solar proton events. *Atmospheric Chemistry and Physics*, **8 (3)**, 765–785, URL https://acp.copernicus.org/articles/8/765/2008/.

Jöckel, P., A. Kerkweg, A. Pozzer, R. Sander, H. Tost, H. Riede, A. Baumgaertner, S. Gromov, and B. Kern, 2010: Development cycle 2 of the modular earth submodel system (messy2). *Geoscientific Model Development*, **3 (2)**, 717–752, URL https://gmd.copernicus.org/articles/3/717/2010/.

Jones, R. and M. Rees, 1973: Time dependent studies of the aurora—i. ion density and composition. *Planetary and Space Science*, **21 (4)**, 537–557, URL https://www.sciencedirect.com/science/article/pii/003206337390069X.

Kalakoski, N., P. T. Verronen, A. Seppälä, M. E. Szeląg, A. Kero, and D. R. Marsh, 2020: Statistical response of middle atmosphere composition to solar proton events in waccm-d simulations: the importance of lower ionospheric chemistry. *Atmospheric Chemistry and Physics*, **20 (14)**, 8923–8938, URL https://acp.copernicus.org/articles/20/8923/2020/.

Kazil, J., E. Kopp, S. Chabrillat, and J. Bishop, 2003: The university of bern atmospheric ion model: Time-dependent modeling of the ions in the mesosphere and lower thermosphere. *Journal of Geophysical Research: Atmospheres*, **108 (D14)**, URL https://agupubs.onlinelibrary.wiley.com/doi/abs/10.1029/2002JD003024, https://agupubs.onlinelibrary.wiley.com/doi/pdf/10.1029/2002JD003024.

Kopp, E. and J. Fritzenwallner, 1997: Chlorine and bromine ions in the d-region. *Advances in Space Research*, **20 (11)**, 2111–2115, URL https://www.sciencedirect.com/science/article/pii/S0273117797006030, middle Atmosphere: Changes and Electrodynamics.

Kvissel, O.-K., Y. J. Orsolini, F. Stordal, I. S. A. Isaksen, and M. L. Santee, 2012: Formation of stratospheric nitric acid by a hydrated ion cluster reaction: Implications for the effect of energetic particle precipitation on the middle atmosphere. *Journal of Geophysical Research: Atmospheres*, **117 (D16)**, URL https://agupubs.onlinelibrary.wiley.com/doi/abs/10.1029/2011JD017257, https://agupubs.onlinelibrary.wiley.com/doi/pdf/10.1029/2011JD017257.

Landgraf, J. and P. J. Crutzen, 1998: An efficient method for online calculations of photolysis and heating rates. *Journal of the Atmospheric Sciences*, **55 (5)**, 863 – 878, URL https://journals.ametsoc.org/view/journals/atsc/55/5/1520-0469_1998_055_0863_aemfoc_2.0.co_2.xml.

Lary, D. J., 1997: Catalytic destruction of stratospheric ozone. *Journal of Geophysical Research: Atmospheres*, **102 (D17)**, 21 515–21 526, URL https://agupubs.onlinelibrary.wiley.com/doi/

abs/10.1029/97JD00912, https://agupubs.onlinelibrary.wiley.com/doi/pdf/10.1029/97JD00912.

LCDR M.Weaver, W. C. D. L. M. K. J. H. L. D. N., NOAA, 2004: Halloween space weather storms of 2003. Tech. rep., Space Environment Center, Boulder, Colorado.

Leo, W. R., 1994: *Techniques for nuclear and particle physics experiments a how-to approach*. 2d ed., Springer, Berlin, URL https://katalog.slub-dresden.de/id/0-152388273.

Limpasuvan, V., D. W. Thompson, and D. L. Hartmann, 2004: The life cycle of the northern hemisphere sudden stratospheric warmings. *Journal of climate*, **17 (13)**, 2584–2596.

López-Puertas, M., B. Funke, S. Gil-López, T. von Clarmann, G. P. Stiller, M. Höpfner, S. Kellmann, H. Fischer, and C. H. Jackman, 2005: Observation of nox enhancement and ozone depletion in the northern and southern hemispheres after the october–november 2003 solar proton events. *Journal of Geophysical Research: Space Physics*, **110 (A9)**, URL https://agupubs.onlinelibrary.wiley.com/doi/abs/10.1029/2005JA011050, https://agupubs.onlinelibrary.wiley.com/doi/pdf/10.1029/2005JA011050.

Makhmutov, V., G. Bazilevskaya, Y. I. Stozhkov, A. Svirzhevskaya, and N. Svirzhevsky, 2016: Catalogue of electron precipitation events as observed in the long-duration cosmic ray balloon experiment. *Journal of Atmospheric and Solar-Terrestrial Physics*, **149**, 258–276.

Marsh, D. R., R. R. Garcia, D. E. Kinnison, B. A. Boville, F. Sassi, S. C. Solomon, and K. Matthes, 2007: Modeling the whole atmosphere response to solar cycle changes in radiative and geomagnetic forcing. *Journal of Geophysical Research: Atmospheres*, **112 (D23)**, URL https://agupubs.onlinelibrary.wiley.com/doi/abs/10.1029/2006JD008306, https://agupubs.onlinelibrary.wiley.com/doi/pdf/10.1029/2006JD008306.

Meilinger, S. K., 2000: Heterogeneous chemistry in the tropopause region: Impact of aircraft emissions. Ph.D. thesis, ETH Zurich.

Meraner, K. and H. Schmidt, 2018: Climate impact of idealized winter polar mesospheric and stratospheric ozone losses as caused by energetic particle precipitation. *Atmospheric Chemistry and Physics*, **18 (2)**, 1079–1089, URL https://acp.copernicus.org/articles/18/1079/2018/.

Mewaldt, R. A., C. M. S. Cohen, A. W. Labrador, R. A. Leske, G. M. Mason, M. I. Desai, M. D. Looper, J. E. Mazur, R. S. Selesnick, and D. K. Haggerty, 2005: Proton, helium, and electron spectra during the large solar particle events of october–november 2003. *Journal of Geophysical Research: Space Physics*, **110 (A9)**, URL https://agupubs.onlinelibrary.wiley.com/doi/abs/10.1029/2005JA011038, https://agupubs.onlinelibrary.wiley.com/doi/pdf/10.1029/2005JA011038.

Meyer, P., E. N. Parker, and J. A. Simpson, 1956: Solar cosmic rays of february, 1956 and their propagation through interplanetary space. *Phys. Rev.*, **104**, 768–783, URL https://link.aps.org/doi/10.1103/PhysRev.104.768.

Millan, R. and R. Thorne, 2007: Review of radiation belt relativistic electron losses. *Journal of Atmospheric and Solar-Terrestrial Physics*, **69 (3)**, 362–377, URL https://www.sciencedirect.com/science/article/pii/S1364682606002768, global Aspects of Magnetosphere-Ionosphere Coupling.

Mironova, I., K. Aplin, F. Arnold, G. Bazilevskaya, R. Harrison, A. Krivolutsky, K. Nicoll, E. Rozanov, E. Turunen, and I. Usoskin, 2015: Energetic particle influence on the earth's atmosphere. *Space Science Reviews*, **194 (1)**, 1–96.

Mironova, I., M. Sinnhuber, G. Bazilevskaya, M. Clilverd, B. Funke, V. Makhmutov, E. Rozanov, M. L. Santee, T. Sukhodolov, and T. Ulich, 2022: Exceptional middle latitude electron precipitation detected by balloon observations: implications for atmospheric composition. *Atmospheric Chemistry and Physics*, **22 (10)**, 6703–6716, URL https://acp.copernicus.org/articles/22/6703/2022/.

Nieder, H., H. Winkler, D. Marsh, and M. Sinnhuber, 2014: Nox production due to energetic particle precipitation in the mlt region: Results from ion chemistry model studies. **119**.

Oelhaf, H., T. von Clarmann, H. Fischer, F. Friedl-Vallon, C. Keim, G. Maucher, C. Sartorius, M. Seefeldner, O. Trieschmann, G. Wetzel, et al., 1995: Remote sensing of the arctic stratosphere with the new balloon-borne mipas-b2 instrument. *Proceedings of the 3rd European Workshop 18 to 22 September 1995*, 270–275.

Porter, H. S., C. H. Jackman, and A. E. S. Green, 1976: Efficiencies for production of atomic nitrogen and oxygen by relativistic proton impact in air. *The Journal of Chemical Physics*, **65 (1)**, 154–167, URL https://doi.org/10.1063/1.432812, https://doi.org/10.1063/1.432812.

Rodger, C. J., P. T. Verronen, M. A. Clilverd, A. Seppälä, and E. Turunen, 2008: Atmospheric impact of the carrington event solar protons. *Journal of Geophysical Research: Atmospheres*, **113 (D23)**, URL https://agupubs.onlinelibrary.wiley.com/doi/abs/10.1029/2008JD010702, https://agupubs.onlinelibrary.wiley.com/doi/pdf/10.1029/2008JD010702.

Roeckner, E., R. Brokopf, M. Esch, M. Giorgetta, S. Hagemann, L. Kornblueh, E. Manzini, U. Schlese, and U. Schulzweida, 2006: Sensitivity of simulated climate to horizontal and vertical resolution in the echam5 atmosphere model. *Journal of Climate*, **19 (16)**, 3771 – 3791, URL https://journals.ametsoc.org/view/journals/clim/19/16/jcli3824.1.xml.

Rohen, G., C. von Savigny, M. Sinnhuber, E. J. Llewellyn, J. W. Kaiser, C. H. Jackman, M.-B. Kallenrode, J. Schröter, K.-U. Eichmann, H. Bovensmann, and J. P. Burrows, 2005: Ozone depletion during

the solar proton events of october/november 2003 as seen by sciamachy. *Journal of Geophysical Research: Space Physics*, **110 (A9)**, URL https://agupubs.onlinelibrary.wiley.com/doi/abs/10.1029/2004JA010984, https://agupubs.onlinelibrary.wiley.com/doi/pdf/10.1029/2004JA010984.

Rusch, D., J.-C. Gérard, S. Solomon, P. Crutzen, and G. Reid, 1981: The effect of particle precipitation events on the neutral and ion chemistry of the middle atmosphere—i. odd nitrogen. *Planetary and Space Science*, **29 (7)**, 767–774, URL https://www.sciencedirect.com/science/article/pii/0032063381900489.

Sander, R., A. Baumgaertner, S. Gromov, H. Harder, P. Jöckel, A. Kerkweg, D. Kubistin, E. Regelin, H. Riede, A. Sandu, et al., 2011: The atmospheric chemistry box model caaba/mecca-3.0. *Geoscientific Model Development*, **4 (2)**, 373–380.

Sander, S., D. Golden, M. Kurylo, G. Moortgat, P. Wine, A. Ravishankara, C. Kolb, M. Molina, B. Finlayson-Pitts, R. Huie, et al., 2006: Chemical kinetics and photochemical data for use in atmospheric studies evaluation number 15. Tech. rep., Pasadena, CA: Jet Propulsion Laboratory, National Aeronautics and Space ....

S.Chapman, 1930: *A Theory of Upper-atmospheric Ozone*. Edward Stanford.

Schmidt, H., G. P. Brasseur, M. Charron, E. Manzini, M. A. Giorgetta, T. Diehl, V. I. Fomichev, D. Kinnison, D. Marsh, and S. Walters, 2006: The hammonia chemistry climate model: Sensitivity of the mesopause region to the 11-year solar cycle and co2 doubling. *Journal of Climate*, **19 (16)**, 3903 – 3931, URL https://journals.ametsoc.org/view/journals/clim/19/16/jcli3829.1.xml.

Sinnhuber, M., F. Friederich, S. Bender, and J. P. Burrows, 2016: The response of mesospheric no to geomagnetic forcing in 2002–2012 as seen by sciamachy. *Journal of Geophysical Research: Space Physics*, **121 (4)**, 3603–3620, URL https://agupubs.onlinelibrary.wiley.com/doi/abs/10.1002/2015JA022284, https://agupubs.onlinelibrary.wiley.com/doi/pdf/10.1002/2015JA022284.

Sinnhuber, M. and B. Funke, 2020: Chapter 9 - energetic electron precipitation into the atmosphere. *The Dynamic Loss of Earth's Radiation Belts*, Jaynes, A. N. and M. E. Usanova, Eds., Elsevier, 279–321, URL https://www.sciencedirect.com/science/article/pii/B9780128133712000093.

Sinnhuber, M., H. Nieder, and N. Wieters, 2012: Energetic particle precipitation and the chemistry of the mesosphere/lower thermosphere. *Surveys in Geophysics*, **33**.

Solomon, S., D. Rusch, J. Gérard, G. Reid, and P. Crutzen, 1981: The effect of particle precipitation events on the neutral and ion chemistry of the middle atmosphere: Ii. odd hydrogen. *Planetary*

and Space Science, **29 (8)**, 885–893, URL https://www.sciencedirect.com/science/article/pii/0032063381900787.

Solomon, S. C. and L. Qian, 2005: Solar extreme-ultraviolet irradiance for general circulation models. *Journal of Geophysical Research: Space Physics*, **110 (A10)**, URL https://agupubs.onlinelibrary.wiley.com/doi/abs/10.1029/2005JA011160, https://agupubs.onlinelibrary.wiley.com/doi/pdf/10.1029/2005JA011160.

Steil, B., M. Dameris, C. Brühl, P. Crutzen, V. Grewe, M. Ponater, and R. Sausen, 1998: Development of a chemistry module for gcms: first results of a multiannual integration. *Annales Geophysicae*, Copernicus GmbH, Vol. 16, 205–228.

Stiller, G. P., M. Kiefer, E. Eckert, T. von Clarmann, S. Kellmann, M. García-Comas, B. Funke, T. Leblanc, E. Fetzer, L. Froidevaux, M. Gomez, E. Hall, D. Hurst, A. Jordan, N. Kämpfer, A. Lambert, I. S. McDermid, T. McGee, L. Miloshevich, G. Nedoluha, W. Read, M. Schneider, M. Schwartz, C. Straub, G. Toon, L. W. Twigg, K. Walker, and D. N. Whiteman, 2012: Validation of mipas imk/iaa temperature, water vapor, and ozone profiles with mohave-2009 campaign measurements. *Atmospheric Measurement Techniques*, **5 (2)**, 289–320, URL https://amt.copernicus.org/articles/5/289/2012/.

Tegtmeier, S., J. Anstey, S. Davis, R. Dragani, Y. Harada, I. Ivanciu, R. Pilch Kedzierski, K. Krüger, B. Legras, C. Long, J. S. Wang, K. Wargan, and J. S. Wright, 2020: Temperature and tropopause characteristics from reanalyses data in the tropical tropopause layer. *Atmospheric Chemistry and Physics*, **20 (2)**, 753–770, URL https://acp.copernicus.org/articles/20/753/2020/.

Thomas, G. E. and K. Stamnes, 2002: *Radiative transfer in the atmosphere and ocean*. Cambridge University Press.

Turco, R. P., 1977a: On the formation and destruction of chlorine negative ions in the d region. *Journal of Geophysical Research (1896-1977)*, **82 (25)**, 3585–3592, URL https://agupubs.onlinelibrary.wiley.com/doi/abs/10.1029/JA082i025p03585, https://agupubs.onlinelibrary.wiley.com/doi/pdf/10.1029/JA082i025p03585.

———, 1977b: On the formation and destruction of chlorine negative ions in the d region. *Journal of Geophysical Research (1896-1977)*, **82 (25)**, 3585–3592, URL https://agupubs.onlinelibrary.wiley.com/doi/abs/10.1029/JA082i025p03585, https://agupubs.onlinelibrary.wiley.com/doi/pdf/10.1029/JA082i025p03585.

Verronen, P. and R. Lehmann, 2015: Enhancement of odd nitrogen modifies mesospheric ozone chemistry during polar winter. *Geophysical Research Letters*, **42 (23)**, 10 445 – 10 452, URL https://www.scopus.com/inward/record.uri?eid=2-s2.0-84953639789&doi=10.1002%

2f2015GL066703&partnerID=40&md5=137adffafb95a948f2ad5ddcf691bd5c, cited by: 14; All Open Access, Bronze Open Access, Green Open Access.

Verronen, P., M. Santee, G. Manney, R. Lehmann, S.-M. Salmi, and A. Seppälä, 2011: Nitric acid enhancements in the mesosphere during the january 2005 and december 2006 solar proton events. *Journal of Geophysical Research: Atmospheres*, **116 (D17)**.

Verronen, P., A. Seppälä, M. Clilverd, C. Rodger, E. Kyrölä, C.-F. Enell, T. Ulich, and E. Turunen, 2005: Diurnal variation of ozone depletion during the october–november 2003 solar proton events. *J. Geophys. Res*, **110**.

Verronen, P. T., M. E. Andersson, D. R. Marsh, T. Kovács, and J. M. C. Plane, 2016a: Waccm-d—whole atmosphere community climate model with d-region ion chemistry. *Journal of Advances in Modeling Earth Systems*, **8 (2)**, 954–975, URL https://agupubs.onlinelibrary.wiley.com/doi/abs/10.1002/2015MS000592, https://agupubs.onlinelibrary.wiley.com/doi/pdf/10.1002/2015MS000592.

———, 2016b: Waccm-d—whole atmosphere community climate model with d-region ion chemistry. *Journal of Advances in Modeling Earth Systems*, **8 (2)**, 954–975, URL https://agupubs.onlinelibrary.wiley.com/doi/abs/10.1002/2015MS000592, https://agupubs.onlinelibrary.wiley.com/doi/pdf/10.1002/2015MS000592.

Verronen, P. T., B. Funke, M. López-Puertas, G. P. Stiller, T. von Clarmann, N. Glatthor, C.-F. Enell, E. Turunen, and J. Tamminen, 2008: About the increase of hno3 in the stratopause region during the halloween 2003 solar proton event. *Geophysical Research Letters*, **35 (20)**, URL https://agupubs.onlinelibrary.wiley.com/doi/abs/10.1029/2008GL035312, https://agupubs.onlinelibrary.wiley.com/doi/pdf/10.1029/2008GL035312.

Verronen, P. T., A. Seppälä, E. Kyrölä, J. Tamminen, H. M. Pickett, and E. Turunen, 2006: Production of odd hydrogen in the mesosphere during the january 2005 solar proton event. *Geophysical Research Letters*, **33 (24)**, URL https://agupubs.onlinelibrary.wiley.com/doi/abs/10.1029/2006GL028115, https://agupubs.onlinelibrary.wiley.com/doi/pdf/10.1029/2006GL028115.

von Clarmann, T., D. A. Degenstein, N. J. Livesey, S. Bender, A. Braverman, A. Butz, S. Compernolle, R. Damadeo, S. Dueck, P. Eriksson, B. Funke, M. C. Johnson, Y. Kasai, A. Keppens, A. Kleinert, N. A. Kramarova, A. Laeng, B. Langerock, V. H. Payne, A. Rozanov, T. O. Sato, M. Schneider, P. Sheese, V. Sofieva, G. P. Stiller, C. von Savigny, and D. Zawada, 2020: Overview: Estimating and reporting uncertainties in remotely sensed atmospheric composition and temperature. *Atmospheric Measurement Techniques*, **13 (8)**, 4393–4436, URL https://amt.copernicus.org/articles/13/4393/2020/.

von Clarmann, T., N. Glatthor, U. Grabowski, M. Höpfner, S. Kellmann, A. Linden, G. Mengistu Tsidu, M. Milz, T. Steck, G. P. Stiller, H. Fischer, and B. Funke, 2006: Global stratospheric hocl distributions retrieved from infrared limb emission spectra recorded by the michelson interferometer for passive atmospheric sounding (mipas). *Journal of Geophysical Research: Atmospheres*, **111 (D5)**, URL https://agupubs.onlinelibrary.wiley.com/doi/abs/10.1029/2005JD005939, https://agupubs.onlinelibrary.wiley.com/doi/pdf/10.1029/2005JD005939.

von Clarmann, T., N. Glatthor, M. Höpfner, S. Kellmann, R. Ruhnke, G. P. Stiller, H. Fischer, B. Funke, S. Gil-López, and M. López-Puertas, 2005: Experimental evidence of perturbed odd hydrogen and chlorine chemistry after the october 2003 solar proton events. *Journal of Geophysical Research: Space Physics*, **110 (A9)**, URL https://agupubs.onlinelibrary.wiley.com/doi/abs/10.1029/2005JA011053, https://agupubs.onlinelibrary.wiley.com/doi/pdf/10.1029/2005JA011053.

von Clarmann, T., A. Linden, G. Echle, A. Wegner, H. Fischer, and M. Lopez-Puertas, 1996: Retrieval of pressure and temperature from mipas-envisat limb emission spectra. *Satellite Remote Sensing and Modeling of Clouds and the Atmosphere*, SPIE, Vol. 2961, 128–135.

Von Clarmann, T., A. Linden, H. Oelhaf, H. Fischer, F. Friedl-Vallon, C. Piesch, M. Seefeldner, W. Völker, R. Bauer, A. Engel, et al., 1995: Determination of the stratospheric organic chlorine budget in the spring arctic vortex from mipas b limb emission spectra and air sampling experiments. *Journal of Geophysical Research: Atmospheres*, **100 (D7)**, 13 979–13 997.

von Glasow, R., R. Sander, A. Bott, and P. J. Crutzen, 2002: Modeling halogen chemistry in the marine boundary layer 1. cloud-free mbl. *Journal of Geophysical Research: Atmospheres*, **107 (D17)**, ACH–9.

Wang, D. Y., M. Höpfner, C. E. Blom, W. E. Ward, H. Fischer, T. Blumenstock, F. Hase, C. Keim, G. Y. Liu, S. Mikuteit, H. Oelhaf, G. Wetzel, U. Cortesi, F. Mencaraglia, G. Bianchini, G. Redaelli, M. Pirre, V. Catoire, N. Huret, C. Vigouroux, M. De Mazière, E. Mahieu, P. Demoulin, S. Wood, D. Smale, N. Jones, H. Nakajima, T. Sugita, J. Urban, D. Murtagh, C. D. Boone, P. F. Bernath, K. A. Walker, J. Kuttippurath, A. Kleinböhl, G. Toon, and C. Piccolo, 2007: Validation of mipas hno_3 operational data. *Atmospheric Chemistry and Physics*, **7 (18)**, 4905–4934, URL https://acp.copernicus.org/articles/7/4905/2007/.

Wetzel, G., T. Von Clarmann, H. Oelhaf, and H. Fischer, 1995: Vertical profiles of n2o5 along with ch4, n2o, and h2o in the late arctic winter retrieved from mipas-b infrared limb emission measurements. *Journal of Geophysical Research: Atmospheres*, **100 (D11)**, 23 173–23 181.

Winkler, H., S. Kazeminejad, M. Sinnhuber, M.-B. Kallenrode, and J. Notholt, 2009: Conversion of mesospheric hcl into active chlorine during the solar proton event in july 2000 in the north-

ern polar region. *Journal of Geophysical Research: Atmospheres*, **114 (D1)**, URL https://agupubs.onlinelibrary.wiley.com/doi/abs/10.1029/2008JD011587, https://agupubs.onlinelibrary.wiley.com/doi/pdf/10.1029/2008JD011587.

———, 2011: Correction to "conversion of mesospheric hcl into active chlorine during the solar proton event in july 2000 in the northern polar region". *Journal of Geophysical Research: Atmospheres*, **116 (D17)**, URL https://agupubs.onlinelibrary.wiley.com/doi/abs/10.1029/2011JD016274, https://agupubs.onlinelibrary.wiley.com/doi/pdf/10.1029/2011JD016274.

Wissing, J., J. Bornebusch, and M.-B. Kallenrode, 2008: Variation of energetic particle precipitation with local magnetic time. *Advances in Space Research*, **41 (8)**, 1274–1278.

Wissing, J.-M., 2011: Analysis of particle precipitation and development of the atmospheric ionization module osnabrück - aimos. Ph.D. thesis, Universität Osnabrück.

Wissing, J. M. and M.-B. Kallenrode, 2009: Atmospheric ionization module osnabrück (aimos): A 3-d model to determine atmospheric ionization by energetic charged particles from different populations. *Journal of Geophysical Research: Space Physics*, **114 (A6)**, URL https://agupubs.onlinelibrary.wiley.com/doi/abs/10.1029/2008JA013884, https://agupubs.onlinelibrary.wiley.com/doi/pdf/10.1029/2008JA013884.

10 List of Figures

11 List of Tables

Acknowledgments

Firstly, I express my sincere gratitude to Dr. Miriam Sinnhuber for letting me work in her group as a doctoral student. Her guidance was very valuable and she helped me establish myself as an independent researcher in some regard. Secondly, I would like to thank my first supervisor Prof. Dr. Peter Braesicke for his help and support along the way and the friendly chats we had. I thank him for letting me vist Prof. Peter Hitchcock at Cornell University for a research stay of about six weeks. I would also like to thank Dr. Stefan Versick for his help with the EMAC model.

I also appreciate the friendly times with the group members and other members from the institute, Dr. Florian Haenel, Dr. Alexandra Laeng, Dr. Thomas Reddmann, Dr. Michael Höpfner, Dr. Gabriele Stiller, Dr. Sören Johansson, Andreas Bartenschlager, Lena Feld.

Finally, I thank my family members, my mother, Mrs. Mauchumi Bhattacharyya and my father, Mr. Dhiren Borthakur and my brother, Uddipta for their mental support during the entire duration of the Ph.D.